TAMPEREEN TEKNILLINEN YLIOPISTO
TAMPERE UNIVERSITY OF TECHNOLOGY

Sharif Chowdhury

Image Analysis Algorithms for Single-Cell Study in Systems Biology

Julkaisu 1381 • Publication 1381

Tampere 2016

Tampereen teknillinen yliopisto. Julkaisu 1381
Tampere University of Technology. Publication 1381

Sharif Chowdhury

Image Analysis Algorithms for Single-Cell Study in Systems Biology

Thesis for the degree of Doctor of Science in Technology to be presented with due permission for public examination and criticism in Tietotalo Building, Auditorium TB109, at Tampere University of Technology, on the 13th of May 2016, at 12 noon.

Tampereen teknillinen yliopisto - Tampere University of Technology
Tampere 2016

Supervisor: Professor Olli Yli-Harja,
Department of Signal Processing
Tampere University of Technology, Finland

Instructor: Associate Professor Andre S. Ribeiro,
Department of Signal Processing,
Tampere University of Technology, Finland

Pre-examiners: Professor Heikki Kälviäinen,
Professor of Computing, Monash University, Malaysia
and
Professor of Computer Science and Engineering,
Lappeenranta University of Technology (LUT), Finland

Antti Lehmussola, DSc
Director of Engineering
Quva Oy, Finland

Opponents: Professor Heikki Kälviäinen,
Professor of Computing, Monash University, Malaysia
and
Professor of Computer Science and Engineering,
Lappeenranta University of Technology (LUT), Finland

Daniel Nicorici, Ph.D.
Senior Researcher
Orion Corporation, Finland

ISBN 978-952-15-3732-5 (printed)
ISBN 978-952-15-3746-2 (PDF)
ISSN 1459-2045

Abstract

With the contiguous shift of biology from a qualitative toward a quantitative field of research, digital microscopy and image-based measurements are drawing increased interest. Several methods have been developed for acquiring images of cells and intracellular organelles. Traditionally, acquired images are analyzed manually through visual inspection. The increasing volume of data is challenging the scope of manual analysis, and there is a need to develop methods for automated analysis. This thesis examines the development and application of computational methods for acquisition and analysis of images from single-cell assays. The thesis proceeds with three different aspects.

First, a study evaluates several methods for focusing microscopes and proposes a novel strategy to perform focusing in time-lapse imaging. The method relies on the nature of the focus-drift and its predictability. The study shows that focus-drift is a dynamical system with a small randomness. Therefore, a prediction-based method is employed to track the focus-drift overtime. A prototype implementation of the proposed method is created by extending the Nikon EZ-C1 Version 3.30 (Tokyo, Japan) imaging platform for acquiring images with a Nikon Eclipse (TE2000-U, Nikon, Japan) microscope.

Second, a novel method is formulated to segment individual cells from a dense cluster. The method incorporates multi-resolution analysis with maximum-likelihood estimation (MAMLE) for cell detection. The MAMLE performs cell segmentation in two phases. The initial phase relies on a cutting-edge filter, edge detection in multi-resolution with a morphological operator, and threshold decomposition for adaptive thresholding. It estimates morphological features from the initial results. In the next phase, the final segmentation is constructed by boosting the initial results with the estimated parameters. The MAMLE method is evaluated with *de novo* data sets as well as with benchmark data from public databases. An empirical evaluation of the MAMLE method confirms its accuracy.

Third, a comparative study is carried out on performance evaluation of state-of-the-art methods for the detection of subcellular organelles. This study includes eleven algorithms developed in different fields for segmentation. The evaluation procedure encompasses a broad set of samples, ranging from benchmark data to synthetic images. The result from this study suggests that there is no particular method which performs superior to others in the test samples. Next, the effect of tetracycline on transcription dynamics of tetA promoter in *Escherichia coli* (*E. coli*) cells is studied. This study measures expressions of RNA by tagging the MS2d-GFP vector with a target gene. The RNAs are observed as intracellular spots in confocal images. The kernel density estimation (KDE) method for detecting the intracellular spots is employed to quantify the individual RNA molecules.

The thesis summarizes the results from five publications. Most of the publications are associated with different methods for imaging and analysis of microscopy. Confocal images with *E. coli* cells are targeted as the primary area of application. However, potential applications beyond the primary target are also made evident. The findings of the research are confirmed empirically.

Preface

This study is performed at the Department of Signal Processing, Faculty of Computing and Electrical Engineering, Tampere University of Technology, under the supervision of Professor Olli Yli-Harja.

I would like to express my sincere gratitude to my supervisor, Professor Olli Yli-Harja, for providing me the opportunity to work in this multidisciplinary field of research, introducing me to the subject and providing guidance throughout this study. I am indebted to my instructor, Associate Professor Andre S. Ribeiro, for his help in executing the research, guidance and advice. I am also thankful to Professor Heikki Kälviäinen and DSc. Antti Lehmussola for pre-examining the manuscript of this thesis and for providing insightful suggestions.

I would also like to take this opportunity to thank all the present and past members of the Laboratory of Biosystem Dynamics and the Computational Systems Biology research group. I show my gratitude to my co-authors for their help and collaboration. I am especially thankful to DSc. Pekka Ruusuvuori, and Assistant Professor Meenakshisundaram Kandhavelu, for their support in different stages of this study. I appreciate supports of my colleagues at my present workplace, Wapice Oy.

I am grateful to the department secretary, Virve Larmila, and the coordinator Elina Orava, for their excellent help with practical matters. The funding from Tampere Graduate School in Information Science and Engineering (TISE) is acknowledged.

Finally, I am indebted to my parents, my sisters and their families. I am especially thankful to my wife, Sakira Hassan, for her endless endurance.

Tampere, March 2016
Sharif Chowdhury

Contents

Acronyms

2D	Two dimensional
3D	Three dimensional
BM3D	Block-matching and 3D filtering
BPF	Band-pass filtering
CCD	Charge-coupled device
E. coli	*Escherichia coli*
EM	Expectation maximization
FPD	Feature point detection
GFP	Green fluorescent protein
HD	h-dome
IMM	Interacting multiple model
KDE	Kernel density estimation
LBD	Laboratory of Biosystem Dynamics, Department of Signal Processing, TUT, Finland
LC	Local comparison
LDI	Linear dynamical system
LEF	Local enhancement filtering
LoG	Laplacian of Gaussian
MAD	Mean absolute deviation
MAMLE	Multi-resolution analysis with maximum-likelihood estimation

MGI	Granulometric analysis
MS2d	Bacteriophage MS2-dimer
MW	Multiscale product of wavelet coefficients
nm	Nanometer
NP-hard	Non-deterministic polynomial-time hard
OS	Over-segmentation
RNA	Ribonucleic acid
RT	Room temperature
S. aureus	*Staphylococcus aureus*
SE	SourceExtractor
SPL	Sub-pixel localization
THE	Top-hat filtering
TN	True negative
TP	True positive
US	Under-segmentation
z-axis	Normal axis to the imaging plane
z-slices	Slice of image along z-axis
µm	Micrometer

List of publications

The publications are referred as [Publications X] in this thesis, where X is a roman numeral.

I S. Chowdhury, M. Kandhavelu, O. Yli-Harja, and A.S. Ribeiro, "An interacting multiple model filter-based autofocus strategy for confocal time-lapse microscopy," *Journal Microscopy*, 245(3):265-275, March 2012.

II S. Chowdhury, M. Kandhavelu, O. Yli-Harja, and A.S. Ribeiro, "Cell segmentation by multi-resolution analysis and maximum likelihood estimation (MAMLE)," *BMC Bioinformatics*, 14(Suppl 10):S8, August 2013.

III P. Ruusuvuori, T. Äijö, S. Chowdhury, C. Garmendia-Torres, J. Selinummi, M. Birbaumer, A.M. Dudley, L. Pelkmans, and O. Yli-Harja, "Evaluation of methods for detection of fluorescence labeled subcellular objects in microscope images," *BMC Bioinformatics*, 11:248, May 2010.

IV A.-B. Muthukrishnan, M. Kandhavelu, J. Lloyd-Price, F. Kudasov, S. Chowdhury, O. Yli-Harja, and A.S. Ribeiro, "Dynamics of transcription driven by the tetA promoter, one event at a time, in live Escherichia coli cells," *Nucleic Acids Research*, 40(17):8472-8483, September 2012.

V S. Chowdhury, P. Ruusuvuori, P. Liberali, P. Rämö, L. Pelkmans, and O. Yli-Harja, "Automated cell tracking and cell lineage construction with improved performance," In *Proceedings of the 6th International Workshop on Computational Systems Biology*,(Århus), Denmark, June 10-12, 2009, pp. 27-30.

The contributions of the author to the included publications:

In Publication I, S. Chowdhury conducted the research, designed and implemented the methods and took part in the experiments. He was responsible for writing the manuscript. Publication I proposes a novel strategy for focusing microscopes in time-lapse imaging.

In Publication II, the author of the thesis (S. Chowdhury) carried out the research, proposed and implemented the ideas, selected samples for evaluation, performed the computational experiments and evaluated the results. He was also responsible for preparing the manuscript. Publication II presents a novel method for segmenting cells from microscopy images.

Publication III[1] evaluates eleven methods for segmenting subcellular organelles from microscopy images. The author of the thesis (S. Chowdhury) contributed in implementing several methods (i.e. h-dome detection (HD), Feature point detection (FPD), Source Extractor(SE), Sub-pixel localization (SPL)) that were studied in this publication. The supplementary material of this publication includes a toolbox as a CellProfiler compatible module for detecting subcellular organelles. S. Chowdhury was also responsible for implementing the toolbox. In addition, he took part in analyzing the results and contributed by describing several methods(HD, FPD, SE, SPL) in the manuscript.

A draft of Publication III is a part of the doctoral thesis of P. Ruusuvuori [1]. As a primary author, P. Ruusuvuori planned the study, wrote majority of the manuscript, was mainly responsible for experimental calculations, and implemented part of the algorithms.

Publication IV[2] presents a multidisciplinary research that studied transcription dynamics in *Escherichia coli* cells. This study acquired *in vivo* measurements in order to score the production events of individual RNA molecules and constructed the interval between transcription events. The measurement protocol required time-lapse images at 60 seconds interval for a period of an hour.

S. Chowdhury contributed to Publication IV by designing the image analysis system to detect individual RNA molecules from the acquired images. Moreover, he was responsible for developing the imaging system that allowed

[1]Publication III is a part of P. Ruusuvuori's doctoral thesis [1].
[2]Publication IV is a part of A.-B. Muthukrishnan's doctoral thesis [2].

acquisition of *in vivo* measurements required for this study. The imaging system was initially proposed as a part of the Publication I. The author of the thesis took part in manuscript preparation by contributing text to the section that describes image analysis methods for the detection of cells and spots.

Publication IV was included by A.-B. Muthukrishnan in her doctoral dissertation [2]. The previous use of this publication concerns the biological results and findings presented in this article.

In Publication V, the author of the thesis planned the study, implemented the method and was responsible for writing the manuscript. A method for segmenting cells was studied as a part of a tracking system in Publication V. Publication V developed the preliminary concept and contributed as the necessary background information for the Publication II.

1 Introduction

Cells are the fundamental building blocks of life. The study of cells provides a compelling insight into biological systems [3–7]. An investigation in systems biology research usually starts with a hypothesis and a model of the underlying system. Next, a set of laboratory experiments is designed for collecting samples to validate the model. The collected samples from the experiment are then analyzed to extract information. Finally, the hypothesis is evaluated against the experimental results for justification [7, 8]. The proceeding of a trivial systems biology study is exemplified by a hypothetical illustration in Figure 1.1. The research carried out within the scope of this thesis, contributes to different parts of this process.

A study in systems biology requires observation of a large number of events due to the inherent stochasticity of biological processes. In addition, studies at the single-cell level are becoming increasingly popular for their inherent capability to provide precise information. Recent advances in microscopy that allow high-throughput imaging and observation of a large number of events at the single-cell level have opened up a new paradigm for systems biology study. Consequently, high-content screening has become an indispensable tool for cell and molecular biology research [9–11].

High-quality, high-content screening with an automated microscope is the first key step toward high-throughput image analysis. Traditional approaches require repetitive and manual assistance to ensure high-quality imaging [7]. Repetitive and manual calibration of a microscope for focusing is expensive and restricted by human efficiency. Recent advancements in microscopy and control systems have achieved a significant improvement in microscope automation [12]. As a part of this thesis, recent developments in microscopy and associated technology are discussed.

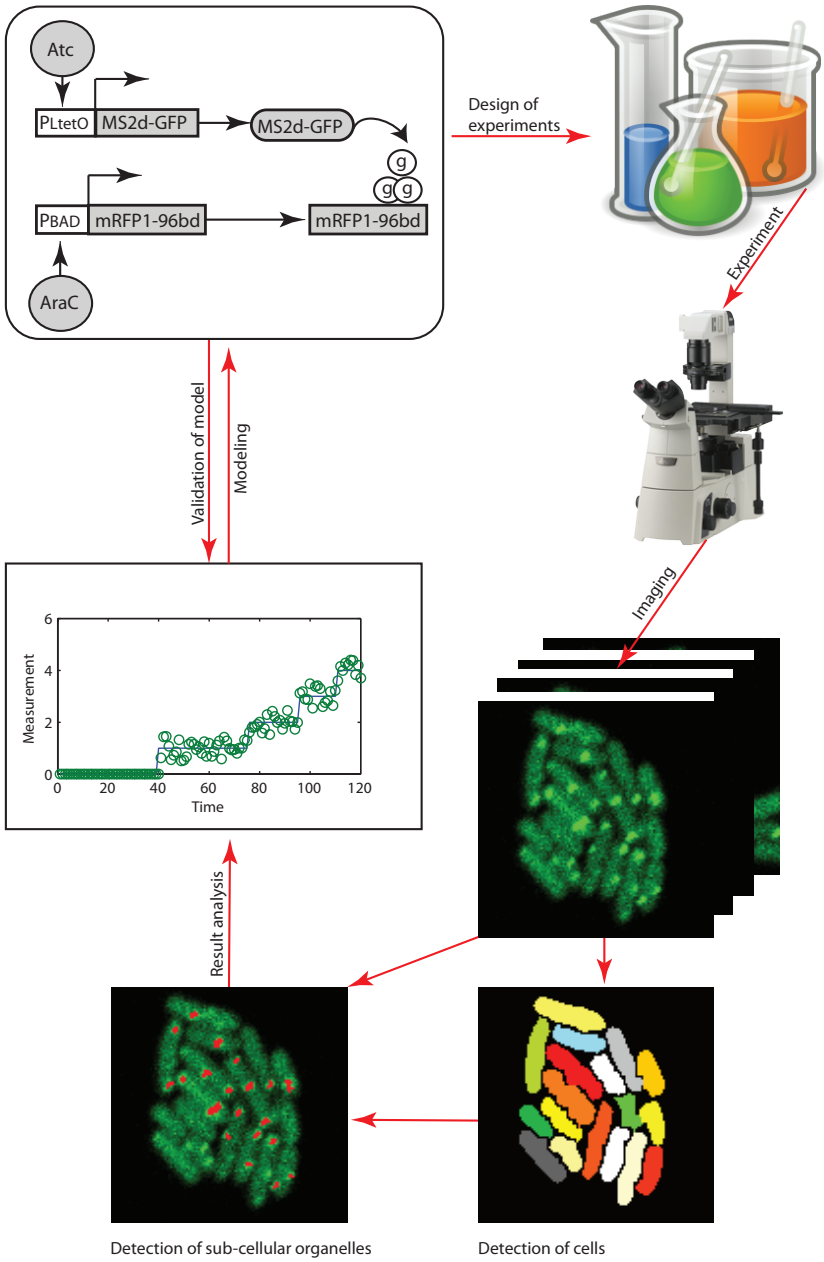

Figure 1.1: *Proceedings of a systems biology study. The subsequent processes are pointed with arrowheads. The detected cells are labelled with colors (bottom right). The red marks represent the detected subcellular organelles (bottom left).*

High-throughput microscopes are generating enormous volumes of data from laboratory experiments. The manual extraction of information from high-content screens is prone to subjective variance and lack in quantitative reproducibility. This indicates the need for developing methods to facilitate automated analysis. Several methods have been proposed for detecting cells from microscopy images [13 – 16]. However, most of the developed algorithms are incapable of handling the phenotypic diversity of cells. Furthermore, the application of most of the developed methods is subjected to imaging modalities.

Apart from these, intracellular organelles and molecules also contain invaluable information regarding cellular processes and interactions. Imaging of intracellular organelles enables the observation and study of individual events at a single-cell level [7]. Intracellular organelles and molecules are usually observed as dimensionless spots and vary in number. The context of detection methods for intracellular organelles is therefore distinct and indicates the need for a study in this area.

1 Research question and aim of the study

The holistic aim of this thesis is to study and develop methods that facilitate high-content screening and enable automated analysis of high-throughput data. In this regard, this study poses following research questions:

Research questions on time-lapse microscopy:

Q1: What is the most suitable objective metric for focusing microscope during time-lapse imaging?

Q2: How to compensate the focus-drift with minimal intervene to the sample?

Research questions on image analysis at the level of single-cell:

Q3: How can individual cells be segmented from a dense cluster of cells?

Q4: Is there any way to incorporate unsupervised

```
learning for boosting the segmentation results?
```

Research question on image analysis at the level of subcellular organelles:

```
Q5: What is the best available approach for segmenting
subcellular organelles?
```

The first group of research questions (Q1 and Q2) are motivated to ensure high-quality imaging. To address these questions, a collection of methods for focusing microscopes is evaluated and the nature of focus-drift is studied. The result of this research is reported in Publication I. The second group of research questions (Q3 and Q4) are targeted to the problem of cell detection, while the Q5 is motivated to detect intracellular organelles from microscopy images. Publication II addresses Q3 and Q4. The answer to the Q5 is one of the main findings reported in Publication III. All these questions are significant when high-quality results are expected from a systems biology study.

2 Outline of the thesis

Chapter 2 begins with a brief introduction to different kinds of microscopy techniques and the challenges of time-lapse microscopy. Classical approaches for segmenting cells from microscopy images are then discussed. In the end, a collection of state-of-the-art methods for segmenting subcellular organelles is reviewed.

Chapter 3 outlines the outcomes of this research. The contributions are primarily targeted to high-throughput imaging and image analysis methods for microscopy. It encompasses the theoretical development of methods as well as practical applications of the developed methods in order to understand systems biology of *E. coli* at the single-cell level.

Chapter 4 makes a remark on the overall study and raises a set of challenges, with an indication of possible routes by which these challenges can be overcome.

Finally, Chapter 5 concludes the dissertation by listing the main results of this study.

2 Imaging systems and analysis algorithms for microscopy images

The discovery of the cell and invention of the microscope have been closely related to each other from an early stage. Microscopy and the understanding of the cell have greatly evolved since then. Different techniques for microscopy are briefly introduced at the beginning of this chapter. In time-lapse imaging, a microscope requires adjustments of focus at a short interval to compensate for drifts in the focal plane. The focus-drift is identified as a major challenge in time-lapse microscopy and this problem is discussed with an indication of possible solutions.

Apart from these, analysis of high-throughput data poses an even greater challenge to single-cell study. Recent advances in pattern recognition algorithms for cell segmentation are making it an indispensable part of cell and molecular biology research. Classical approaches for cell segmentation are then discussed. Subcellular organelles and intracellular molecules are also vital sources of information regarding dynamics of the gene regulation [7]. Considering their increasing importance, several approaches for the detection of subcellular organelles are reviewed.

1 The microscope

The microscope is a device that allows observation of small objects by enlarging their projections on the plane of image construction. It utilizes optical magnification techniques for increasing the distance among rays on the plane of projection. Microscopes have improved greatly since their initial invention. Modern micro-

scopes are capable of projecting nanometer-scale objects with a high degree of precision [17].

1.1 Bright-field microscope

A bright-field microscope is the simplest type of microscope. The optical schematic of a bright-field microscope is illustrated in Figure 2.1 [12]. It illuminates the specimen by placing a lamp underneath the stage. A condenser lens is used for focusing light on the specimen. The focused light is then transmitted through the objective lens. The orientation of the image is often altered by a projector lens. Finally, the specimen is viewed through the ocular.

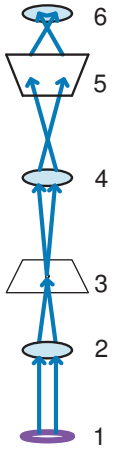

Figure 2.1: *Schematic diagram of a bright-field microscope. (1) Light source, (2) Condenser lens, (3) Specimen, (4) Objective lens, (5) Projector lens, (6) Ocular lens.*

1.2 Fluorescence microscope

A fluorescence microscope allows imaging with fluorescent tagging of cells and subcellular organelles, which in turn enhances the contrast in the acquired image. The working principle of a fluorescence microscope is depicted in Figure 2.2. First, fluorescent molecules are excited with high-energy photons. Consequently, the fluorescent molecules absorb the excitation photons and transit from the ground state to the E2 state (Figure 2.2(b)). A part of the absorbed energy is released through non-radiative processes (for instance, mechanical vibration or heat) and the molecules reach the state E1 [11, 18, 19]. Finally, the molecules return back to the ground state and the remaining energy is released as a photon emission.

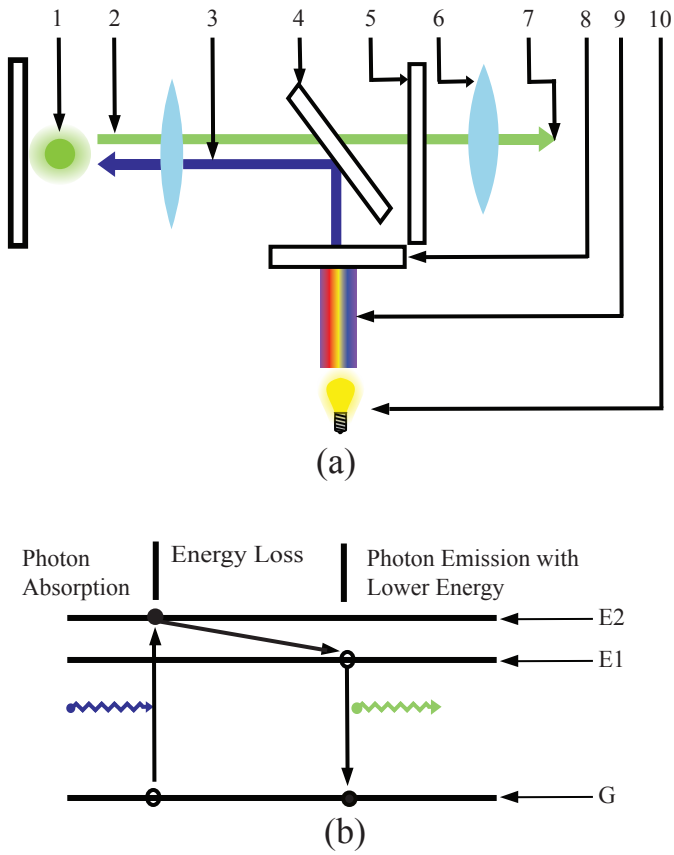

Figure 2.2: *The fluorescence microscope and its principles. (a) Optical schematic of a fluorescence microscope. (1) Specimen, (2) Fluorescent wave, (3) Excitation wave, (4) Dichroic mirror, (5) Emission filter, (6) Ocular lens, (7) Image generation plane, (8) Excitation filter, (9) Wide-band light and (10) Light source. (b) Principles of fluorescence. (G) Ground state, (E1) Energy state E1 and (E2) Energy state E2 (E2 > E1).*

Since the energy gap between E1 (Figure 2.2(b)) and the ground state is constant for a certain type of fluorescent molecules, the resulting photons have identical energy. Moreover, according to Planck's relation $E = h\nu$, where E is the photon energy, h is the Planck's constant, and ν is the frequency of the emitted wave. As a result, the emitted wave has a constant wavelength [12, 18, 19].

Figure 2.2(a) represents a simplified schematic of a fluorescence microscope. The wide-band lamp acts as the primary source of light. An excitation filter is used to prohibit transmission of the unwanted band of light wave. A dichroic mirror reflects the excitation wave toward the specimen and the fluorescent wave is

emitted. The emitted wave passes through the dichroic mirror. An emission filter separates the fluorescent wave from any other interfering sources. Finally, the filtered wave is either viewed or captured in digital format [12].

1.3 Confocal microscope

A confocal microscope is an integrated system that includes a fluorescence microscope, laser sources, a system for scanning, and a computing unit [18]. Unlike in classical microscopy, a confocal microscope scans only a single point at a time from a certain depth. The image is constructed by arranging the collection of scanned pixels into a grid [20]. The working principle of a regular confocal microscope is illustrated in Figure 2.3.

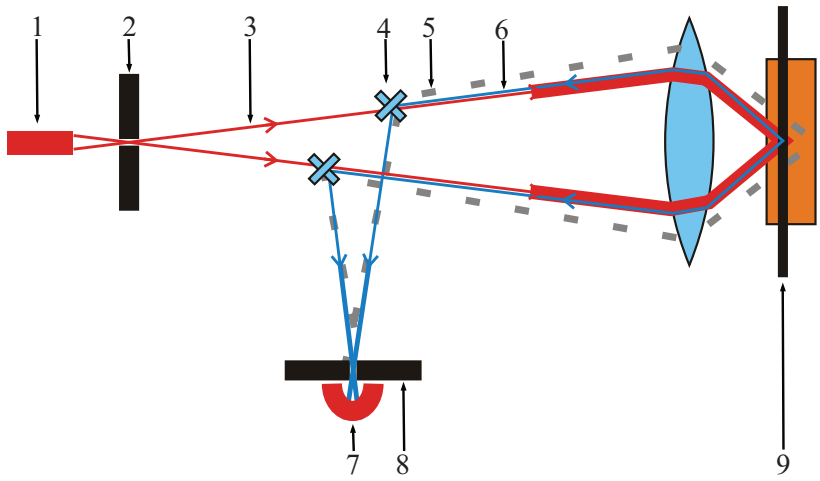

Figure 2.3: *Schematic diagram of a confocal microscope. (1) LASER source, (2) Aperture, (3) Excitation wave, (4) Dichroic mirror, (5) Fluorescent wave(wrong focal plane), (6) Fluorescent wave(proper focal plane), (7) Image construction plane, (8) Aperture, (9) Focal plane. (Inspired from "Wikipedia, the free encyclopedia," published with GNU free documentation license agreement).*

In confocal microscopy, the excitation laser and the detector are placed on the same side of the specimen. The purpose of the dichroic mirror is identical as it has been mentioned in the section on fluorescence microscopy (Section 1.2). The scan controller orchestrates the projection of laser that illuminates only a specific point on the specimen. A pinhole of a small diameter allows the fluorescent beams only from a specific focal depth. The scan controller is equipped with two mirrors that rotate in synch to ensure precise scanning of a single point. Finally, the

fluorescent beam emitted through the pinhole is detected and stored in digital form [18]. The combination of the raster scanner along with the small aperture provides superior images to those obtained with most other modalities [21].

Confocal microscopy has been become a regular tool in biological imaging due to its precision. However, a confocal microscope has a narrow depth of focus and can acquire an image only from a certain depth [12]. Therefore, the objective method for automated focusing is considered as an integral part of a confocal microscope.

2 Challenges in live-cell imaging: focus-drift and photobleaching

The continuous alteration of position of the focal plane is a regular phenomenon that occurs during time-lapse imaging [22, 23]. This phenomenon is known as focus-drift. The focus-drift in time-lapse microscopy is demonstrated with two examples in Figure 2.4. A periodic execution of the focus adjustment is indeed an essential part of the system for time-lapse microscopy [22]. Traditional systems for drift compensation acquire a stack of images along the normal axis (z-axis) to the imaging plane [24]. Therefrom, the position of the focal plane is determined by maximizing an objective function. The resolution required for focusing is often coarser than the resolution required for analysis purposes. Thus, a focusing system performs the imaging in two steps. First, it acquires a stack of images with a lower resolution to determine the position of the focal plane. Then an image with full resolution is acquired from the neighborhood of the selected position [25].

Time-lapse imaging acquires a series of images from a single specimen over a prolonged period. Multiple exposures of the laser to the specimen cause a gradual decline in the fluorescence level, which is known as photobleaching [26, 27]. It imposes a critical limit on the duration of imaging [26]. The images that are acquired for focusing react to the bleaching even more severely. In order to reduce the number of image acquisitions, state-of-the-art methods resort to various optimization techniques for focusing (for example, adaptive step size [28], function fitting [29], and Fibonacci search [30]). In Publication I, a novel strategy for drift compensation is proposed. The proposed method is based on the prediction of focus-drift.

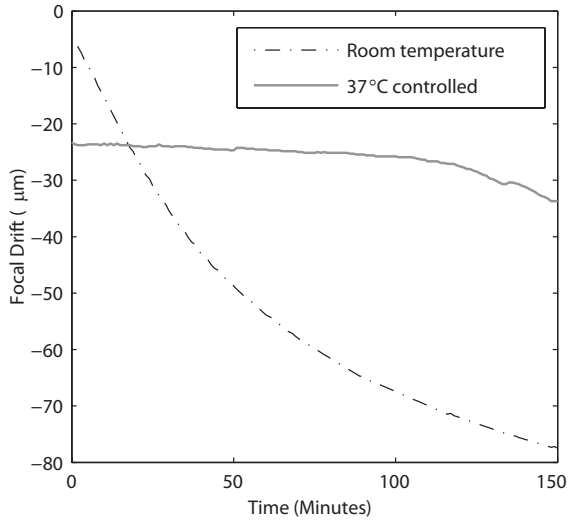

Figure 2.4: *Focus-drift as a function of time in two different thermal conditions (at room temperature and at 37°C) (source Publication I).*

3 Objective functions for focusing

An objective function, that evaluates the degree of focus in an image, is commonly referred to as a focus-function [24, 31]. A focused image contains information from a single imaging plane with a narrow depth of focus and contains sharper edges [32, 33]. Conversely, a defocused system acts as a low-pass filter that blurs the sharp transition of intensity or edges in the acquired image. Conventional focus-functions exploit the degree of sharpness as the objective criterion for focusing. Several metrics have been mentioned in scientific literature as a quantitative measure for focus [34]. A collection of contemporary methods for focusing is revisited [24, 33, 35−40]. The numerical realization of these focus-functions are expressed in Table 2.1.

Classical focus-functions often estimate gradient vectors as the indirect measure of the degree of sharpness. The Tenegrad function (f_{Tenegrad}) is a well-known metric for focusing that relies on this ideology. This function estimates the gradient vectors in horizontal and vertical directions and then, enumerates the squared sum of the gradient vectors to obtain the focus metric [35]. Gradient vectors are obtained as the linear convolution between the Sobel operator and the respective image [35, 41]. Vollath F4 ($f_{\text{VollathF4}}$) is another function, widely reported as a

Table 2.1: Objective functions for focusing

Method	Comment
$f_{\text{Tenegrad}} = \sum_{x=1}^{D_h} \sum_{y=1}^{D_v} \left(\mathbf{G}_h(x,y)^2 + \mathbf{G}_v(x,y)^2 \right)$	$\mathbf{G}_h$, and $\mathbf{G}_v$ are horizontal and vertical gradient vectors in respective order.
$f_{\text{VollathF4}} = \sum_{x=1}^{D_v-1} \sum_{y=1}^{D_v} \mathbf{I}(x,y) \times \mathbf{I}(x+1,y) - \sum_{x=1}^{D_h-2} \sum_{y=1}^{D_v} \mathbf{I}(x,y) \times \mathbf{I}(x+2,y)$	$\mathbf{I}(x,y)$ is the intensity of a pixel located at the coordinate (x,y).
$f_{\text{Brenner}} = \sum_{x=1}^{D_h-n} \sum_{y=1}^{D_v} \left(\mathbf{I}(x,y) - \mathbf{I}(x+n,y) \right)^2$	n is an arbitrary positive integer constant.
$f_{\text{Fano}} = \frac{1}{D_h \times D_v \times E[\mathbf{I}(.)]} \sum_{x=1}^{D_h} \sum_{y=1}^{D_v} \left(\mathbf{I}(x,y) - E[\mathbf{I}(.)] \right)^2$	$E[\mathbf{I}(.)]$ is the expected value of the intensity of an image.
$f_{\text{Power}} = \sum_{x=1}^{D_h} \sum_{y=1}^{D_v} \mathbf{I}(x,y)^2$	

compelling metric for focusing [33, 36, 42]. It is enumerated as the difference between the autocorrelation functions at lag '1' and at lag '2' [36]. The Brenner gradient (f_{Brenner}) is defined as the squared sum of the first difference of intensities separated by n pixels [37]. The n is an arbitrary integer usually set to a small and positive value; for example, '2'. The first difference is realized in either the horizontal or the vertical direction.

The Fano factor, or normalized variance, has recently been reported as a robust function for focusing [33]. The Fano factor (f_{Fano}) of an image is estimated as the intensity variance normalized with the expected value ($E[\mathrm{I}(.)]$) of pixel intensity [43]. Apart from these, image power (f_{Power}), or the squared sum of pixel intensity,

is also mentioned as a reliable metric for focusing [24].

Focus-functions listed in the Table 2.1 perform focusing solely based on a stack of images acquired at a single time point. Their applications are therefore mostly targeted to *in vitro* imaging, where measurements are independent of each other. In contrast, subsequent frames in time-lapse imaging, acquired from an *in vivo* experiment, are highly correlated. It is imperative to consider this correlation while focusing. Because, it is not rare that more than one z-planes are scored equally by a certain focus-function, which, combined with the stochastic nature of the biological systems under measurements, might lead to a repetitious alteration of the focus from one plane to another. An unstable or incoherent time series is difficult to analyze, especially when the analysis is performed automatically. The Figure 2.5 exemplifies the stated artifact. Here, the Tenegrad function is adopted for focusing that led to an 'incoherent' time series by switching the focal plane between consecutive frames. The defocused regions are depicted inside the rectangles. This limitation is mitigated by addressing the dependence between subsequent frames during focusing.

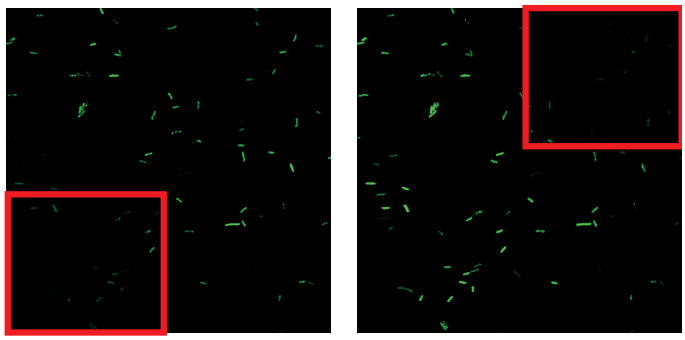

Figure 2.5: *Two consecutive frames in time-lapse microscopy. The Tenegrad function is used for focusing. The defocused region is highlighted by placing a red rectangle in the respective frames (source Publication I).*

Pearson's correlation is a well-founded metric to evaluate the linear correlation between two sets of data [44]. Time-lapse microscopy often resorts to Pearson's correlation to quantify the similarly between subsequent frames [38]. The focusing is achieved by maximizing Pearson's correlation between consecutive frames in time. The reference frame at the start is selected either manually or by using a secondary method. Pearson's correlation between two images is computed as the covariance of the pixel intensities of the respective images normalized by their

standard deviations as

$$f_{\text{Pearson's}} = \frac{1}{D_h \times D_v} \sum_{x=1}^{D_h} \sum_{y=1}^{D_v} \frac{\left(\mathbf{I}^r_{t-1}(x,y) - E\left[\mathbf{I}^r_{t-1}(.)\right]\right) \times \left(\mathbf{I}_t(x,y) - E\left[\mathbf{I}_t(.)\right]\right)}{\sigma^r_{t-1} \times \sigma_t}, \tag{2.1}$$

where $\mathbf{I}^r_{t-1}(.)$ is the reference image selected at $t-1$, $\mathbf{I}_t(.)$ is an image from stack at t and σ^r_{t-1} , σ_t are the standard deviations of the pixel intensities of the respective images.

4 Cell segmentation

The primary objective of an algorithm for cell segmentation is to detect individual cells from an image-based assay. A regular method for cell segmentation can be viewed as a pipeline with three logical steps: i) image enhancement and preprocessing, ii) detection of the foreground from the background or the initial segmentation and, iii) post-processing or the correction of initial segmentation [13, 45, 46]. Table 2.2 briefly describes a collection of contemporary methods for cell detection. The paradigm of the cell segmentation is illustrated with a hypothetical example in Figure 2.6.

4.1 Image enhancement and preprocessing

Noise is an inherent property of imaging systems [47]. Regular systems for imaging are prone to both linear and nonlinear noise. Classical approaches realize noise as an additive process. Linear filters are applied in the spatial domain to suppress the noise [47]. The resultant output from the filtering is formed according to

$$\bar{\mathbf{f}}(x,y) = \mathbf{W} \otimes \mathbf{f}(x,y) = \sum_{i=\frac{-M}{2}}^{\frac{+M}{2}} \sum_{j=\frac{-N}{2}}^{\frac{+N}{2}} (\mathbf{W}(\frac{M}{2}+i, \frac{N}{2}+j) \times \mathbf{f}(x-i, y-j)), \tag{2.2}$$

where $\mathbf{f}(x,y)$ is the noisy image, $\bar{\mathbf{f}}(x,y)$ is the filtered image, $\mathbf{W}$ is the filtering window and M, N are the size of a two dimensional window. Although a spatial-domain filter suppresses the noise by a certain factor, it is incapable of removing the noise completely [47].

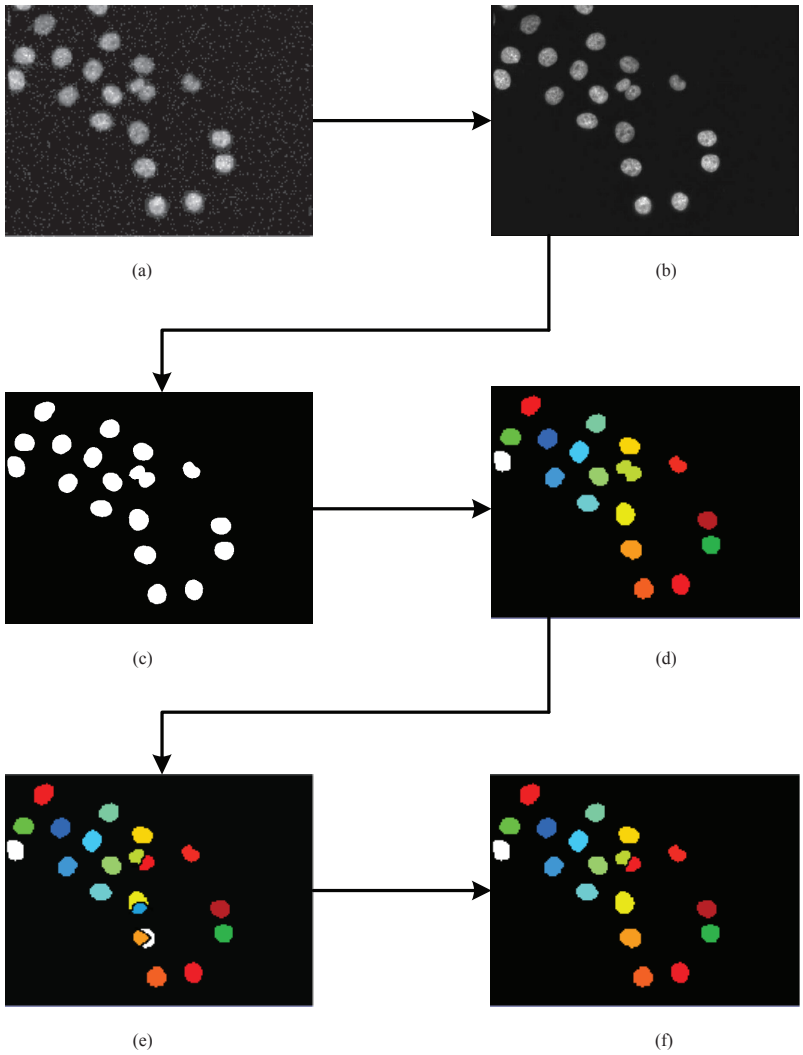

Figure 2.6: *Illustration of different steps of cell segmentation. (a) Noisy image, (b) Enhanced image, (c) Segmentation of foreground objects from the background, (d) Region labeling after segmentation, (e) Cell detection from under-segmented colony, (f) Correction of over-segmentation.*

Table 2.2: Contemporary methods for cell detection

Method	Description	Features and free parameters
Cellprofiler [13]	Cell segmentation in Cellprofiler is performed in two steps. First, it separates objects from the background by thresholding. Next, the clumped objects are segmented by considering shape or intensity as the feature for discrimination. Cellprofiler provides several alternatives for the automated selection of threshold and the segmentation of the clumped cells.	Intensity and shape are considered as the primary feature. There is no fixed number of parameters, it provides several alternatives and the number of parameters is also varied accordingly.
Nuclei segmentation [46]	Nuclei segmentation method employs the Otsu's procedure [48] to detect foreground objects from the background. Next, the Watershed algorithm [49] is applied for segmenting the under-segmented colonies. The fragments of the over-segmented nuclei are merged by a post-processing step.	Nuclei segmentation method has one free parameter, minimum size of a nuclei. Compactness and intensity are used as the primary feature. This method is specifically tailored for detecting objects from fluorescence microscopy images containing compact and circular shaped nuclei.
Schnitzcells [16]	Schnitzcells provides solutions for segmentation and tracking of cells from images acquired with a confocal or phase contrast microscope. The segmentation of cells in Schnitzcells is a multi-stepped process. First, it applies edge detection for generating the initial segmentation. Next, it splits long or clumped cells into smaller fragments. Finally, it discriminates the false positives based on size.	It has more than 10 free parameters that, without proper tuning, cause the accuracy of the segmentation to decrease notably. The parameters and the method are specially designed for detecting *E. coli* and *Bacillus subtilis* cells. The parameters are related to several features i.e. the area, width, length, edge, solidity of the detected object.
FarSIght [50]	FarSIght toolkit exploits graph-cuts [50] algorithm for segmenting foreground signals from the background. Then, the nuclear seed points are detected with the Laplacian of Gaussian (LoG) filter [50] in multi-resolution.	It has three parameters i) scaling factor for the graph-cut, determined by the smoothness of the intensity, ii) a range of scales to parameterize the LoG filter and, iii) a parameter for resolution.
Level set segmentation and tracking [Publication V]	This method is designed for simultaneously tracking and segmentation cells in time-series images. The cells are initially detected with Otsu's threshold [48]. Then, the level set[51] evolution is performed to finalize the segmentation and tracking of cells.	This method has two parameters related to the level set evolution. The parameters act as weight factors for combining individual features i.e. motion of cells, edges.

Noise reduction in the frequency domain is preferred under the assumption of a noisy signal as a convolved copy of the original source. The arrangements of sensory elements in the sensor array or the optical systems are often responsible for introducing systematic artifacts. The original source is often recovered by inverse filtering [47]. The classical approach for inverse filtering is based upon the Fourier transform and expressed as

$$\bar{\mathbf{f}}(x, y) = \mathcal{F}^{-1}\left(\frac{\mathbf{F}(u, v)}{\mathbf{H}(u, v)}\right). \tag{2.3}$$

Here the image after denoising is represented by $\bar{\mathbf{f}}(x, y)$. The frequency spectrum of the corrupted signal is denoted as $\mathbf{F}(u, v)$. Transfer function of the process, altering the original source, is presented by $\mathbf{H}(u, v)$. The $\mathcal{F}^{-1}(.)$ function symbolizes the inverse operation of the Fourier transform.

The Wiener filter is a robust variant of the classical approach for inverse filtering. It is applicable for removing noise from both linear and nonlinear sources. However, it requires additional information regarding the power spectrum of the noise process. This filter minimizes the expected value of the noise power. The denoised image is obtained as the inverse Fourier transform of the resulting frequency spectrum as

$$\bar{\mathbf{F}}(u, v) = \frac{1}{\mathbf{H}(u, v)} \frac{\mathbf{H}(u, v)^* \times \mathbf{H}(u, v)}{\mathbf{H}(u, v)^* \times \mathbf{H}(u, v) + \mathbf{C}_K} \mathbf{G}(u, v), \tag{2.4}$$

where $\bar{\mathbf{F}}(u, v)$ and $\mathbf{G}(u, v)$ are frequency spectrums of the filtered image and the degraded image in respective order. $\mathbf{H}(u, v)$ is the transfer function of the system that introduces linear noise and $\mathbf{H}(u, v)^*$ is its complex conjugate. $\mathbf{C}_K$ is an arbitrary constant that can be derived from the power spectrum of signal and noise. Depending on the value of the constant $\mathbf{C}_K$, the Wiener filter maintains a balance between the inverse filter and noise-removal filter [52].

In Publication II, a recently developed technique known as block-matching and 3D filtering (BM3D) is adopted for noise removal [53]. BM3D is a cutting-edge variation of classical approaches for inverse filtering. BM3D is based on enhanced and sparse representation of an image in the transform domain. BM3D fragments a 2D image into fixed-size blocks and then searches for blocks that match a certain reference block as the first step to obtain enhanced sparse representation. The matching blocks are then arranged into a 3D stack called a 'group'. On each group, a 3D transformation is applied and the transformed coefficients are thresholded.

BM3D inverse transforms the thresholded coefficients and aggregates it with weights to augment the basic estimate. This basic estimate is used as a pilot for the final step that applies a collaborative Wiener filter to construct the noise free image.

Apart from the noise, the intensity profile of the source also varies with respect to imaging modality [12]. Background correction or image intensity negation is often suggested as a part of the preprocessing. A recent study suggested a comprehensive approach for image enhancement in low contrast images [54]. It exploits intensity variance along the z-axis as an enhanced representation of the original image for the segmentation purpose.

4.2 Segmentation of foreground objects

The objective of the foreground segmentation is to classify the image-pixels into two separate classes, namely foreground pixels and background pixels. Classifiers, based on thresholding are often used for foreground segmentation. Intensity is predominantly considered as the primary feature for classifying pixels [55, 56]. However, a pipeline for segmentation should select the threshold in an automated manner. Otsu's method is often suggested as the optimal method to obtain the threshold for differentiating foreground objects from the background [13, 45, 46, 48]. Otsu's procedure for threshold selection is a global optimization technique that minimizes the within-class variance or maximizes the between-class variance in a bimodal distribution.

4.3 Cell detection from an under-segmented colony

The foreground segmentation step often detects a colony of cells as a single object. An additional step is therefore required to identify individual cells within a large cluster. Standard methods for edge detection are commonly used for determining the cell contour [57 – 59]. An edge in a digital image consists of a set of pixels that forms an intensity minimum in a certain direction [47]. Geometric features, such as the cell shape or the Euclidean distance from the perimeter of the object, are also employed for identifying individual cells from a cluster [14, 16, 30, 60].

There exist several methods based on image morphology that can act as an edge detection filter [61, 62]. Most of the edge detection techniques exploit the intensity gradient as the primary feature for detection. Apart from these, the Watershed procedure gradually increases or decreases the threshold level in an

iterative manner to identify individual objects from a cluster [13, 49]. Graph-based segmentation methods model the image as a flow network with the source and the sink, then construct a cut along the perimeter of the cell that follows the gradient in pixel intensity [50, 63, 64].

4.4 Over-segmentation correction

Over-segmentation is a common artifact that occurs while detecting individual cells within a large colony. A correction procedure that merges the over-segmented parts is executed to improve the detection accuracy. Classical approaches (Publication V) rely on heuristics for identifying the over-segmented parts as candidates for merging [45, 46]. The selection of heuristics is mostly arbitrary and is subjected to the expected size and shape of the cells. An arbitrary heuristic is not preferred for the cells with phenotypic diversity, since it restricts the applicability of the detection method. In Publication II, the description of the cell shape is parameterized and combined with the maximum-likelihood estimation. This enables the applicability of the proposed method for a diverse type of cells.

5 Methods for the detection of subcellular organelles

Several methods have been developed in recent times to detect subcellular organelles [65–68]. In general, the detection of subcellular organelles is realized in three logical steps. At first, the preprocessing phase attenuates the background structure and reduces the random noise. Next, the enhancement step enhances the signal to ease the detection process. Finally, objects of interest are segmented by applying a threshold in the enhanced image. The overall process is illustrated in Figure 2.7.

In Publication III, band-pass filtering (BPF) is proposed as a method for the detection of intracellular organelles. The method hypothesizes that the objects of interest are of roughly identical in shape and size. A band-pass transfer function would therefore enhance the objects while suppressing noise and background structures. However, the choice of pass-band and stop-band is not trivial in the spatial domain, thus, it is imperative to consider the frequency spectrum for the band selection. Finally, the filtered image is thresholded to detect the organelles.

Kernel density estimation (KDE) for object detection is proposed in [65]. Its working principle is based upon the density estimation of a predefined kernel at

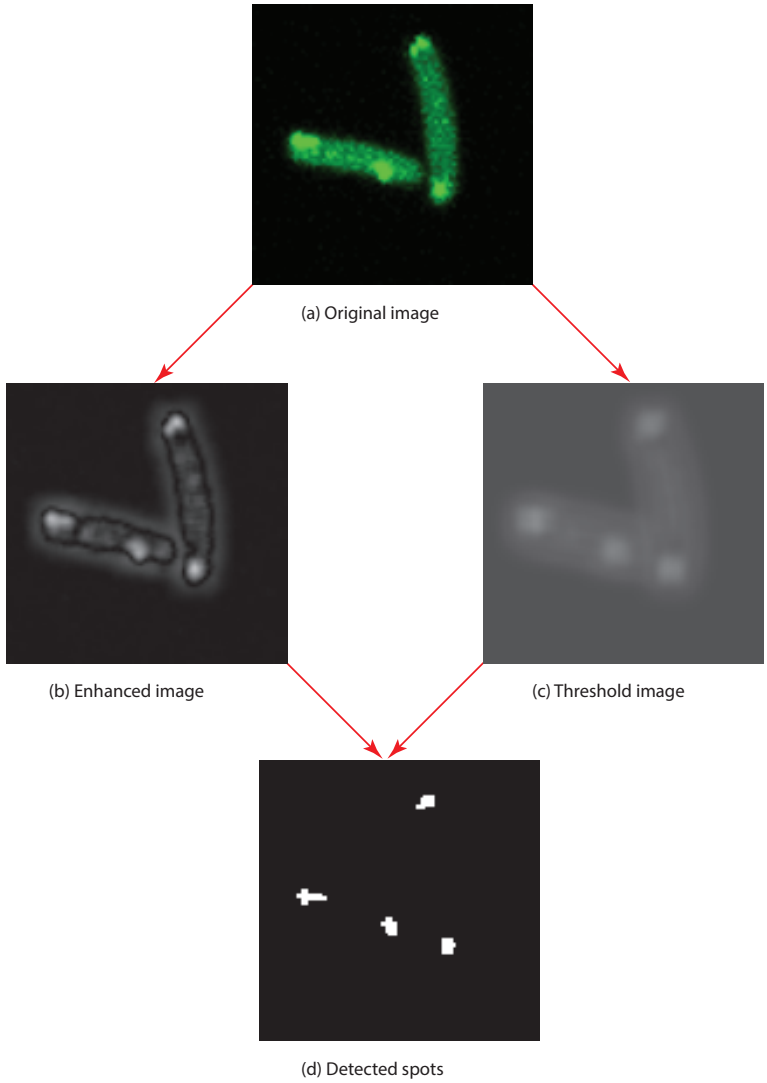

Figure 2.7: *Detection of subcellular organelles. Cells in the original image (a) are tagged with green fluorescent protein (GFP). The enhanced image (b) and the threshold image(c) are shown in grayscale. The detected spots are marked as white areas in (d).*

each spatial point. The method allows for selection of a kernel from a predefined set, such as circular, Gaussian, Epanechnikov, triangle, quartic, triweight, and cosine kernels [69]. The resulting image from the density estimation is viewed as an enhanced representation of the original sources. In the end, Otsu's method is applied to detect foreground objects from the background [48].

Local enhancement filtering (LEF) is another novel approach proposed in Publi-

cation III. It employs matched filtering to enhance spots [70]. The LEF method makes an assumption on shape and size of the object in question. Matched filtering is executed in two parts. The first part consists of a circular support that boosts the local maxima of intensity. The second part uses a square-shaped kernel, which is a complement to the first part. An enhanced representation of the objects is formed by taking the pixel-wise ratio of these two filtered images. Thereafter, the intracellular organelles are detected by applying a threshold to the enhanced image.

A similar approach for spot detection with top-hat filtering (THE) is proposed in [66, 71]. Here, a grayscale kernel is used for filtering. The top-hat filter performs background suppression while enhancing the spot-like structure whose size approximates the size of the kernel. The filtered image is then thresholded for object detection. After evaluating several histogram-based methods for thresholding [72], an entropy-based method is selected for thresholding [73].

The feature point detection (FPD) algorithm is adapted from [67, 74]. FPD detects the center of the mass of an object rather than detecting the whole object. The detected center is referred to as the feature point [74]. FPD initially normalizes the intensity of an image. It then executes a combined step of mean filtering and Gaussian filtering. The filtered image is considered as an enhanced representation of the actual source with background correction. An initial estimate of the feature points is constructed by percentile thresholding followed by detection of local maxima. The initial feature points are further refined to mimic the weighted center of the object. Finally, zeroth order moment and second order intensity moment of each object are assessed to eliminate the false positives.

A detection method, based on morphological h-dome (HD) transform [75], is reported as one of the best performing methods in [68, 76, 77]. The h-dome detector interprets an image as a composite signal containing three types of component: the N_o number of objects, the nonhomogeneous background structures, and the random noise. Relying on these, it attempts to locate the objects in an image. At first, the detection procedure executes LoG filtering for the background correction [57, 77]. It applies an h-dome transform on the filtered image with a height parameter h. The h-dome transform enhances the dome-shaped structures whose height is higher than the preset value of h. Next, it treats the transformed image as a probability field for drawing samples. Finally, objects of interest are detected by mean shift clustering the drawn samples [78].

The local comparison (LC) method for spot detection is formulated in Publication III. It utilizes local information for object detection. In spite of this, the original image is at first filtered with four directional kernels. The filtering constructs spatial information around each pixel. Object detection is performed by comparing each pixel in the original image against corresponding pixel in the filtered image. The actual procedure for pixel comparison is formally expressed as

$$b_{ij} = \begin{cases} 1 & \text{if } \max\{f_{i,j}^{NE}, f_{i,j}^{SE}, f_{i,j}^{SW}, f_{i,j}^{NW}\} > \alpha f_{i,j} \\ \\ 0 & \text{otherwise,} \end{cases} \tag{2.5}$$

where b_{ij} is the binary image and $f_{i,j}^{XY}$ is the image convolved with the kernel XY. Each kernel is directed to one of the four directions as shown in Figure 2.8.

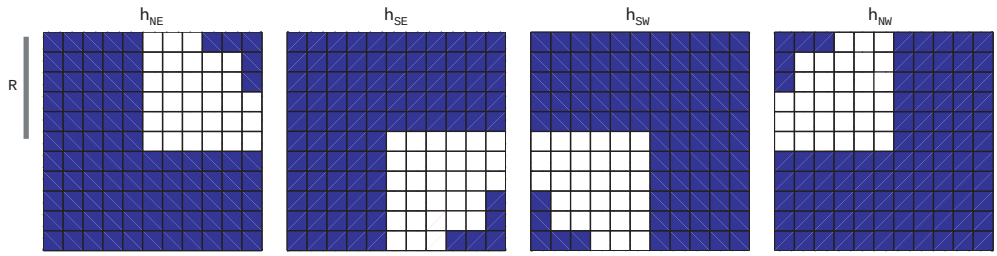

Figure 2.8: *Kernels for the local comparison method. Kernels are specified with directions i.e. h_{NE}, h_{SE}, h_{SW} and h_{NW}. White area indicates the pixels that are considered around each filtering position (i, j). Here, the radius R is set to 5 pixels (source Publication III).*

A detection method employing the multiscale product of wavelet coefficients (MW), is followed from [79]. It hypothesizes that in multiscale wavelet decomposition, a spot would be presented in each of the decomposition levels, whereas the random noise or large structure would be rejected in most of the decomposition levels. The method begins with the multiscale wavelet decomposition of the original image. The pixel-wise product of the sub-band images is then scored to enhance the object, while suppressing noise and background structures. The detection result is enhanced by applying a threshold on the individual sub-band prior to the multiscale product operation. The method adopts à-trous wavelet transform as the standard procedure for sub-band decomposition [80].

The morphometry and granulometric analysis (MGI)-based method for detection is adapted from [81]. First, the detection procedure carries out the granulometric analysis to determine the lower (d_{low}) and higher (d_{high}) limits of the granulometric

scale of indices [66, 81, 82]. It executes grayscale opening with the obtained limits that construct I_{low} and I_{high} respectively. An image containing only the objects falling within the desired scale is formed by subtracting I_{high} from I_{low}. Finally, k-means clustering and binary thresholding are applied to detect the respective objects of interest.

The sub-pixel localization (SPL) algorithm is proposed in [83]. The detection procedure at first constructs a parameter estimation on background intensity to determine the threshold. The initial candidates are determined by thresholding, followed by a procedure for selecting local maxima. Finally, the objects are detected by fitting Gaussian kernels on each of the selected candidates. It is plausible to detect multiple objects as a single spot. Hence, the kernel fitting procedure evaluates the possibility for fitting multiple kernels by using maximization of likelihood as an objective criterion [83, 84].

The SourceExtractor (SE) software was designed to analyze data obtained from the astronomical survey [85]. In Publication III, its applicability for the detection of subcellular organelles is assessed. The object detection pipeline of SE consists of two stages. It first removes the background and then deblends the overlapping objects. The background estimation is carried out in rectangular blocks to cope up with local variations in intensity. The image obtained after background subtraction is further thresholded for constructing the initial estimates. Finally, the initial estimates are subdivided by an iterative procedure to construct the final estimation.

3 Summary of the study

This chapter outlines the main results of this study. The chapter begins with a discussion from Publication I that proposes a novel strategy for focusing microscopes in time-lapse imaging. Then, the MAMLE method for cell segmentation, described in Publication II, is presented. Next, the result from Publication III is reviewed. This result represents a comparative study that evaluates state-of-the-art methods for the detection of subcellular organelles. The chapter wraps up by listing a few applications of the studied and proposed methods in systems biology research, which are mentioned in Publication IV.

1 Compensation of focus-drift

Studies have shown that temperature has a strong effect on the degree of focus-drift [23, 86]. Figure 2.4 (Chapter 2, Section 2) provides examples of focus-drift in different thermal conditions. In Publication I, the focus-drift is modeled as a linear dynamical system (LDI). The modeling allows a prediction-based search of the focal plane, which significantly reduces the number of z-slices required for focusing. The interacting multiple model (IMM) filter is employed for prediction-based tracking of the drift [87]. The proposed strategy models the focus-drift as

$$\text{Drift Model: } \mathbf{x}_t = \mathbf{F}^{(i)}\mathbf{x}_{t-1} + \mathbf{u}_{t-1}^{(i)},\ i = 1, 2, ...M \tag{3.1}$$

and the measurement of focus position is modeled as

$$\text{Measurement Model: } \mathbf{y}_t = \mathbf{H}\mathbf{x}_t + \mathbf{v}_t, \tag{3.2}$$

where $\mathbf{x}_t$ is the state vector which comprises the position of the focal plane (z_t), the velocity ($\dot{z}_t$), and acceleration ($\ddot{z}_t$) of the drift at time t. $\mathbf{F}^{(i)}$ is state transition

matrix which is conditioned with three dynamics, and $\mathbf{H}$ is the measurement matrix that transforms the state vector into a measurement vector. $\mathbf{u}_{t-1}^{(i)}$ and $\mathbf{v}_t$ are the noise vectors. The noise vectors are assumed as uncorrelated Gaussian with zero means. The covariance matrices of the noise components are denoted by $\mathbf{Q}^{(i)}$, and $\mathbf{R}$. Publication I considers three different dynamics ($M = 3$) for state transition, namely, the random-walk model (3.4), the constant-velocity model (3.5), and the constant-acceleration model (3.6). In these transition models, T represents the temporal interval of imaging. Publication I defines the measurement matrix as

$$\mathbf{H} = \begin{bmatrix} 1 & 0 & 0 \end{bmatrix}, \tag{3.3}$$

and the dynamics (M = 3) for state transition are modeled as

$$\mathbf{F}^{(1)} = \begin{bmatrix} 1 & 0 & 0 \\ 0 & 0 & 0 \\ 0 & 0 & 0 \end{bmatrix}, \tag{3.4}$$

$$\mathbf{F}^{(2)} = \begin{bmatrix} 1 & T & 0 \\ 0 & 1 & 0 \\ 0 & 0 & 0 \end{bmatrix}, \tag{3.5}$$

$$\mathbf{F}^{(3)} = \begin{bmatrix} 1 & T & \frac{T^2}{2} \\ 0 & 1 & T \\ 0 & 0 & 1 \end{bmatrix}. \tag{3.6}$$

The modeling enables IMM filtering as a solution for focus-drift compensation. The focus-drift is compensated in three consecutive steps: i) prediction of the focus position, ii) measurement of the position of focal plane, and iii) correction of parameters. At time t, the measurement step starts with an estimate of the state vector ($\hat{\mathbf{x}}_{t-1}^{(i)}$), covariance matrix ($\mathbf{c}_{t-1}^{(i)}$) and weight of the respective model ($\mathbf{w}_{t-1}^{(i)}$) as a set of parameters. The parameters are fed from the previous time point $(t-1)$. Given these parameters, a prediction is made on the mixed initial state and covariance matrices. The prediction step is followed by measurement of the focus position. The measurement step determines the focus position ($\mathbf{y}_t$) by acquiring a stack of low-resolution images. The size of the acquired stack is varied with the accuracy of the prediction. The stack of images is acquired from the predicted position until either the focus-function is maximized or a fixed upper

bound is reached. The initial direction of the search is determined by the slope of the defocusing curve and it is altered if the slope continues to a negative direction.

The correction step acts as a feedback of information from the measurement step to the prediction step. The feedback enhances the accuracy of the prediction for future measurements. It estimates the posterior mean of the state vector ($\hat{\mathbf{x}}_t^{(i)}$), covariance matrix ($\mathbf{c}_t^{(i)}$) and the weight of the model ($\mathbf{w}_t^{(i)}$). The corrected parameters are finally exploited for making predictions at the next time point $t+1$ as (3.1). An algorithm of the proposed method for focusing is presented in Appendix-A:Algorithm 6.2. Publication I provides further details on the prediction and measurement of the focus-drift as well as steps for parameter correction.

1.1 Evaluation of IMM filter-based focusing

The proposed strategy for focusing is evaluated with several sets of images containing MS2d-GFP tagged *E. coli* cells. The cells are cultured in the Laboratory of Biosystem Dynamics (LBD), Department of Signal Processing, TUT, Finland. The images are acquired by a Nikon Eclipse (Nikon, Japan) confocal microscope equipped with a 100x Apo TIRF 1.49 oil + DIC objective (Nikon, Japan). GFP fluorescence is measured with 488 nm laser. Because the diameter of *E. coli* is notably small (0.5 µm), the sampling interval along the z-axis is set to 0.1 µm. Some of the test sequences are captured on a temperature controlled chamber, while others are obtained at room temperature. A set of representative results from two different conditions is exemplified in Figure 3.1, where the imaging is carried out at 60 seconds intervals for a period of 150 minutes. The results from the quantitative evaluation are presented in Table 3.1. The results confirm a very high accuracy in prediction, which leads to a very low number of image acquisitions for focusing.

2 Focus-function for time-lapse imaging

The focusing methods based on Pearson's correlation are generally preferred for time-lapse imaging [38]. However, Pearson's correlation relies solely on correlation coefficients between consecutive frames. Its performance drops significantly if the correlation among consecutive frames is degraded during the course of the experiment. The correlation between consecutive frames can be affected by several factors, such as drift in the lateral position, changes in the cell phenotype, or variations in the expression level. Pearson's correlation is also sensitive to

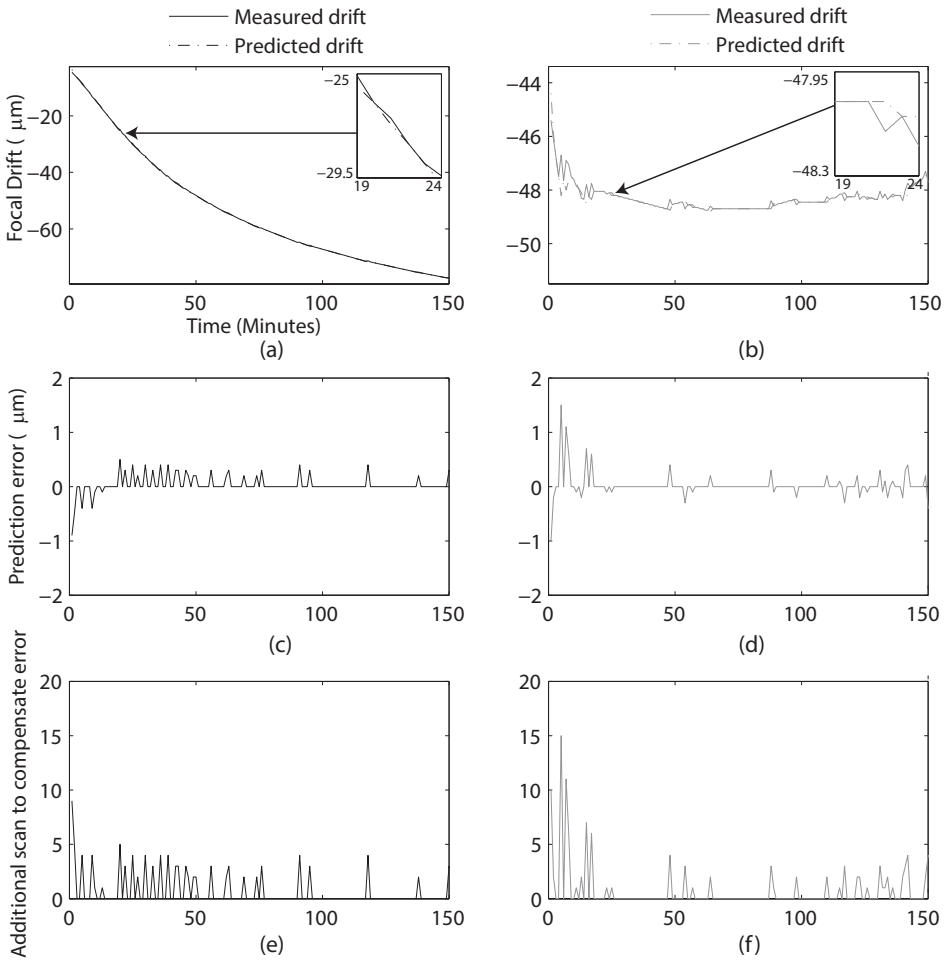

Figure 3.1: *Focus-drift and its prediction. (a) Focus-drift and drift prediction at room temperature (RT). (b) Focus-drift and drift prediction at 37°C. (c) Error in drift prediction at RT. (d) Error in prediction at 37°C. (e),(f) Additional scans required for prediction error compensation in (a), (b) respectively (source Publication I).*

the imaging intervals. To summarize, the focus-functions listed in Table 2.1 (Chapter 2, Section 3) opt for the individual frame without considering the temporal correlation; on the other hand, Pearson's correlation-based approach maximizes the correlation between consecutive frames discounting the individual frame [Publication I]. Simultaneous optimization of both metrics is not realizable by addressing them independently. In Publication I, these approaches are unified as a combined product of the resulting score of each approach.

Table 3.1: Performance evaluation of the prediction-based method for focusing (source Publication I)

Evaluation method	Thermal condition	Imaging interval (minute)	Number of frames	Error (μm)	Mean additional scans
Simulation	Room temperature(RT)	1	272	0.0972	-
	37°C	1	272	0.1392	-
Experimental	RT	1	512	0.0820	0.85
	37°C	1	492	0.0980	1.03
	RT	5	50	0.3680	3.91
	37°C	5	50	0.2510	2.93

2.1 Evaluation of focus-function for time-lapse imaging

Publication I evaluates the performance of six focus-functions. The evaluation procedure uses four objective metrics for validation, i.e., 'accuracy', 'rate of local maxima', 'interval sensitivity', and 'range'. The 'accuracy' is realized as the mean absolute deviation (MAD) between the true position of the focal plane and the position where a certain focus-function is maximized. The 'interval sensitivity' measures the variance of focal plane positions with respect to a change in imaging intervals.

By definition, the focus-function that is solely based on a single stack of images has zero 'interval sensitivity'. The 'rate of local maxima' accounts for the average number of local maxima in a single stack of images. The 'range' is estimated as the expected value of the difference of normalized focus scores between global and local maxima. An ideal focus-function is expected to maintain a high 'accuracy' with a large 'range' and a single maximum point. Moreover, it should be invariant to imaging intervals. The results of the empirical evaluation are shown in Table 3.2, where the rank of each focus-function is denoted inside the parenthesis. The ground truth for evaluation is estimated by the cross-validation method [88]. Considering these results, the combined approaches are preferred and implemented in an operational environment for focusing.

Table 3.2: Evaluation of focus-function (source Publication I)

Method	Accuracy (μm)	Interval sensitivity (μm)	Local maxima	Range	Overall score
f_{Tenegrad}	0.021(3)	0(1)	0.395(5)	0.681(5)	14(3)
$f_{\text{VollathF4}}$	0.035(7)	0(1)	0.584(9)	0.622(9)	26(7)
f_{Fano}	0.031(5)	0(1)	0.376(3)	0.667(6)	15(4)
f_{Brenner}	0.050(10)	0(1)	0.626(10)	0.433(10)	31(10)
f_{Power}	0.043(9)	0(1)	0.512(8)	0.655(9)	27(8)
$f_{\text{Pearson's}}$	0.205(11)	0.149(11)	0.689(11)	0.178(11)	44(11)
$f_{\text{Pearson's}} \times f_{\text{Tenegrad}}$	0.010(1)	0.013(7)	0.371(2)	0.807(2)	12(1)
$f_{\text{Pearson's}} \times f_{\text{VollathF4}}$	0.035(7)	0.011(6)	0.447(7)	0.783(3)	25(6)
$f_{\text{Pearson's}} \times f_{\text{Fano}}$	0.026(4)	0.013(7)	0.344(1)	0.779(4)	18(5)
$f_{\text{Pearson's}} \times f_{\text{Brenner}}$	0.034(6)	0.028(10)	0.415(6)	0.660(7)	29(9)
$f_{\text{Pearson's}} \times f_{\text{Power}}$	0.016(2)	0.013(7)	0.378(4)	0.811(1)	14(2)

3 Proposed method for cell detection

Detection of cells from image-based assay poses a major challenge for studying biological systems at the single-cell level. In the Publication V, a classical approach for the cell segmentation is adopted as a part of a system for tracking cells [13, 48]. However, this approach is suitable for the image where cells are sparsely populated and inadequate for segmenting cells from a dense colony. The cell segmentation problem is reinvestigated in Publication II and a novel method for cell detection is proposed that alleviates the shortcomings of the earlier approaches. The proposed method is based upon multi-resolution analysis and maximum-likelihood estimation (MAMLE). In brief, the MAMLE method begins by preprocessing the images which in turn prepares them for segmentation. The foreground objects or the regions of interest are then detected by applying thresholds. The foreground objects contain properly segmented cells as well as under-segmented colonies and over-segmented cells.

Therefore, additional steps are required to enrich the initial results. A learning step continues along with the segmentation which enhances the overall results obtained by the proposed pipeline. The result of this study is made available in Publication II. The complete paradigm of the proposed method is illustrated in Figure 3.2 and a detail discussion is presented in the next.

3.1 Segmentation of foreground objects

The purpose of foreground segmentation is to isolate foreground objects or regions of interest from the background. Otsu's method is considered as the state-of-the-art for automated thresholding [48]. This method partitions the histogram by minimizing the variance within a certain class or by maximizing the variance between two separate classes [48, 89]. However, the intensity of the background is often non-uniform. A single and global threshold is therefore inadequate. Several modifications have been proposed to Otsu's method concerning local variation in background intensity [13, 90, 91]. In Publication II, a robust variant of Otsu's method is adopted that estimates threshold values in blocks and interpolates the estimated values among neighboring blocks to avoid abrupt changes [13].

Otsu's technique is also optimized for bimodal distribution of intensity. However, the distributions of background intensity are often far from bimodal and non-separable by applying a threshold, such as in phase-contrast images [12]. As an alternative, an iterative range filtering-based approach is applied for this kind of images [15]. The iterative range filtering executes the dilation and erosion operation by varying morphological support [15]. The filtered image is then segmented with percentile thresholding.

3.2 Cell detection from under-segmented colony

The results obtained from foreground segmentation often contain under-segmented cells. Trivial methods for cell segmentation resort to edge detection techniques for detecting individual cells from an under-segmented colony [58, 59]. Traditional methods for edge detection are highly sensitive to random noise and local variations of intensity [92]. Furthermore, it has been shown that the robustness of the edge detection algorithms improves when edge detection is performed in multiple resolutions rather than in a single resolution [62, 93, 94]. A novel technique is thereby formulated in Publication II that incorporates edge detection in multi-resolution with threshold decomposition.

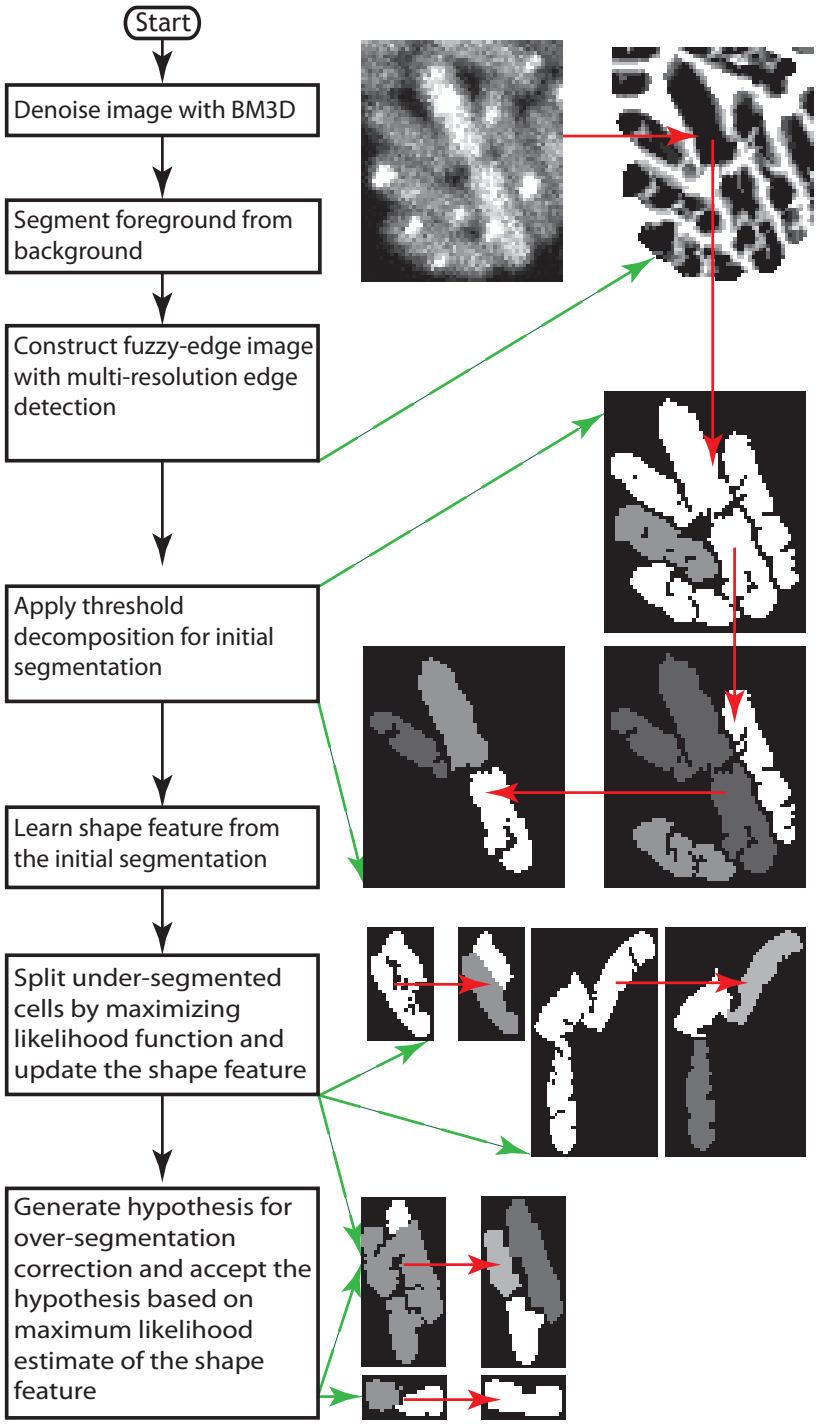

Figure 3.2: *The flowchart of the MAMLE method for cell detection. The left column describes the steps and corresponding results are shown in the right column (source Publication II).*

The proposed approach constructs a 'fuzzy-edge image ($E(f)$)' according to

$$E(f) = \sum_{s=1}^{S} E_s(f), \tag{3.7}$$

$$E_s(f) = \bigcup_{d} E_s^d(f), \tag{3.8}$$

$$E_s^d(f) = \begin{cases} 1 & \text{if } f = f \circ \mathbf{B_s^d} \\ 0, & \end{cases} \tag{3.9}$$

where $E_s^d(f)$ is the image containing edge in the direction d and the symbol ($\circ$) represents the morphological erosion with the support ($\mathbf{B_s^d}$). Each pixel in the fuzzy-edge image ($E(f)$) holds an integer value within the range from 0 to S, where S is the cardinality of the multi-resolution analysis. The construction of the fuzzy-edge image ($E(f)$) is shown in the Appendix-B:Algorithm 7.1. It is hypothesized that a pixel lying on a clear edge of intensity is more likely to be detected as a part of an edge in most of the resolution levels. The corresponding pixel in the fuzzy-edge image would hold a value close to the limit S. Conversely, a pixel on a smooth region is prone to hold a near-zero value in the fuzzy-edge image ($E(f)$). A representative example of the fuzzy-edge image is shown in Figure 3.3.

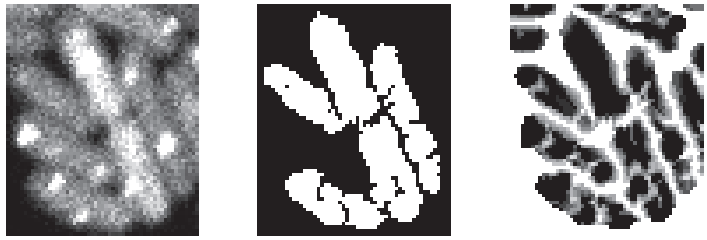

Figure 3.3: *Edge detection in multi-resolution. Original image (left), background segmented image (center), fuzzy-edge image (right).*

The fuzzy-edge image is considered as an initial estimate for the edge. It requires thresholding to detect individual cells. However, with an exhaustive test, Publication II concludes that a suitable threshold that is robust against different kind of artifacts and noises is implausible. A novel approach for threshold selection is therefore proposed. The proposed approach is based on threshold decomposition

and it is adapted independently for each of the objects. Threshold decomposition is a process that decomposes an image with a series of gradually increasing or decreasing values of threshold [95–98]. This process is formulated according to

$$T^i(l) = \begin{cases} 1 & \text{if } l \geq i \\ 0 & \text{if } l < i. \end{cases} \tag{3.10}$$

The decomposition procedure starts with an initial threshold $i = S$, that subdivides an individual foreground object along the line where the presence of an edge is most certain. Thereafter, the whole process is repeated and continued by lowering the threshold values until the size of the foreground object is reduced to a predefined limit. The overall procedure is recursive. The decomposition level is adapted for each object based on its size and appearance of edges. The decomposition procedure is presented as an algorithm in the Appendix-B:Algorithm 7.2. The image obtained from this process is considered as an initial segmentation. The initial segmentation is comprised of properly segmented cells as well as over-segmentation and under-segmentation artifacts. The initial segmentation forms the coarse approximation for the final segmentation.

3.3 Unsupervised learning

The unsupervised learning of shape parameters is carried out by considering the initial result as a reference for estimation. The parameters are then fed for boosting the classifier that yields to an improved accuracy. The classifier approximates each cell as a simple and convex polygon. The area and the length of the major and minor axes are taken into account as necessary features for boosting. The major axis (a) and the minor axis (b) are formed according to

$$a = 4\sqrt{\frac{m_{00}m_{11} - m_{01}m_{01}}{A\lambda_1}}, \tag{3.11}$$

$$b = 4\sqrt{\frac{m_{00}m_{11} - m_{01}m_{01}}{A\lambda_2}}, \tag{3.12}$$

respectively [99], where m_{xy} is the centroidal moment, A is the area. λ_1, and λ_2 are respectively the first and second orthogonal eigenvalues of a convex polygon. A comparison of these parameters, describing the underlying shape is illustrated in Figure 3.4. Publication II realizes the distribution of the parameters as a multivariate Gaussian distribution.

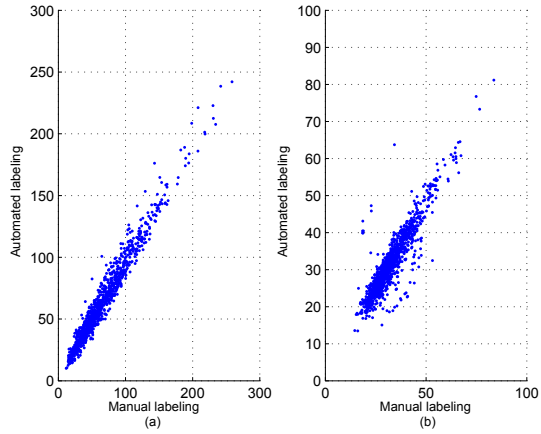

Figure 3.4: *A parametric comparison between manual and automated segmentation of cells. (a) The measured length of the major axis. (b) The measured length of the minor axis.*

3.4 Boosting accuracy by binary-split

The estimated parameters are utilized to discriminate the colonies that are not segmented properly by the threshold decomposition and remained as under-segmented in the initial results. First, the segmented object whose area is larger than the expected value of the cell area is identified as the under-segmented cell and considered as a candidate for the split. The splitting is then constructed by maximizing likelihood estimation in the parametric space. The log-likelihood function of a detected object being a cell is formulated as

$$\begin{aligned} ll(\mathbf{X}_i) &= \log\left(\frac{1}{(2\pi)^{\frac{d}{2}}|\Sigma|^{\frac{1}{2}}} e^{-(\mathbf{X}_i-\mu)^T\Sigma^{-1}(\mathbf{X}_i-\mu)}\right) \\ &= \log\left(\frac{1}{(2\pi)^{\frac{d}{2}}|\Sigma|^{\frac{1}{2}}}\right) - (\mathbf{X}_i-\mu)^T\Sigma^{-1}(\mathbf{X}_i-\mu), \end{aligned} \tag{3.13}$$

where μ and Σ are the mean vector and the covariance matrix of the multivariate Gaussian distribution respectively [88]. The discriminant function for the maximum-likelihood estimation is further simplified as

$$D(\mathbf{X}_i) = (\mathbf{X}_i-\mu)^T\Sigma^{-1}(\mathbf{X}_i-\mu). \tag{3.14}$$

The maximum-likelihood estimation for the discriminant function in (3.14) can be obtained by minimizing the distance norm from the mean vector (μ). The

optimization procedure employs an iterative technique for the maximization of likelihood. This optimization procedure starts by splitting an under-segmented colony of cells into two parts. The likelihood of the best matching part is regarded as the objective criterion for splitting. The procedure reevaluates the resulting parts for further division and the process continues recursively until the size of the respective object is reduced to the expected size of a cell. The iterative technique for likelihood maximization is advantageous over classical approaches, such as the expectation-maximization (EM) algorithm [88] in several ways:

i) The iterative procedure for likelihood maximization does not require any prior knowledge about the number of existing mixtures.
ii) This technique is capable of handling a scenario where a single cluster contains multiple cells as well as fragmented parts of a cell.
iii) It also has direct control on the shape of the extracted cells.

It should be noted that the split procedure often over-segments a cell into multiple parts. The MAMLE method does not prohibit the occurrence of over-segmentation; most of these over-segmentation errors are reconciled in the subsequent steps. The algorithm of the binary-split procedure is presented in the Appendix-B: Algorithm 7.3. These ideas are presented as a part of the MAMLE method in Publication II.

3.5 Correction of over-segmentation

The MAMLE method recognizes over-segmentation as a plausible artifact. It adopts a merging step based on the maximum-likelihood estimation in this concern. The correction procedure is exhibited as an algorithmic in the Appendix-B:Algorithm 7.4. It constructs a set of hypotheses that contains candidates for merging. Each of the candidates holds a list with two or more objects, and the likelihood of the augmented object, resulting from their merging. Candidates for merging are selected by satisfying the logical quantifier as

$$\forall c_i \in C \exists c_j \in C \left(D(\mathbf{X}_i) + D(\mathbf{X}_j) \geq D(\mathbf{X}_{ij}) \wedge c_i \neq c_j \right), \tag{3.15}$$

where c_i represents a segmented cell or a part of cell and $\mathbf{X}_i$ is the feature vector of the respective object. $\mathbf{X}_{ij}$ is the feature vector of the resulting object c_{ij}, obtained by merging the object c_i with the object c_j. The procedure generates all possible combinations of merging two or three objects together and constructs the feature

vector of the resulting object. The likelihood of the feature vector is estimated by evaluating it against parameters obtained during the learning phase. The selection of hypotheses is made by maximizing the likelihood while maintaining the topological constraint. The topological constraint restricts the assignment of an entity to multiple hypotheses. Consequently, each part of the object is strictly assigned to a single cell. The maximum-likelihood solution for the stated problem belongs to the class of non-polynomial (NP) hard problems [100]. A deterministic solution is thereby infeasible for practical purpose. However, the maximization problem is addressed in a quasi-optimal manner with a linear programming-based branch-and-bound technique that is able to obtain a solution in polynomial time [100 – 102].

4 Results and evaluation of the proposed method for cell detection

Publication II evaluates the MAMLE method empirically with *de novo* data sets containing *E. coli* and *Staphylococcus aureus* cells as well as images from external sources [13, 15, 16, 103, 104]. The data sets for evaluation are listed in the Table 3.3. A part of the *E. coli* and *S. aureus* cells are cultured in the LBD. The cultured *E. coli* strain contains a bacterial expression vector carrying the MS2-dimer (MS2d) fused with green fluorescent protein (MS2d- GFP). GFP fluorescence is excited using a 488 nm laser and measured with a 515/30 nm detection filter (100-120 detector gain). In case of *S. aureus*, cells are stained with 4'6-diamidino-2'phenylindole (DAPI, Sigma) and grown in a nutritionally rich medium. The expression is measured using a 406 nm laser and a 450/35 nm detection filter (100-120 detector gain). The imaging is performed at room temperature (22°C) using a Nikon Eclipse (Nikon, Japan) confocal laser-scanning microscope equipped with an objective of 100X magnification (1.5NA).

Table 3.3: Data set used for the evaluation of MAMLE

Cell type	Imaging modality	Image source
E. coli	Confocal microscope	LBD and [16]
E. coli	Epifluorescence microscope	LBD
E. coli	Phase contrast microscope	[15], [16] and [103]
Staphylococcus aureus	Epifluorescence microscope	LBD
HT29 colon cancer	Cellomics ArrayScan	[13, 104]

The evaluation procedure categorizes the segmentation results into four types. i) True positive (TP); or the cells that are segmented properly. ii) Over-segmentation (OS); if a single cell is detected as multiple cells. iii) Under-segmentation (US); the segmented cell that contains parts from multiple cells. iv) True negative (TN); if a clearly visible cell is not detected by the segmentation procedure.

The method is first evaluated with a set of test images containing *E. coli* cells. The images are acquired with a confocal microscope. The test set includes altogether 30 images that contain an approximate total of 12818 cells. The results from this evaluation are listed in three different dense groups in Table 3.4. The proposed method is then assessed with several test sets comprising of images from different imaging modalities and containing cells with diverse phenotypes. Table 3.5 shows parts of the results from this evaluation. The quantitative results reveal the very high accuracy of the MAMLE method. In addition to these, a set of illustrative examples from several test samples is shown in Figure 3.5.

Automated segmentation of cells with a high accuracy is a challenging problem. Till now, there exist no means to solve it completely [56]. As a part of this study, the MAMLE method is formulated that aims to address this problem. The method is primarily motivated to detect MS2d-GFP tagged *E. coli* cells from fluorescence microscopy images. Indeed, the results listed in Table 3.5 and in Figure 3.5 clearly indicate its applicability to diverse cell types as well as in various imaging modalities.

Table 3.4: Test results on confocal images of *E. coli* cells expressing MS2d-GFP (source Publication II).

Test case	Number of images	Number of cells	TP	OS	US	TN	Seg. accuracy (%)
Dense	10	7947	7335	236	170	206	92.30
Medium	10	4014	3616	87	184	127	90.10
Sparse	10	857	817	20	16	4	95.33
Total	30	12818	11768	343	370	337	91.80

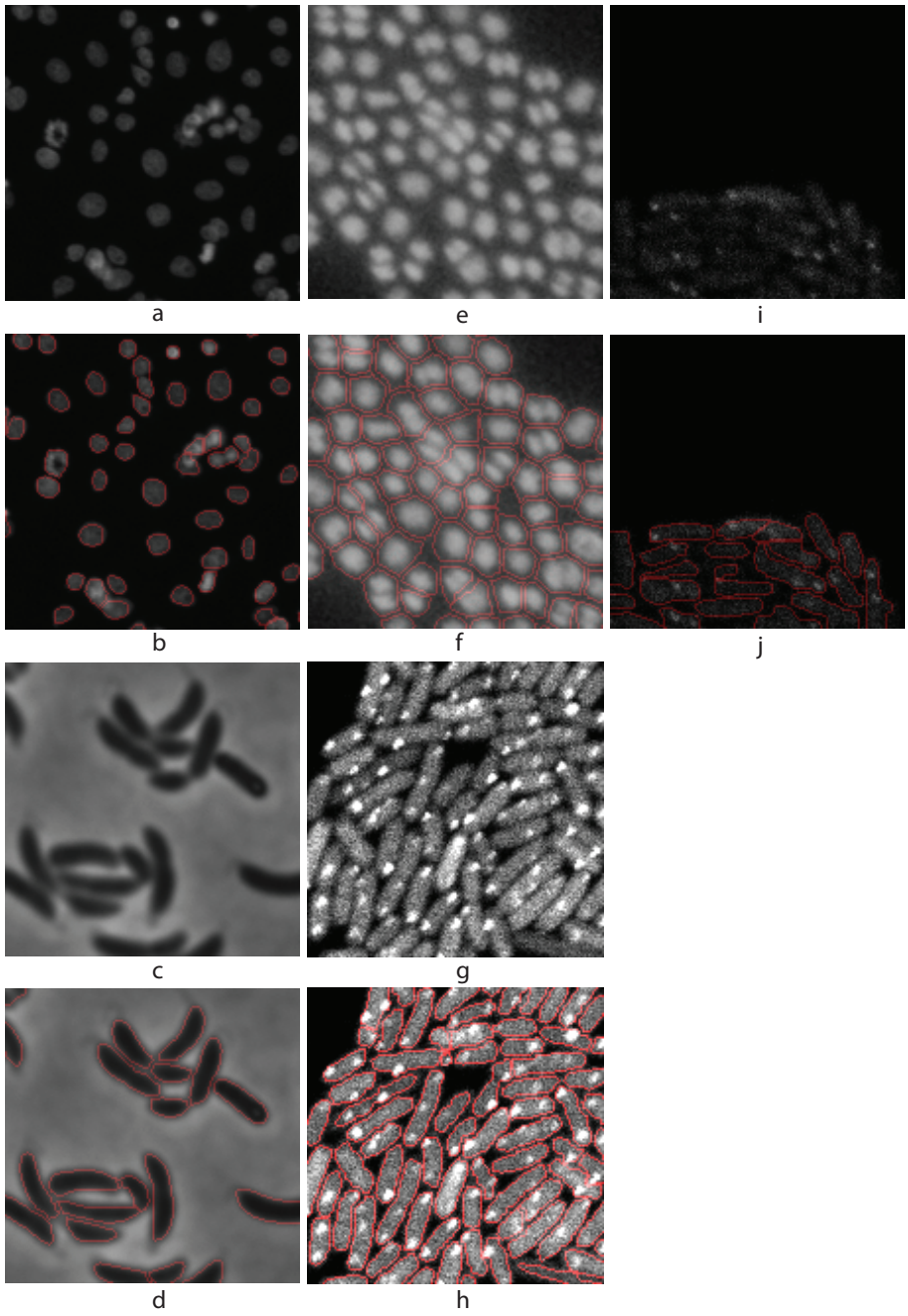

Figure 3.5: *Representative results obtained with the MAMLE method. (a) Sample image from Human HT29 colon cancer set (source [13, 104]), (b) Segmented result of (a); (c) E. coli cells acquired with phase contrast microscope (source [16]), (d) Segmented result of (c); (e) Fluorescent protein labeled Staphylococcus cells observed with Epifluorescence microscope. (f) Segmented result of (e); (g) Fluorescent protein labeled E. coli cells acquired with confocal microscope, (h) Segmented result of (g); (i) Dense cluster of E. coli cell acquired with confocal microscope, (j) Segmented result of (i); (i) E. coli cell acquired with confocal microscope (very low contrast), (j) Segmented result of (i).*

Table 3.5: Test results from phase-contrast images of *E. coli* cells, from fluorescence microscopy images of *S. aureus*, and from epifluorescence microscopy images of *E. coli* (source Publication II).

Test case	Number of images	Number of cells	TP	OS	US	TN	Seg. accuracy (%)
Phase contrast *E. coli*	4	381	376	3	2	0	98.69
S. aureus	3	768	710	18	40	0	92.45
Epifluorescences *E. coli*	3	160	146	5	6	3	91.25
Total	10	1309	1232	26	48	3	94.12

5 Study on methods for the detection of subcellular organelles

Publication III examines a collection of methods for the detection of subcellular organelles. The studied methods are listed in Table 3.6. There exists several metrics for performance evaluation, for example location, correct number, and precise area of object [105, 106]. The harmonic mean of precision and recall, known as the F-score, is selected as an objective criterion for evaluation [105]. The F-score unifies precision and recall as a single quantity, turning it as a preferable metric for the comparison. In accordance with [105], precision (p) and recall (r) can be defined as

$$p = \frac{\mathrm{TP}}{\mathrm{TP} + \mathrm{FP}}, \tag{3.16}$$

$$r = \frac{\mathrm{TP}}{\mathrm{TP} + \mathrm{FN}}, \tag{3.17}$$

respectively. Here a true positive (TP) is defined as a correctly detected object, and a false positive (FP) is a detected object for which there is no real object in the reference image. A false negative (FN) accounts for a missed object which is clearly visible in the original image. The F-score is formed by combining these metrics as

$$\frac{2pr}{p + r}. \tag{3.18}$$

Table 3.6: Summary of the methods for the detection of subcellular organelles (source Publication III)

Algorithm	Description	Number of free parameters
Feature point detection (FPD) [67, 74]	Percentile thresholding with non-particle discrimination	3
h-dome detection (HD) [75]	h-dome transform and clustering	5
Kernel methods (KDE) [65]	Kernel density estimation with a set of kernels	3
Morphometry (MGI) [81]	Morphometry and granulometric analysis	0
Multiscale wavelets (MW) [79]	Multiscale product of wavelet coefficients	2
Source Extractor (SE) [85]	Background estimation and deblending	4
Sub-pixel localization (SPL) [83]	Detection of local maxima and fitting of Gaussian kernels	1
Top-hat filtering (THE) [66, 71]	Top-hat filtering and entropy-based thresholding	1
Band-pass filtering (BPF) (Publication III)	Intensity enhancement of object with bandpass filtering	4
Local comparison (LC) (Publication III)	Maximization among direction -specific filtered image	2
Locally enhancing filtering (LEF) (Publication III)	Local enhancement of signal and background suppression	1

First, the performance is assessed with a set of simulated images. The simulated images are software-generated, thus the signal-to-noise ratio and other image statistics are known [107, 108]. Synthetic images are preferred as a reference for evaluation at the pixel-level as well as at the object-level [109]. The comparison for a set of 20 images is presented in Figure 3.6. The pixel-level comparison is presented in Figure 3.6(a) and the corresponding object-level comparison is shown in Figure 3.6(b). It should be noted, however, that the FPD and SPL methods are excluded from the pixel-level comparison because they were developed for estimating spot location rather than segmenting the object.

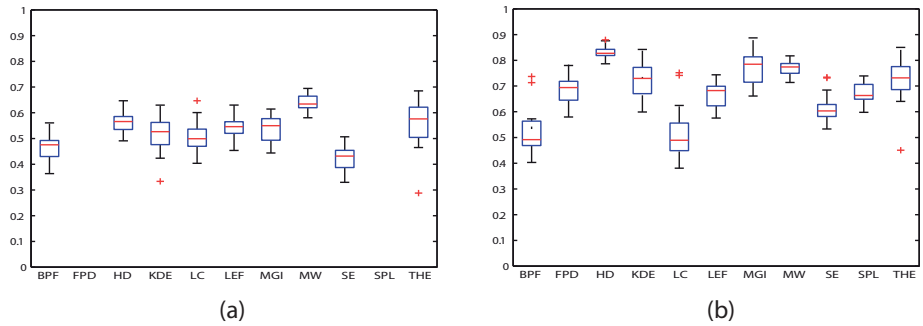

Figure 3.6: *Evaluation result on synthetic images. F-scores at pixel-level (a) and object-level (b). Note that, the FPD and SPL are not included for pixel-level comparison in (a) (source Publication III).*

The performance of the methods are then scored for a set of 28 wide-field images containing 262 P-bodies altogether. The noise and the contrast against background act as the main limiting factor for accuracy in this test set. However, objects are well-scattered in the entire field of view, making occlusion negligible for detection accuracy. The reference images for the comparison are constructed manually. Segmentation results are compared against the manual reference to compute precision, recall, and F-score. The obtained results are listed in Table 3.7.

In brief, the performance of aforementioned methods for subcellular object detection has been studied in Publication III. In the case of simulated images, the highest object-level performance (in terms of F-score) is 0.8249, which is attained by the HD method. MGI (0.7698), THE (0.7244), and FPD (0.6905) also perform well for the images that have enough spots. In wide-field images, BPF (0.9459), LC (0.9450), and SE (0.9354) attain the highest F-scores. The performances of the FPD, MGI, and THE are lowered due to their difficulty in handling images

Table 3.7: Results for wide-field microscope image frames (source Publication III)

Algorithm	Precision	Recall	F-score
BPF	0.9570	0.9351	0.9459
FPD	0.5964	0.8969	0.7165
HD	0.8682	0.7290	0.7925
KDE	0.9116	0.8664	0.8885
LC	0.9396	0.9504	0.9450
LEF	0.8712	0.8779	0.8745
MGI	0.6175	0.8626	0.7198
MW	0.7645	0.8550	0.8072
SE	0.9318	0.9389	0.9354
SPL	0.8167	0.9351	0.8719
THE	0.0062	0.9733	0.0123

without any object. However, the performances of all these methods are improved when the empty frames are discounted, which is reassured by the high level of recall values.

Finally, Publication III concludes that three detection methods i.e. FPD, HD, and SPL were originally proposed for the tracking of intracellular organelles or molecules. These methods adopt different approaches for the detection. In principal, FPD holds an approximation on the number of objects and attempts to detect a roughly constant number of spots for a set of images. The result for the simulated images agrees with this assumption, since the number of objects stays constant in this set. In images with a varying number of objects, the HD and SPL approaches are more likely to perform better.

6 Application

The computational methods developed during the course of this study have direct impacts on single-cell analysis. In this section, a few representative examples are mentioned which incorporate the developed methods for image acquisition and analysis purposes. The author of the thesis has contributed actively in all the listed applications.

Publication IV studies the effect of the tetA promoter on the transcription dynamics in *E. coli* cells. This study acquires *in vivo* measurements in order

to score the production events of individual RNA and constructs the intervals between transcription events. The measurement procedure acquires time-lapse images at 60 seconds intervals for a period of an hour.

Photobleaching poses a major challenge toward time-lapse imaging, in particular when the imaging interval is short. It is intuitive that the reduction of the required number of images for focusing would improve photobleaching. The expression level of the fluorescent protein would therefore remain sufficient for a prolonged period. The hypothesis is confirmed with an experiment performing focusing according to two different strategies as follows: i) focusing based on the IMM filtering and, ii) focusing based on the fixed-size stack. The experiments were conducted for a period of 150 minutes at an imaging interval of 60 seconds. The fixed-size stack acquired 15 frames for focusing while the IMM filter-based method required only 5.49 frames on an average. The result of this experiment is shown in Figure 3.7.

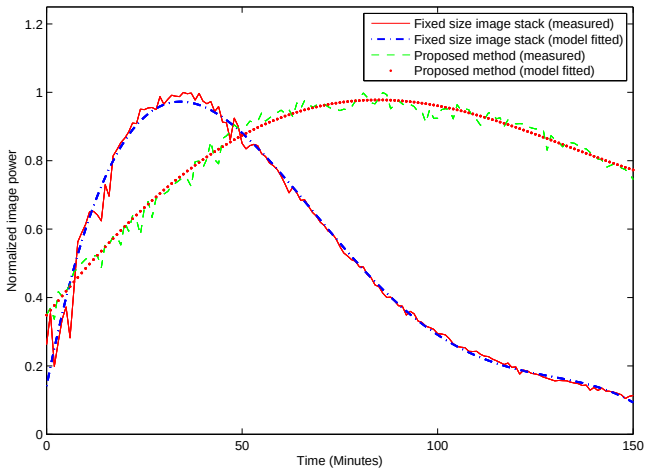

Figure 3.7: *Photobleaching in IMM filter-based focusing vs fixed-size image stack-based focusing (source Publication I).*

The reduced number of required frames directly improved photobleaching and therefore, the expression level of the fluorescent protein declined at a later time point. Based on this finding, the IMM filter-based focusing is employed in Publication IV to study the effect of the tetA promoter on transcription dynamics of the *E. coli* cell.

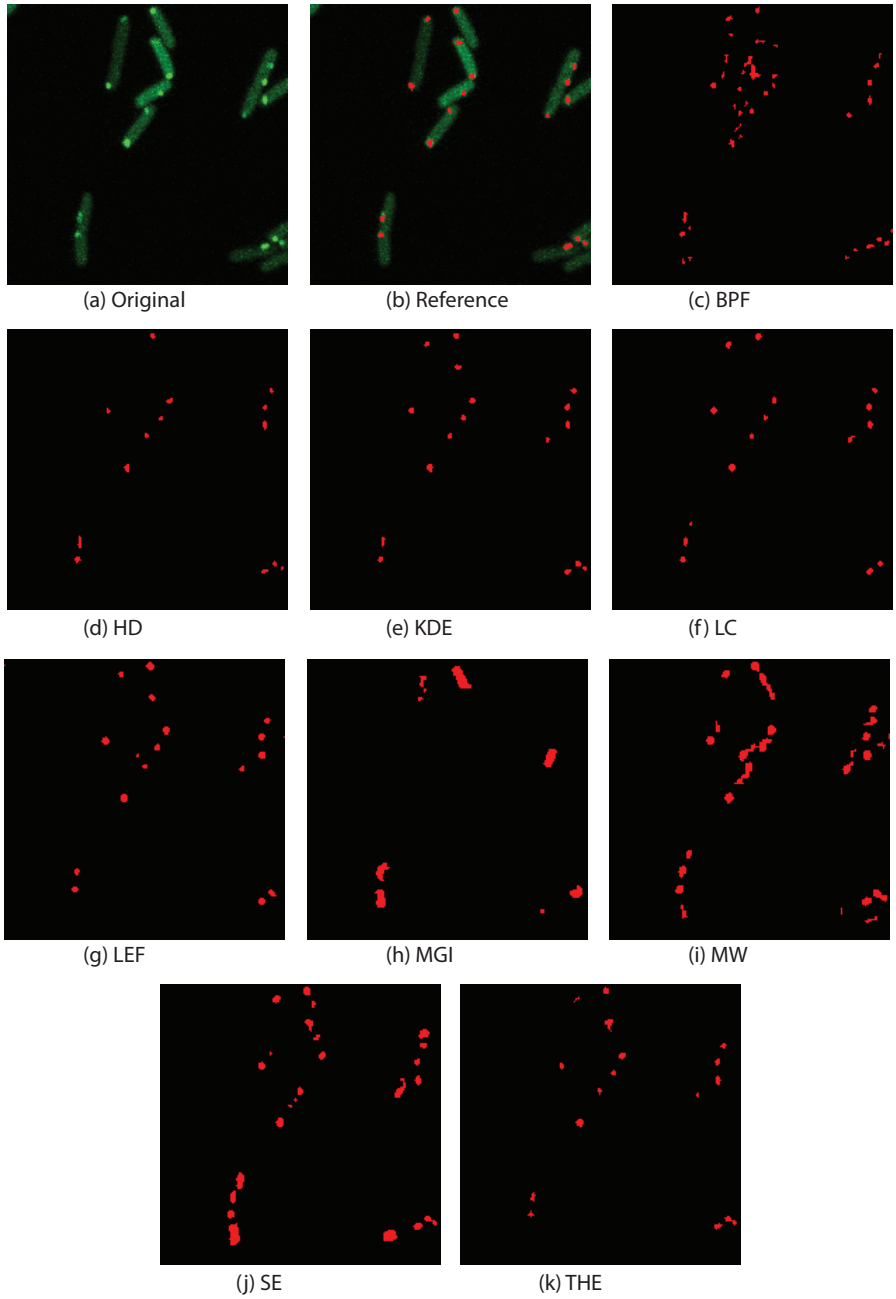

Figure 3.8: *Representative example of MS2-GFP tagged RNA detection in E. coli cell. The original image is shown in green and the detected RANs are shown in red.*

This study measures the individual RNA molecules as a bright spot in confocal images. The distribution of the time interval between productions of individual RNA molecules is inferred from the acquired images. The production event of an RNA molecule is detected by counting RNA molecules at each time point in a time-series. The inference procedure requires a reliable method for the detection of individual RNA molecules. An exhaustive evaluation is carried out to select a method to segment the RNA molecules from the images. A representative result from the evaluation is presented in Figure 3.8. In the evaluation, the kernel density estimation (KDE) [65] method for spot detection is found as one of the most reliable methods and it is applied to detect RNA molecules in the images.

Apart from this, several studies are conducted exploring the nature of the partitioning of RNA molecules during cell division [110, 111]. These studies also measure RNA molecules tagged with MS2-GFP in *E. coli* cells. The KDE method exhibits robust performance for detecting RNA spots in these studies as well.

4 Discussion and future work

Single-cell studies represent a large step forward in the understanding of biological systems. Image-based assays are becoming increasingly popular for single-cell studies. Methods for image analysis are playing a significant role in systems biology research more than ever before. The aim of this thesis is to study and develop methods that facilitate the acquisition and analysis of high-throughput data for single-cell studies. The results of the conducted research activities are reported in the following publications:

[Publication I] *S. Chowdhury, M. Kandhavelu, O. Yli-Harja, and A.S. Ribeiro, An interacting multiple model filter-based autofocus strategy for confocal time-lapse microscopy,* Journal Microscopy*, 245(3):265-275, March 2012.*

Publication I proposes a novel strategy for focusing in time-lapse imaging. The proposed strategy relies on the nature of the focus drift and its predictability. At first, the focus-drift in different thermal conditions is studied and then, the interacting multiple model (IMM) filter is employed to predict the drift prior to the measurement. This allows a drastic reduction of the number of z-slices required for the continuous tracking of the focal plane, which in turn curtails the problem of photobleaching significantly. In addition, a set of functions for focusing in time-lapse imaging is derived from existing ones. The performance of the proposed method is exhibited in simulation as well as in an operational environment.

To the best of our knowledge, the method proposed in Publication I, is the first of its kind that applies a probabilistic filter for focus-drift correction. Relevantly, the Publication I realizes classical approaches for focusing as a special case of the proposed framework that considers only the random walk model, disregarding the velocity and acceleration of the drift. Thus, earlier efforts for optimizing focusing system can be incorporated well within the proposed framework. It is worthwhile

to note that, the proposed method for focusing is completely software-based and is not dependent on any assistive hardware i.e. light emitting diode (LED).

[Publication II] *S. Chowdhury, M. Kandhavelu, O. Yli-Harja, and A.S. Ribeiro, Cell segmentation by multi-resolution analysis and maximum likelihood estimation (MAMLE),* BMC Bioinformatics*, 14(Suppl 10):S8, August 2013.*

Segmentation of individual cells from an image-based assay is a challenging problem of cell image analysis. Publication II proposes a novel segmentation method, MAMLE, for the detection of cells within a dense cluster. The MAMLE performs cell segmentation in two stages. The first stage relies on image denoising, edge detection with multi-resolution analysis and threshold decomposition for adaptive thresholding. From this result, a correction procedure is applied that maximizes the likelihood estimate as the objective criterion. Simultaneously, it constructs a parametric estimation on the morphological features from the initial segmentation for evaluating the likelihood, after which the final segmentation is obtained. The proposed method is evaluated with a diverse set of samples that includes images from different sources. The MAMLE method has attained a very high (above 90%) accuracy in the empirical evaluation. Finally, its is compared to a collection of existing methods, and in all tests, MAMLE outperformed the existing ones in segmentation accuracy.

The MAMLE method has four parameters, whose settings are intuitive. Either knowledge of the cells' morphology or a quick observation of the images, along with the metadata from the imaging system suffice to introduce parameter values that lead to robust results. Nevertheless, the parametric robustness of the MAMLE method is also studied in Publication II. The foremost strength of the MAMLE relies on its ability to segment cells in a dense colony as well as its robustness across a wide range of cell types or imaging modalities.

[Publication III] *P. Ruusuvuori, T. Äijö, S. Chowdhury, C. Garmendia-Torres, J. Selinummi, M. Birbaumer, A.M. Dudley, L. Pelkmans, and O. Yli-Harja, Evaluation of methods for detection of fluorescence labeled subcellular objects in microscope images,* BMC Bioinformatics*, 11:248, May 2010.*

Publication III conducts a comprehensive evaluation of a broad set of methods for detecting subcellular organelles. Several methods have been proposed for detecting subcellular organelles in microscope images. A vast majority of these methods have been designed for solving specific tasks and evaluated with a limited set of images. Therefore, a comprehensive evaluation is indeed invaluable. A few of the

included methods, that have never been mentioned earlier in this context, enriches the set of available methods for detection and compares them against the current state-of-the-art methods for the detection of subcellular organelles. The test sets are selected justifiably from the experimentally derived images that represent the realistic scenario in systems biology applications. It also encompasses simulated images in order to evaluate the methods with full reference. The study reveals major differences in the performance of the different methods. Publication III recommends that the selection of detection algorithm for subcellular organelles should be done carefully and take into account different conditions, such as the possibility of acquiring empty images or images with a very low number of objects.

[**Publication IV**] *A.-B. Muthukrishnan, M. Kandhavelu, J. Lloyd-Price, F. Kudasov, S. Chowdhury, O. Yli-Harja, and A.S. Ribeiro, Dynamics of transcription driven by the tetA promoter, one event at a time, in live Escherichia coli cells,* Nucleic Acids Research*, 40(17):8472-8483, September 2012.*

Publication IV studies the effect of tetracycline on the dynamics of gene expression in the *E. coli*. It infers the *in vivo* kinetics of production of individual RNA molecules of the target gene as a function of temperature and inducer concentration. From the distributions of intervals between transcription events, it manifests that RNA production by P_{tetA} is a sub-Poissonian process. The number and duration of the prominent sequential steps in transcription initiation are also inferred. Under optimal condition, three major steps are observed. The experimental procedure in this study is based on *in vivo* imaging in time-series with a confocal microscope. An implementation of the method proposed in the Publication I is employed for imaging in time-series. The acquired time-series are then analyzed with the kernel density estimation (KDE) method, which is reported as one of the best performing methods in Publication III.

[**Publication V**] *S. Chowdhury, P. Ruusuvuori, P. Liberali, P. Rämö, L. Pelkmans, and O. Yli-Harja, Automated cell tracking and cell lineage construction with improved performance, In* Proceedings of the 6th International Workshop on Computational Systems Biology,*(Århus), Denmark, June 10-12, 2009, pp. 27-30.*

Automated nuclei tracking is another challenging problem in cell image analysis. The Publication V proposes improvements on a state-of-the-art method that solved this problem by exploiting level set method and interacting multiple model (IMM) filter. It shows that the level set method often suffered from imbalanced area distribution among cells that are in close contact; whose continuation in several

frames led to false positive cell divisions. In order to equalize the distribution of area among the nuclei, the Publication V applies k-means clustering algorithm as a post-processing step of level set and this post-processing improved the accuracy of lineage construction in the range of 9-16%.

The challenges of cell detection are initially addressed in Publication V as a part of a system for tracking cells. Publication II studies the cells detection problem more closely and makes a leap forward regarding these challenges.

All the publications are closely related to the thesis topic. Publication I proposes a novel method for time-lapse microscopy. The Publication II, III, and V study and propose several methods to analyze microscopy images containing cells and subcellular organelles. The Publication IV exemplifies the application of the studied methods in a multidisciplinary research which studies the dynamics of gene regulation in *E. coli* cells.

1 Future work

Several methods for microscopy and its analysis are proposed and studied in this thesis. The studied methods perform effectively and are integrated into systems biology research. However, in the future, following challenges can be addressed as a continuation.

1.1 Extension of existing methods for cell detection

A significant part of this study contributes to the development of the MAMLE method for cell detection. This method relies on two principles: i) multi-resolution analysis for the generation of initial segmentation, and ii) maximum-likelihood estimation for the correction of segmentation artifacts. The aforementioned principles are generic. It can be hypothesized that their incorporation might enhance many of the existing solutions for cell detection. Further study is required to test this hypothesis, however. A positive result of this hypothesis would certainly be a complement to the essence of the MAMLE method.

1.2 Systems for cell detection and validation

Despite the abundance of methods for image analysis, the power of automated analysis has not yet been harnessed to full capacity. Most of the methods for image analysis are demonstrated as a part of research articles. Indeed, a very

few methods are made available to the research community for the application in systems biology research. The lack of availability of systems for image analysis is recognized as a significant bottleneck in this regard. Such systems would bring cutting-edge developments in the field of image analysis to biologists. The system of image analysis should be modular and it would support extension for the inclusion of novel methods. This concept is adopted in CellProfiler [13] and ImageJ [112] platforms. In addition to these, the system should define a standard protocol for storing results. A common standard would ease interoperability among different modules within a single system as well as allow data-sharing across different systems.

Systematic approach for validation is also essential to assess the reliability of a method. Traditional approaches construct the reference result for validation by manual segmentation. However, manual segmentation is a tiresome task and often subject to individual preference [104]. Synthetic images are becoming a leading-edge solution for the validation of methods. In a synthetic image, the reference result of the image segmentation is known *a priori*. Thereby, turns the comparison of different segmentation methods straightforward. Moreover, the reference result is free from subjective variance. Existing methods for synthetic image generation are still at their early stages, but developing rapidly. Synthetic image generation and validation procedures should be paired together and made available as an integral part of image analysis system. Further efforts will be required in the future to develop a complete system of image analysis and validation.

5 Conclusion

This thesis studies and introduces methods for microscopy and its analysis for systems biology research. The main challenges addressed in this study are as follows: focus-drift compensation in time-lapse microscopy, cell detection from a cluster of cells, and the detection of subcellular organelles. The research conducted during the course of study yields to following results and conclusions:

1. The performance of the focusing algorithm is enhanced when two distinct focus-functions are combined. One optimizes for focus quality in a single stack of images, while the other maintains temporal correlation between successive frames. The results presented in Table 3.2 (Chapter 3) exhibit that the $f_{\text{Pearson's}} \times f_{\text{Tenegrad}}$ metric has outperformed all other alternatives in quantitative evaluation [Publication I].

2. This study confirms that the focus-drift can be modeled and tracked with probabilistic filter. The probabilistic filter enables prediction of the focus-drift. This prediction in turn, significantly reduces the number of required scans for focusing [Publication I]. Photobleaching is therefore reduced. The proposed strategy is evaluated in simulation as well as implemented in an operational environment for microscopy.

3. The challenge of cell detection is first addressed in Publication V. Later, in Publication II, the multi-resolution analysis with threshold decomposition is demonstrated as a suitable approach for detecting individual cells from a dense cluster of cells.

4. The maximum-likelihood estimation of the shape parameters is favored to enhance the segmentation accuracy. The parameters are estimated from partially segmented results that are obtained from the multi-resolution analysis. The combination of multi-resolution analysis and maximum-likelihood estimation, proposed as MAMLE, is validated with multiple sets of sample containing cells

[Publication II].

5. In concern to the detection of subcellular organelles, it is concluded that there is no method which is exclusively superior to all other methods. Thereby, the exact method for this challenge is subjected to the specific application [Publication III].

These findings are associated with the research questions raised in the Chapter 1. A few of these findings are contributed in designing the experimental and analysis protocol of Publication IV. In addition, the results are also incorporated in several systems biology studies as a regular method for imaging and analysis [2, 7, 110, 111, 113, 114]. Some of these conclusions are reinforced later on by independent research group [115].

The subject matter of this thesis, microscopy and its analysis at the single-cell level, is an active field of research and has been evolving for more than half a century. A complete solution to this challenge has always been projected within a few years ahead, however, such a complete solution has never been grasped in practice. This thesis manifests an effort to make an advancement regarding this prolonged challenge. Indeed, ingenious pipelines for microscopy and analysis are still emerging. For instance, solution for analyzing time-lapse microscopy is not fully fledged yet. The multimodal microscopy is another kind of imaging that is drawing increased attentions. The demands for seamless analysis of multimodal microscopy and time-lapse imaging are extending this challenge further.

6 Appendix-A: IMM filter-based focusing

Definition of the variables and notations:

T - Imaging intervals

$\hat{\mathbf{x}}_t^{(j)}$ - The state vector of the model j at time t

$\mathbf{w}_t^{(j)}$ - The weight of the model j at time at time t

$\mathbf{c}_t^{(j)}$ - The covariance of the model j at time t

M - Number of models, in this case fixed to 3

$\mathcal{G}(.)$ - The focus-function

$\mathbf{y}_t$ - Measured focus position at time t

$\mathbf{K}_t^{(j)}$ - The Kalman gain of the model j at time at time t

$\prime$ - The transpose operation of a matrix

$$\mathbf{F}^{(1)} = \begin{bmatrix} 1 & 0 & 0 \\ 0 & 0 & 0 \\ 0 & 0 & 0 \end{bmatrix}$$

$$\mathbf{F}^{(2)} = \begin{bmatrix} 1 & T & 0 \\ 0 & 1 & 0 \\ 0 & 0 & 0 \end{bmatrix}$$

$$\mathbf{F}^{(3)} = \begin{bmatrix} 1 & T & \frac{T^2}{2} \\ 0 & 1 & T \\ 0 & 0 & 1 \end{bmatrix}$$

$$\mathbf{H} = \begin{bmatrix} 1 & 0 & 0 \end{bmatrix}$$

$$\mathbf{P} = \begin{bmatrix} 0.90 & 0.05 & 0.05 \\ 0.05 & 0.90 & 0.05 \\ 0.05 & 0.05 & 0.90 \end{bmatrix}$$

Algorithm 6.1 IMMFocusPredict($\hat{\mathbf{x}}_{t-1}^{(1..M)}$, $\mathbf{w}_{t-1}^{(1..M)}$, $\mathbf{c}_{t-1}^{(1..M)}$)

Input: $\hat{\mathbf{x}}_{t-1}^{(1..M)}$, $\mathbf{w}_{t-1}^{(1..M)}$, $\mathbf{c}_{t-1}^{(1..M)}$
Output: $\hat{\mathbf{x}}_{t|t-1}$, $\hat{\mathbf{y}}_{t|t-1}$, $\mathbf{c}_{t|t-1}$

1: $\mathbf{w}_{t|t-1}^{(j)} \leftarrow \sum_{i=1}^{M} \mathbf{P}^{(i,j)} \mathbf{w}_{t-1}^{(i)}$
2: $\mathbf{w}_{t-1}^{(i|j)} \leftarrow \frac{\mathbf{P}^{(i,j)} \mathbf{w}_{t-1}^{(i)}}{\mathbf{w}_{t|t-1}^{(j)}}$
3: $\hat{\mathbf{x}}_{t-1}^{(0j)} \leftarrow \sum_{i=1}^{M} \mathbf{w}_{t-1}^{(i|j)} \hat{\mathbf{x}}_{t-1}^{(i)}$
4: $\mathbf{c}_{t-1}^{(0j)} \leftarrow \sum_{i=1}^{M} \mathbf{w}_{t-1}^{(i|j)} \left[\mathbf{c}_{t-1}^{(i)} + \left(\hat{\mathbf{x}}_{t-1}^{(i)} - \hat{\mathbf{x}}_{t-1}^{(0j)} \right) \left(\hat{\mathbf{x}}_{t-1}^{(i)} - \hat{\mathbf{x}}_{t-1}^{(0j)} \right)' \right]$
5: $\hat{\mathbf{x}}_{t|t-1}^{(j)} \leftarrow \mathbf{F}^{(j)} \hat{\mathbf{x}}_{t-1}^{(0j)}$
6: $\mathbf{c}_{t|t-1}^{(j)} \leftarrow \mathbf{F}^{(j)} \mathbf{c}_{t-1}^{(0j)} \left(\mathbf{F}^{(j)} \right)' + \mathbf{Q}^{(j)}$
7: $\hat{\mathbf{x}}_{t|t-1} \leftarrow \sum_{j=1}^{M} \mathbf{w}_{t|t-1}^{(j)} \hat{\mathbf{x}}_{t|t-1}^{(j)}$
8: $\hat{\mathbf{y}}_{t|t-1} \leftarrow \mathbf{H} \hat{\mathbf{x}}_{t|t-1}$
9: $\mathbf{c}_{t|t-1} \leftarrow \sum_{j=1}^{M} \mathbf{w}_{t|t-1}^{(j)} \left[\mathbf{c}_{t|t-1}^{(j)} + \left(\hat{\mathbf{x}}_{t|t-1}^{(j)} - \hat{\mathbf{x}}_{t|t-1} \right) \left(\hat{\mathbf{x}}_{t|t-1}^{(j)} - \hat{\mathbf{x}}_{t|t-1} \right)' \right]$
10: Return $\hat{\mathbf{x}}_{t|t-1}$, $\hat{\mathbf{y}}_{t|t-1}$, $\mathbf{c}_{t|t-1}$

Algorithm 6.2 IMMFocus($\hat{\mathbf{x}}_{t-1}^{(1..M)}$, $\mathbf{w}_{t-1}^{(1..M)}$, $\mathbf{c}_{t-1}^{(1..M)}$)

Input: $\hat{\mathbf{x}}_{t-1}^{(1..M)}$, $\mathbf{w}_{t-1}^{(1..M)}$, $\mathbf{c}_{t-1}^{(1..M)}$
Output: $\hat{\mathbf{x}}_{t}^{(1..M)}$, $\mathbf{w}_{t}^{(1..M)}$, $\mathbf{c}_{t}^{(1..M)}$

1: IMMFocusPredict($\hat{\mathbf{x}}_{t-1}^{(1..M)}$, $\mathbf{w}_{t-1}^{(1..M)}$, $\mathbf{c}_{t-1}^{(1..M)}$)
2: $\mathbf{y}_t \leftarrow \arg\max_{\mathbf{y}} \mathcal{G}(\mathbf{y} | \hat{\mathbf{y}}_{t|t-1})$
3: $\mathbf{K}_t^{(j)} \leftarrow \mathbf{c}_{t|t-1}^{(j)} \mathbf{H}' \left(\mathbf{H} \mathbf{c}_{t|t-1}^{(j)} \mathbf{H}' + \mathbf{R} \right)^{-1}$
4: $\hat{\mathbf{x}}_t^{(j)} \leftarrow \hat{\mathbf{x}}_{t|t-1}^{(j)} + \mathbf{K}_t^{(j)} \left(\mathbf{y}_t - \mathbf{H} \hat{\mathbf{x}}_{t|t-1}^{(j)} \right)$
5: $\mathbf{c}_t^{(j)} \leftarrow \mathbf{c}_{t|t-1}^{(j)} - \mathbf{K}_t^{(j)} \mathbf{H} \mathbf{c}_{t|t-1}^{(j)}$
6: $\mathbf{w}_t^{(j)} \leftarrow \mathbf{w}_{t|t-1}^{(j)} \Lambda_t^{(j)}$
7: Return $\hat{\mathbf{x}}_t$, $\mathbf{w}_t$, $\mathbf{c}_t$

7 Appendix-B: The MAMLE method

Definition of the variables and notations:

f - The 2D image under consideration for fuzzy-edge detection

$\mathcal{S}$ - The number of scales for multi-resolution analysis

$\mathcal{D}$ - The set of directions for the edge detection

$\mathbf{B_s^d}$ - The morphological kernel for detecting edge in the direction d at scale s

E - The fuzzy-edge image

l - The edge-threshold

T_a - The area-threshold

S - The image containing region-labells

P - The set of boundary-pixels (p_1, p_2 p_3 ... p_n) of an object

$\mathbf{X}$ - The feature vector of the object represented by P = (p_1, p_2 p_3 ... p_n)

$\mathbf{X}_{i\to j}$ - The feature vector of the object represented by $\mathrm{P}_{i\to j}$ = (p_i, p_{i+1} p_{i+2} ... p_j) and $\mathrm{P}_{i\to j} \subset \mathrm{P}$

μ - The mean vector

Σ - The covariance matrix of the feature vector

$\mathbf{X}_i$ - The feature vector of i^{th} object

$\mathbf{X}_{ij}$ - The feature vector of the augmented object, obtained by merging i^{th} object with j^{th}

$\mathbf{X}_{ijk}$ - The feature vector of the augmented object, obtained by merging i^{th}, j^{th} and k^{th} object together

$D(\mathbf{X}_i)$ - The distance function enumerated as $(\mathbf{X}_i - \mu)' \Sigma^{-1} (\mathbf{X}_i - \mu)$

$\circ$ - The the morphological erosion operation

$\prime$ - The transpose operation of a matrix

Algorithm 7.1 ConstructFuzzy-EdgeImage(f, $\mathcal{S}$, $\mathcal{D}$, $\mathbf{B_s^d}$)

Input: f, $\mathcal{S}$, $\mathcal{D}$, $\mathbf{B_s^d}$
Output: Fuzzy-edge image: E

1: **for** s:=1 **to** $\mathcal{S}$ **do**
2: Construct f_s by filtering f with an uniform kernel of the scale s
3: **for each** $d \in \mathcal{D}$ **do**
4: $E_s^d(f_s) \leftarrow \begin{cases} 1 & \text{if} f_s = f_s \circ \mathbf{B_s^d} \\ 0, & \end{cases}$
5: **end for**
6: $E_s(f_s) \leftarrow \bigcup_d E_s^d(f_s)$
7: **end for**
8: $E(f) \leftarrow \sum_{s=1}^{S} E_s(f_s)$
9: Return E

Algorithm 7.2 ThresholdDecompositon(E, l, T_a)

Input: E, l, T_a
Output: S

1: Initialize S $\leftarrow \emptyset$
2: Select the edges in E that are stronger than l and generate region labelled image $\mathcal{R}$
3: $l^- \leftarrow l - 1$
4: **for each** $R_i \in \mathcal{R}$ **do**
5: **if** Area(R_i) $> T_a$ **then**
6: $S_i \leftarrow$ ThresholdDecompositon(E $\cap$ R_i, l^-, T_a)
7: Update S with S_i
8: **else**
9: Update S with R_i
10: **end if**
11: **end for**
12: Return S

Algorithm 7.3 BinarySplit(P, X)

Input: P = (p_1, p_2 p_3 ... p_n), X
Output: S (Region labelled image after splits)

Initialize S $\leftarrow \emptyset$
$\mathbf{X}^* \leftarrow \arg\min_{i,j} D(\mathbf{X}_{i \rightarrow j})$
$\mathrm{P}^c \leftarrow \mathrm{P} \setminus \mathrm{P}^*$
$\mathrm{S} \leftarrow \mathrm{S} \bigcup \mathrm{P}^*$
if Area($\mathbf{X}^c$) > Area($\mathbf{X}$) **then**
    $\mathrm{S}^c \leftarrow$ BinarySplit(P^c,$\mathbf{X}^c$)
    Update S with S^c
else
    Update S with P^c
end if
Return S

Algorithm 7.4 Over-segmentationCorrection(S)

Input: S

Output: S_{out}

Initialize $S_{out} \leftarrow S$
Initialize $h \leftarrow 0$
for each region $S_i \in S$ **do**
  Generate the feature vector $\mathbf{X}_i$
end for
Construct $\mathbf{C}$ as: $\forall c_i \in \mathbf{C} \exists c_j \in \mathbf{C}(D(\mathbf{X}_i) + D(\mathbf{X}_j) \geq D(\mathbf{X}_{ij}) \wedge i \neq j)$
for each $c_i \in \mathbf{C}$ **do**
  Update $h \leftarrow h + 1$
  $\mathbf{L}(h) \leftarrow -D(\mathbf{X}_i)$
  $\mathbf{H}(h, l) \leftarrow \begin{cases} 1 & \text{if } l = i \\ 0 & \text{Otherwise} \end{cases}$
end for
Construct $\mathbf{C}_2$ as: $\forall c_{ij} \in \mathbf{C}_2 \exists c_j, c_j \in \mathbf{C}(D(\mathbf{X}_i) + D(\mathbf{X}_j) \geq D(\mathbf{X}_{ij}) \wedge i \neq j)$
for each $c_{ij} \in \mathbf{C}_2$ **do**
  Update $h \leftarrow h + 1$
  $\mathbf{L}(h) \leftarrow -D(\mathbf{X}_{ij})$
  $\mathbf{H}(h, l) \leftarrow \begin{cases} 1 & \text{if } l = i \vee l = j \\ 0 & \text{Otherwise} \end{cases}$
end for
Construct $\mathbf{C}_3$ as: $\forall c_{ijk} \in \mathbf{C}_3 \exists c_j, c_j, c_k \in \mathbf{C}(D(\mathbf{X}_i) + D(\mathbf{X}_j) + D(\mathbf{X}_k) \geq D(\mathbf{X}_{ijk}) \wedge i \neq j \neq k)$
for each $c_{ijk} \in \mathbf{C}_3$ **do**
  Update $h \leftarrow h + 1$
  $\mathbf{L}(h) \leftarrow -D(\mathbf{X}_{ijk})$
  $\mathbf{H}(h, k) \leftarrow \begin{cases} 1 & \text{if } l = i \vee l = j \vee l = k \\ 0 & \text{Otherwise} \end{cases}$
end for
$\mathbf{b}^* \leftarrow \arg\max_{\mathbf{b}}(\mathbf{L}'\mathbf{b}),$ such that $\mathbf{H}'\mathbf{b}^* = \mathbf{1}$
Update S_{out} by merging the objects according to the selected hypotheses, $\mathbf{b}^*$.
Return S_{out}

Bibliography

[1] P. Ruusuvuor. *Methods for image analysis, object classification and validation in biomedical microscopy applications.* PhD thesis, Tampere University of Technology, Publication 864, 2010.

[2] A.-B. Muthukrishnan. *Studies of the plasticity of transcription in Escherichia coli using single-molecule, in vivo detection techniques.* PhD thesis, Tampere University of Technology, Publication 1238, 2014.

[3] I. Golding, J. Paulsson, S.M. Zawilski, and E.C. Cox. Real-time kinetics of gene activity in individual bacteria. *Cell*, 123(6):1025 – 1036, 2005.

[4] A.B. Lindner, R. Madden, A. Demarez, E.J. Stewart, and F. Taddei. Asymmetric segregation of protein aggregates is associated with cellular aging and rejuvenation. *Proceedings of the National Academy of Sciences*, 105(8):3076 – 3081, 2008.

[5] Y. Taniguchi, P.J. Choi, G.-W. Li, H. Chen, M. Babu, J. Hearn, A. Emili, and X.S. Xie. Quantifying e. coli proteome and transcriptome with single-molecule sensitivity in single cells. *Science*, 329(5991):533 – 538, 2010.

[6] M. Kandhavelu, H. Mannerström, A. Gupta, A. Häkkinen, J. Lloyd-Price, O. Yli-Harja, and A.S. Ribeiro. In vivo kinetics of transcription initiation of the lar promoter in escherichia coli. evidence for a sequential mechanism with two rate-limiting steps. *BMC Systems Biology*, 5(149), 2011.

[7] J. Mäkelä, M. Kandhavelu, S.M.D. Oliveira, J.G. Chandraseelan, J. Lloyd-Price,
kinetics of activation and subsequent activity of the arabinose promoter. *Nucleic Acids Research*, 2013.

[8] B.N. Kholodenko and H.M. Sauro. Mechanistic and modular approaches to modeling and inference of cellular regulatory networks. In L. Alberghina and H.V. Westerhoff, editors, *Systems Biology: Definitions and Perspectives*, volume 13 of *Topics in Current Genetics*, page 357 – 451. Springer Berlin Heidelberg, 2005.

[9] S.A. Haney, P. LaPan, J. Pan, and J. Zhang. High-content screening moves to the front of the line. *Drug Discovery Today*, 11(19 – 20):889 – 894, 2006.

[10] A. Tárnok. A focus on high-content cytometry. *Cytometry Part A*, 73(5):381 – 383, 2008.

[11] S. Pitchiaya, L.A. Heinicke, T.C. Custer, and N.G. Walter. Single molecule fluorescence approaches shed light on intracellular rnas. *Chemical Reviews*, 114(6):3224 – 3265, 2014.

[12] R. Wayne. *Light and video microscopy.* Academic Press, USA, 2009.

[13] A.E. Carpenter, T.R. Jones, M.R. Lamprecht, C. Clarke, I.H. Kang, O. Friman, D.A. Guertin, J.H. Chang, R.A. Lindquist, J. Moffat, P. Golland, and D. Sabatini. Cellprofiler: image analysis software for identifying and quantifying cell phenotypes. *Genome Biology*, 7:R100, 2006.

[14] J.M. Guberman, A. Fay, J. Dworkin, N.S. Wingreen, and Z. Gitai. Psicic: Noise and asymmetry in bacterial division revealed by computational image analysis at sub-pixel resolution. *PLoS Computational Biology*, 4(11):e1000233, 2008.

[15] Q. Wang, J. Niemi, C.-M. Tan, L. You, and M. West. Image segmentation and dynamic lineage analysis in single-cell fluorescence microscopy. *Cytometry Part A*, 77A(1):101 – 110, 2010.

[16] J.W. Young, J.C. Locke, A. Altinok, N. Rosenfeld, T. Bacarian, P.S. Swain, E. Mjolsness, and M.B. Elowitz. Measuring single-cell gene expression dynamics in bacteria using fluorescence time-lapse microscopy. *Nature Protocols*, 7(1):80 – 88, 2011.

[17] W.J. Croft. *Under the microscope: A brief history of microscopy.* World Scientific Publishing Co. Pte. Ltd., Singapore, 2006.

[18] D.B. Murphy. *Fundamentals of light microscopy and electronic imaging.* John Wiley and Sons Inc., USA, 2001.

[19] J.M. Senior. *Optical fiber communications: principles and practice*. Second Edition, Prentice Hall International Ltd., USA, 1993.

[20] D. Semwogerere and E.R. Weeks. *Encyclopedia of Biomaterials and Biomedical Engineering*. Taylor and Francis, USA, 2005.

[21] T. Wilson. *Biomedical Optical Imaging*. Oxford University Press, UK, 2009.

[22] D.J. Stephens and V.J. Allan. Light microscopy techniques for live cell imaging. *Science*, 300(5616):82 – 86, 2003.

[23] D.C. Mason and D.K. Green. Automatic focusing of a computer-controlled microscope. *IEEE Transactions on Biomedical Engineering*, 22(4):312 – 317, 1975.

[24] F.C.A. Groen, I.T. Young, and G. Ligthart. A comparison of different focus functions for use in autofocus algorithms. *Cytometry*, 6:81 – 91, 1985.

[25] S. Brázdilová and M. Kozubek. Image division technique in pre-acquisition analysis of information content for automated microscopy. *Journal of Microscopy*, 242(3):629 – 639, 2011.

[26] R.A. Hoebe, C.H. Van Oven, T.W.J. Gadella, P.B. Dhonukshe, C.J.F Van Noorden, and E.M.M. Manders. Controlled light-exposure microscopy reduces photobleaching and phototoxicity in fluorescence live-cell imaging. *Nature Biotechnology*, 25:249.

[27] J. Widengren and R. Rigler. Mechanisms of photobleaching investigated by fluorescence correlation spectroscopy. *Bioimaging*, 4(3):149 – 157, 1996.

[28] S. Brázdilová and M. Kozubek. Information content analysis in automated microscopy imaging using an adaptive autofocus algorithm for multimodal functions. *Journal of Microscopy*, 236(3):194 – 202, 2009.

[29] O. Osibote, R. Dendere, S. Krishnan, and T. Douglas. Automated focusing in bright-field microscopy for tuberculosis detection. *Journal of Microscopy*, 240(2):155 – 163, 2010.

[30] X.Y. Liu, W.H. Wang, and Y. Sun. Dynamic evaluation of autofocusing for automated microscopic analysis of blood smear and pap smear. *Journal of Microscopy*, 227(1):15 – 23, 2007.

[31] F.R. Boddeke, L.J. Van Vliet, and I.T. Young. Calibration of the automated z-axis of a microscope using focus functions. *Journal of Microscopy*, 186(3):270 – 274, 1997.

[32] T.T.E. Yeo, S.H. Ong, Jayasooriah, and R. Sinniah. Autofocusing for tissue microscopy. *Image and Vision Computing*, 11(10):629 – 639, 1993.

[33] A. Santos, C. Ortiz De Solórzano, J.J. Vaquero, J. M. Peña, N. Malpica, and F. Del Pozo. Evaluation of autofocus functions in molecular cytogenetic analysis. *Journal of Microscopy*, 188:264 – 272, 1997.

[34] M.A. Bueno-Ibarra, J. Alvarez-Borrego, L. Acho, and M.C. Chavez-Sanchez. Fast autofocus algorithm for automated microscopes. *Optical Engineering*, 44(063601), 2005.

[35] J.M. Tenenbaum. *Accommodation in computer vision*. PhD thesis, Stanford University, 1970.

[36] D. Vollath. Automatic focusing by correlative methods. *Journal of Microscopy*, 147(3):279 – 288, 1987.

[37] J.F. Brenner, B.S. Dew, J.B. Horton, T. King, P.W. Neurath, and W.D. Selles. An automated microscope for cytologic research a preliminary evaluation. *Journal of Histochemistry and Cytochemistry*, 24(1):100 – 111, 1976.

[38] M. Kreft, M. Stenovec, and R. Zorec. Focus-drift correction in time-lapse confocal imaging. *Annals of the New York Academy of Sciences*, 1048:321 – 330, 2005.

[39] Y. Sun, S. Duthaler, and B.J Nelson. Autofocusing in computer microscopy: Selecting the optimal focus algorithm. *Microscopy Research and Technique*, 65:629 – 639, 2004.

[40] L. Firestone, K. Cook, K. Culp, N. Talsania, and K. Preston. Comparison of autofocus methods for automated microscopy. *Cytometry*, 12:195 – 206, 1991.

[41] N. Kanopoulos, N. Vasanthavada, and R.L. Baker. Design of an image edge detection filter using the sobel operator. *IEEE Journal of solid-state circuits*, 23(2):358 – 367, 1988.

[42] L.-C. Chen, H.-W. Laia, Y.-T. Huang, J.-C. Chang, C.C. Chang, and J.-L. Chen. Dynamic nano-scale surface profilometry using stroboscopic interferometry. In *Proceedings of the 33rd Annual Conference of the IEEE Industrial Electronics Society*, pages 3027 – 3032, Taipei, Taiwan, Nov 2007.

[43] U. Fano. Ionization yield of radiations. ii. the fluctuations of the number of ions. *Physical Review*, 72(1):26, 1947.

[44] K. Pearson. Notes on regression and inheritance in the case of two parents. *Proceedings of the Royal Society of London*, 58:240 – 242, 1895.

[45] F. Li, X. Zhou, J. Zhu, J. Ma, X. Huang, and S.T.C Wong. High content image analysis for human h4 neuroglioma cells exposed to cuo nanoparticles. *BMC Biotechnology*, 7:66, 2007.

[46] F. Li, X. Zhou, J. Ma, and S.T.C Wong. Multiple nuclei tracking using integer programming for quantitative cancer cell cycle analysis. *IEEE Transaction on Medical Imaging*, 29:96 – 105, 2010.

[47] R.C. Gonzalez and R.E. Woods. *Digital image processing*. Second Edition, Prentice Hall International Ltd., USA, 2002.

[48] N. Otsu. A threshold selection method from gray-level histograms. *IEEE Transactions on Systems Man and Cybernetics*, 9(1):62 – 66, 1979.

[49] L. Vincent and P. Soille. Watersheds in digital spaces: An efficient algorithm based on immersion simulations. *IEEE Transactions on Pattern Analysis and Machine Intelligence*, 13(6):583 – 598, 1991.

[50] Y. Al-Kofahi, W. Lassoued, W. Lee, and B. Roysam. Improved automatic detection and segmentation of cell nuclei in histopathology images. *IEEE Transactions on Biomedical Engineering*, 57(4):841 – 852, 2010.

[51] K. Li, E.D. Miller, M. Chen, T. Kanade, L.F. Weiss, and P.G. Campbell. Cell population tracking and lineage construction with spatiotemporal context. *Medical Image Analysis*, 12(5):546 – 566, 2008.

[52] N. Wiener. *Extrapolation, interpolation, and smoothing of stationary time series*. The MIT Press, Cambridge, Massachusetts, USA, 1949.

[53] K. Dabov, A. Foi, V. Katkovnik, and K. Egiazarian. Image denoising by sparse 3-d transform-domain collaborative filtering. *IEEE Transactions on Image Processing*, 16(8):2080 – 2095, 2007.

[54] J. Selinummi, P. Ruusuvuori, I. Podolsky, A. Ozinsky, E. Gold, O. Yli-Harja, A. Aderem, and I. Shmulevich. Bright field microscopy as an alternative to whole cell fluorescence in automated analysis of macrophage images. *PLOS One*, 4(10):e7497, 2009.

[55] Q. Wu, F.A. Merchant, and K.R. Castleman. *Microscope Image Processing*. Academic Press, Burlington, 2008.

[56] E. Meijering. Cell segmentation: 50 years down the road [life sciences]. *IEEE Signal Processing Magazine*, 29(5):140 – 145, 2012.

[57] H. Kong, H.C. Akakin, and S.E. Sarma. A generalized laplacian of gaussian filter for blob detection and its applications. *IEEE Transactions on Cybernetics*, 43(6):1719 – 1733, 2013.

[58] C.G. Loukas, G.D. Wilson, B. Vojnovic, and A. Linney. An image analysis-based approach for automated counting of cancer cell nuclei in tissue sections. *Cytometry Part A*, 55A(1):30 – 42, 2003.

[59] F. Sadeghian, Z. Seman, A.R. Ramli, B.H.A. Kahar, and M.-I. Saripan. A framework for white blood bell segmentation in microscopic blood images using digital image processing. *Biological Procedures Online*, 11:196 – 206, 2009.

[60] M. Farhan, O. Yli-Harja, and A. Niemistö. A novel method for splitting clumps of convex objects incorporating image intensity and using rectangular window-based concavity point-pair search. *Pattern Recognition*, 46(3):741 – 751, 2013.

[61] Z. Yu-qian, G. Wei-hua, C. Zhen-cheng, T. Jing-tian, and L. Ling-yun. Medical images edge detection based on mathematical morphology. In *Proceedings of the 27th Annual International Conference of the Engineering in Medicine and Biology Society,*, pages 6492 – 6495, 2005.

[62] K. Wang, J. Wu, L. Gao, Z. Pian, and L. Guo. Magnetic resonance images edge detection based on multi-scale morphology. In *Proceedings of the*

IEEE/ICME International Conference on Complex Medical Engineering, pages 744 – 747, May 2007.

[63] J. QI. Dense nuclei segmentation based on graph cut and convexity – concavity analysis. *Journal of Microscopy*, 253(1):42 – 53, 2014.

[64] O. Daněk, P. Matula, C. Ortiz de Solórzano, A. Muñoz-Barrutia, M. Maška, and M Kozubek. Segmentation of touching cell nuclei using a two-stage graph cut model. In A.-B. Salberg, J. Hardeberg, and R. Jenssen, editors, *Image Analysis*, volume 5575 of *Lecture Notes in Computer Science*, pages 410 – 419. Springer Berlin Heidelberg, 2009.

[65] T.-B. Chen, H.H.-S. Lu, Y.-S. Lee, and H.-J. Lan. Segmentation of cdna microarray images by kernel density estimation. *Journal of Biomedical Informatics*, 41(6):1021 – 1027, 2008.

[66] E.R. Dougherty and R.A. Lotufo. *Hands-on morphological image processing*. Spie Press Series, Bellingham, 2003.

[67] J.C. Crocker and D.G. Grier. Methods of digital video microscopy for colloidal studies. *Journal of Colloid and Interface Science*, 179(1):298 – 310, 1996.

[68] I. Smal, E. Meijering, K. Draegestein, N. Galjart, I. Grigoriev, A. Akhmanova, M.E. van Royen, A.B. Houtsmuller, and W. Niessen. Multiple object tracking in molecular bioimaging by rao-blackwellized marginal particle filtering. *Medical Image Analysis*, 12(6):764 – 777, 2008.

[69] L. Devroye, L. Györfi, and G. Lugosi. *A Probabilistic Theory of Pattern Recognition*. Springer, New York, first edition, 1996.

[70] G.L. Turin. An introduction to matched filters. *IRE Transactions on Information Theory*, 6(3):311 – 329, June 1960.

[71] P. Soille. *Morphological Image Analysis: Principles and Applications*. Secaucus: Springer-Verlag, New York, 2003.

[72] C.A. Glasbey. An analysis of histogram-based thresholding algorithms. *CVGIP: Graphical Models and Image Processing*, 55(6):532 – 537, 1993.

[73] J.N. Kapur, P.K. Sahoo, and A.K.C. Wong. A new method for gray-level picture thresholding using the entropy of the histogram. *Computer Vision, Graphics, and Image Processing*, 29(3):273 – 285, 1985.

[74] I.F. Sbalzarini and P. Koumoutsakos. Feature point tracking and trajectory analysis for video imaging in cell biology. *Journal of Structural Biology*, 151(2):182 – 195, 2005.

[75] L. Vincent. Morphological grayscale reconstruction in image analysis: applications and efficient algorithms. *IEEE Transactions on Image Processing*, 2(2):176 – 201, Apr 1993.

[76] I. Smal, M. Loog, W. Niessen, and E. Meijering. Quantitative comparison of spot detection methods in live-cell fluorescence microscopy imaging. In *Proceedings of the IEEE International Symposium on Biomedical Imaging: From Nano to Macro, 2009. ISBI '09*, pages 1178 – 1181, 2009.

[77] I. Smal, M. Loog, W. Niessen, and E. Meijering. Quantitative comparison of spot detection methods in fluorescence microscopy. *IEEE Transactions on Medical Imaging*, 29(2):282 – 301, 2010.

[78] D. Comaniciu and P. Meer. Mean shift: a robust approach toward feature space analysis. *IEEE Transactions on Pattern Analysis and Machine Intelligence*, 24(5):603 – 619, May 2002.

[79] J.-C. Olivo-Marin. Extraction of spots in biological images using multiscale products. *Pattern Recognition*, 35(9):1989 – 1996, 2002.

[80] J.-L. Starck, F. Murtagii, and A. Bijaoui. Multiresolution support applied to image filtering and restoration. *Graphical Models and Image Processing*, 57(5):420 – 431, 1995.

[81] D. Prodanov, J. Heeroma, and E. Marani. Automatic morphometry of synaptic boutons of cultured cells using granulometric analysis of digital images. *Journal of Neuroscience Methods*, 151(2):168 – 177, 2006.

[82] G. Matheron. *Random Sets and Integral Geometry*. Wiley, New York, 1975.

[83] K. Jaqaman, D. Loerke, M. Mettlen, H. Kuwata, S. Grinstein, S.L. Schmid, and G. Danuser. Robust single-particle tracking in live-cell time-lapse sequences. *Nature Methods*, 5(8):695 – 702, 2008.

[84] D. Thomann, R.R. Rines, P.K. Sorger, and G. Danuser. Automatic fluorescent tag detection in 3d with super-resolution: application to the analysis of chromosome movement. *Journal of Microscopy*, 208(1):49 – 64, 2002.

[85] E. Bertin and S. Arnouts. Sextractor: Software for source extraction. *Astronomy and Astrophysics Supplement Series*, 117(2):393 – 404, 1996.

[86] J. Adler and S.N. Pagakis. Reducing image distortions due to temperature-related microscope stage drift. *Journal of Microscopy*, 210(2):131 – 137, 2003.

[87] H.A.P. Blom. An efficient filter for abruptly changing systems. In *Proceedings of the 23rd IEEE Conference on Decision and Control*, pages 23:312 – 317, Las Vegas, Nevada, USA, December 1984.

[88] R.O. Duda, P.E. Hart, and D.G. Stork. *Pattern Classification*. Wiley, Hoboken, NJ, 2nd edition.

[89] X. Ye, M. Cheriet, and C.Y. Suen. Stroke-model-based character extraction from gray-level document images. *IEEE Transactions on Image Processing*, 10(8):1152 – 1161, 2001.

[90] O. Nina, B. Morse, and W. Barrett. A recursive otsu thresholding method for scanned document binarization. In *Proceedings of the IEEE Workshop on Applications of Computer Vision (WACV)*, pages 307 – 314, Jan 2011.

[91] R.F. Moghaddam and M. Cheriet. Adotsu: An adaptive and parameterless generalization of otsu's method for document image binarization. *Pattern Recognition*, 45(6):2419 – 2431, 2012.

[92] R. Maini and H. Aggarwal. Study and comparison of various image edge detection techniques. *International Journal of Image Processing (IJIP)*, 3(1):1 – 11, 2009.

[93] S. Mukhopadhyay and B. Chanda. Multiscale morphological segmentation of gray-scale images. *IEEE Transactions on Image Processing*, 12(5):533 – 549, May 2003.

[94] P. Bao, D. Zhang, and W. Xiaolin. Canny edge detection enhancement by scale multiplication. *IEEE Transactions on Pattern Analysis and Machine Intelligence*, 27(9):1485 – 1490, 2005.

[95] F.Y. Shih and O.R. Mitchell. Threshold decomposition of gray-scale morphology into binary morphology. *IEEE Transactions on Pattern Analysis and Machine Intelligence*, 11(1):31 – 42, 1989.

[96] O. Yli-Harja. *Median filters: extensions, analysis and design.* PhD thesis, Lappeenranta University of Technology, Publication 13, 1989.

[97] O. Yli-Harja, J. Astola, and Y. Neuvo. Analysis of the properties of median and weighted median filters using threshold logic and stack filter representation. *IEEE Transactions on Signal Processing*, 39(2):395 – 410, Feb 1991.

[98] F.Y. Shih and C.C. Pu. Analysis of the properties of soft morphological filtering using threshold decomposition. *IEEE Transactions on Signal Processing*, 43(2):539 – 544, Feb 1995.

[99] R.J. Prokop and A.P. Reeves. A survey of moment-based techniques for unoccluded object representation and recognition. *CVGIP: Graphical Models and Image Processing*, 54(5):438 – 460, 1992.

[100] F.S. Hillier and G.S. Lieberman. *Introduction to Operations Research.* McGraw-Hill, Boston, 2001.

[101] G.L. Nemhauser and L.A. Wolsey. *Integer and Combinatorial Optimization.* John Wiley and Sons, Hoboken, NJ, 1988.

[102] L.A. Wolsey. *Integer Programming.* John Wiley and Sons, Hoboken, NJ, 1998.

[103] O. Sliusarenko, J. Heinritz, T. Emonet, and C. Jacobs-Wagner. High-throughput, subpixel precision analysis of bacterial morphogenesis and intracellular spatio-temporal dynamics. *Molecular Microbiology*, 80(3):612 – 627, 2011.

[104] V. Ljosa, K.L. Sokolnicki, and A.E. Carpenter. Annotated high-throughput microscopy image sets for validation. *Nature Methods*, 9(7):637, 2012.

[105] T. Fawcett. An introduction to {ROC} analysis. *Pattern Recognition Letters*, 27(8):861 – 874, 2006.

[106] A. Popovic, M. de la Fuente, M. Engelhardt, and K. Radermacher. Statistical validation metric for accuracy assessment in medical image segmentation.

International Journal of Computer Assisted Radiology and Surgery, 2(3-4):169 – 181, 2007.

[107] A. Lehmussola, P. Ruusuvuori, J. Selinummi, H. Huttunen, and O. Yli-Harja. Computational framework for simulating fluorescence microscope images with cell populations. *IEEE Transactions on Medical Imaging*, 26(7):1010 – 1016, 2007.

[108] A. Lehmussola, P. Ruusuvuori, J. Selinummi, T. Rajala, and O. Yli-Harja. Synthetic images of high-throughput microscopy for validation of image analysis methods. *Proceedings of the IEEE*, 96(8):1348 – 1360, 2008.

[109] P. Ruusuvuori, A. Lehmussola, J. Selinummi, T. Rajala, H. Huttunen, and O. Yli-Harja. Benchmark set of synthetic images for validating cell image analysis algorithms. In *Proceedings of the 16th European Signal Processing Conference, EUSIPCO*, 2008.

[110] J. Lloyd-Price, M. Lehtivaara, M. Kandhavelu, S. Chowdhury, A.-B. Muthukrishnan, O. Yli-Harja, and A.S. Ribeiro. Probabilistic rna partitioning generates transient increases in the normalized variance of rna numbers in synchronized populations of escherichia coli. *Molecular BioSystems*, 8:565 – 571, 2012.

[111] J. Lloyd-Price, A. Häkkinena, M. Kandhavelu, I.J. Marquesa, S. Chowdhury, E. Lihavainena, O. Yli-Harja, and A.S. Ribeiro. Asymmetric disposal of individual protein aggregates in escherichia coli, one aggregate at a time. *Journal of Bacteriology*, 194:1747 – 1752, 2012.

[112] M.D. Abramoff, P.J. Magelhaes, and S.J. Ram. Image processing with imagej. *Biophotonics International*, 11:36 – 42, 2004.

[113] A. Gupta, J. Lloyd-Price, R. Neeli-Venkata, S.M.D. Oliveira, and A.S. Ribeiro. In vivo kinetics of segregation and polar retention of ms2-gfp-rna complexes in escherichia coli. *Biophysical Journal*, 106(9):1928 – 1937, 2014.

[114] S.M.D Oliveira, R. Neeli-Venkata, N.S.M. Goncalves, J.A. Santinha, L. Martins, H. Tran, J. Mäkelä, A. Gupta, M. Barandas, A. Häkkinen, J. Lloyd-Price, J.M. Fonseca, and A.S. Ribeiro. Increased cytoplasm viscosity hampers aggregate polar segregation in escherichia coli. *Molecular Microbiology*, 2015.

[115] S.K. Sadanandan, O. Baltekin, K.E.G. Magnusson, A. Boucharin, P. Ranefall, J. Jalden, J. Elf, and C. Wahlby. Segmentation and track-analysis in time-lapse imaging of bacteria. *Selected Topics in Signal Processing, IEEE Journal of*, 2015.

Publications

Publication I

S. Chowdhury, M. Kandhavelu, O. Yli-Harja, and A.S. Ribeiro, "An interacting multiple model filter-based autofocus strategy for confocal time-lapse microscopy," *Journal Microscopy*, 245(3):265-275, March 2012.

Journal of Microscopy

Journal of Microscopy, Vol. 245, Pt 3 2012, pp. 265–275
Received 2 May 2011; accepted 7 October 2011

doi: 10.1111/j.1365-2818.2011.03568.x

An interacting multiple model filter-based autofocus strategy for confocal time-lapse microscopy

S. CHOWDHURY*, M. KANDHAVELU*, O. YLI-HARJA*,† & A.S. RIBEIRO*

**Computational Systems Biology Research Group, Department of Signal Processing, Tampere University of Technology, Finland*

†Institute for Systems Biology, Seattle, Washington, U.S.A.

Key words. Fluto focus, confocal microscopy, focus drift, interacting multiple model filter, thermal drift, time-lapse imaging.

Summary

Gene expression and other cellular processes are stochastic, thus their study requires observing multiple events in multiple cells. Therefore, confocal microscopy cell imaging has recently gained much interest. In time-lapse imaging, adjustments are needed at short intervals to compensate for focus drift. There are several automated methods for this purpose. In general, before acquiring higher resolution images, software-based autofocus algorithms require a set of low-resolution images along the *z*-axis to determine the plane for which a predefined focusing function is maximized. These algorithms require 10–100 *z*-slices each time, and there is no fixed number or upper limit of required *z*-slices that ensures optimal focusing. The higher is this number, the stronger is photo bleaching, hampering the feasibility of long-time series measurements.

We propose a new focusing strategy in time-lapse imaging. The algorithm relies on the nature and predictability of the focus drift. We first show that the focus drift curve is predictable within a small error bound in standard experimental setups. We, then, exploit the interacting multiple model filter algorithm to predict the drift at time, t, based on the measurement at time $t-1$. This allows a drastic reduction of the number of required *z*-slices for focus drift correction, largely overcoming the problem of photo bleaching. In addition, we propose a new set of functions for focusing in time-lapse imaging, derived from preexisting ones. We demonstrate the method's efficiency in time-lapse imaging of *Escherichia coli* cells expressing MS2d-GFP tagged RNA molecules.

Introduction

With the incremental power of computing and microscopy technology, digital imaging has become a valuable tool for cell and molecular biology studies. The value of these studies is further enhanced by the increasing need to observe many individual cells to understand their functioning. Focusing on the specimen is the first step towards imaging. In time-lapse microscopy, this is needed before the acquisition of each image, because the focus drift (i.e. shifting of the focus position) is ubiquitous in present microscopy. Defocused images hamper quantitative analysis. Correcting focusing problems is particularly critical in *in vivo* measurements. The erroneous focus position selection and subjective variance hamper the use of manual focusing, leaving autofocusing as the only reliable alternative.

Current autofocus systems are categorized in two groups: hardware and software autofocus. Hardware autofocus systems are usually equipped with an infrared light emitting diode (LED) that projects a predefined shape on the specimen slide and measures the distance between slide and objective lens from the reflection of the projected shape. Hardware autofocus is fast and performs optimally, as long as the specimen is ultra thin (Bezzubik & Ustinov, 2009; Brázdilová & Kozubek, 2011). However, even in trivial experimental setups, this assumption does not always hold.

By contrast, software autofocus systems acquire images in stack along the *z*-axis. After, the reference image is selected by maximizing a predefined focus function. The required resolution for reference image selection is often far smaller than the resolution required for biological analysis. Thus, software autofocus methods perform the imaging in two steps. First, a low-resolution image stack is acquired to determine the focus position. Next, a full-resolution image or a full-resolution image stack is captured around the selected position (Brázdilová & Kozubek, 2011). Here, by 'autofocus', we imply 'software autofocus', unless stated otherwise.

Irrespective of the focusing strategy, the procedure has to be executed routinely to compensate/correct the focus drift. Studies showed that temperature is a major determinant of the degree of focus drift (Mason & Green, 1975; Adler & Pagakis, 2003). Figure 1 illustrates the focus drift in two

Correspondence to: Andre S. Ribeiro, Computational Systems Biology Research Group, Department of Signal Processing, Tampere University of Technology, Finland. fax: +358 3 3115 4989; e-mail: andre.ribeiro@tut.fi

[Correction added after online publication 1 December 2011: Author name corrected from O. YI-HARJA to O. YLI-HARJA.]

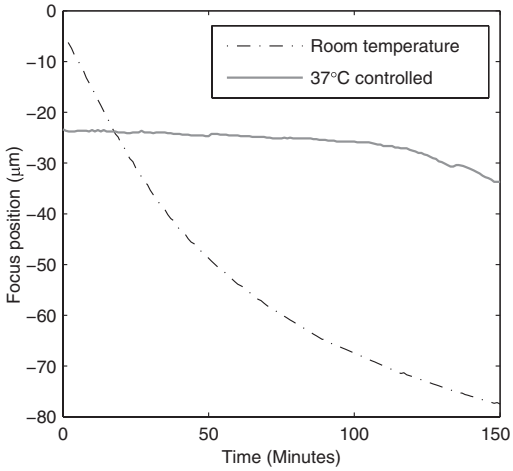

Fig. 1. Focus position as a function of time. Interval between successive focus position measurements was 60 s.

thermal conditions. Relying on the empirical results depicted in Figure 1, we argue that the drift is quasi-deterministic and can be 'optimally predicted', aside random, uncorrelated, small fluctuations.

Given the above, it is possible to develop a method for focus drift correction based on the nature of the drift. The algorithm proposed here, predicts the focus drift one-time point ahead. Therefore, it requires a number of *z*-slices for autofocus that is close to the theoretical minimum (three slices).

Photo bleaching is directly proportional to the number of captured *z*-slices. This photochemical process reduces the emitted light intensity by destroying fluorophore, as a result of the excitation light used for scanning (Hoebe *et al.*, 2007). The proposed method allows a more efficient acquisition of long time series at a fast rate as it reduces photo bleaching. Efficiency is further enhanced by the reduction of computational load and memory use, as they are also directly proportional to the number of *z*-slices. Finally, besides focus drift correction, we also implement a new set of focus functions, developed from preexisting ones, and show by comparison that, in general, they outperform commonly used counterparts.

Related works

Several methods for focusing microscope have been proposed (Tenenbaum, 1970; Brenner *et al.*, 1976; Vollath, 1987; Bueno-Ibarra *et al.*, 2005; Kreft *et al.*, 2005) in different contexts. Such methods have been evaluated several times using various criterion for optimality (Groen *et al.*, 1985; Firestone *et al.*, 1991; Santos *et al.*, 1997; Sun *et al.*, 2004). Both image power (Groen *et al.*, 1985) and image gradient power (first difference of the image in spatial domain; Tenenbaum, 1970; Brenner *et al.*, 1976) are suitable metrics

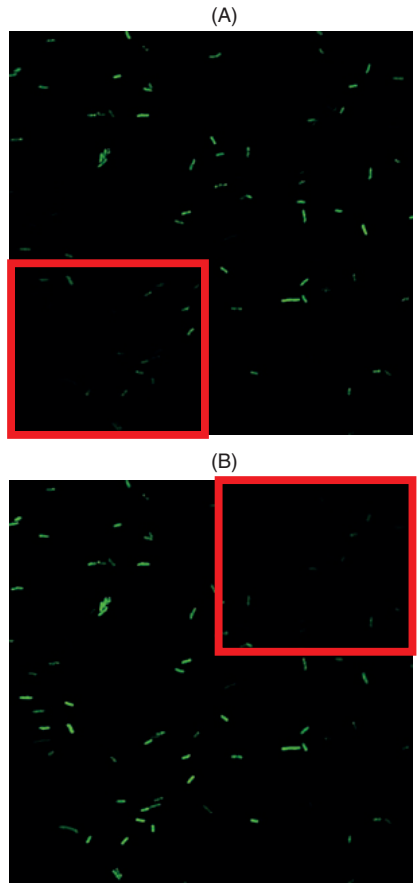

Fig. 2. Two images captured by applying the 'Tenegrad' focus function. (A) at $t = 5$ min and (B) at $t = 6$ min. The defocused region of each frame is depicted by a red rectangle.

for focus function. In addition, different image statistics, such as variance (Santos *et al.*, 1997; Sun *et al.*, 2004; Brázdilová & Kozubek, 2009) and autocorrelation (Vollath, 1987), have been exploited for focusing microscope.

Notably, all the above-mentioned focus metrics perform optimally, whereas the imaging is carried out in a nontime-lapse fashion or *in vitro*. However, their focusing performance in *in vivo* imaging has not yet been assessed. Different frames from *in vitro* measurements are independent from one another. By contrast, consecutive frames from *in vivo* time-lapse microscopy are highly correlated. This correlation cannot be disregarded at the focusing step because, for example, it is possible to have more than one *z*-plane in identical focus. This, combined with the stochastic nature of the biological process under observation, might lead to focus switching between planes in a repetitive manner. Figure 2

exemplifies this artefact (defocused regions are depicted by the rectangles), where the focusing was done with a benchmark method known as 'Tenegrad' (Tenenbaum, 1970). Visibly, it led to an 'incoherent' time series that switched the focus plane between consecutive frames. This limitation of current autofocusing systems can be overcome by accounting for the dependence between consecutive frames at the focusing step.

Kreft *et al.* exploited the Pearson's correlation to account for such dependence between consecutive images in time-lapse confocal microscopy (Kreft *et al.*, 2005). The algorithm selects the reference frame at t by maximizing Pearson's correlation with the reference frame selected at $t-1$. The initial reference frame is selected either by manual inspection or by a focus function. The performance of this method degrades significantly as consecutive frames become more uncorrelated, because it relies solely on maximizing similarities between consecutive frames.

The correlation between consecutive frames during a time-lapse microscopy session may decrease for several reasons, such as sudden lateral drift or as the cells' phenotype change in an unpredictable fashion. This method is also sensitive to the imaging interval. Namely, different intervals lead to different selected images at corresponding time points. A robust autofocus algorithm should select identical images in the corresponding time points irrespective of the imaging intervals.

Another critical issue in autofocusing methods for time-lapse microscopy is the number of required frames for focusing, because it affects the degree of photo bleaching. Current state-of-the-art focus searching methods exploit various optimization strategies, such as adaptive step size (Brázdilová & Kozubek, 2009), function fitting (Osibote *et al.*, 2010) and Fibonacci search (Liu *et al.*, 2007), to attempt to reduce the number of frames required for focusing. However, none of these algorithms attempts to minimize the required number of scans by drift estimation. As show later, from drift estimation and focus position prediction, it is possible to reduce drastically the number of frames required for focusing.

Materials and methods

Focus drift compensation

Given that the thermal drift is quasi-deterministic in common experimental setups (as shown ahead), a linear prediction algorithm is likely suitable for focus drift estimation. A similar argument can be comprehended in (Mason & Green, 1975). Figure 1 illustrates the stated phenomenon in measurements conducted for 150 min. The dotted-dash line shows the focus drift at room temperature, whereas the solid line represents the drift when the specimen is in a sample chamber at 37°C. Relying on these observations, we use the Kalman filter (Kalman, 1960) with multiple models, also known as 'interacting multiple model' (IMM) filter, for focus drift prediction (Blom, 1984; Blom & Bar-Shalom, 1988).

The Kalman filter is a hidden Markov model (HMM) for a system whose state can be described by a continuous function (Barber & Cemgil, 2010). The Kalman filter is an optimal state estimator for a system with linear dynamics and Gaussian noise (Kalman, 1960). However, the underlying dynamic model in the Kalman filter is fixed over time. The IMM filter is an extension of the Kalman filter and incorporates multiple dynamic models. The IMM filter allows switching from one model to another at runtime (Blom & Bar-Shalom, 1988). Due to this, and because the kinetics of focus drift may differ with the thermal conditions, we opted for the IMM filter.

To formulate focus drifting as an estimation problem, its model and the focus position measurement model need to be described as a system of linear equations:

$$\textit{Drift Model:} \qquad \mathbf{x}_t = \mathbf{F}^{(i)}\mathbf{x}_{t-1} + \mathbf{u}_{t-1}^{(i)} \quad i = 1, 2, \ldots M,$$

$$\textit{Measurement Model:} \quad \mathbf{y}_t = \mathbf{H}\mathbf{x}_t + \mathbf{v}_t,$$

where $\mathbf{x}_t$ is the state vector that comprises focus position (z_t), velocity ($\dot{z}_t$) and acceleration ($\ddot{z}_t$) of the focus drift at time t. $\mathbf{F}^{(i)}$ is the model conditioned state transition matrix while the matrix $\mathbf{H}$ transforms the state vector into a measurement vector. $\mathbf{u}_{t-1}^{(i)}$ and $\mathbf{v}_t$ are the state and measurement noise, respectively. The noise components are assumed to be uncorrelated Gaussian with zero mean and $\mathbf{Q}^{(i)}$ and $\mathbf{R}$ covariance matrices. The model accounts for three different state transition dynamics ($M = 3$), namely, the random-walk, the constant-velocity and the constant-acceleration models. The numerical realization of the measurement matrix and the state transition matrices for the aforementioned dynamic models are,

$$\mathbf{H} = [\,1 \quad 0 \quad 0\,]$$

$$\mathbf{F}^{(1)} = \begin{bmatrix} 1 & 0 & 0 \\ 0 & 0 & 0 \\ 0 & 0 & 0 \end{bmatrix} \mathbf{F}^{(2)} = \begin{bmatrix} 1 & T & 0 \\ 0 & 1 & 0 \\ 0 & 0 & 0 \end{bmatrix} \mathbf{F}^{(3)} = \begin{bmatrix} 1 & T & \frac{T^2}{2} \\ 0 & 1 & T \\ 0 & 0 & 1 \end{bmatrix}.$$

In the state transition models, T represents the imaging interval. Based on this parametric model, the IMM filter solution for focus drift correction can be obtained in three consecutive steps: (i) Focus position prediction, (ii) focus position measurement and (iii) parameter correction. The overall workflow of the algorithm is depicted in Figure 3.

Focus position prediction. At moment t, the prediction step of IMM filter starts with an estimated state ($\hat{\mathbf{x}}_{t-1}^{(i)}$), covariance matrix ($\mathbf{c}_{t-1}^{(i)}$) and respective weight ($\mathbf{w}_{t-1}^{(i)}$) as the set of inputs followed from $(t-1)$. Given these parameters, the model conditioned mixed initial state and covariance matrices are,

$$\hat{\mathbf{x}}_{t-1}^{(0j)} = \sum_{i=1}^{M} \mathbf{w}_{t-1}^{(i|j)} \hat{\mathbf{x}}_{t-1}^{(i)},$$

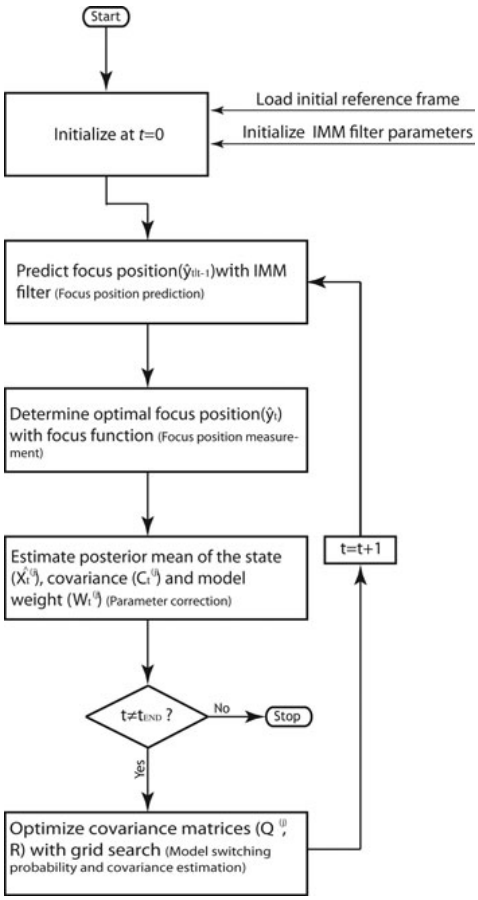

Fig. 3. Flowchart of the proposed IMM filter-based autofocus system. In parenthesis is named the section in the manuscript where this step is described in detail.

$$\mathbf{c}_{t-1}^{(0j)} = \sum_{i=1}^{M} \mathbf{w}_{t-1}^{(i|j)} \left[\mathbf{c}_{t-1}^{(i)} + \left(\hat{\mathbf{x}}_{t-1}^{(i)} - \hat{\mathbf{x}}_{t-1}^{(0j)} \right) \left(\hat{\mathbf{x}}_{t-1}^{(i)} - \hat{\mathbf{x}}_{t-1}^{(0j)} \right)' \right],$$

where $(')$ is the matrix transpose operator and $\mathbf{w}_{t-1}^{(i|j,)}$ is the model conditioned weight, which is obtained from predicted model weight $(\mathbf{w}_{t|t-1}^{(j)})$ as,

$$\mathbf{w}_{t|t-1}^{(j)} = \sum_{i=1}^{M} \mathbf{P}^{(i,j)} \mathbf{w}_{t-1}^{(i)},$$

$$\mathbf{w}_{t-1}^{(i|j)} = \frac{\mathbf{P}^{(i,j)} \mathbf{w}_{t-1}^{(i)}}{\mathbf{w}_{t|t-1}^{(j)}}.$$

In these expressions, $\mathbf{P}^{(i,j)}$ represents the switching probability of model i to model j, which is assumed as a design parameter. The exact form of the switching probability matrix is discussed in a following section. Given the model conditioned mixed initial state and the covariance matrix, the model conditioned prediction of the state and the covariance matrices are formed as,

$$\hat{\mathbf{x}}_{t|t-1}^{(j)} = \mathbf{F}^{(j)} \hat{\mathbf{x}}_{t-1}^{(0j)},$$

$$\mathbf{c}_{t|t-1}^{(j)} = \mathbf{F}^{(j)} \mathbf{c}_{t-1}^{(0j)} \left(\mathbf{F}^{(j)} \right)' + \mathbf{Q}^{(j)}.$$

The predicted mean state and mean covariance for different models are obtained by taking the weighted sum of various model conditioned prediction of the state,

$$\hat{\mathbf{x}}_{t|t-1} = \sum_{j=1}^{M} \mathbf{w}_{t|t-1}^{(j)} \hat{\mathbf{x}}_{t|t-1}^{(j)},$$

$$\mathbf{c}_{t|t-1} = \sum_{j=1}^{M} \mathbf{w}_{t|t-1}^{(j)} \left[\mathbf{c}_{t|t-1}^{(j)} + \left(\hat{\mathbf{x}}_{t|t-1}^{(j)} - \hat{\mathbf{x}}_{t|t-1} \right) \left(\hat{\mathbf{x}}_{t|t-1}^{(j)} - \hat{\mathbf{x}}_{t|t-1} \right)' \right].$$

The expected focus position $(\hat{\mathbf{y}}_{t|t-1})$ at time t is estimated from the predicted state with the measurement model equation as,

$$\hat{\mathbf{y}}_{t|t-1} = \mathbf{H} \hat{\mathbf{x}}_{t|t-1}.$$

Focus position measurement. This procedure determines the optimal focus position $(\mathbf{y}_t)$ from a stack of low-resolution images. The size of this stack is not constant in the proposed framework, depending on the accuracy of the prediction algorithm. The accuracy is determined by the mean absolute error between predicted $(\hat{\mathbf{y}}_{t|t-1})$ and actual focus positions $(\mathbf{y}_t)$. The image stack is captured from the predicted position until the focus function is maximized or an upper bound is reached. The initial direction of the search is obtained from the slope of the defocusing curve and it switches if the slope remains negative for a predefined number of frames in a row. Ideally, the defocusing curve is monotone around a unique maximum point. In practice, it may contain multiple local maxima and, often, one is reached before reaching the global maximum. Nonetheless, finding the global maximum given multiple local maxima is plausible by setting a minimum threshold for the expected value of the focus function at the optimal focus position. We set this threshold at 80% of the focus value of the most recent reference image. A detail argument on the method for computing focus score and local minima avoidance are provided in the sections "*Focus Functions*" and "*Local Maxima Avoidance*".

Parameter correction. For this we provide information from the measurement step to the prediction step, allowing the correction to be an adaptive process that improves the accuracy of prediction at each subsequent time point. The correction steps estimate the posterior mean of state $(\hat{\mathbf{x}}_t^{(j)})$, covariance $(\mathbf{c}_t^{(j)})$ and model weight $(\mathbf{w}_t^{(j)})$.

$$\mathbf{K}_t^{(j)} = \mathbf{c}_{t|t-1}^{(j)} \mathbf{H}' \left(\mathbf{H} \mathbf{c}_{t|t-1}^{(j)} \mathbf{H}' + \mathbf{R} \right)^{-1},$$

$$\hat{\mathbf{x}}_t^{(j)} = \hat{\mathbf{x}}_{t|t-1}^{(j)} + \mathbf{K}_t^{(j)}\left(\mathbf{y}_t - \mathbf{H}\hat{\mathbf{x}}_{t|t-1}^{(j)}\right),$$

$$\mathbf{c}_t^{(j)} = \mathbf{c}_{t|t-1}^{(j)} - \mathbf{K}_t^{(j)}\mathbf{H}\mathbf{c}_{t|t-1}^{(j)},$$

$$\mathbf{w}_t^{(j)} = \mathbf{w}_{t|t-1}^{(j)}\,\Lambda_t^{(j)}.$$

Here, $\Lambda_t^{(j)}$ is the model likelihood assuming zero mean normal distribution while $\mathbf{w}_t^{(j)}$ is normalized so that the sum over all models equals one.

Model switching probability and covariance estimation. We consider the model switching probability matrix, **P**, as a system variable. The numerical realization of the model switching probability in the proposed implementation is fixed to:

$$\mathbf{P} = \begin{bmatrix} 0.90 & 0.05 & 0.05 \\ 0.05 & 0.90 & 0.05 \\ 0.05 & 0.05 & 0.90 \end{bmatrix}.$$

Model conditioned covariance matrices ($\mathbf{Q}^{(j)}$) and the measurement covariance matrix (**R**) affect the efficiency of the IMM filter. We assume that these matrices are diagonal and independent from one another. The covariance matrices are estimated independently by a grid search in a logarithmic search space within the range 2^{-10}–2^{10}. Extending this range is pointless due to practical bounds (i.e. quantization limit at the hardware level). However, we acknowledge expectation-maximization (EM) and fixed lag smother-based techniques for covariance estimation (Helmick *et al.*, 1995; Li *et al.*, 2008). Thus, we tested both approaches in a virtual environment. We found that the grid search outperformed the expectation-maximization-based algorithm in this context (data not shown).

Focus functions

A focus function provides a quantitative measure of the degree of focus of an image. The central assumption behind focus functions is that, due to the convolution with a low-pass point-spread function, defocused images are more blurry (Groen *et al.*, 1985; Santos *et al.*, 1997). A focused image should contain more information and sharper edges (Yeo *et al.*, 1993; Santos *et al.*, 1997). Relying on this, trivial focus functions use the degree of sharpness or the amount of information as the quantitative metric of the focus. We revisited six such focus functions. We chose those methods generally considered the best (Firestone *et al.*, 1991; Santos *et al.*, 1997; Sun *et al.*, 2004) and listed them in Table 1.

The first five methods in Table 1 maximize focus quality of an individual image at a time point while disregarding correlations with previous time points. By contrast, the Pearson's correlation-based approach maximizes only the correlation or similarities between consecutive images, but disregards the focus quality of each image. An ideal focus function should maximize the focus quality of each image while maintaining the correlation between consecutive time points. Because it is not possible to optimize both features simultaneously, we propose using the two approaches in a combined fashion. The combination consists in taking the product of the resulting solutions from each approach.

Test sample and equipments

We apply our method to time-lapse measurements of *Escherichia coli* cells expressing an RNA target for MS2d-GFP proteins (Golding *et al.*, 2005), where GFP stands for green fluorescent protein. The method of tagging RNA molecules with MS2-GFP-based fluorescent proteins is so far the only that allows *in vivo* detection of individual RNA molecules, thus allowing to study transcription dynamics in live cells (Raj & van Oudernaarden, 2009).

The method of RNA detection and quantification in *E. coli* DH5α-PRO (Golding *et al.* 2005) exploits the ability of bacteriophage MS2 coat protein to tightly bind specific RNA sequences. It allows detection of single RNA transcripts with 96 tandem repeats of MS2 binding sites for MS2d fused to GFPmut3 (MS2d-GFP fusion protein). The method uses the controlled expression of two genetic constructs: a medium-copy vector that expresses the MS2d-GFP fused protein, whose promoter (P_{tetO1}) is regulated by tetracycline repressor, and a single copy F-based vector, with Plar controlling production of the transcript target, mRFP1 followed by a 96 MS2 binding site array. Constructs were generously provided by I. Golding (University of Illinois).

Cells were grown overnight in Miller LB medium, supplemented by kanamycin at 37°C with aeration, and diluted into fresh medium to maintain exponential growth until reaching an approximate optical density of OD600 0.3–0.5. aTc (100 ng mL^{-1}) was used to get full induction of MS2d-GFP expression. Approximately 60-min incubation was maintained for sufficient protein production. Maximum induction of the RNA target for MS2d-GFP is achieved with 1 mM IPTG and 0.1% arabinose (Golding & Cox, 2004).

Following induction of the target RNA, a few microliter of culture are placed on a microscopic slide between a cover slip and 0.8% LB-agarose gel pad set. Cells are visualized by a Nikon Eclipse (TE2000-U, Nikon, Japan) inverted confocal laser-scanning microscope with 100× Apo TIRF 1.49 oil + DIC objective (Nikon, Japan). GFP fluorescence is measured with 488 nm laser (Melles-Griot, New Mexico, CA, USA) and 515/30 nm filter (100–110 gain). Images of cells are taken by Nikon EZ-C1 Version 3.30 software (Tokyo, Japan). Some of the test sequences were captured on an FCS2 (Bioptechs Inc., PA, USA) temperature controlled sample chamber (sequences S8, S9, S17 and S13–S15, Table 2). The rest were obtained at room temperature. The test samples include 17 sets of time series acquired in *z*-stack. Because the diameter of *E. coli* is notably small (0.5 μm), the sampling interval along the *z*-axis was set to 0.1 μm. Test sequences

Table 1. Focus functions tested.

Method name	Brief description	Comment
Tenegrad (f_{Tenegrad}; Tenenbaum, 1970)	Maximizing gradient image power.	Based on individual image stack.
Vollath F4($f_{\text{VollathF4}}$; Vollath, 1987)	Maximizing difference between the autocorrelation function at lags 1 and 2.	
Fano factor (f_{Fano}; Santos *et al.*, 1997)	Maximizing the pixel intensity variance normalized by the expected pixel intensity.	
Brenner gradient (f_{Brenner}; Brenner *et al.*, 1976)	Maximizing the squared sum of the first difference of pixel intensities separated by n pixels (n is set to a small positive integer, i.e. 2).	
Image power (f_{Power}; Groen *et al.*, 1985)	Maximizing the squared sum of pixel intensities.	
Pearson's correlation ($f_{\text{Pearson's}}$; Kreft *et al.*, 2005)	Maximizing the Pearson's correlation between consecutive time points.	Based on a reference image from previous time point.

Table 2. Test set description.

Set ID	Thermal condition	Imaging interval (min)	Number of frames	Stack size (steps)
S1	Room temperature (RT)	1	30	32
S2	RT	1	30	32
S3	RT	1	30	32
S4	RT	1	50	24
S5	RT	1	50	24
S6	RT	1	121	24
S7	RT	1	151	24
S8	37°C	1	121	24
S9	37°C	1	151	24
S10	RT	1	121	–
S11	RT	1	200	–
S12	RT	1	200	–
S13	37°C	1	121	–
S14	37°C	1	70	–
S15	37°C	1	301	–
S16	RT	5	50	–
S17	37°C	5	50	–

S1–S5 were used for evaluating the focus functions. Time series S6–S9 constitute the set for testing the proposed algorithm. Finally, test sets S10–S17 were acquired by the proposed method to assess its performance in a real working environment.

Results

Local maxima avoidance

The proposed focusing strategy needs to account for the existence of local maxima in the search space. An ideal focus function has one clear global maximum and the focus metric decreases monotonically with the distance from the maximum (Fig. 4(A)). A single realization of the focus function $f_{\text{Pearson's}} \times f_{\text{Tenegrad}}$ is exemplified in Figure 4(B). As seen, in a realistic setting, a focus function can contain more than one maximum. We carried out a statistical test with five time series comprised of 190 stacks in total. Figure 4(C) shows the distributions of the normalized focus metrics of local maxima and global maximum. The normalization at time t is done by the focus metric of the global maximum at $t-1$. Local maxima and global maximum have very distinct distributions. Further, there are local maxima that overlap with the global maximum (Fig. 4(C)), i.e. they can be considered as equally well focused, (Fig. 4(B)).

The knowledge of the value of the focus function at the global maximum at $t-1$ can be used for setting a threshold for finding the global maximum at moment t. A higher threshold would significantly reduce the acceptance of local maximum, thus it might increase the number of scans needed to find the global maximum. Figure 4(D) shows the rate of false maximum selection (acceptance of local maximum as a global maximum) for different thresholds and window sizes. We selected window size 5 and threshold value 0.8 for maxima selection. These selections entail that the global maximum is either bigger or equal to 80% of the value of the preceding global maximum and that it is a global maximum within this window. This assumption was found to be correct 97.9% of the times, namely, it attained 97.9% accuracy in selecting true maximum, whereas the false maximum was less than 2% off the true maximum (Fig. 4(D)). Note that, the theoretical minimum window size for determining a global maximum is 3, because a maximum must be assessed against at least one point below and one point above the optimal focal plane.

Note that, because the focus drift is virtually continuous in time during these experiments, exhaustive searching of global maxima is pointless in this case, because after completing the search, most likely, the solution is no longer valid. This implies that the accuracy ratios achieved (97.9%) are close to the best possible solution.

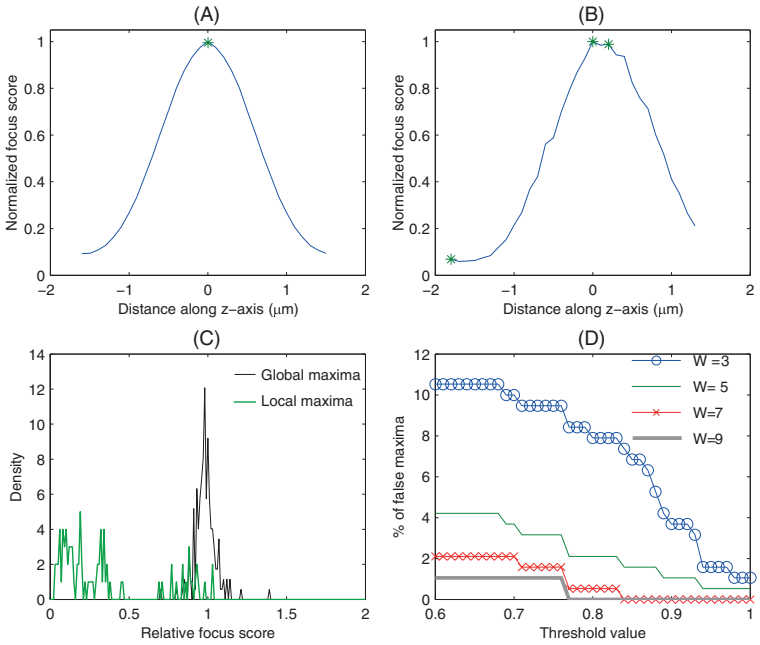

Fig. 4. Defocusing curve, local maxima and distribution of local maxima. (A) An ideal defocusing curve. (B) One realization of a defocusing curve in a real setting (maxima marked with the symbol '*'). (C) Distribution of local maxima and global maxima (the maxima at time t are normalized with the global maximum found at $t - 1$). (D) Fraction of false maxima selection as a function of maxima threshold for different window sizes (W).

Focus function selection

We studied the performance of the aforementioned focus functions, from which we selected the most efficient one. The performance metric comprises four features: accuracy, rate of local maxima, interval sensitivity and range. The accuracy is determined by the mean absolute difference between true focus position and the position where the focus function is maximized. The true focus position is obtained by applying an objective method that avoids subjective variance. Here, we used the median of the first five methods as an unbiased estimate of the true focus position.

The 'interval sensitivity' of a function is here defined as the expected spreadness in focus position selections for different imaging intervals. This quantity is equivalent to the scale parameter of the Laplace distribution. The first five methods have, by definition, zero interval sensitivity because the focus selection is solely based on a single image stack. By contrast, Pearson's correlation-based methods select the focus position by maximizing the correlation with the most recent reference frame. Accordingly, the results are sensitive to the imaging interval as well as the starting frame. Here, the interval sensitivity is estimated by simulating the focus position selection process for imaging interval from 1 to 5 min and then computing the mean absolute difference of selected positions for different intervals. The rate of local maxima is estimated as the average number of local maxima in a stack.

Finally, the range is defined as the difference between the expected normalized focus score of the global maxima and the expected normalized focus score of the local maxima. The normalization at t is done by the quantitative focus metric of the global maxima at $t - 1$. An optimal algorithm should have high accuracy with a large range and very few local maxima besides the global maximum (ideally, none). Moreover, it should be insensitive to the imaging interval. The results of the quantitative evaluation of the algorithms are shown in Table 3, where the rank of each focus function is marked in parenthesis. The results indicate that the combined algorithm outperformed each of the two algorithms when not combined with each other. The 'Pearson's correlation' with 'Tenegrad' function was the best combination, followed closely by the combination of 'Pearson's correlation' with 'Image power' metric. Among the five basic methods, f_{Tenegrad} and f_{Fano} exhibited equally satisfactory performances. In reference to these empirical results, we opted for implementing the $f_{\text{Pearson's}} \times f_{\text{Tenegrad}}$ focus function in the real operational system.

Table 3. Focus function selection. Type 1 is based on a single stack. Type 2 is based on correlation between consecutive frames. Type 3 is based on correlation between consecutive frames and on quality of individual frame.

Method	Accuracy (μm)	Interval sensitivity (μm)	Local maxima/ stack	Range	Overall score	Comment
f_{Tenegrad}	$0.021^{(3)}$	$0^{(1)}$	$0.395^{(5)}$	$0.681^{(5)}$	$14^{(3)}$	Type 1
$f_{\text{VollathF4}}$	$0.035^{(7)}$	$0^{(1)}$	$0.584^{(9)}$	$0.622^{(9)}$	$26^{(7)}$	
f_{Fano}	$0.031^{(5)}$	$0^{(1)}$	$0.376^{(3)}$	$0.667^{(6)}$	$15^{(4)}$	
f_{Brenner}	$0.050^{(10)}$	$0^{(1)}$	$0.626^{(10)}$	$0.433^{(10)}$	$31^{(10)}$	
f_{Power}	$0.043^{(9)}$	$0^{(1)}$	$0.512^{(8)}$	$0.655^{(9)}$	$27^{(8)}$	
$f_{\text{Pearson's}}$	$0.205^{(11)}$	$0.149^{(11)}$	$0.689^{(11)}$	$0.178^{(11)}$	$44^{(11)}$	Type 2
$f_{\text{Pearson's}} \times f_{\text{Tenegrad}}$	$0.010^{(1)}$	$0.013^{(7)}$	$0.371^{(2)}$	$0.807^{(2)}$	$12^{(1)}$	Type 3
$f_{\text{Pearson's}} \times f_{\text{VollathF4}}$	$0.035^{(7)}$	$0.011^{(6)}$	$0.447^{(7)}$	$0.783^{(3)}$	$25^{(6)}$	
$f_{\text{Pearson's}} \times f_{\text{Fano}}$	$0.026^{(4)}$	$0.013^{(7)}$	$0.344^{(1)}$	$0.779^{(4)}$	$18^{(5)}$	
$f_{\text{Pearson's}} \times f_{\text{Brenner}}$	$0.034^{(6)}$	$0.028^{(10)}$	$0.415^{(6)}$	$0.660^{(7)}$	$29^{(9)}$	
$f_{\text{Pearson's}} \times f_{\text{Power}}$	$0.016^{(2)}$	$0.013^{(7)}$	$0.378^{(4)}$	$0.811^{(1)}$	$14^{(2)}$	

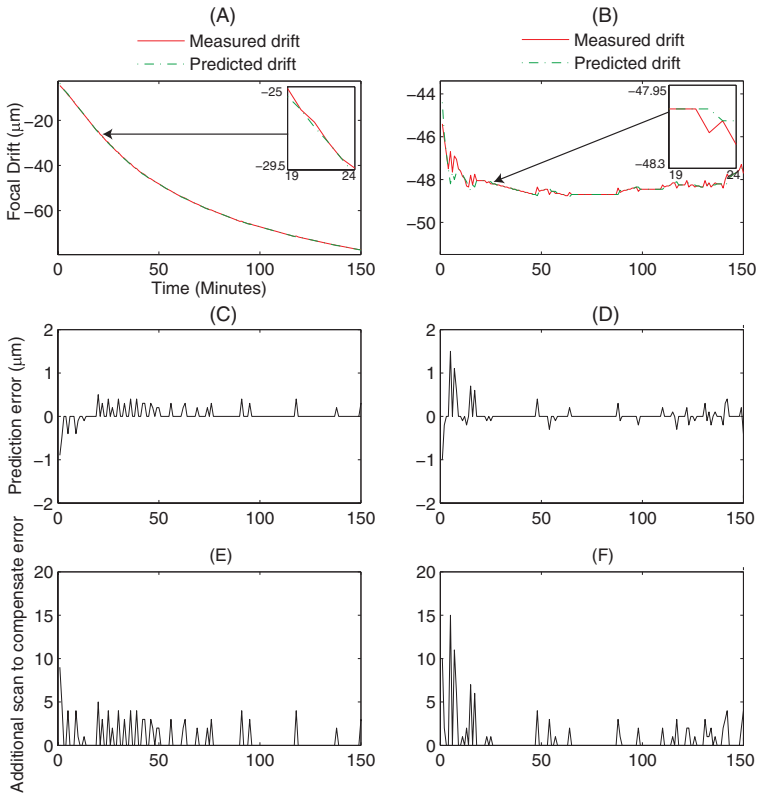

Fig. 5. Focus drift and error predictions in two test scenarios. Focus drift and drift prediction at (A) room temperature and (B) at 37°C in the temperature-controlled chamber. Drift prediction error at (C) room temperature and (D) at 37°C. Additional scans required for prediction error compensation at (E) room temperature and (F) at 37°C.

Table 4. Performance evaluation of the prediction based method.

Method	Thermal condition	Interval (min)	Test set	Number of frames	Error (μm)	Mean number of additional scans (steps)
Simulation	RT	1	S6–S7	272	0.0972	–
	37°C	1	S8–S9	272	0.1392	–
	RT	5	S6–S7	272	0.2302	–
	37°C	5	S8–S9	272	0.3260	–
Experimental	RT	1	S10–S12	521	0.0820	0.85
	37°C	1	S13–S15	492	0.0980	1.03
	RT	5	S16	50	0.3680	3.91
	37°C	5	S17	50	0.2510	2.93

Focus prediction accuracy

A statistical evaluation of the proposed method was carried out in simulated environment as well as in a real operational environment. Representative results from two sets (S11 and S15) are depicted in Figure 5 for the first 150 min and reveal very high prediction accuracy. Very few scans, aside from the predefined minimum number of required scans, were necessary when compared to recent results using other methods (Brázdilová & Kozubek, 2009; Osibote *et al.*, 2010). As mentioned, we set the minimum number of required scans for focusing to five.

We also conducted an exhaustive evaluation of the algorithm with 12 time series acquired in different thermal conditions and imaging intervals. Table 4 describes the results of the prediction method in each test scenario. The four top rows show the results when applying the algorithm on time series S6–S9, stack size 24. The 5-min interval set of time series in a simulation setting are obtained by subsampling frames from 1-min interval time series (S6–S9). The positive results motivated us to extend the evaluation to the real experimental environment.

We implemented the method in the Nikon EZ-C1 software as a visual basic application (VBA) and tested it on a Nikon TE2000-U (Nikon, Japan) microscope in varying thermal conditions and imaging intervals. The results are shown in Table 4, and indicate that the proposed method performs near-optimally in the real operational environment as well. Moreover, the prediction errors and, consequently, the required number of scans increase with the increment of imaging interval irrespective of the thermal condition. The major sources of the increase in error are the residual stochasticity in the drift, the convergence delay of the filter and the quantization error at the hardware level. The larger errors observed in 5 min tests resulted from the initialization process and the convergence delay.

Besides the results above, it is also possible to demonstrate that the proposed algorithm excels in reducing photo bleaching in time-lapse imaging. Figure 6(A) illustrates the effect of photo bleaching in time-lapse confocal laser-scanning fluorescence microscopy. The upper right part of the image was scanned each minute for 1 h. After, the full image was captured. Photo bleaching strongly faded out the signal. In time series fluorescence microscopy, photo bleaching is a strong limiting factor of either the imaging interval or the duration of the experiment (Hoebe *et al.*, 2007). Because the proposed method drastically reduces the required number images for focusing, it reduces photo bleaching, thus allowing increasing the length of the experiment. Figure 6(B) is a comparison of two scenarios. The red line represents the normalized light intensity of the image after image acquisitions for 150 min, with focusing done every minute from an image stack of size 15. By contrast, the green line represents the same quantity for the same period of time while focusing with the proposed algorithm, which resulted in using image stacks of average size 5.49. The normalization allows excluding other sources of variance (i.e. fraction of cell area in the field of view, gain of the photomultiplier tube detector, etc.) from the comparison. Because the obtained intensity curves are noisy, we fitted a polynomial for better characterization. The results verify the assumption that lesser number of scans significantly reduces photo bleaching, because the intensity declination phase differ significantly (39th vs. 86th min).

Discussion and conclusion

We presented a novel strategy for automatic focusing in time-lapse imaging with confocal microscopy. The method works in three steps: (i) Focus position prediction with IMM filter; (ii) focus position measurement with the specified focus function and (iii) parameter update for the IMM filter prediction. These steps are taken prior acquiring each image in a time series. The method's efficiency was assessed against several time series of *E. coli* cells expressing RNA target for MS2d-GFP in two thermal conditions (room temperature and controlled temperature). We demonstrated the improvement with empirical evaluation. The performance of the prediction-based focus search was evaluated in terms of mean absolute

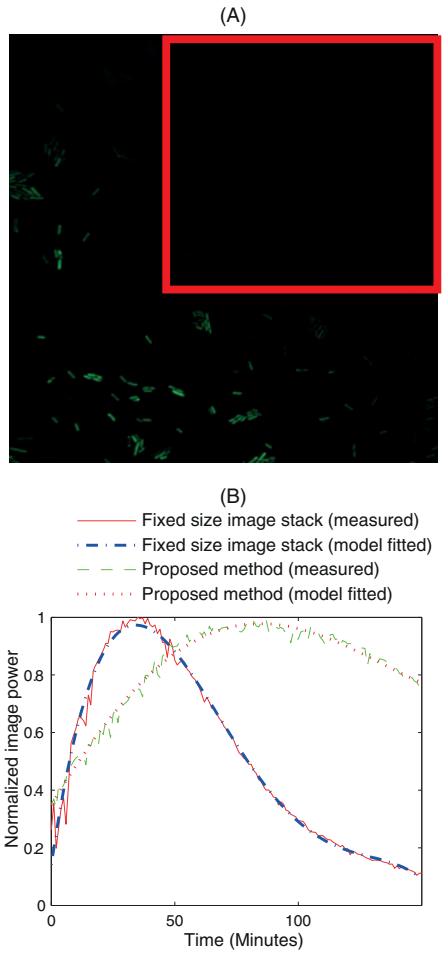

Fig. 6. (A) Effect of photo bleaching. The image inside the red rectangle faded out due to being subject to more scanning. (B) Normalized image intensity over time. A comparison is shown between the proposed method and a trivial method with stack size 15 (trivial method means 'pick the best from a fixed-size stack').

prediction error as well as in average number of required additional scans. The former is independent of the step size. Besides the tests shown here, this method can also be validated with the results shown in (Mason & Green, 1975; data not shown). The efficiency of the algorithm depends on the accuracy of the focus drift prediction. In general, the algorithm was found to converge after a short startup phase, exhibiting thereafter, high prediction accuracy.

As a side result, because the proposed method reduces significantly the number of images required for focusing than previous methods (Brázdilová & Kozubek, 2009; Osibote *et al.*, 2010), it allows a significant reduction of photo bleaching in time-lapse measurements. This may prove to be critical in the context of studies of gene expression dynamics. Most genes in *E. coli* express once to a few times during the cell's lifetime (Bernstein *et al.*, 2002). Because gene expression is stochastic (Yu *et al.*, 2006), to characterize the dynamics of expression of a protein under the control of a given promoter, one will need to observe many cells, each for long periods of time, using short intervals between observations. Photo bleaching imposes strong limitations, which our method may allow overcoming.

To the best of our knowledge, the method proposed here, is the first application of probabilistic filtering for focus drift correction in confocal microscopy. Relevantly, the traditional focusing approach can be viewed as a special case in our framework, in that it considers only the random walk model, disregarding the velocity and acceleration of the drift. Thus, earlier efforts for optimizing autofocus system are also applicable within our framework.

Finally, it is worthwhile mentioning that the performance of the focusing algorithm was boosted by combining, at least, two distinct focus metrics. One optimizes focus quality in a single stack and the other ensures sufficient correlation between successive frames. The combined approach aims at maximizing the product of both approaches. The combination of Tenegrad with Pearson's correlation was found to best perform in the empirical evaluation.

In the future, the results here presented may be further enhanced, regarding the reduction of photo bleaching, by imaging smaller areas for the purpose of focusing only, and by using more efficient search strategies of global maximum as proposed in (Brázdilová & Kozubek, 2009; 2011).

Acknowledgements

Work supported by Tampere Doctoral Programme in Information Science and Engineering (TISE; S.C.), Academy of Finland (M.K., A.S.R.), FiDiPro programme of Finnish Funding Agency for Technology and Innovation (A.S.R., S.C., O.Y-H) and Finnish Centre of Excellence program 2006–2011 (O.Y-H). The funders had no role in study design, data collection and analysis, decision to publish or preparation of the manuscript. We thank J. Lloyd-Price, M. Barathi, H. Mannerstrom and J. Mäkelä for useful advices.

References

Adler, J. & Pagakis, S.N. (2003) Reducing image distortions due to temperature-related microscope stage drift. *J. Microsc.* **210**, 131–137.

Barber, D. & Cemgil, A.T. (2010) Graphical models for time-series. *IEEE Signal Proc. Mag.* **27**(6), 18–28.

Bernstein, J.A., Khodursky, A.B., Lin, P.H., Lin-Chao, S. & Cohen, S.N. (2002) Global analysis of mRNA decay and abundance in Escherichia coli at single-gene resolution using two-color fluorescent DNA microarrays. *Proc. Natl. Acad. Sci. USA.* **99**(15), 9697–9702.

Bezzubik, V.V. & Ustinov, S.N. (2009) Optimization of algorithms for autofocusing a digital microscope. *J. Opt. Technol.* **76**(10), 603–608.

Blom, H.A.P. (1984) An efficient filter for abruptly changing systems. *Proceedings of the 23rd IEEE Conference on Decision and Control*, Las Vegas, U.S.A., pp. 656–658.

Blom, H.A.P. & Bar-Shalom, Y. (1988) The interacting multiple model algorithm for systems with markovian switching coefficients. *IEEE T. Automat. Contr.* **33**(8), 780–783.

Brázdilová, S. & Kozubek, M. (2009) Information content analysis in automated microscopy imaging using an adaptive autofocus algorithm for multimodal functions. *J. Microsc.* **236**, 194–202.

Brázdilová, S. & Kozubek, M. (2011) Image division technique in pre-acquisition analysis of information content for automated microscopy. *J. Microsc.* **242**, 279–289.

Brenner, J.F., Dew B.S., Horton, J.B., King, T., Neurath, P.W. & Selles, W.D. (1976) An automated microscope for cytologic research a preliminary evaluation. *J. Histochem. Cytochem.* **24**(1), 100–111.

Bueno-Ibarra, M.A., Alvarez-Borrego, J., Acho, L. & Chavez-Sanchez, M.C. (2005) Fast autofocus algorithm for automated microscopes. *Opt. Eng.* **44**, 06 3601.1–063601.8.

Firestone, L., Cook, K., Culp, K., Talsania, N. & Preston, K. (1991) Comparison of autofocus methods for automated microscopy. *Cytometry* **12**, 195–206.

Golding, I. & Cox, E.C. (2004) RNA dynamics in live Escherichia coli cells. *Proc. Natl. Acad. Sci. USA.* **101**(31), 11 310–11 315.

Golding, I., Paulsson, J., Zawilski, S.M. & Cox, E.C. (2005) Real-time kinetics of gene activity in individual bacteria. *Cell* **123**(6), 1025–1036.

Groen, F.C.A., Young, I.T. & Ligthart, G. (1985) A comparison of different focus functions for use in autofocus algorithms. *Cytometry* **6**, 81–91.

Helmick, R.E., Blair, W.D. & Hoffman, S.A. (1995) Fixed-interval smoothing for Markovian switching systems. *IEEE T. Inform. Theory* **41**(6), 1845–1855.

Hoebe, R.A., Van Oven, C.H., Gadella, T.W.J, Dhonukshe, P.B., Van Noorden, C.J.F. & Manders, E.M.M. (2007) Controlled light-exposure microscopy reduces photobleaching and phototoxicity in fluorescence live-cell imaging. *Nat. Biotechnol.* **25**, 249–253.

Kalman, R.E. (1960) A new approach to linear filtering and prediction problems. *Trans. ASME J. Basic Eng.Ser. D* **82**, 35–45.

Kreft, M., Stenovec, M. & Zorec, R. (2005) Focus-drift correction in time-lapse confocal imaging. *Ann. N.Y. Acad. Sci.* **1048**, 321–330.

Li, K., Miller, E.D., Chen M., Kanade, T., Weiss, L.E. & Campbell, P.G. (2008) Cell population tracking and lineage construction with spatiotemporal context. *Med. Image Anal.* **12**(5), 546–566.

Liu, X.Y., Wang, W.H. & Sun, Y. (2007) Dynamic evaluation of autofocusing for automated microscopic analysis of blood smear and pap smear. *J. Microsc.* **227**, 15–23.

Mason, D.C. & Green, D.K. (1975) Automatic focusing of a computer-controlled microscope. *IEEE T. Bio-Med. Eng.* **22**(4), 312–317.

Osibote, O., Dendere, R., Krishnan, S. & Douglas, T. (2010) Automated focusing in bright-field microscopy for tuberculosis detection. *J. Microsc.* **240**, 155–163.

Raj, A. & van Oudernaarden, A. (2009) Single-molecule approaches to stochastic gene expression. *Annu. Rev. Biophy.* **38**, 255–270.

Santos, A., Ortiz De Solórzano, C., Vaquero, J.J., Peña, J.M., Malpica, N. & Del Pozo, F. (1997) Evaluation of autofocus functions in molecular cytogenetic analysis. *J. Microsc.* **188**, 264–272.

Sun, Y., Duthaler, S. & Nelson, B.J. (2004) Autofocusing in computer microscopy: selecting the optimal focus algorithm. *Microsc. Res. Tech.*, **65**, 139–149.

Tenenbaum, J.M. (1970) *Accommodation in computer vision.* PhD Thesis, Stanford University, Stanford, U.S.A.

Vollath, D. (1987) Automatic focusing by correlative methods. *J. Microsc.* **147**(3), 279–288.

Yeo, T.T.E., Ong, S.H., Jayasooriah & Sinniah, R. (1993) Autofocusing for tissue microscopy. *Image Vision Comput.* **11**(10), 629–639.

Yu, J., Xiao, J., Ren, X., Lao, K. & Xie, S. (2006) Probing gene expression in live cells, one protein molecule at a time. *Science* **311**, 1600–1603.

Publication II

S. Chowdhury, M. Kandhavelu, O. Yli-Harja, and A.S. Ribeiro, "Cell segmentation by multi-resolution analysis and maximum likelihood estimation (MAMLE)," *BMC Bioinformatics*, 14(Suppl 10):S8, August 2013.

Chowdhury et al. BMC Bioinformatics 2013, 14(Suppl 10):S8
http://www.biomedcentral.com/1471-2105/14/S10/S8

BMC Bioinformatics

RESEARCH Open Access

Cell segmentation by multi-resolution analysis and maximum likelihood estimation (MAMLE)

Sharif Chowdhury[1], Meenakshisundaram Kandhavelu[1], Olli Yli-Harja[1,2], Andre S Ribeiro[1*]

From 10th International Workshop on Computational Systems Biology
Tampere, Finland. 10-12 June 2013

Abstract

Background: Cell imaging is becoming an indispensable tool for cell and molecular biology research. However, most processes studied are stochastic in nature, and require the observation of many cells and events. Ideally, extraction of information from these images ought to rely on automatic methods. Here, we propose a novel segmentation method, MAMLE, for detecting cells within dense clusters.

Methods: MAMLE executes cell segmentation in two stages. The first relies on state of the art filtering technique, edge detection in multi-resolution with morphological operator and threshold decomposition for adaptive thresholding. From this result, a correction procedure is applied that exploits maximum likelihood estimate as an objective function. Also, it acquires morphological features from the initial segmentation for constructing the likelihood parameter, after which the final segmentation is obtained.

Conclusions: We performed an empirical evaluation that includes sample images from different imaging modalities and diverse cell types. The new method attained very high (above 90%) cell segmentation accuracy in all cases. Finally, its accuracy was compared to several existing methods, and in all tests, MAMLE outperformed them in segmentation accuracy.

Background

Single cell microscopy and subsequent analysis has gained much interest recently in areas ranging from studies of gene expression dynamics [1-3], to studies of cell aging [4,5] to disease classification [6]. However, as most processes in cells are stochastic in nature [7] their study requires high-throughput measurements and analysis. The manual extraction of the results from the raw image data is thus prohibitive, causing a need for accurate and robust methods of cell segmentation.

Most existing methods lack in generic applicability and require strong assumptions on cell features i.e. cell shape, size, etc. Additionally, their performance is highly sensitive to cell density and signal to noise ratio. One of the presently most successful and used cell image analysis tools is 'Cellprofiler' [8], an open source software platform for automated cell segmentation from microscopy images. Cell segmentation in Cellprofiler is performed in two steps. First, it separates objects from image background by thresholding. Next, the clumped objects are segmented again by considering intensity or shape as a feature for discrimination. Cellprofiler provides several alternatives for automated threshold selection and clumped cell segmentation. The major drawback of its segmentation algorithm is that its accuracy decreases significantly when cells are in large, dense clumps.

Another state of the art software tool is 'Schnitzcells' [9]. Schnitzcells provides solutions for segmentation and tracking of *Escherichia coli* cells from images by confocal or phase contrast microscopy. The segmentation of cells in Schnitzcells is a multi-stepped process. First, it applies edge detection for generating initial segmentation. Next, it splits long or clumped cells. Finally, it considers too small objects as false positives and discards them. The major problem is the large number of parameters that, without

* Correspondence: andre.ribeiro@tut.fi
[1]Laboratory of Biosystem Dynamics, Computational Systems Biology Research Group, Department of Signal Processing, Tampere University of Technology, 33101 Tampere, Finland
Full list of author information is available at the end of the article

proper tuning, cause the accuracy of the segmentation to decrease notably. Further, it has a limited scope of application, i.e. it only handles *E. coli* and *Bacillus subtilis* cells and often presents a significant number of false positives.

Finally, it is worth mentioning the cell segmentation algorithm for histopathology images, whose implementation was made available in the Farsight toolkit [10]. This method exploits graph-cuts-based segmentation for segmenting foreground signals from the image background. Then, the nuclear seed points are detected by a multi-resolution edge detection method. Aside these, other methods for cell segmentation were proposed (see e.g. [11,12]). In general, these split the overall segmentation task into three steps. First, a separation of foreground objects from image background is made. Next, a post processing step is applied to split the under-segmented clumped cells. Finally, false positives are discarded by some criteria.

Here, we propose a novel cell segmentation method, MAMLE, which maintains very high cell segmentation accuracy in dense cell clusters with low signal to noise ratio (SNR). Moreover, MAMLE requires very few assumptions on cell shape or size, thus, it can handle a wide range of cell types in different imaging modalities. MAMLE is novel in that i) it adopts a state of the art image denoising technique for improving SNR in image, ii) unifies multi-resolution edge detection and threshold decomposition to accomplish the initial segmentation iii) corrects the over-segmented and under-segmented cells based on likelihood estimate, which is shown to be adaptive to varying conditions. Above all, MAMLE innovates in that it learns different shape features on the fly and exploits the learnt parameters for cell segmentation correction. A properly combined usage of all features is implemented to obtain robust and accurate cell segmentation.

MAMLE is primarily targeted towards one of the most challenging cell types for automated segmentation, *E. coli*, a model organism in cell and molecular biology research [13-15]. The high division rate, the formation of dense colonies and the cells' morphology make the segmentation more challenging than for most other cell types. We first describe the method, after which we evaluate its cell segmentation accuracy and compare it with state of the art cell segmentation platforms. Next, the robustness of MAMLE is studied in its parametric space. In the end, we present our conclusions.

Methods

MAMLE cell segmentation method comprises 7 steps: i) image denoising, ii) foreground and background segmentation, iii) multi-scale morphological edge detection, iv) threshold decomposition and initial segmentation, v) shape learning form the initial segmentation, vi) likelihood optimization based splitting and vii) maximum likelihood based merging. A flow chart of the algorithm is illustrated in Figure 1. Next, we describe each step in detail:

i) **Image denoising:** fluorescent images often have low SNR, which leads to cell detection artifacts. Hence, denoising filters are often applied as a pre-processing step for segmentation. MAMLE exploits a state of the art image denoising technique known as Block-Matching and 3D filtering (BM3D) [16]. We opted for BM3D due to its balance between noise cancellation and edge preservation capability [16]. BM3D splits a noisy 2D image into fixed size blocks (8x8) and searches for the blocks that match the reference block. The matching blocks are arranged into a 3D array, known as 'group'. On each group, a 3D transformation is executed and thresholded. Afterwards, BM3D inverse transforms the group and aggregates it with weights to augment the basic estimate. The augmented basic estimate acts as a pilot signal for subsequent steps. Finally, a collaborative Wiener filtering is executed on the noisy signal to obtain the noise removed image.

ii) **Foreground and background segmentation:** this step (second step in Figure 1) separates individual cell colonies from the image background. In fluorescence microscopy, cells are stained with fluorophores or they express a fluorescent protein. As a result, the image background appears darker than foreground objects (i.e. cells). Therefore, a block-wise Otsu threshold, followed by bilinear interpolation, is applied to separate each cell colony from the background [8,17]. Phase contrast images, on the other hand, have different intensity profiles for foreground and background. For these, we use iterative range filtering to segment foreground objects from the image's background [18]. In both cases, the extracted foreground mask is used to select the region of interest.

iii) **Multi-scale morphological edge detection:** this is a key step of MAMLE (third step in Figure 1). Recent studies showed that multi-scale edge detection has, in general, a more robust performance than single scale edge detection strategies [10], particularly when combined with morphological operators [18,19]. We propose a novel multi-scale morphological edge detector to generate the fuzzy edge image for cell segmentation. An edge in a digital image (f) can be realized as a local intensity minimum with direction. Thus, a pixel at an edge should not be altered by the morphological erosion operation. With this assumption, a binary edge ($E_s(f)$) image at scale level S can be defined as in (1) and (2).

$$E_s(f) = \bigcup_d E_s^d(f) \tag{1}$$

$$E_s^d(f) = \begin{cases} 1 \, if \, f = f \circ \mathbf{B}_\mathbf{s}^\mathbf{d} \\ 0 \end{cases} \tag{2}$$

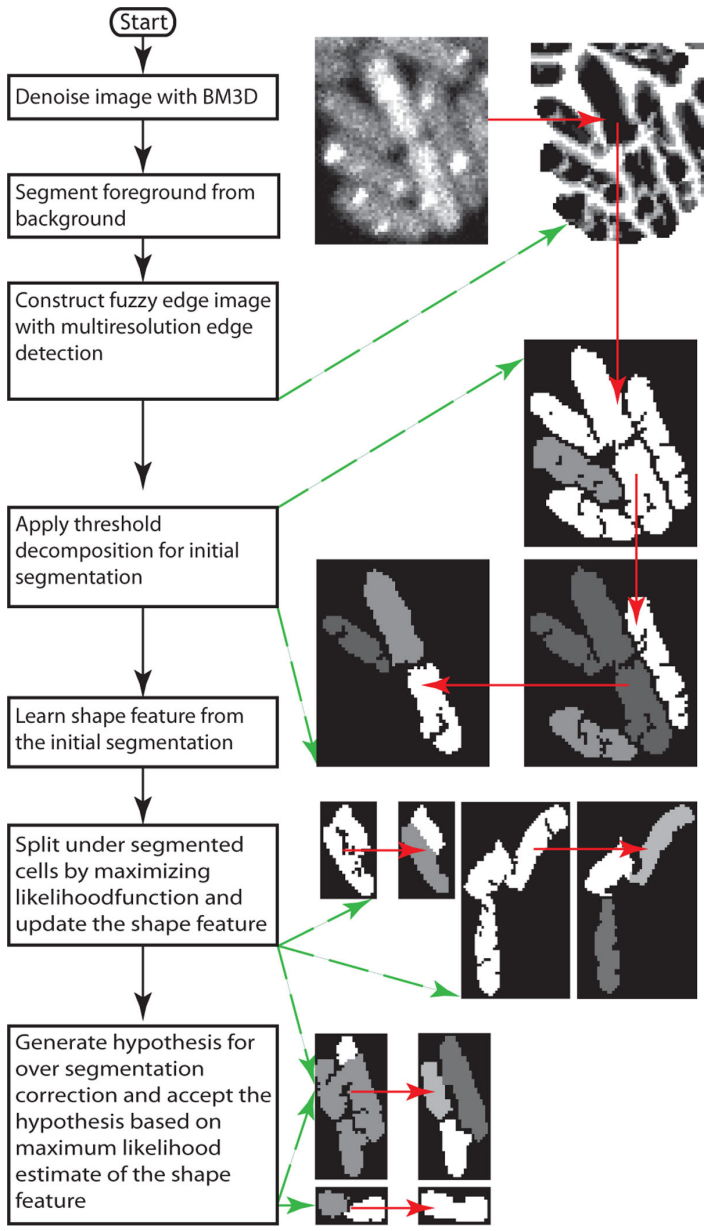

Figure 1 Schematic flow chart of the proposed method. The green arrow points to the result of the respective operation and the red arrow indicates the input/output data flow from one operation to another.

where $E_s^d(f)$is the edge image in the direction d and the symbol (○) represents the morphological erosion operator with the respective support $\mathbf{B}_\mathbf{s}^\mathbf{d}$. The direction d is such that that it allows choosing four possible directions, 1 to 4, corresponding to horizontal, vertical, diagonal from left to right, and diagonal from right to left, respectively. The support $\mathbf{B}_\mathbf{s}^\mathbf{d}$, at scale level $s$and in direction d, can be defined as in (3) - (6).

$$\mathbf{B}_s^1 = [1 \quad 0_{1\times s-1} \quad 1 \quad 0_{1\times s-1} \quad 1] \tag{3}$$

$$\mathbf{B}_s^2 = \left(\mathbf{B}_s^1\right)^T \tag{4}$$

$$\mathbf{B}_s^3 = \mathbf{B}_s^1 \mathbf{I}_{2s+1\times 2s+1} \tag{5}$$

$$\mathbf{B}_s^4 = \frac{R\pi}{2}\left(\mathbf{B}_s^3\right) \tag{6}$$

Here, $0_{1\times s-1}$ is a row vector of zeros of the size $s-1$, $\mathbf{I}_{2s+1\times 2s+1}$ is the identity matrix of the size $2s+1$, T is the transpose operator and $\frac{R\pi}{2}(|.|)$ is the rotational operation. The fuzzy edge image is computed as (7)

$$E(f) = \sum_{s=1}^{S} E_s(f) \tag{7}$$

Each pixel in the fuzzy edge image ($E(f)$) is a real valued integer within the range 0 to S, where S is the maximum scaling factor. A pixel on the most certain edges in the original gray scale images holds a value close to S, while a pixel on the smooth region holds a value close to zero in the fuzzy edge image.

iv) **Threshold decomposition:** the obtained fuzzy edge image is treated as an initial estimate of intensity edge in the grayscale image (forth step in Figure 1). Like more traditional edge detection algorithms [20], MAMLE thresholds this fuzzy edge image to obtain edges for cell segmentation. However, even with an exhaustive search, we were unable to obtain a rational threshold value for selecting edges from the fuzzy edge image. Therefore, we use instead an adaptive method for threshold selection, namely, a 'threshold decomposition' technique [21], which increases or decreases the threshold by a constant amount within an interval for a fixed number of times. Mathematically, this procedure can be expressed as (8) [21].

$$T^i(f) = \begin{cases} 1 \; if \; f \geq i \\ 0 \; if \; f < i \end{cases} \tag{8}$$

The decomposition starts with the strongest threshold ($i = S$) that subdivides the foreground object, based on most certain or strongest edges. Afterwards, it lowers the threshold gradually to a predefined bound, unless the foreground object is already reduced to a size smaller than a predefined value (i.e. the expected maximum size of a cell). The threshold decomposition is recursive and the exact number of decomposition levels is specific for each of the detected objects. The details are listed in 'Algorithm 1'. The segmentation result is treated as an initial segmentation mask for the following steps. As noted, the initial segmentation results show several over and under-segmentation artifacts, which should be corrected.

Algorithm 1: Threshold Decompositon(E, f)

Input: fuzzy edge image(E), edge threshold(f), area threshold T_a

1. Initialize: S ← Ø
2. Select the edges that are stronger than f and label the image based on edge selection
3. ASSIGN $f^- \leftarrow f - 1$
4. FOR EACH labelled region S_i
   a) IF area (S_i) >T_a THEN
      a.1) UPDATE S ← S∪ ThresholdDecomposiiton(E ∩ S_i, f^-);
   b) ELSE
      b.1) UPDATE S ← S ∪ S_i
5. Return S;

v) **Learning shape parameter:** First, we need to acquire a morphological or shape feature from the initial segmentation. As the initial results are partially correct, they can be used to obtain different shape features. Afterwards, they can be categorized into classes, namely 'correct segmentation', 'under-segmentation' or 'over-segmentation', based on the morphological features. However, to maintain the classifier tractable, we treat each object as a simple polygon and consider its area, the major axis length and the minor axis length as the discriminant features for classification. The major (a) and the minor (b) axes are computed according to (9) and (10) [22].

$$a = 4\sqrt{\frac{m_{00}m_{11} - m_{01}m_{01}}{A\lambda_1}} \tag{9}$$

$$b = 4\sqrt{\frac{m_{00}m_{11} - m_{01}m_{01}}{A\lambda_2}} \tag{10}$$

Here, m_{xy} is the centroidal moment, A is the area and λ_2, λ_2 are two orthogonal eigenvalues of the polygon. The ideal cell shape and shape distribution are assumed as multivariate Gaussian distributions on the feature space. The parameter of this distribution can be estimated from the sample mean vector and the covariance matrix in the feature space of the initial segmentation results.

vi) **Binary split:** this step (sixth step in Figure 1) is the first that re-evaluates the initial segmentation results for correction. Binary split considers the initially segmented cells that are larger than the average cell size as a candidate for the split. The splitting is done by maximizing the likelihood function. The log-likelihood of a detected object to be a cell is formulated as (11).

$$ll(\mathbf{X}_i) = \log\left(\frac{1}{(2\pi)^{\frac{d}{2}}|\Sigma|^{\frac{1}{2}}} e^{-(\mathbf{X}_i-\mu)^T\Sigma^{-1}(\mathbf{X}_i-\mu)}\right) = \log\left(\frac{1}{(2\pi)^{\frac{d}{2}}|\Sigma|^{\frac{1}{2}}}\right) - (\mathbf{X}_i-\mu)^T\Sigma^{-1}(\mathbf{X}_i-\mu) \quad (11)$$

Here, μ and Σ are the mean and covariance of the multivariate Gaussian distribution, estimated from the initial segmentation. Since the covariance matrix is invariant with respect to the object under selection, the log-likelihood function can be simplified as (12).

$$D(\mathbf{X}_i) = (\mathbf{X}_i-\mu)^T\Sigma^{-1}(\mathbf{X}_i-\mu) \quad (12)$$

A closer look at the objective function ($D(\mathbf{X}_i)$) reveals that, given the considered metric, the minimization of the variance of the normalized distance from the mean vector (μ) would maximize the likelihood function. This problem is usually realized as a Gaussian mixture model problem and is solved with the expectation maximization (EM) algorithm [23]. However, we did not consider EM as a solution since: i) EM needs to know the number of existing mixtures, ii) EM does not have direct control on the shape of the distribution and, iii) since EM considers global optimization, there is no straight forward way to consider the case where a part of one cell is clumped with one or more cells. Thus, we formulate an iterative procedure for likelihood maximization that splits a clumped object into two parts by maximizing the likelihood only in one of the parts, disregarding the other.

After the split, the disregarded part is reconsidered for split and processed recursively, unless its size is already smaller than the average cell size. The split procedure is not completely flawless. Occasionally, it over-segments a single cell into multiple parts. Nevertheless, most over-segmented cells are re-merged in the subsequent merge procedure.

vii) **Over-segmentation correction:** this step (seventh and eight steps in Figure 1) merges the over-segmented cells based on a maximum likelihood estimate of the shape feature vector. The maximum likelihood estimate based merging is obtained by transforming the problem into a binary integer programming problem [24]. Similar approaches have been used for cell tracking [25]. The merging scheme first constructs a candidate set (C) for merging. Each member in the candidate set needs to satisfy the logical quantifier expressed in (13).

$$\forall c_i \in C \exists c_j \in C \begin{pmatrix} D(\mathbf{X}_i) + D(\mathbf{X}_j) \geq \\ D(\mathbf{X}_{ij}) \wedge c_i \neq c_j \end{pmatrix} \quad (13)$$

Here, $c_i$is a cell or part of cell identified in the prior steps and $\mathbf{X}_i$ is the respective feature vector. $\mathbf{X}_{ij}$ represents the feature vector of the object c_i merged with c_j. The first $|C|$ rows of the hypothesis matrix $\mathbf{H}$ and likelihood vector $\mathbf{L}$ are initialized as (14) and (15) respectively.

$$\mathbf{H}(i,j) = \begin{cases} 1 \; if \; i = j \\ 0 \; if \; i \neq j \end{cases} \quad (14)$$

$$\mathbf{L}(i) = -D(\mathbf{X}_i) \quad (15)$$

Subsequently, it generates all possible hypotheses of merging two objects from the candidate list by satisfying the merging constraint (16). Additionally, for each of the accepted hypotheses, a single row is appended in the hypothesis matrix according to (17) and an element in the likelihood vector is added as (18).

$$\forall c_{ij} \in C_2 \exists c_i, c_j \in C \left(D(\mathbf{X}_i) + D(\mathbf{X}_j) \geq D(\mathbf{X}_{ij}) \wedge c_i \neq c_j\right) \quad (16)$$

$$\mathbf{H}(h',k) = \begin{cases} 1 \; if \quad \left(k = i \vee k = j\right) \wedge c_{ij} \in C_2 \\ 0 \; otherwise \end{cases} \quad (17)$$

$$\mathbf{L}(h') = -D(\mathbf{X}_{ij}) \quad (18)$$

Similarly, it generates hypothesis list (C_3) for merging three objects and adds a single row in the hypothesis matrix and likelihood vector for each of the generated hypotheses. This can be extended further, beyond the third level. We did not find any evidence to justify such expansion. Hence, we limited the hypothesis generation process to level three. The generated hypothesis matrix has $m = |C| + |C_2| + |C_3|$ rows and $n = |C|$ columns, while the likelihood vector has m rows. Given this, the maximum likelihood estimate for merging can be obtained by selecting the hypotheses that includes each of the identified objects exactly in one hypothesis and, at the same time, maximizes the total likelihood. This problem can be solved by solving a standard binary integer programming problem formulated in (19).

$$\mathbf{x}^* = \arg\max_{\mathbf{x}}(\mathbf{L}^T\mathbf{x}) \quad (19)$$

Here, $\mathbf{x}^*$is a column vector of ones that restricts the inclusion of each candidate exactly in one hypothesis. However, the stated problem belongs to the class of NP-hard problems [24]. Thus, there is no known polynomial time solution for solving it. We exploited a linear programming (LP)-based branch-and-bound technique to obtain an approximate solution [24]. Finally, the selected hypotheses are accepted and the objects are merged to construct the final segmentation result.

Materials

E. coli DH5α-PRO strain containing a bacterial expression vector PROTET-K133 carrying the MS2-dimer (MS2d) fused with green fluorescent protein (MS2d-GFP) was used for this study [26,27]. This vector has an inducible promoter P(LtetO-1), which is under tight regulation of anhydrotetrachycline (aTc, IBA GmbH, Göttingen, Germany). Constructs were generously provided by Dr. Ido Golding, University of Illinois. Cells were grown in LB medium, supplemented with kanamycin antibiotic for the selection of cell containing the $P_{LtetO-1}$-Ms2d-GFP plasmid. For full induction of gene expression, cells were grown overnight at 37 °C with aeration to reach an optical density of OD600 ≈ 0.3-0.5. The cells were incubated with inducer aTc (100 ng/ml) for 45 minutes to attain full induction of MS2d-GFP. Following induction, a few micro litres of culture were placed between a coverslip and a thick slab of 1% agarose containing LB. Microscopy was performed at room temperature (22 °C) using a Nikon Eclipse (TE-2000-U, Nikon, Tokyo, Japan) inverted confocal laser-scanning microscope equipped with a 100X magnification (1.5NA) objective. GFP fluorescence was measured using a 488 nm laser (Radius 405 laser, Coherent, Inc., Santa Clara, CA) and a 515/30 nm detection filter (100-120 detector gain).

In case of *Staphylococcus aureus*, cells were grown in LB medium. OD600 ≈ 0.3-0.5 cells were incubated with 0.5 mg ml-1 DNA binding stain, 4'6-diamidino-2-phenylindole (DAPI, Sigma) for 1 hour at 37 °C and centrifuged at 7000 RPM for 10 min. Cell pellet was diluted 1:100 time and few micro litres of cells were placed in a microscopic slide as mentioned above to perform the image acquisition. DAPI stain expression was measured using a 406 nm laser (Radius 405 laser, Coherent, Inc., Santa Clara, CA) and a 450/35 nm detection filter (100-120 detector gain).

Results

We carried out an empirical evaluation of the algorithm with several test sets. The results are categorized into four classes: i) true positive (TP), if a cell is segmented properly; ii) over-segmentation, if a cell is split into more than one piece; iii) under-segmentation, if more than one cell is recognized as a single cell; and iv) false negative (FN), if a clearly visible cell is not detected. Apart from these, some cells were undergoing division which, depending on the stage, is classified as a single cell or as two independent cells, according to the specifications of the algorithm (these classifications are not considered in errors estimation). A small fraction of detections were false positives (less than 0.1%), and since the overall contribution of false positives is insignificant, we discard this result from the evaluation. The results from the fluorescent labelled *E. coli* test sample are listed in the Table 1, and compared to the manual annotation. The results in Tables 1 and 2 reveal the high segmentation accuracy and generality of the method. Illustrative examples from test samples are presented in Figure 2.

As a proof of concept, the efficiency of the segmentation method is evaluated against manually labelled cells at pixel level. This is carried out for three illustrative features: total cell intensity, cell length, and cell width. The test comprises approximately 1100 GFP labelled *E. coli* cells collected from 13 images. Figure 3 shows the quantitative results in scatter plots with a least square regression line. The horizontal axis represents the results from manual labelling and the vertical axis represents the results from the automated segmentation. A strong

Table 1 Test results on confocal images of *E. coli* cells expressing a fluorescent protein, MS2d-GFP

Test Case	No. images	No. cells	TP	Over -seg. (total/ %)	Under -seg. (total/ %)	FN (total/ %)	Segmentation accuracy (%)
Dense	10	7947	7335	236/2.96	170/2.13	206/2.59	92.30
Medium	10	4014	3616	87/2.16	184/4.58	127/3.16	90.10
Sparse	10	857	817	20/2.33	16/1.86	4/0.46	95.33
Total	30	12818	11768	343/2.67	370/2.88	337/2.63	91.80

TP and FN stand for true positive and false negative, respectively.

Table 2 Test results from phase contrast images of *E. coli* cells, from fluorescence images of *S. aureus*, and from epifluorescence images of *E. coli*.

Test Case	No. images	No. cells	TP	Over seg. (total/ %)	Under-seg. (total/ %)	FN	Seg. accuracy (%)
Phase contrast - *E. coli*	4	381	376	3/0.787	2/0.52	0/0	98.69
S. aureus	3	768	710	18/2.34	40/5.21	0/0	92.45
Epi - *E. coli*	3	160	146	5/3.12	6/3.75	3/1.87	91.25
Total	10	1309	1232	26/1.99	48/3.67	0.23	94.12

TP and FN stand for true positive and false negative, respectively.

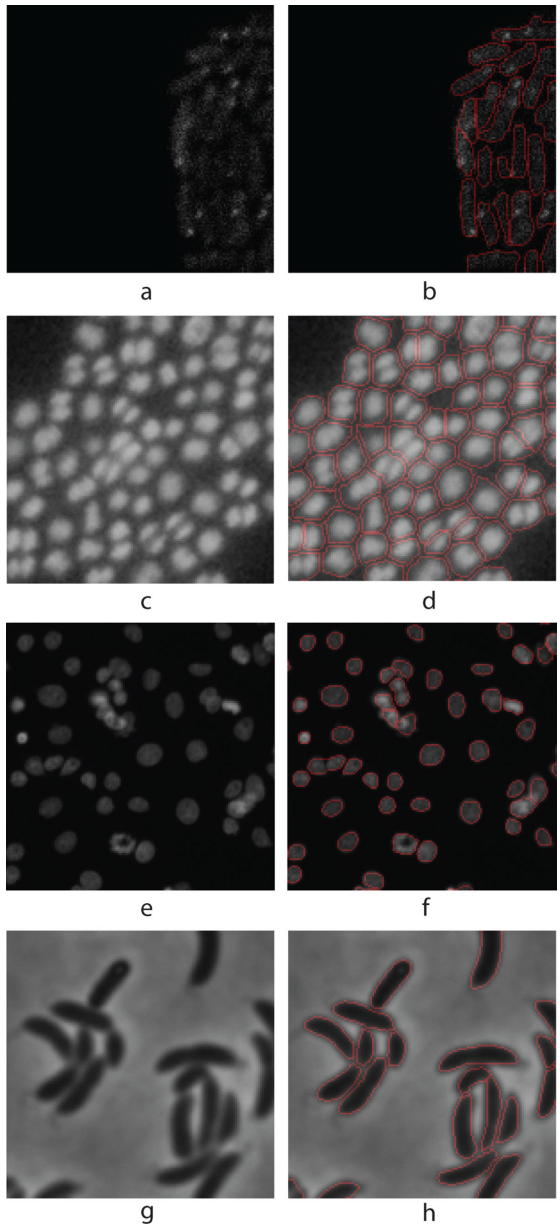

Figure 2 Illustrative examples from the test samples. (a) Fluorescent protein labelled *E. coli* cells captured with confocal microscope, (b) Segmented result of (a), (c) Fluorescent protein labelled *Staphylococcus* cells in Epifluorescence microscopy image. (d) Segmented result of (c), (e) Human HT29 Colon Cancer 1 image set (Source [8]), (f) Segmented result of (e), (g) *E. coli* cells captured with phase contrast microscope (Source [11]), (h) Segmented result of (g).

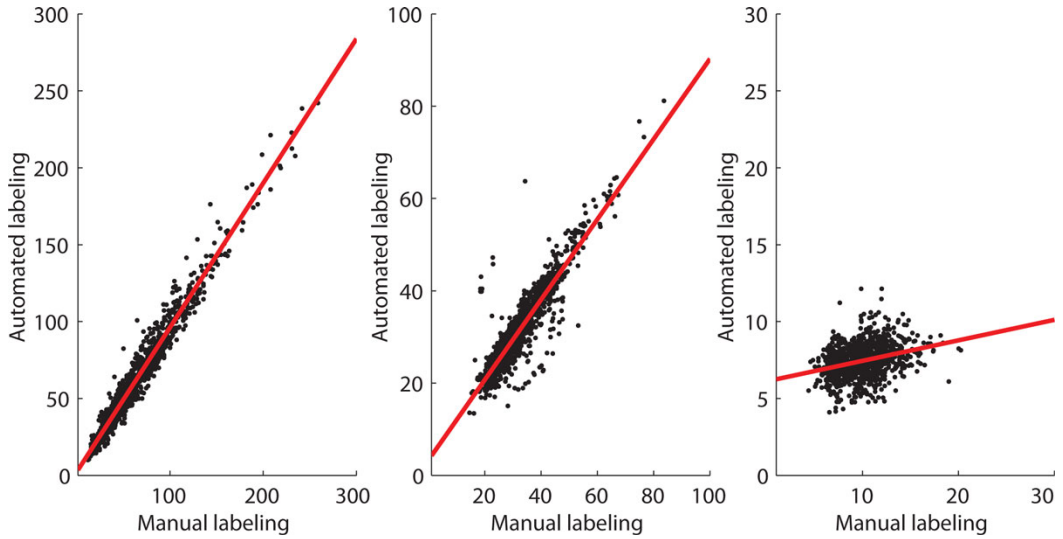

Figure 3 Scatter plot of total cell intensity (left plot), length of the cell (middle plot) and width of the cell (right plot) in pixel by pixel comparison test.

correspondence between manual and automated segmentation is evident. The correlation coefficients for the listed features were 0.98 (total cell intensity), 0.91 (cell length) and 0.31 (cell width), respectively. The correlation of the cell width feature is lower due to substantial inaccuracy in the manual segmentation of this feature. The presence of cells dividing was the other main cause for this error rate.

The cell segmentation accuracy of the algorithm is next compared with three state-of-the-art cell image analysis platforms, namely, Cellprofiler [8], Farsight [10], and Schnitzcells [9]. For the comparison to be unbiased, test samples were included from publicly available online repositories [8-10]. A set of sample results is shown in Figure 4. In general, we found the method proposed here to outperform the others in segmentation accuracy. Schnitzcells was the second best in *E. coli* segmentation (Figure 5). To further compare the proposed method and Schnitzcells we extended the evaluation. This additional test is carried out using publicly available bench mark images for cell counting [8]. The benchmark data contains roughly 2162 human HT29 colon cancer cells in 6 images. The cells were manually labelled and scored by two human observers and the average of the manual score is considered the ground truth. The human labelling had a mean absolute deviation of 11% and the best know result for this data set was attained by Cellprofiler, with a mean absolute deviation of only 6.2% [8]. In this benchmark data, our method exhibited a mean absolute deviation of only 1.79%.

Finally, we consider the usability of the novel method. In addition to accurate segmentation, the number of parameters and a robust performance in the parametric space are critical aspects of an accurate segmentation method. Ideally, an automated method should have as few free parameters as possible, and their tuning should be intuitive. Also, the optimal range of parameters should be large enough for tuning properly. Such 'parametric robustness' is what enables the segmentation method to be applicable to large scale analysis without the need for significant effort regarding the parameter tuning.

The proposed method has only 4 free parameters for tuning, namely, maximum cell size, scaling or resolution level, decomposition level and threshold window size, which affect the segmentation accuracy. The first three are intuitive in the sense that the maximum cell size can be estimated from knowledge of the phenotype of the cells (or a quick observation of the test samples) and microscope settings. The maximum scaling factor should be smaller than the cell width and, finally, the decomposition level should be less than the maximum scaling factor.

The parametric robustness of MAMLE is studied in 10 sample images containing approximately 8000 cells. It considers cell count as an objective metric for evaluation. The result is shown in Figure 6. Figure 6 (top) illustrates the effect of varying the scale level and the decomposition level. The cell count is stable across a wide range of the respective parameters. The results in

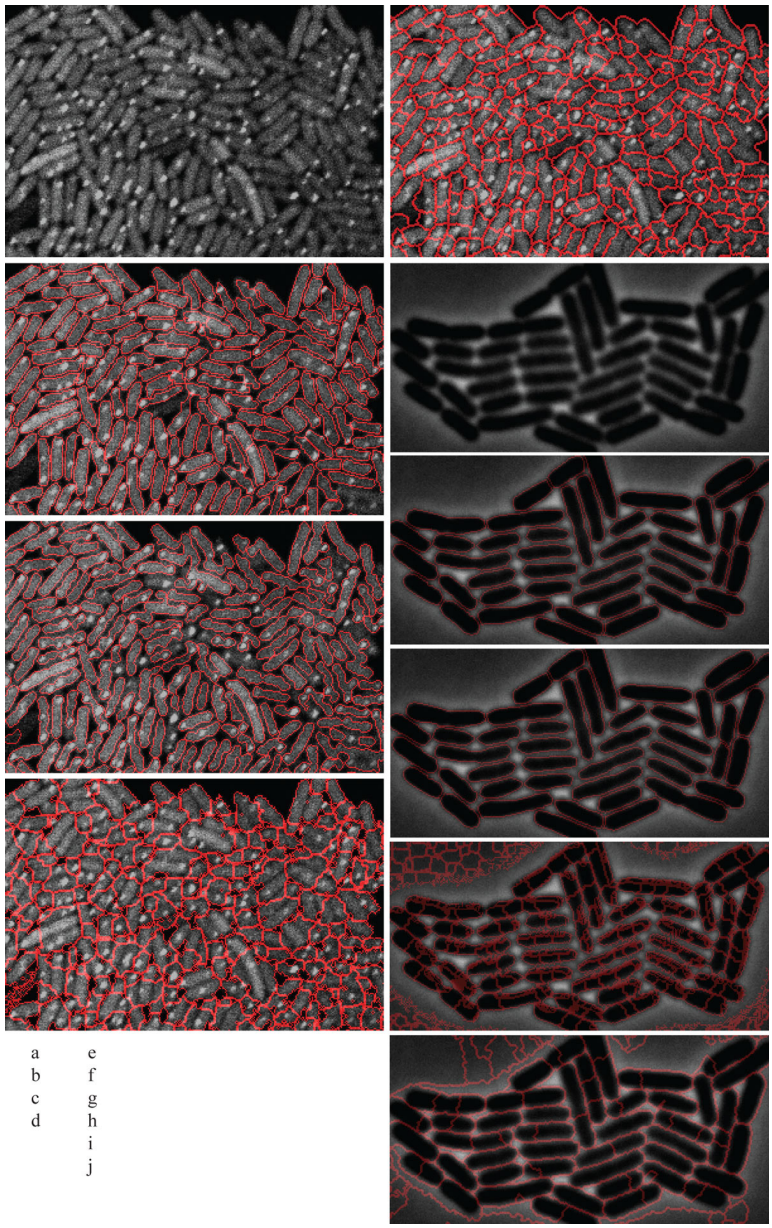

Figure 4 Segmentation comparison result. Fluorescent protein labelled *E. coli* cells captured with confocal microscope, (b) Segmented result of (a) by the proposed method, (c) Segmented result of (a) by Schnitzcells software, (d) Segmented result of (a) by the Farsight toolkit, (e) Segmented result of (a) by Cellprofiler, (f) *E. coli* cells captured with phase contrast microscope(Source [9]), (g) Segmented result of (f) by the proposed method, (h) Segmented result of (f) by Schnitzcells software, (i) Segmented result of (f) by the Farsight toolkit, (j) Segmented result of (f) by Cellprofiler. Figures are labelled as follows: on the left side, from top to bottom, are figures a) to d). On the right side, from top to bottom, are figures e) to j). This labelling is also indicated in the bottom left of the image.

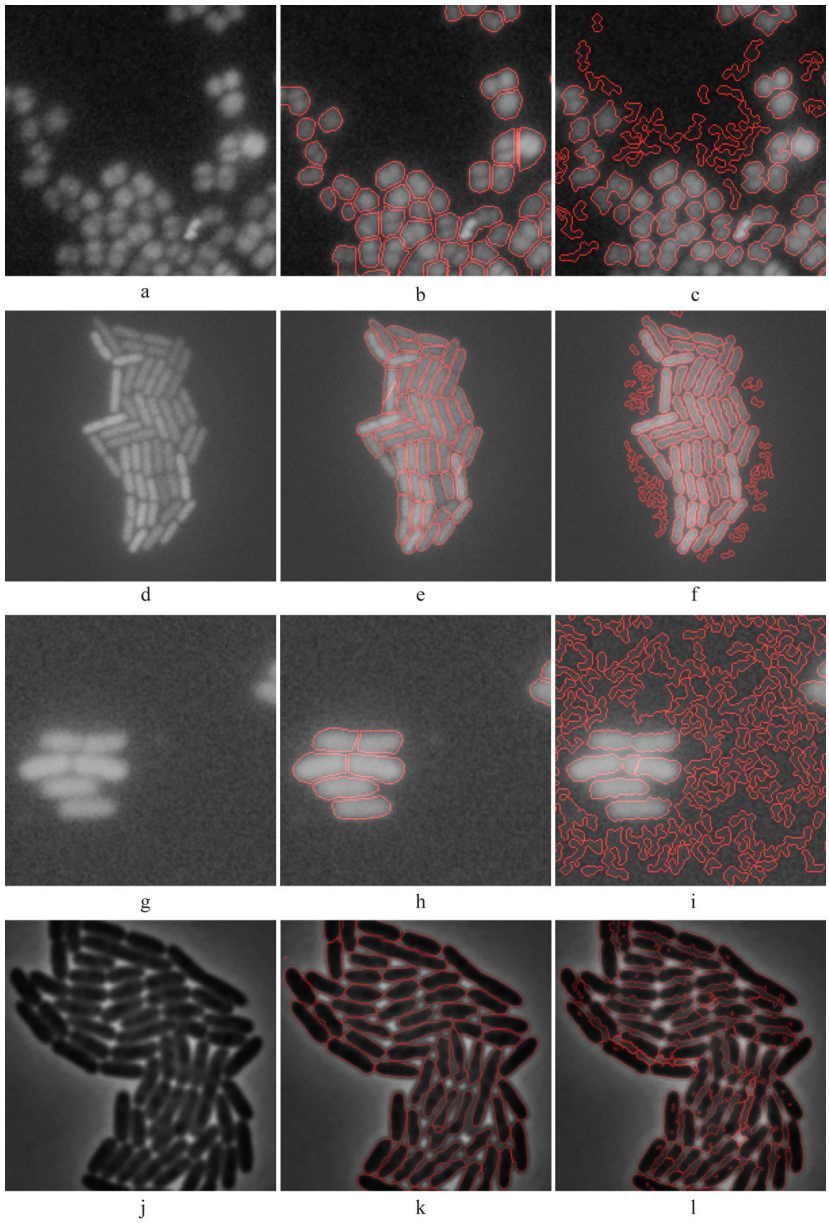

Figure 5 Comparison between the proposed method and Schnitzcells software. (a) Fluorescent protein labelled *Staphylococcus* cells in Epifluorescence microscopy image, (b) Segmented result of (a) by the proposed method, (c) Segmented result of (a) by Schnitzcells software, (d) Fluorescent protein labelled *E. coli* cells captured with confocal microscope (Source [9]), (e) Segmented result of (d) by the proposed method, (f) Segmented result of (d) by Schnitzcells software, (g)) Fluorescent protein labelled *E. coli* cells captured with Epifluorescence microscope, (h) Segmented result of (g) by the proposed method, (i) Segmented result of (g) by Schnitzcells software, (j) *E. coli* cells captured with phase contrast microscope (Source [12]), (k) Segmented result of (j) by the proposed method, (l) Segmented result of (j) by Schnitzcells software.

the Figure 6 (bottom) are obtained by varying the maximum cell size. They indicate that this parameter affects the cell count in a linear fashion. Note that the coefficient of variation of cell count was much lower (0.057) than the coefficient of variation of the input parameter 'maximum cell size' (0.32). Thus, it can be stated that the algorithm obtains robust cell detection results within a wide range of numerical settings of the free parameters.

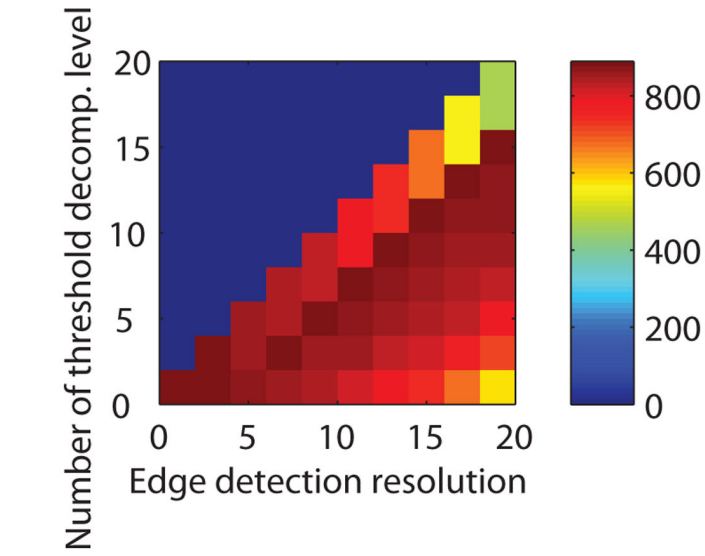

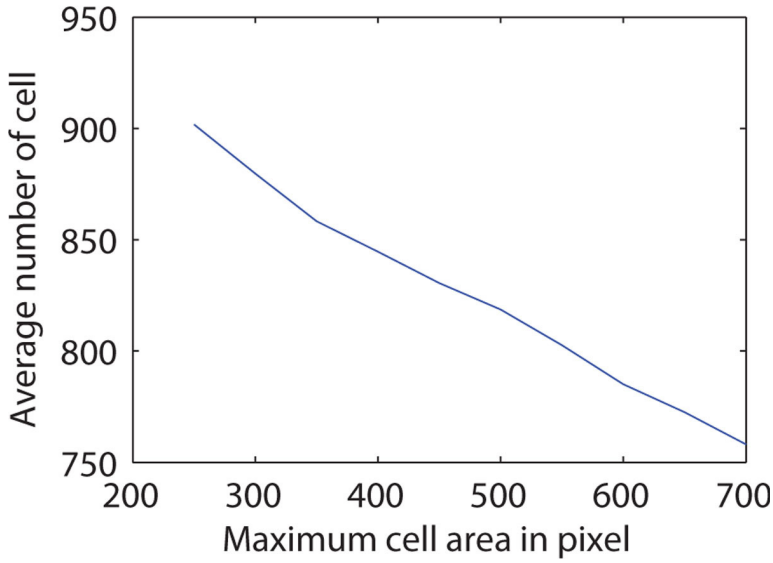

Figure 6 Parametric robustness. Top: Number of detected cells (color encoded, encoding scheme is shown on right side color bar) for different combinations of edge detection resolution level (X-axis) and number of maximum threshold decomposition level (Y-axis). Bottom: Number of cells detected for different values of the free parameter 'length of the cell'.

The parameter, 'threshold window size' depends on the spatial distribution of cell background and foreground illumination levels. The largest possible window with homogeneous illumination level is the optimum for this parameter.

Conclusions and discussion

Automated cell segmentation with high accuracy is a major challenge as well as a necessity towards high throughput analysis in cell biology, whose research is increasingly relying on *in vivo* single-cell studies. Here, we presented a novel method for automatically segmenting cells within colonies from microscopy images. The segmentation scheme exploits image de-noising techniques in transform-domain followed by multi-resolution edge detection and threshold decomposition for generating initial segmentation results. Then, a machine learning procedure is carried out to learn morphological shape parameters from the initial segmentation. Next, a likelihood optimization based splitting and maximum likelihood estimate based merging steps are executed to construct the accurate segmentation result.

The method was primarily evaluated for segmenting GFP labelled *E. coli* cells, but it was also tested for different cell types and imaging modalities. The test set comprises both de novo data set as well as samples from publicly available off-the-shelf benchmark data set. The segmentation results were found highly accurate by manual inspection, and denote high segmentation accuracy when compared with existing methods. The main strength of MAMLE relies on its ability to segment dense cell colonies as well as it robustness across a wide range of imaging modalities of different cell types.

Relevantly, the parameter selection is limited to three parameters, whose setting is intuitive. Either knowledge of the cells' morphology or a quick observation of the images, along with knowledge on the magnification settings of the microscope suffice to introduce parameter values that lead to robust results. Nevertheless, the overall performance was found robust to sub-optimal parameter settings as well. A forth parameter, 'threshold window size', as discussed, should be obtained from the spatial distribution of cell background and foreground illumination levels.

In the future, MAMLE can be extended in several ways. One plausible improvement is to add the possibility of training the method beforehand and update the trained knowledge base at runtime, rather than building the entire knowledgebase at runtime. This may be of use to research groups that focus on a specific organism and desire close to optimal results without the need to test the method and its parameters for each study.

Availability and additional materials

http://www.cs.tut.fi/~sanchesr/CellSegment/index.htm

List of abbreviations used

BM3D: Block-Matching and 3D filtering; FN: False Negative; GFP: Green fluorescent protein; MAMLE: Multi-resolution Analysis and Maximum Likelihood Estimation; NP-hard: Non-deterministic Polynomial-time hard; TP: True positive.

Competing interests

The authors declare that they have no competing interests.

Authors' contributions

SC has planned the study, developed necessary software and executed the testing for result preparation. MSK has cultured the samples cells, provided image data for evaluation empirical evaluation and evaluated the result. ASR conceived the study. ASR and SC wrote the manuscript. All authors performed research.

Acknowledgements

Work supported by Academy of Finland, Finnish Funding Agency for Technology and Innovation (TEKES), and Tampere Doctoral Programme in Information Science and Engineering (TISE). The funders had no role in study design, data collection and analysis, decision to publish, or preparation of the manuscript.

Declarations

The publication costs for this article were funded by the Finnish Funding Agency for Technology and Innovation (grant no. 40226/12).
This article has been published as part of BMC Bioinformatics Volume 14 Supplement 10, 2013: Selected articles from the 10th International Workshop on Computational Systems Biology (WCSB) 2013: Bioinformatics. The full contents of the supplement are available online at http://www.biomedcentral.com/bmcbioinformatics/supplements/14/S10.

Authors' details

[1]Laboratory of Biosystem Dynamics, Computational Systems Biology Research Group, Department of Signal Processing, Tampere University of Technology, 33101 Tampere, Finland. [2]Institute for Systems Biology, 401 Terry Avenue North, Seattle, WA 98109-5234, USA.

Published: 12 August 2013

References

1. Golding I, Paulsson J, Zawilski SM, Cox EC: **Real-time kinetics of gene activity in individual bacteria.** *Cell* 2005, **123(6)**:1025-1036.
2. Kandhavelu M, Mannerström H, Gupta A, Häkkinen A, Lloyd-Price J, Yli-Harja O, Ribeiro AS: **In vivo kinetics of transcription initiation of the lar promoter in *Escherichia coli*. Evidence for a sequential mechanism with two rate limiting steps.** *BMC Syst Biol* 2011, **5**:149.
3. Taniguchi Y, Choi PJ, Li GW, Chen H, Babu M, Hearn J, Emili A, Xie XS: **Quantifying *E. coli* proteome and transcriptome with single-molecule sensitivity in single cells.** *Science* 2000, **329(5991)**:533-538.
4. Lindner AB, Madden M, Demarez A, Stewart EJ, Taddei F: **Asymmetric segregation of protein aggregates is associated with cellular aging and rejuvenation.** *Proc Natl Acad Sci USA* 2008, **105**:3076-3081.
5. Lloyd-Price J, Häkkinen A, Kandhavelu M, Marques IJ, Chowdhury S, Lihavainen E, Yli-Harja O, Ribeiro AS: **Asymmetric disposal of individual protein aggregates in *Escherichia coli*, one aggregate at a time.** *J Bacteriol* 2012, **194(7)**:1747-1752.
6. Lihavainen E, Mäkelä J, Spelbrink JN, Ribeiro AS: **Mytoe: Automatic analysis of mitochondrial dynamics.** *Bioinformatics* 2012, **7(28)**:1050-1051.
7. Kaern M, Elston TC, Blake WJ, Collins JJ: **Stochasticity in gene expression: from theories to phenotypes.** *Nat Rev Genet* 2005, **6**:451-464.
8. Carpenter AE, Jones TR, Lamprecht MR, Clarke C, Kang IH, Friman O, Guertin DA, Chang JH, Lindquist RA, Moffat J, Golland P, Sabatini D: **CellProfiler: image analysis software for identifying and quantifying cell phenotypes.** *Genome Biol* 2006, **7**:R100.
9. Young JW, Locke JC, Altinok A, Rosenfeld N, Bacarian T, Swain PS, Mjolsness E, Elowitz MB: **Measuring Single-Cell Gene Expression Dynamics in Bacteria Using Fluorescence Time-lapse Microscopy.** *Nat Protoc* 2011, **7(1)**:80-88.
10. Al-Kofahi Y, Lassoued W, Lee W, Roysam B: **Improved automatic detection and segmentation of cell nuclei in histopathology images.** *IEEE T Biomed Eng* 2010, **57(4)**:841-852.

11. Sliusarenko O, Heinritz J, Emonet T, Jacobs-Wagner C: **High-throughput, subpixel-precision analysis of bacterial morphogenesis and intracellular spatio-temporal dynamics.** *Mol Microbiol* 2011, **80(3)**:612-627.
12. Wang Q, Niemi J, Tan CM, You L, West M: **Image segmentation and dynamic lineage analysis in single-cell fluorescence microscopy.** *Cytometry* 2010, **77(1)**:101-110.
13. Bernstein JA, Khodursky AB, Lin PH, Lin-Chao S, Cohen SN: **Global analysis of mRNA decay and abundance in *Escherichia coli* at single-gene resolution using two-color fluorescent DNA microarrays.** *Proc Natl Acad Sci USA* 2002, **99**:9697-9702.
14. Elowitz MB, Leibler S: **A synthetic oscillatory network of transcriptional regulators.** *Nature* 2000, **403(6767)**:335-338.
15. Lutz R, Lozinski T, Ellinger T, Bujard H: **Dissecting the functional program of *Escherichia coli* promoters: the combined mode of action of Lac repressor and AraC activator.** *Nucleic Acids Res* 2001, **29**:3873-3881.
16. Dabov K, Foi A, Katkovnik V, Egiazarian K: **Image denoising by sparse 3D transform-domain collaborative filtering.** *IEEE T Image Process* 2007, **16(8)**:2080-2095.
17. Otsu N: **A threshold selection method from gray-level histograms.** *IEEE T Syst Man Cyb* 1979, **9(1)**:62-66.
18. Wang K, Wu J, Gao L, Pian Z, Guo L: **Magnetic Resonance Images Edge Detection Based on Multi-scale Morphology.** *IEEE/ICME International Conference on Complex Medical Engineering* 2007, 744-747.
19. Mukhopadhyay S, Chanda B: **Multiscale morphological segmentation of gray-scale images.** *IEEE T Image Process* 2003, **12(5)**:533-549.
20. Canny J: **A Computational Approach To Edge Detection.** *IEEE T Pattern Anal* 1986, **8(6)**:679-698.
21. Shih FYC, Mitchell OR: **Threshold Decomposition of Gray-Scale Morphology into Binary Morphology.** *IEEE T Pattern Anal* 1989, **11(1)**:31-42.
22. Prokop RJ, Reeve AP: **A Survey of Moment-Based Techniques For Unoccluded Object Representation and Recognition.** *CVGIP: Graph Model Im* 1992, **54(5)**:438-460.
23. Duda RO, Hart PE, Stork DG: *Pattern classification.* 2 edition. John Wiley & Sons; 2001.
24. Hillier FS, Lieberman GJ: *Introduction to Operations Research* McGraw-Hill; 2001.
25. Li F, Zhou X, Ma J, Wong ST: **Multiple Nuclei Tracking Using Integer Programming for Quantitative Cancer Cell Cycle Analysis.** *IEEE T Med Imaging* 2010, **29(1)**:96-105.
26. Peabody DS, Lim F: **Complementation of RNA Binding Site Mutations in Heterodimers of Bacteriophage MS2 Coat Protein.** *Nucleic Acids Res* 1996, **24**:2352-2359.
27. Peabody DS: **Role of the coat protein-RNA interaction in the life cycle of the bacteriophage MS2.** *Mol Gen Genet* 1997, **254**:358-364.

doi:10.1186/1471-2105-14-S10-S8
Cite this article as: Chowdhury *et al.*: Cell segmentation by multi-resolution analysis and maximum likelihood estimation (MAMLE). *BMC Bioinformatics* 2013 **14**(Suppl 10):S8.

Publication III

P. Ruusuvuori, T. Äijö, S. Chowdhury, C. Garmendia-Torres, J. Selinummi, M. Birbaumer, A.M. Dudley, L. Pelkmans, and O. Yli-Harja, "Evaluation of methods for detection of fluorescence labeled subcellular objects in microscope images," *BMC Bioinformatics*, 11:248, May 2010.

Ruusuvuori *et al. BMC Bioinformatics* 2010, **11**:248
http://www.biomedcentral.com/1471-2105/11/248

BMC Bioinformatics

RESEARCH ARTICLE Open Access

Evaluation of methods for detection of fluorescence labeled subcellular objects in microscope images

Pekka Ruusuvuori*[1], Tarmo Äijö[1], Sharif Chowdhury[1], Cecilia Garmendia-Torres[2], Jyrki Selinummi[1], Mirko Birbaumer[3], Aimée M Dudley[2], Lucas Pelkmans[3] and Olli Yli-Harja[1]

Abstract

Background: Several algorithms have been proposed for detecting fluorescently labeled subcellular objects in microscope images. Many of these algorithms have been designed for specific tasks and validated with limited image data. But despite the potential of using extensive comparisons between algorithms to provide useful information to guide method selection and thus more accurate results, relatively few studies have been performed.

Results: To better understand algorithm performance under different conditions, we have carried out a comparative study including eleven spot detection or segmentation algorithms from various application fields. We used microscope images from well plate experiments with a human osteosarcoma cell line and frames from image stacks of yeast cells in different focal planes. These experimentally derived images permit a comparison of method performance in realistic situations where the number of objects varies within image set. We also used simulated microscope images in order to compare the methods and validate them against a ground truth reference result. Our study finds major differences in the performance of different algorithms, in terms of both object counts and segmentation accuracies.

Conclusions: These results suggest that the selection of detection algorithms for image based screens should be done carefully and take into account different conditions, such as the possibility of acquiring empty images or images with very few spots. Our inclusion of methods that have not been used before in this context broadens the set of available detection methods and compares them against the current state-of-the-art methods for subcellular particle detection.

Background

Recent advances in cell imaging technologies include accurate stage controllers, improved optics, increased camera resolution, and, perhaps most importantly, fluorescent staining of specific cellular components. Together these advances enable automated image acquisition of small subcellular objects with the goal of providing insight into phenotypes and cellular functions [1-4]. With increased imaging throughput and large-scale data acquisition, the challenge of image interpretation and information extraction has also shifted from visual inspection or interactive analysis to more automated methods [5,6].

Accurate and automated subcellular object segmentation is essential for a variety of applications. For example, interpreting complex cellular phenotypes is typically dependent on identifying and quantifying various parameters associated with small organelles, setting high requirements for the accuracy of the image analysis [7]. Also the analysis of cellular structures based on 3D images obtained with fluorescence and confocal microscopes requires accurate detection. Advances in such methods will improve our ability to model small organelles in 3D [8]. Further, live-cell imaging with specific molecular probes has brought image tracking to subcellular level, and thus reliable object detection over the course of the imaging period adds a temporal dimension to image analysis [9,10].

A variety of subcellular object detection methods have been described in the literature (examples are listed in Table 1). Due to the specific applications they have been designed for, the algorithms are usually very problem-

* Correspondence: pekka.ruusuvuori@tut.fi
[1] Department of Signal Processing, Tampere University of Technology, P.O.Box 553, Tampere, 33101, Finland
Full list of author information is available at the end of the article

Table 1: Summary of methods.

Algorithm	Description	Free parameters
Band-pass filtering (BPF)	Object intensity enhancement with bandpass FIR filtering	4
Feature point detection (FPD) [9]	Percentile detection with non-particle discrimination	3
h-dome detection (HD) [16]	h-dome morphological filtering	5
Kernel methods (KDE) [21]	Kernel density estimation with a family of kernels	3
Local comparison (LC)	Maximization between direction-specific image convolutions	2
Locally enhancing filtering (LEF)	Local signal enhancement and background suppression	1
Morphometry (MGI) [23]	Morphometry with granulometric analysis	0
Multiscale wavelets (MW) [26]	Multiscale product of wavelet coefficients	2
Source Extractor (SE) [27]	Convolution applied for background clipped image	4
Sub-pixel localization (SPL) [10]	Fitting of Gaussian kernels to local intensity maxima	1
Top-hat filtering (THE) [29]	Top-hat filtering and entropy-based thresholding	1

Summary of methods, with method abbreviation used in this study and short description of main principle. The number of free parameters refers to the parameters that were tuned when optimizing the methods for the image sets.

specific. However, it is rare to see choice of a detection method based on experimental thorough testing under a variety of conditions or comparisons against other previously proposed spot detection methods. Rather, it is still common to use naïve comparisons of particle detection algorithms against histogram thresholding methods applied on intensity information. For example, Otsu's thresholding [11], which seeks to maximize between-class variance, is widely applied as a reference method. However, for the segmentation of small spots in the presence of relatively high background fluorescence global thresholding approaches usually fail. Thus, comparative studies of the performance of subcellular object detection methods under a variety of different conditions are needed.

Evaluating the performance of image segmentation algorithms has been a long-standing challenge. Validating segmentation results usually requires a ground-truth reference, and in biomedical applications the task of generating such reference falls to an expert biologist. This burdensome and error-prone strategy becomes even more challenging when evaluating small, but numerous subcellular organelles, particularly in the context of high-throughput experiments. In these cases, common limitations in the focus, contrast and resolution of the images render reliable pixel-level outlining of objects nearly impossible. Alternative evaluation methods include the use of computer-generated images for direct comparisons to ground truth results, experimentally derived control vs. test samples, and evaluations that measure performance as a function of an input stimulus that enable indirect comparisons between different conditions. Recently, benchmark image collections of cells and other types of biological samples have been developed to facilitate comparison and validation of image analysis methods [12-14].

In this study, we compare the performance of several algorithms for finding subcellular objects (i.e. small, bright spots) in fluorescence microscopy images. The algorithms employ various approaches for segmenting small structures, all aimed at detecting spot-like local intensity peaks, as opposed to the general separation of signal from background that is common in cell segmentation. We also propose an objective and comprehensive approach for evaluating algorithms for small particle detection. We use indirect comparisons with high-throughput well plate data, comparisons against manually scored objects in frames of 3D image stacks, and pixel-level comparisons against ground truth results in simulated images.

Importantly, our comparison study takes into account various situations, such as cases where a part of spots are severely blurred, emulating the typical situations of out-of-focus and diffraction limited appearance. Our comparison also considered cell heterogeneity (in this case images with varying number of spots), a factor commonly encountered in high throughput screening assays. In such case, the detection algorithms must be able to cope both with a range of conditions, such as cells ranging from low to high spot concentration in cells. Especially in high-throughput settings, tuning of parameters needs to be done for the whole screen, not for individual images.

Recently, a comparative study of nine commonly used spot detection methods has been published [15,16]. Here, we expand the set of methods evaluated while also taking into account the results in [15,16] by including the top-performing unsupervised method in our study. Further, our study covers a wide set of usage scenarios by applying

three different image sets, providing a set of methods tested in various conditions, including methods that have not been used in the context of subcellular object detection before. The set of methods serves also as a resource for developers of novel particle detection algorithms, enabling more reasonable and informative comparison than histogram thresholding of intensity values.

Methods

Methods for detecting subcellular objects

A set of eleven algorithms covering a wide range of techniques for spot detection was selected for this study. Our selection includes eight previously published methods that were initially developed for applications other than subcellular spot detection. In addition, we formulate three filtering-based methods that, to the best of our knowledge, have not been previously applied to subcellular object detection. The detection of small subcellular particles from images can be divided into three phases [16]: First, an optional preprocessing phase can be used to reduce noise and to attenuate objects of a desired shape or size. Due to limitations in imaging technology, an accurate representation of the biological sample can be degraded by several error sources, resulting in a noisy observation of the underlying object. To decrease the effect of these errors, an optional low-pass filtering phase for noise suppression can be applied, and here the linear low pass filtering has been applied depending on whether the method has been observed to suffer from false detections due to background noise and the choice has been made through testing separately for each image set and method. We leave, however, experimenting with various preprocessing methods out of the scope of this article. Next, signal enhancement may be used to make the desired objects more easily detectable than they were in the original image. Many of the methods studied here involve user-definable parameters for controlling this phase. We use grid-search for tuning such parameters (described below). Finally, the actual detection is obtained by thresholding the enhanced signal. Because we do not consider segmentation threshold as a parameter for the detection methods unless it has been defined as such in method description, the presented methods derive the detection result automatically based on heuristics rather than stepping through multiple threshold levels. As a result, our comparison shows the results as given by the methods after tuning their parameters in a grid-search manner, not after fixing the operation point by tuning the segmentation threshold. In this way, the methods can be compared based on their performance when operating in a fully automated manner.

The large number and wide variety of methods designed for intensity detection in different image analysis applications preclude an analysis of all possible methods described in the literature. We chose to exclude methods relying on statistical learning, such as in [17], to avoid the problem of selecting training data. We also left of methods relying on pure intensity thresholding, since they are are likely to perform poorly due to non-uniform background and staining in the cell bodies. However, our selection does cover a variety of different approaches, which are relatively comparable in terms of accuracy and processing time. The selected algorithms are listed in Table 1 with a brief note on their operation principle and the abbreviations of their names used throughout the manuscript. Below is a more detailed description of each algorithm.

Band-pass filtering

In this method we formalize a detection method based on band-pass filtering (BPF). Here the image is band-pass filtered using a filter with transfer function H in a frequency domain that produces an image in which the objects of interest are emphasized. In addition to emphasizing the objects, the band-pass filter can be used to suppress the presence of noise, e.g. shot noise can be taken out by filtering the high-frequency components.

The filter H is designed such that the normalized cut-off frequencies are $0 < \omega_{s_1} < \omega_{p_1} < \omega_{p_2} < \omega_{s_2} < 1$. Because the choice of cut-off frequencies is not a straightforward task from the spatial domain, it is advisable to consider the spectrum while choosing the desired band-passes. After filtering, Otsu's method [11] is used to automatically obtain a threshold value th for binarizing the band-pass filtered image. Thus, the four cut-off frequencies are the only user-defined variables.

Feature point detection

The feature point detection (FPD) algorithm proposed as a part of a tracking framework in [9] was originally designed for colloidal studies in [18]. The algorithm first reduces background effects in an image restoration step by box-car average estimation, and simultaneously enhances spot-like structures by convolving with a Gaussian kernel [9]. More formally, the convolution kernel is given as

$$K^w(i,j) = \frac{1}{K_0^w}\left[\frac{1}{B}\exp\left(-\frac{i^2+j^2}{4\lambda_n^2}\right) - \frac{1}{(2w+1)^2}\right], \quad (1)$$

where K_0^w and B are normalization constants, λ_n defines the Gaussian kernel width, and w is a user-tunable

kernel window size [9]. Thus, the filtered image after the convolution with $K^w(i, j)$ is given as

$$\hat{f}(x, y) = \sum_{i=-w}^{w} \sum_{j=-w}^{w} f(x - i, y - j) K^w(i, j), \quad (2)$$

where $f(x, y)$ is the original image, (x, y) and (i, j) are pixel coordinates in the image and kernel, respectively.

The initial point locations are then estimated by finding local intensity maxima. A point is considered to be a local maximum if it has the highest intensity within a local window, and the intensity value falls within the r highest percentile. The algorithm then proceeds by refining the point locations. Finally, all detected points are subjected to non-particle discrimination in the zeroth and second order intensity moment space, where a user-defined threshold T_s controls the discrimination. A detailed description of the discrimination step can be found in [9]. Thus, the percentile threshold, the discrimination threshold, and the window size parameter (related to the particle size) are the three free parameters for FPD in this study. We note that one feature of the applied FPD implementation is that it was used for giving the object locations as an output instead of a segmentation result. As a result, detection of an object can be evaluated but direct comparison of the segmentation result is not done here.

h-dome transform

The morphological h-dome transform (HD) [19] has been applied to subcellular object detection in a tracking context [20]. Smal et al. [15,16] reported the best results among unsupervised object detectors were achieved with the h-dome transform based detector. The h-dome detector, according to [16], assumes that the image is formed by N_o objects of interest, heterogeneous background structures and intensity distribution $B(i, j)$, and a noise term $\eta(i, j)$. The aim of the method is to estimate the number of objects N_o and the object locations in image.

Briefly, the h-dome detection method as presented in [16] proceeds as follows. First, the input image $f(i, j)$ is LoG filtered to obtain a background subtracted image $\hat{f}$, where spots are enhanced. Filtering is controlled by a parameter σ_L which defines the scale. Next, a grayscale reconstruction of the filtered image is created using a mask $\hat{f}(i, j) - h$, where $h > 0$. Thus, the image decomposition is given as

$$I_\sigma(i, j) = H_\sigma(i, j) + B_\sigma(i, j) \quad (3)$$

where H_σ contains the small objects, the grayscale reconstruction B_σ represents larger background structures, and intensities of height h are cut-off from the top. The h-dome transformed image H_σ, where the bright objects should all have an intensity value of h, is used as a probability map for sampling and where pixel values of H_σ are raised to the power of s. The map H_σ^s reveals areas that are likely to contain spots. After sampling, the samples are divided into clusters using the mean-shift algorithm. Using the mean value and variance of each cluster, the samples are divided into real objects and other structures, while the parameter σ_M controls the maximum allowed size for an object of interest. Details about sampling and object discrimination can be found in [16]. Overall the h-dome transformation based method has several parameters that need to be tuned based on the data in order to obtain useful results. As reported in [15,16], the method is a very powerful detector when the parameters are tuned reasonably and when the data supports the assumptions made by the model.

Kernel density estimation

A segmentation algorithm based on the use of kernel density estimation (KDE) is presented in detail in [21], this method is also known as the Parzen window method. Briefly, the method estimates the probability density function over the image by combining local information. The estimation step results in a smoothed version of the original image where the effect of noise is suppressed.

The method processes the image f by filtering it with a desired kernel in a circular window placed in coordinate (i, j) as follows:

$$\hat{f}(i, j) = \frac{1}{\mathrm{card}(\mathcal{C}(i, j))h} \sum_{(k,l)\in\mathcal{C}(i,j)} K\left(\frac{f(i, j) - f(k, l)}{h}\right) \quad (4)$$

where h is the smoothing parameter, (k, l) denotes pixel coordinate inside kernel, card is the cardinality of the set, and the kernel $K(u)$ could be, e.g., uniform $K(u) = \frac{1}{2}[|u| \leq 1]$. Other implemented kernels are Gaussian, Epanechnikov, triangle, quartic, triweight and cosine [22]. Finally, Otsu's method [11] is used to obtain a binarized version

of the original image. In this method there are three parameters that can be set by the user: the radius R, the smoothing parameter h and the kernel. However, the choice of the kernel used is not crucial [21] to the result.

Local comparison and selection

The local comparison and selection (LC) algorithm is a novel method for subcellular object detection. LC uses multiple spatial filters and performs comparison between their outputs. First, we start with a circular filter h of the radius R, which is then separated into four quarters: h_{NE}, h_{SE}, h_{SW}, h_{NW}. For example, with filter h_{NE} coefficients, the other three quarters are set to zero, as is shown for the example filters in Figure 1. Due to this choice of separation of the sub-filters, the method might have difficulties detecting objects with complex shapes, e.g. cones or curly objects.

The original image f is filtered with the four filters in order to obtain spatial information from four directions around each pixel, giving insight into whether a specific pixel is part of an object or not. The binary output image is obtained by comparing the maximum pixel value from the filtered images to the original pixel value scaled by the factor α at each image coordinate (i, j). Formally, the binary image bw is defined at pixel location (i, j) as

$$\mathrm{bw}_{i,j} = \begin{cases} 1 & \text{if } \max\left\{ \hat{f}_{ij}^{NE}, \hat{f}_{ij}^{SE}, \hat{f}_{ij}^{SW}, \hat{f}_{ij}^{NW} \right\} > \alpha f_{ij} \\ 0 & \text{otherwise} \end{cases} \quad (5)$$

where $\hat{f}_{i,j}^{NE}$ is the image filtered with the kernel at direction NE (and similarly for the other directions). The filtering directions are illustrated in Figure 1. Hence, the user-definable parameters are the radius R which relates to the object size, and the scaling factor α which can be used for tuning the segmentation threshold. By using the aforementioned binarization method one can take into account the possibility of non-uniform background, i.e., object presence is decided based on the local features.

Local spot enhancement filtering

Local enhancement filtering (LEF) is another novel method for subcellular object detection. LEF is based on a matched filter that enhances spot-like structures and suppresses background intensity. The method starts by scaling the average intensity of the image into a predefined mean, thereby reducing the effect of global intensity differences between images. The square filtering kernel H that is used for matched filtering is defined in two parts. First, the inner part is a circular support area $\mathcal{C}(i, j)$ that enhances local intensity peaks. Second, the area in square kernel that is left outside the circular area $(\mathcal{S}(i, j))$ is used for suppressing the background by division. Thus, the filtering operation for pixel coordinate (i, j) can be expressed as follows

$$\hat{f}(i,j) = \frac{\Sigma_{(k,l)\in\mathcal{C}(i,j)} f(k,l)}{\Sigma_{(m,n)\in\mathcal{S}(i,j)} f(m,n)}, \quad (6)$$

where the filtering provides a so-called spot likelihood image $\hat{f}$ that needs to be thresholded. The thresholding, performed by the product of the sensitivity threshold and the standard deviation of the spot likelihood image ($th_s \times \sigma_{\hat{f}}$) provides the final detection result. The division of the kernel area into inner and outer areas is not limited

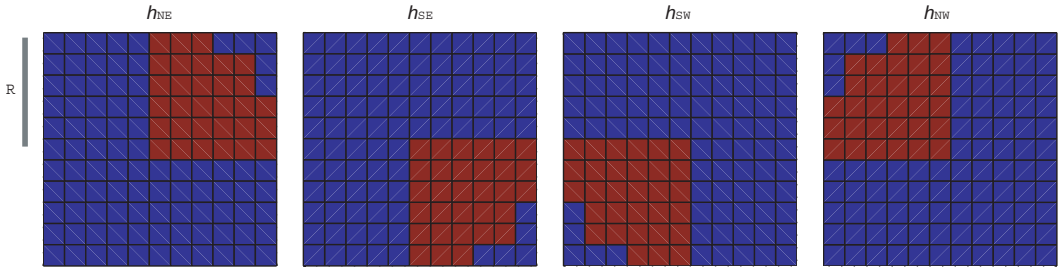

Figure 1 Direction-specific filters h_{NE}, h_{SE}, h_{SW}, and h_{NW} for the local comparison method. Red pixels show the area that is taken into account around each filtering position (i, j). Here the radius R is set to 5.

and it could be done based on assumed objects shape, enabling adjustments based on prior knowledge about the objects of interest. In this study, we keep the kernel fixed in order to avoid additional parameter tuning. In this case, the weighting parameter th_s for thresholding is the only free parameter.

Morphometry based on granulometric analysis

The morphometry method for spot detection, abbreviated here as MGI, is adapted from [23] where automated morphometry was proposed for the quantification of synaptic boutons in neurons. The automated morphometry is based on granulometric analysis. The method first calculates granulometry by using morphology with varying disc sizes d, yielding a so-called granulometric index, or size density, $G(d)$ [23-25]. The granulometric index is then used to select the scale of interest, which in our case involved automatically choosing the two highest peaks in $G(d)$, denoted as d_{low} and d_{high}. Choosing the scale of interest is critical for the outcome, but for compatibility with high-throughput analysis, we chose to automate the scale selection. The scale of interest is used for constructing the corresponding opening images $I_{low} = I \circ E(d_{low})$ and $I_{high} = I \circ E(d_{high})$, where $\circ$ means grayscale opening and E is the disk-shape structuring element. Subtracting I_{high} and I_{low}gives the image where the structures of the desired scale should be present. Further, the structures of interest are extracted by masking with binary image obtained with k-means clustering. Finally, integral thresholding [23] gives the particle detection result within the area that was masked with k-means clustering. Notably, we used our version of the automated morphometry algorithm with default parameters, requiring no parameter tuning.

Multiscale product of wavelet coefficients

Detection based on the multiscale product of wavelet coefficients (MW) was presented in [26]. This method extracts bright spots by calculating the products between different support scales of the à trous wavelet transform. Briefly, the algorithm is based on the assumption that, unlike noise or large objects, spots will be present at each scale of the wavelet decomposition, and thus will appear in the multiscale product. The MW method is adapted from [26], where the wavelet representation is obtained as a separable B3-spline wavelet transform by convolving the image $A_0(x, y)$ column by column and row by row with a [1/16, 1/4, 3/8, 1/4, 1/16] kernel, resulting in a smoothed image $A_1(x, y)$. The corresponding wavelet layer is given as $W_1(x, y) = A_0(x, y) - A_1(x, y)$. The convolution is then repeated recursively J times, augmenting the kernel at each step i by padding $2^{i-1} - 1$ zeros between the kernel coefficients. By reaching level J in recursion a total of $J + 1$ images are obtained and are used to construct the wavelet representation $W = W_1,..., W_J, A_J$ of the original image, where $W_i(x, y) = A_{i-1}(x, y)-A_i(x, y)$, and $1 < i < J$. Spot detection is based on the pixelwise multiscale product of the reconstruction layers W_i, defined for pixel position (x, y) as follows:

$$P_J(x, y) = \prod_{i=1}^{J} W_i(x, y), \tag{7}$$

where J denotes the scales. To repress noise, the wavelet coefficients are thresholded prior to multiplication. Here, we use the hard thresholding scheme proposed in [26], where the threshold is given as $3 \times \sigma_i$, and σ_i is estimated to be $\mathrm{MAD}(W_i)/0.67$. The heuristics for choosing the actual objects from the multiscale product include thresholding according to a user-specified detection level. In this study, we use the number of scales J and the detection level l_d as free parameters.

Source extractor

Unlike most filtering methods examined in this study, SourceExtractor (SE) [27] estimates the background in blocks and removes it before filtering with a Gaussian kernel. Background removal is also performed in blocks, the size of which is controlled here by a user-definable parameter. The background estimate is achieved by clipping the intensity histogram at both ends until the histogram converges at three standard deviations around the median. When the standard deviation is changed by less than 20% during the clipping process, the mean is taken to be the background intensity. Otherwise, the background is estimated to be BG = 2.5 × Median - 1.5 × Mean. Pixelwise, the background estimate is then obtained by interpolating the blockwise background estimates.

After filtering, the result is thresholded to provide an initial estimate of the objects. In our implementation, we use two scaling parameters to control the thresholding: th_{detect} for scaling the standard deviation of background subtracted intensities and th_{BG} for scaling the background removal. Thus, the thresholding is defined as:

$$\mathrm{bw}_{i,j} = \begin{cases} 1 & \text{if } f_{ij} > (th_{\mathrm{BG}} \times \mathrm{BG}(i, j) + th_{\mathrm{detect}} \times \sigma(i, j)) \\ 0 & \text{otherwise,} \end{cases} \tag{8}$$

where BG is the estimate for the background, σ is standard deviation of the intensity, f is the input image, and bw gives the binary detection result, each defined here in pixel location (i, j). By setting $th_{\mathrm{BG}} = 0$, the version given in [27] is obtained. The detected objects, i.e. the areas in the intensity image under the connected components in

the binary image bw, are then processed further in the deblending phase, where possible overlapping sources are separated. Briefly, the deblending proceeds by splitting the detected object into 30 slices inside the intensity range (from the detection threshold to the highest intensity peak) of the object. Starting with the highest intensity peaks, the algorithm takes each slice and determines whether two branches originating from different intensity peaks within the same object should be separated as different objects. The deblending algorithm considers the integrated pixel intensity of the branch relative to the total integrated intensity of the detected object as a basis for determining the separation, as explained in [27].

The original application area of Source Extractor is as far from subcellular object detection as possible; it was designed for analysis of galaxy-survey data [27]. Though the method has been widely applied across many disciplines, to the best of our knowledge, its use in subcellular spot detection has not been reported. The applicability of Source Extractor in the analysis of subcellular structures underscores the generality of the problem of finding bright spots within images.

Sub-pixel location detection

The detection method in [10] was used for defining subpixel locations (SPL) of single molecules in low SNR (signal-to-noise ratio) images. The detection, though originally intended to be used in tracking, can be used as an independent module for identifying spots. The algorithm detects local intensity maxima by comparing to neighboring pixel intensities and the standard deviation of the local background. In [10], temporal averaging is used to reduce intensity variation prior to detection. However, we omitted the time averaging step since it is only applicable in the context of time-lapse imaging.

The method proceeds as follows. Within a window, the central pixel is chosen to be a potential spot if it is brighter than its surrounding pixels. The initial detection is further controlled by testing against the standard deviation of the local background. A user-defined parameter α, the only free parameter for SPL used in this study, controls the local maxima detection. This parameter defines the limit for type I errors in the initial local maxima detection. Sub-pixel locations are estimated for the local maxima that pass the criteria by fitting a 2D Gaussian kernel iteratively as described in [10,28]. Like the feature point detection method, we use SPL only for estimating the locations of detected spots, therefore it can be used to count the number of spots and for object-level comparisons, but not for pixel-level evaluation.

Top-hat filtering by grayscale morphological opening

The grayscale morphological top-hat filtering [25,29] acts as a local background removal function, simultaneously enhancing round, spot-like structures. Here we combine top-hat filtering and automated thresholding to form a spot detection method, abbreviated as THE. Essentially, the filtering phase performs grayscale opening with a flat disk-shaped structuring element E of radius r and subtracts it from the original image f. More formally, the top-hat filtering result is given as $f_{\text{diff}} = f - f \circ E(r)$, where $\circ$ denotes grayscale opening. In the filtering result, the objects roughly of size determined by r should be enhanced, and background removed.

The resulting image f_{diff} needs to be thresholded in order to obtain a binary mask for spots. We tested several histogram-based segmentation methods [30,31], and applied an entropy-based thresholding [32] which produced slightly more conservative values for images with spots than many other thresholding methods. Thus, instead of parameterizing the detection threshold or applying any post-segmentation constraints, we use top-hat filtering in a more automated manner, which requires considerably less parameter tuning.

Data

Simulated experiments

The most natural way of comparing segmentation algorithms is by a pixelwise comparison. However, constructing a reference segmentation in which all of the pixels belong to biologically meaningful small spots would be difficult. Creating a reliable and representative reference result is difficult because, on the one hand, it is extremely tedious to manually analyze a large number of spots in a reliable manner, and on the other hand, analyzing a relatively small number of spots is statistically inadequate. Thus, to enable pixelwise comparisons against a reference result, we used simulated experiments published previously as a benchmark set in [12].

The simulated image set, generated by using the SIMCEP cell image simulation framework [33,34], consists of 20 images with nuclei, cytoplasmic areas, and subcellular objects each having their own channel in the RGB image. Noise, i.e. intensity variations in cell texture, and blurring for out-of-focus objects are also introduced in the simulation process [34] in order to give the simulated images some level of error akin to that encountered in experimentally derived images. Prior to the analysis, the images are converted to grayscale using the standard conversion of $0.2989 \times R + 0.5870 \times G + 0.1140 \times B$. After this conversion, subcellular objects in the grayscale images have slightly higher intensities than their surroundings.

Frames from image stacks of yeast cells

The second data set contains frames from image stacks obtained with wide-field imaging. The objects are P-bodies, visualized by Edc3 protein fused to green fluorescent protein (using a strain created by Huh, et al., [35]). Stacks of 28 frames along the z-axis (every 0.3 μm) were acquired using a Leica DMGI 6000B microscope equipped with motorized X-Y stage, a high quantum effi-

ciency cooled back-illuminated Qimaging Rolera-MGi CCD camera, and integrated software control (BD Bioscience Bioimaging IPLab). The images were acquired under oil using a 63× objective/1.40 NA Plan APO oil lens.

Stacks usually consist of a set of frames starting with images in which the objects of interest are not yet in focus. As the microscope scans through the sample in the Z plane, objects come in focus, appear in a set of frames, and then vanish as the scanning proceeds past the object's focus area. The implication for the analysis task is that the spot detection methods must be able to detect objects only in the in-focus frames. We selected seven stacks of images and from each stack chose four frames such that one frame is empty (only out-of-focus objects are in the image and no P-bodies are marked in the reference result) and three frames with varying number of P-bodies that are present and in focus. In total, 28 frames are used in this study.

For the selected frames a reference result was manually determined by two observers. In order to limit the number of comparisons we chose to combine the results from two observers such that we included all spots in our reference. Due to the small spot size and the noisy appearance of the wide-field microscope image, the objects are marked with a fixed-size spot but the area is not outlined in detail. As a consequence, the manual reference result can be used for object level comparison, i.e. to assess whether an object is found or not, but not as a pixel-level ground truth result.

Well plate experiments of a human osteosarcoma cell line

A major application of bright spot detection of subcellular organelles is in high-throughput screening, where for example the effects of gene knock-outs or differences in responses to varying dose levels of a particular stimulus are of interest. To test the ability of the various methods to detect differences in populations of cells stimulated with different doses of a drug, we used the SBS CompuCyte Transfluor image set provided by Dr. Ilya Ravkin and available from the Broad Bioimage Benchmark Collection [13]. The images are of a human osteosarcoma cell line. The image set consists of a portion of a 96-well plate containing 3 replica rows and 12 different concentrations of isoproterenol. Importantly, stimulation with different doses of isoproterenol affects the appearance of small vesicle-like spots. There are four acquired fields per well, resulting in 144 total images. The image set also contains specific staining for nuclei, which we used to determine the number of cells per image. Thus, the outcome of the analysis is an assessment of the average number of vesicles per cell in each image, with the images grouped by dose level. These results can be used for indirectly comparing different methods, since no ground truth information for the vesicles is available.

Performance evaluation metrics

Several metrics for performance evaluation exist when reference result, for example object number and locations are known [36,37]. For measuring the accuracy of detection algorithms, we chose the following commonly applied metrics.

First, a true positive (TP) is defined as a correctly found object, and a false positive (FP) is a detected object for which there is no match in the reference image. A false negative (FN) corresponds to a missing object in the detection result. The same definitions may also be applied for pixel-level analysis. In accordance with [36], we define precision p (also noted as positive predictive value) as

$$p = \frac{\mathrm{TP}}{\mathrm{TP}+\mathrm{FP}}, \tag{9}$$

and recall r (also noted as sensitivity) as

$$r = \frac{\mathrm{TP}}{\mathrm{TP}+\mathrm{FN}}. \tag{10}$$

By intuition, detecting objects where no true objects exist is penalized in p, whereas failure to detect true objects is penalized in r.

Furthermore, the F-score can be obtained as a harmonic mean of precision and recall [36],

$$\frac{2pr}{p+r}. \tag{11}$$

The F-score combines precision and recall as a single measure of segmentation accuracy, making it a useful parameter for evaluation purposes.

Results and Discussion

Parameter optimization

Many of the detection methods proposed in the literature incorporate one or more parameters which can be tuned to enable detection in different situations. The methods proposed in this study also require user-defined values for input parameters. In spot detection, parameters typically provide information about object size (e.g. LC, BPF, THE, HD) and probability (FPD), permit tuning of the detection threshold (LC, KDE, LEF), or specify the applied option within a family of methods (such as in KDE). Because the parameter values have a significant effect on the detection accuracy and need to be tuned specifically for the applied data, we performed parameter optimization for the two datasets with ground truth references and recall r (also noted as sensitivity) as by sampling the parameter space in a grid search manner. By using the F-score described in Equation 11 as a measure of detecting performance, the grid-search can be used to

tune the parameters optimally within the search space for the applied data. The results of parameter tuning for the simulated data and for yeast image stack data are shown in Figure 2 and Figure 3, respectively. We note that for methods with more that two free parameters, we have chosen two for visualization purposes, and a grid search was carried out to identify the optimal combination of the remaining parameters to construct the images shown.

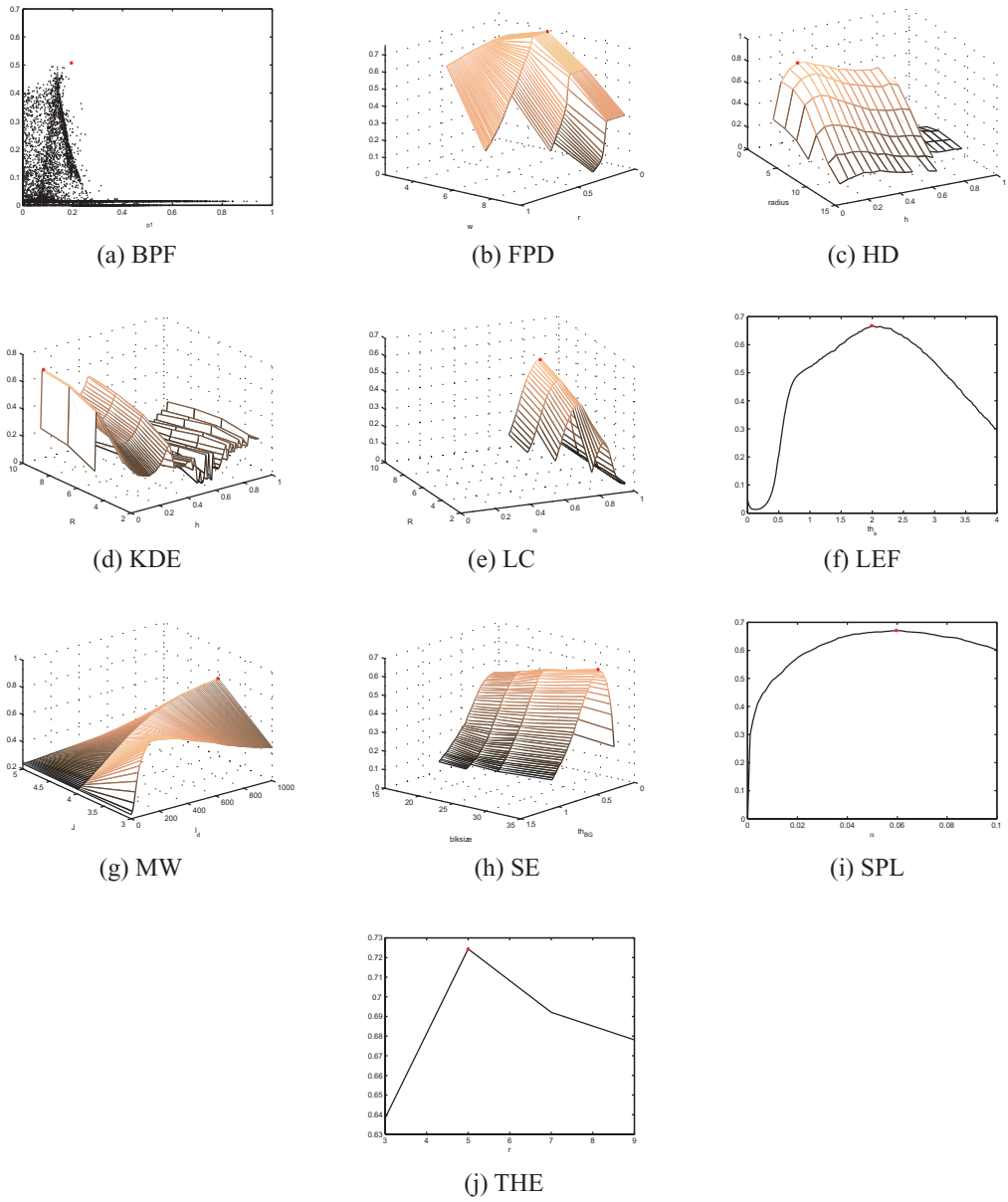

Figure 2 Parameter tuning for spot detection methods was performed in exhaustive grid search manner using F-score as the measure of detection accuracy. The optimal settings within the search space (yielding maximum F-score) are shown with a red dot.

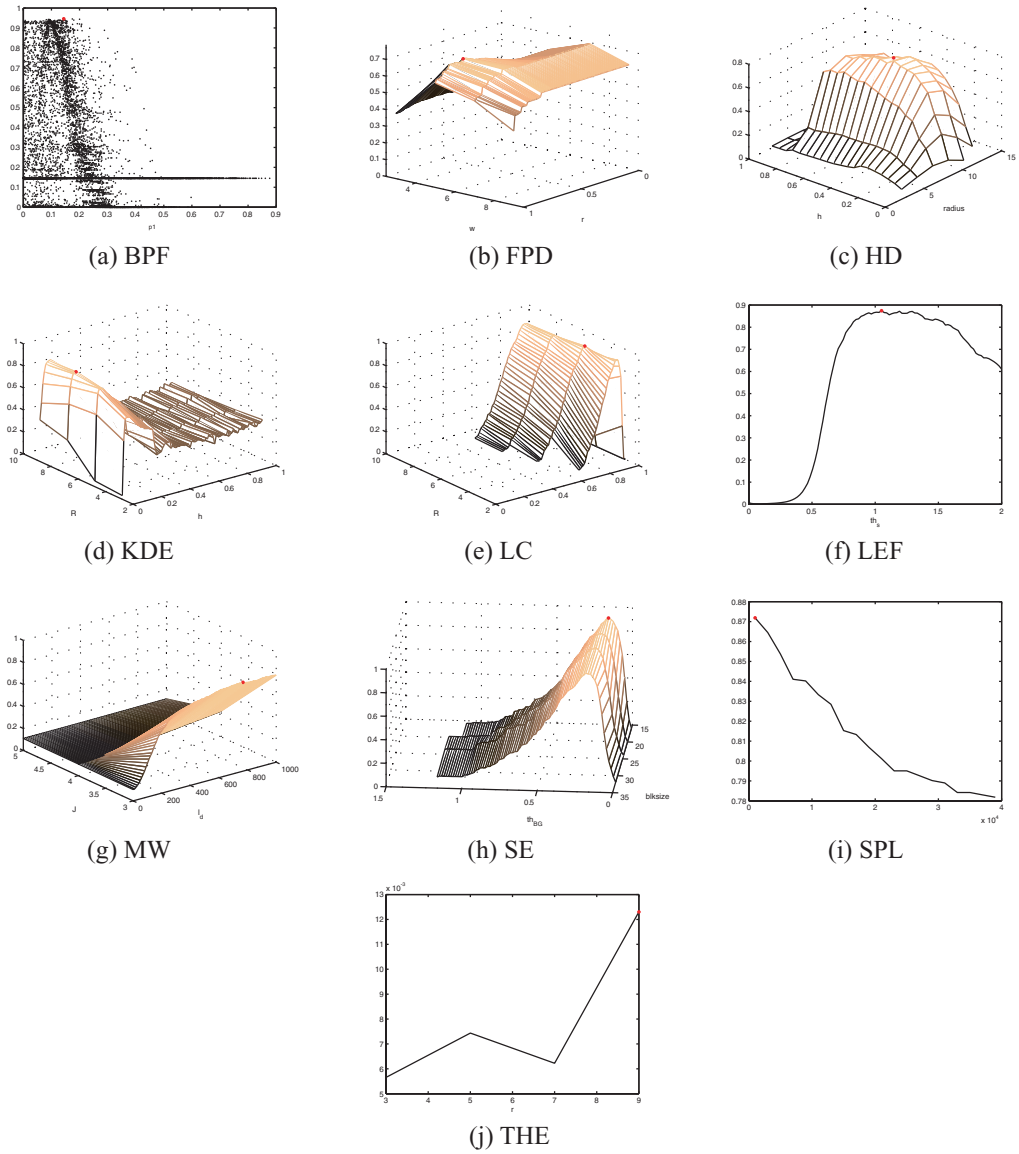

Figure 3 Parameter tuning results for yeast image stacks. Red dot denotes the result with optimal parameter settings within the search space for the applied data.

The detection accuracies as a function of all free parameters can be found in the supplementary materials. To facilitate an objective comparison of these methods, we used of a common measure (F-score), which is optimized within the parameter ranges. The results obtained represent the best possible result within the input parameter space. The parameter tuning results in Figure 2 and 3 also provide information about the sensitivity to changes in parameter values, which may be useful when tuning methods to new data. The grid search approach also solves the difficult problem of parameter tuning, with the cost of exhaustive computations requiring large amounts

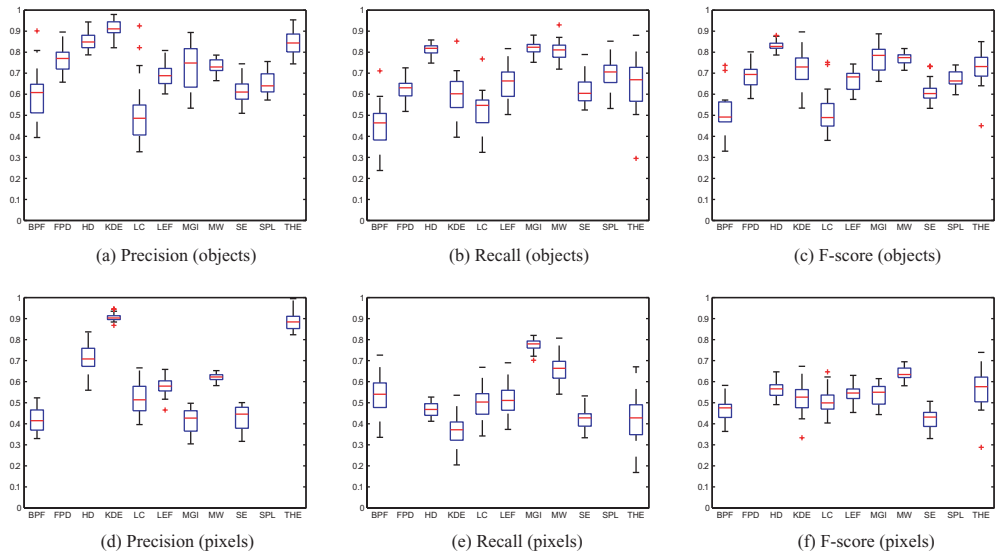

Figure 4 Precision, recall, and F-score are calculated using computer-generated ground truth as reference at object level (a-c) and pixel level (d-f). Note that the two algorithms (FPD and SPL) are omitted from pixel-level comparison in d-f.

of processor time. Although parameter tuning can be accomplished by performing the calculations in parallel on a grid-computer network (as was done in this study), the problem of setting the value range and sampling the parameters remains. For some parameters, such as those related to object size, reasonable value ranges may be set intuitively. The fact that many parameters are natural numbers makes the process easier. However, real-valued parameters, such as probabilities and tuning factors need to be sampled more densely and their dynamics is less predictable. For example, the size of the structuring element can be defined by testing with a few values (Figure 2i and 3i), whereas the significance value α needs to be sampled more densely (Figure 2h and 3h). Furthermore, parameter sampling when parameters depend on each other becomes even more challenging. As an example, the parameters of BPF defining the pass band need to be in increasing order, leading to sparse point-cloud type sampling (Figure 2a and 3a) instead of a smooth curve or surface.

Allowing the user to tune many parameters leads to a highly adaptable method, but also requires considerable effort to ensure reasonable (or ideally optimal) performance. Thus, the calculation times for the optimization procedures vary greatly between methods. While a detailed discussion of the effect of each parameter for the 11 methods is beyond the scope of this article, we offer a list of parameters for each method along with the applied ranges in the supplementary materials. Lastly, we note that by tuning different parameters than the ones in this study, and by adding more parameters to the methods, the methods may be further customized for analysis tasks.

Results for simulated images with pixel-level reference

First, we consider the validation of algorithm performance with simulated images in which the noise-level and other image characteristics are known. In this case, we calculated the number of objects detected in the 20 images by each method and determined whether the differences between object counts were significant, using the non-parametric Kruskal-Wallis test of whether the medians of multiple groups are equal. Our results suggest that detection results do infact differ significantly ($p \sim 0$ while $p < 0.01$ was considered statistically significant). Wilcoxon rank sum tests between result pairs further support this claim by showing that most of the results do not have the same median.

For synthetic images the comparison can be made at both the pixel-level, which is perhaps the most natural way of defining segmentation accuracy, and at the object level, as was done for the wide-field microscope images. The object level comparison for the set of 20 simulated images is presented in Figure 4a-c, and the corresponding pixelwise comparison is presented in Figure 4d-f. We note that two of the methods, namely FPD and SPL, cannot be included in pixel-level comparison because they were used for estimating spot locations instead of seg-

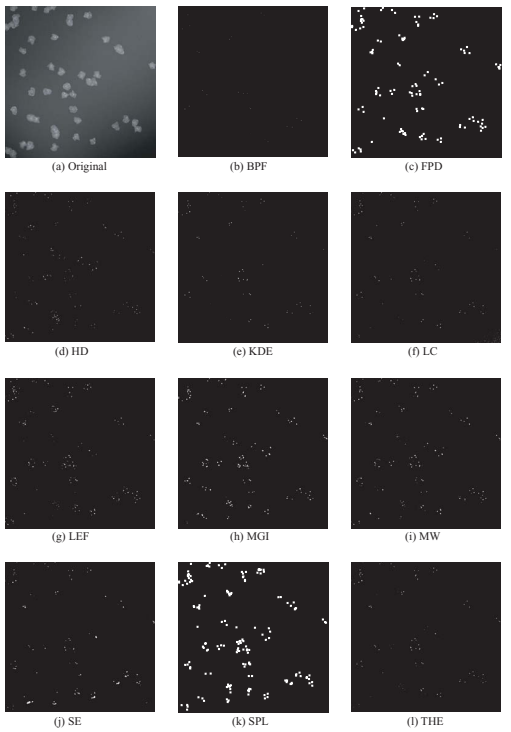

Figure 5 Examples of detection results for a simulated image. Note that for FDP and SPL, the detection has been visualized as a cross centered in the detected point. For others, the result is shown as a binary segmentation mask.

menting objects. The results in this article are calculated for the low quality simulated image set (described in [12]).

In the pixel-level comparison none of the methods stand out with superior accuracy, although MW received a slightly better F-score value than the other algorithms. For object-level comparison, HD had the most accurate F-score, followed by MGI and MW. In considering the relationship between method performance at the pixel and object levels, clearly there is some level of correlation between the two sets of results. Intuition would suggest that it is easier to merely detect an object than it is to define its area accurately. Consistent with this view, the pixelwise results are generally lower than the object level results. The relatively subtle differences in the pixel-level results Figure 4d-f do not allow identification of a single algorithm that would be superior in both categories. For example, HD seems to find the objects well, but its performance in pixelwise comparison does not stand out from others. Conversely, the accuracy of LC is lower than average for object detection, but its performance in pixel level is close to the average accuracy. Examples of segmentation results are shown in Figure 5.

Results for yeast images with object level reference

After the analysis of the simulated images, we considered subcellular detection in wide-field images. Wide-field microscope images of yeast P-bodies give insight into algorithm performance in the context of actual experimentally derived data. In these images noise and contrast limit the detection accuracy, but objects are well scattered, and the object count per image is relatively low. We used the manually constructed reference images and the performance measures given in Eqs. 9-11 to numerically compare the algorithms. The performance metrics were calculated for a set of 28 images containing a total of 262 objects, and the results are listed in Table 2.

We compared the precision value, which penalizes extra detections and the recall value, which penalizes missed objects. With the exception of THE, most methods produced sufficiently accurate results, as evaluated by F-score (Table 2). Within that set of accurate methods, BPF, LC, and SE provided the best results, and KDE, LEF, and SPL (with F-scores close to 0.9) were the next most satisfactory. In contrast, the precision results reveal clear differences that require further attention. The precision of the THE, MGI and FPD methods stand out as having significantly high variance. Inspection of the segmentation results reveals that the poor performance of all three is due to their performance in the empty images, i.e. images with no objects located in manual analysis. In these cases, false positive detections in empty images lead to low precision. The majority of the images have in-focus P-bodies, and for those images THE, FPD and MGI gave reasonable results. With respect to the recall values, THE is the highest while both FPD and MGI also score well. Examples of detection results are shown in Figure 6, where a zoomed area in a single frame and the corresponding reference result are shown together with the detection results produced by all eleven algorithms.

Results for osteosarcoma well plate images

Next, we considered the analysis of well plate experiments as an example of image-based high-throughput measurements. High-throughput experiments typically challenge image analysis with high object density, high levels of background staining, and high variation of image characteristics across the experiment. The images used for our analysis contain cell populations that are expected respond to a given dose of a drug with varying levels of vesicle-like structures. We obtained an estimate of the average number of vesicles per cell in each image by calculating the number of vesicles in all 144 images and dividing the number of vesicles by the number of cells in each image. We then grouped the results by the reported dose level. The result is

Table 2: Results for yeast image frames

Algorithm	precision	recall	F-score
BPF	0.9570	0.9351	0.9459
FPD	0.5964	0.8969	0.7165
HD	0.8682	0.7290	0.7925
KDE	0.9116	0.8664	0.8885
LC	0.9396	0.9504	0.9450
LEF	0.8712	0.8779	0.8745
MGI	0.6175	0.8626	0.7198
MW	0.7645	0.8550	0.8072
SE	0.9318	0.9389	0.9354
SPL	0.8167	0.9351	0.8719
THE	0.0062	0.9733	0.0123

Summary of numerical results for the frames from image stacks of yeast cells. The reported results are the precision, recall, and F-score values calculated for 28 frames, seven out of which had no objects according to manual analysis. The results are the maximum F-scores obtained in parameter tuning by grid search, i.e., the F-score shown with red dots in Fig. 3.

a measure of the dose responses for the cell populations determined by each of the eleven algorithms. We then used these dose responses as an indirect comparison between the detection algorithms. The results are shown in Figure 7, and a sample image with corresponding detection results is shown in Figure 8.

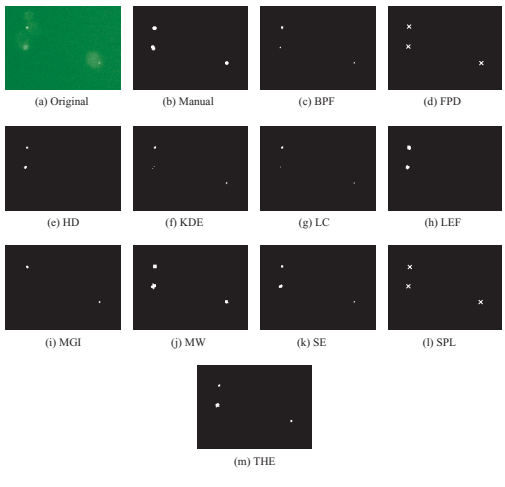

Figure 6 Example frame of yeast P-body image stacks and detection results by the algorithms. Manually marked objects in reference result are also shown for the same area. Note that the objects detected by FPD and SPL are illustrated as crosses whereas the actual segmentation results are shown for other algorithms. Note that the parameters of different methods are tuned for the whole dataset, not for this particular image. The original image has been enhanced for illustration purposes.

The dose responses in Figure 7 form a step-like pattern, with very few vesicles per cell in low-dose populations (dose levels I to VI), increasing vesicle numbers beginning with dose level VII and peak vesicle numbers at dose level XI. Increasing the dosage beyond that of level XI (i.e. level XII) does not appear to increase the average number of vesicle structures per cell. This behavior is consistent with saturation as the dose concentration increases.

Although there are differences in the absolute number of vesicles per cell in low dose images and the magnitude of the difference between the low and high dose images, all methods (except MGI and THE) produce this step-like dose response curve. For example, the step given by FPD, LC, and KDE is substantially lower than those by BPF, SE, and SPL. The result given by MGI and THE resemble the others for the high dose values where the images contain a large number of vesicles. When vesicles are few in number or not present at all, the methods give false detections. The clear differences in the dose responses obtained with different algorithms suggests that any downstream analysis, such as clustering or classification of populations based on the vesicle counts could produce significantly different results.

Comparison of relative similarities

To further explore the results (i.e. the number of objects detected across all images) obtained for all three image sets, we preformed hierarchical clustering and visualized the results as a dendrogram (Figure 9). Figure 9 illustrates the extent of the similarity between some of the algorithms across the set of close to 200 images, with FPD and HD being the closest matches and SE, MW, and SPL also forming a tight cluster. Some of the closest matches include algorithms that have similar detection principles.

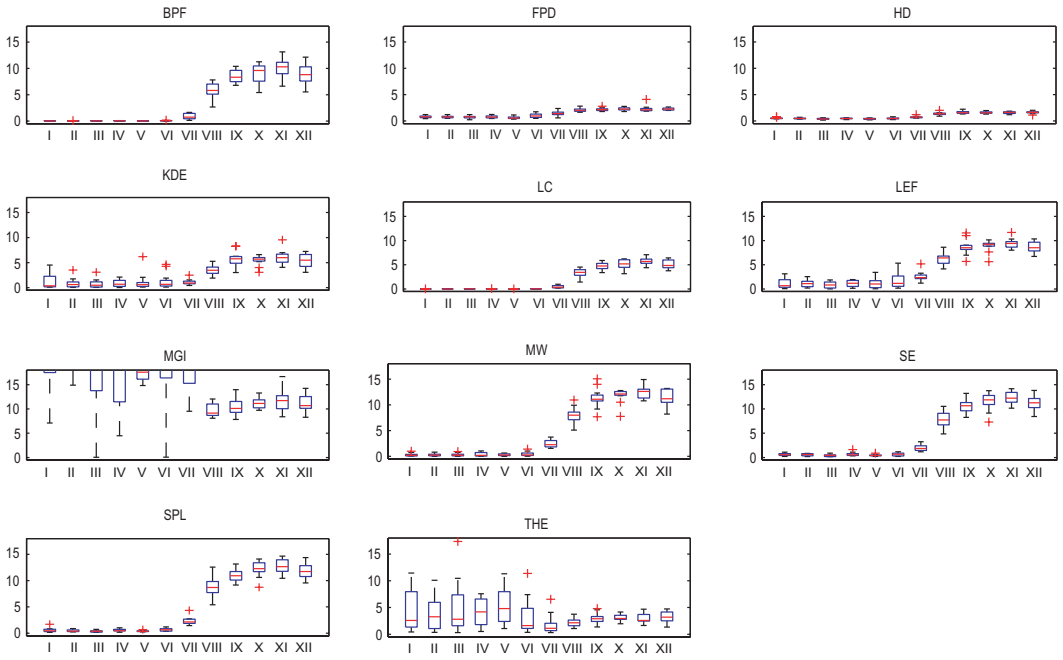

Figure 7 Results for the well plate experiment. The boxplots show number of spots detected per cell in each image, grouped according to the dose level. Parameters of each detection method have been tuned for the data, but here the lack of ground truth reference renders parameter optimization through comparison against reference impossible.

For example, both SE and SPL use matching of a Gaussian kernel into local maxima as their backbone, SE by filtering into a background subtracted image and SPL by repeated fitting into a local maximum point. However, similar results were also obtained by algorithms with different approaches, e.g. HD and FPD. The dendrogram also identifies methods whose results are significantly different from those obtained by the other methods. For example, both MGI and THE use a morphology-driven detection strategy with automated thresholding. This detection approach is different from that of the filtering-based methods, and as the results in Figure 7 and Table 2 show, these methods perform poorly on empty images when used with a completely automated thresholding as has been done here. In contrast, MGI and THE did perform fairly accurately on the simulated images. Thus, the use of these two methods may be warranted under conditions other than those in which the majority of the other methods perform well.

Finally, we calculated the pairwise correlation coefficients between the object counts obtained for all images. The pairwise correlation values between methods are shown in Figure 9. These correlation results further support the clustering results, namely that results given by MGI and THE differ significantly from the others (low correlation with other results) whereas SE, SPL and MW performed similarly (correlation >0.99). The object counts for all image sets that were used for constructing the dendrogram and calculating the correlations are available at the supplementary site.

Conclusions

We have studied the performance of eleven subcellular object detection algorithms under different analysis scenarios. Our study included real images of high-throughput well plate experiments for indirect comparison of the algorithms, as well as frames from image stacks of yeast P-bodies for which the object-level reference information was available. In addition, we used simulated images with small subcellular objects, thereby enabling a pixel-level comparison of algorithms against a computer-generated ground truth.

Results for the simulated images gave detailed insight into the performance of the methods. In the simulated image set all the images had the same number of subcellular objects. The object counts obtained for the image

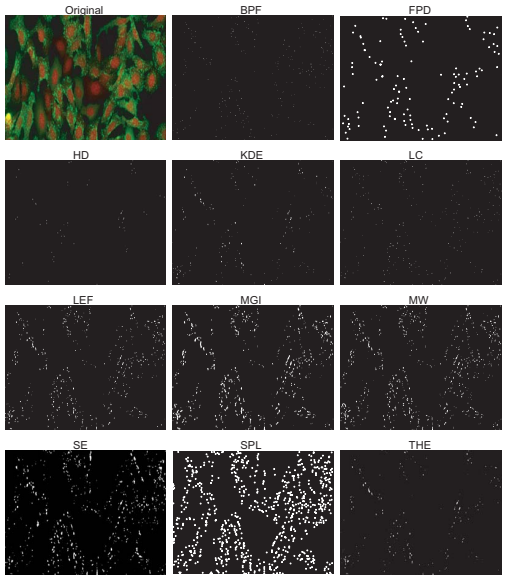

Figure 8 Example of well plate images and detection results by eleven algorithms. Note that the objects detected by FPD and SPL are illustrated as crosses whereas the actual segmentation results are shown for other algorithms. The original image has been contrast and intensity enhanced for illustration purposes.

set revealed that statistically significant differences exist between the algorithms. The small spots proved to be rather difficult to detect, highest object level accuracy (in terms of F-score) being 0.8249 given by HD. Worth noting is that also MGI (0.7698), THE (0.7244), and FPD (0.6905) all perform well for the set where all images had spots, all of which had problems with the empty images. Simulation allowed also pixel-level comparison, where MW gave the most accurate segmentation by a slight difference when measured by F-score, but none of the methods provided outstanding accuracy. The pixel-level results confirm how challenging it is to accurately segment small particles in noisy and partially blurred images with heavy background fluorescence. Moreover, the limitations in segmentation performance on pixel-level raise a question about the reliability of shape, size or morphology features extracted from subcellular objects in standard fluorescence microscopy measurements.

Second, the high level of F-score values for the detection of GFP labeled P-bodies in wide-field microscope images proved that all methods can be used for accurate detection of bright spots when background intensity is on a moderate level. The highest F-scores between manually located reference result and automated analysis result were given by BPF (0.9459), LC (0.9450), and SE (0.9354). Furthermore, FPD, MGI, and THE had difficulties in the handling of empty frames of wide-field microscope images, which shows as a high number of false positives leading to low precision values. Excluding the empty frames, all these three algorithms were accurate for the frames with in-focus P-bodies, which is confirmed by the high recall values.

Third, results for the human osteosarcoma well plate measurement data further confirmed how some of the algorithms failed to cope with a large data set where images contain varying amount of small spots. Examples of poor handling of varying conditions were THE and MGI algorithms. Our implementation of MGI detects

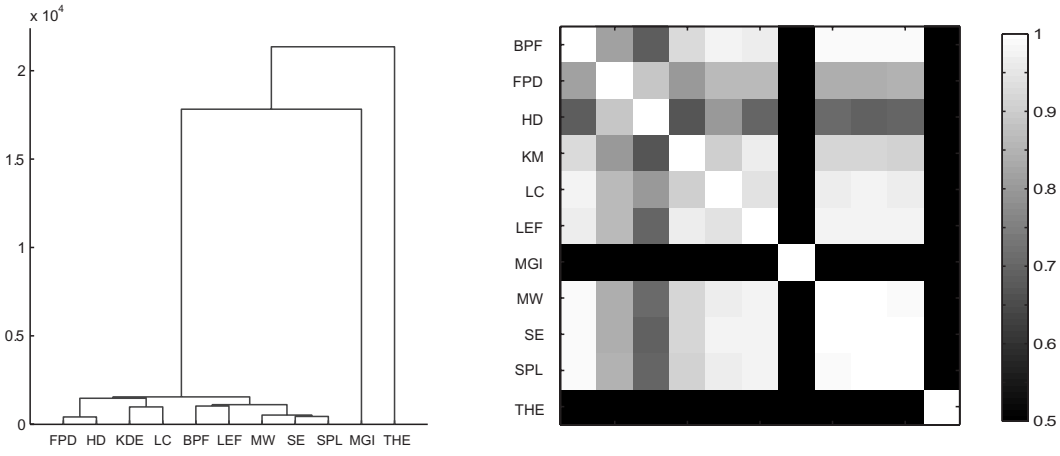

Figure 9 Dendrogram and pairwise correlation coefficients calculated based on object counts for all three image sets show similarities between algorithms. Correlation values lower than 0.5 are shown as black in the figure.

automatically the scale of interest, and in case of no or very few vesicles it fits to the scale of cells. The implementation of THE included automated thresholding, which in this case assumed the data to include two groups: objects and background. Thus, neither of these two algorithms was able to handle all images with same parameter settings when used in the way described here. However, including free parameters for tuning the segmentation or preprocessing steps could lead to better results. Also FPD and HD produced less obvious ramp as a dose response. FPD assumes certain level of spots to be present in all images (percentile-based detection), which explains why varying probability for spots within experiment may cause problems in detection. HD method, despite its heavy parametrization, seems to make a compromise where very few false objects are detected, but also part of true objects are missed. Apart from MGI and THE, all of the compared algorithms produced a step-like dose response, suggesting that the methods can be used for detecting differences between populations exposed under varying levels of stimulus. The results given by the 11 algorithms confirm that they all are very useful in spot detection tasks, but the results also show clear differences in terms of their ability to detect small, vesicle-like objects and to adjust to varying conditions. The handling of images containing very few, if any, small spots, in particular, brought out significant differences between the algorithms. Since handling such images can be fundamental for some applications, the algorithms should be chosen with care.

Finally, some remarks on the performance of the three detection algorithms originally developed for tracking purposes, i.e. FPD, HD, and SPL. Though developed for similar purposes, the methods have different approaches for detection. By definition, FPD tends to detect roughly the same number of objects for a set of images when used with fixed parameter settings. From a tracking point of view, this is a reasonable assumption if the number of particles is expected to be rather constant throughout the imaging sequence. The results for simulated image set support this conclusion, since the the number of particles stays constant in this set. On the other hand, when the number of particles present in the images changes dramatically over the course of the imaging period, the HD and SPL approaches are likely to give more accurate performance. This assertion is supported by our results. SPL adjusts well to varying conditions in well plate and wide-field images, and HD performs reasonably well in varying conditions, avoiding excessive false positive detections for empty yeast images (high precision value), though doing so at the cost of missing some spots (low recall value). We note that for the yeast stack images, even tuning the five free parameters of HD did not provide results as accurate as those with the single open parameter of SPL. For the simulated images, on the other hand, HD gave the most accurate results among all 11 algorithms, outperforming both FPD and SPL. Although detection accuracy does not directly predict subsequent tracking performance, choosing a method based on careful testing may be beneficial.

Thus, although detection algorithms are problem-specific, the systematic comparison of methods with a large set of test images can help choose the best method for the particular imaging challenge. Using a systematic approach, algorithms can be compared under varying conditions, providing useful information for various use cases. Our study also makes use of recently published benchmark datasets in order to evaluate algorithms. Importantly, evaluation based on a wide range of images tests the algorithms with an objective framework in which performance has not been tuned for a small set of images with specific characteristics. For example, subcellular object detection in modern high-throughput imaging experiments provides a challenge for image analysis because contrast, intensity, and number of spots may vary significantly within the same experiment. Systematic testing of algorithm performance with large image sets, as was done in this study, allows one to predict algorithm performance in such tasks. Supplementary material, including additional result figures and an algorithm toolbox as a CellProfiler [38] compatible module written in MATLAB (The MathWorks, Natick, MA) are available for download at http://www.cs.tut.fi/sgn/csb/subcell.

Authors' contributions

PR planned the study, and wrote the manuscript. PR and TÄ carried out experimental calculations. TÄ, SC, PR, and JS were responsible of algorithm implementations. CG-T carried out experimental work related to yeast imaging, and CG-T & JS performed manual analysis for the yeast image set. TÄ, SC, CG-T, JS, MB and AMD helped in manuscript editing. MB and LP participated in design of the study. AMD supervised the experimental work with yeast. LP and OY-H conceived of the study. All authors read and approved the final manuscript.

Acknowledgements

This work was supported by the Academy of Finland, (application number 129657, Finnish Programme for Centres of Excellence in Research 2006-2011) and by the National Technology Agency of Finland. PR was supported by Tampere Graduate School in Information Science and Engineering (TISE) and Nokia Foundation. CGT was supported by a grant from the NIH/NIGMS (P50GMO76547). AMD was supported by an NIH/NHGRI Genome Scholar/Faculty Transition Award (K22 HG002908). The authors would like to thank Dr. Prisca Liberali for her help. This work benefited from the Tampere Center for Scientific Computing (TCSC) and Techila Technologies's grid computing solution.

Author Details

[1]Department of Signal Processing, Tampere University of Technology, P.O.Box 553, Tampere, 33101, Finland, [2]Institute for Systems Biology, 1441 N. 34th Street, Seattle, WA, 98103-8904, USA and [3]Institute of Molecular Systems Biology, ETH Zürich, Wolfgang-Pauli-Str. 16, Zürich, 8093, Switzerland

Received: 17 September 2009 Accepted: 13 May 2010
Published: 13 May 2010

References

1. Boutros M, Kiger AA, Armknecht S, Kerr K, Hild M, Koch B, Haas SA, Paro R, Perrimon N, Consortium HFA: **Genome-wide RNAi analysis of growth and viability in Drosophila cells.** *Science* 2004, **303(5659):**832-835.
2. Wheeler DB, Carpenter AE, Sabatini DM: **Cell microarrays and RNA interference chip away at gene function.** *Nat Genet* 2005, **37(Suppl):**S25-S30.
3. Pepperkok R, Ellenberg J: **High-throughput fluorescence microscopy for systems biology.** *Nat Rev Mol Cell Biol* 2006, **7:**690-696.
4. LaPan P, Zhang J, Pan J, Hill A, Haney SA: **Single cell cytometry of protein function in RNAi treated cells and in native populations.** *BMC Cell Biol* 2008, **9:**43.
5. Zhou X, Wong S: **Informatics challenges of high-throughput microscopy.** *IEEE Signal Proc Mag* 2006, **23:**63-72.
6. Carpenter AE: **Software opens the door to quantitative imaging.** *Nat Methods* 2007, **4(2):**120-121.
7. Sacher R, Stergiou L, Pelkmans L: **Lessons from genetics: interpreting complex phenotypes in RNAi screens.** *Curr Opin Cell Biol* 2008, **20(4):**483-489.
8. Khodade P, Malhotra S, Kumar N, Iyengar MS, Balakrishnan N, Chandra N: **Cytoview: development of a cell modelling framework.** *J Biosci* 2007, **32(5):**965-977.
9. Sbalzarini IF, Koumoutsakos P: **Feature point tracking and trajectory analysis for video imaging in cell biology.** *J Struct Biol* 2005, **151(2):**182-195.
10. Jaqaman K, Loerke D, Mettlen M, Kuwata H, Grinstein S, Schmid SL, Danuser G: **Robust single-particle tracking in live-cell time-lapse sequences.** *Nat Methods* 2008, **5(8):**695-702.
11. Otsu N: **A threshold selection method from gray-level histograms.** *IEEE T Syst Man Cyb* 1979, **9:**62-66.
12. Ruusuvuori P, Lehmussola A, Selinummi J, Rajala T, Huttunen H, Yli-Harja O: **Benchmark set of synthetic images for validating cell image analysis algorithms.** *Proceedings of the 16th European Signal Processing Conference, EUSIPCO* 2008.
13. **Broad Bioimage Benchmark Collection** [http://www.broad.mit.edu/bbbc]
14. Gelasca ED, Byun J, Obara B, Manjunath B: **Evaluation and Benchmark for Biological Image Segmentation.** *IEEE International Conference on Image Processing, San Diego* 2008:1816-1819.
15. Smal I, Loog M, Niessen W, Meijering E: **Quantitative comparison of spot detection methods in live-cell fluorescence microscopy imaging.** *Proc IEEE International Symposium on Biomedical Imaging: From Nano to Macro ISBI '09* 2009:1178-1181.
16. Smal I, Loog M, Niessen W, Meijering E: **Quantitative Comparison of Spot Detection Methods in Fluorescence Microscopy.** *IEEE Transactions on Medical Imaging* 2010, **29:**282-301.
17. Jiang S, Zhou X, Kirchhausen T, Wong STC: **Detection of molecular particles in live cells via machine learning.** *Cytometry A* 2007, **71(8):**563-575.
18. Crocker JC, Grier DG: **Methods of digital video microscopy for colloidal studies.** *J Coll Interface Sci* 1996, **179:**298-310.
19. Vincent L: **Morphological grayscale reconstruction in image analysis: applications and efficient algorithms.** *IEEE Trans Image Process* 1993, **2(2):**176-201.
20. Smal I, Meijering E, Draegestein K, Galjart N, Grigoriev I, Akhmanova A, van Royen ME, Houtsmuller AB, Niessen W: **Multiple object tracking in molecular bioimaging by Rao-Blackwellized marginal particle filtering.** *Med Image Anal* 2008, **12(6):**764-777.
21. Chen TB, Lu HHS, Lee YS, Lan HJ: **Segmentation of cDNA microarray images by kernel density estimation.** *J Biomed Inform* 2008, **41(6):**1021-1027.
22. Devroye L, Györfi L, Lugosi G: *A Probabilistic Theory of Pattern Recognition* first edition. Springer, New York; 1996.
23. Prodanov D, Heeroma J, Marani E: **Automatic morphometry of synaptic boutons of cultured cells using granulometric analysis of digital images.** *J Neurosci Methods* 2006, **151(2):**168-177.
24. Matheron G: *Random Sets and Integral Geometry* New York: Wiley; 1975.
25. Dougherty ER, Lotufo RA: *Hands-on morphological image processing* Bellingham: Spie Press Series; 2003.
26. Olivo-Marin JC: **Extraction of spots in biological images using multiscale products.** *Pattern Recogn* 2002, **35:**1989-1996.
27. Bertin E, Arnouts S: **SExtractor: Software for source extraction.** *Astron Astrophys Sup* 1996, **117:**393-404.
28. Thomann D, Rines DR, Sorger PK, Danuser G: **Automatic fluorescent tag detection in 3D with super-resolution: application to the analysis of chromosome movement.** *J Microsc* 2002, **208(Pt 1):**49-64.
29. Soille P: *Morphological Image Analysis: Principles and Applications* Secaucus: Springer-Verlag New York, Inc; 2003.
30. Niemistö A: **HistThresh toolbox for MATLAB.** 2004 [http://www.cs.tut.fi/~ant/histthresh/].
31. Glasbey CA: **An analysis of histogram-based thresholding algorithms.** *CVGIP: Graph. Models Image Process* 1993, **55:**532-537.
32. Kapur JN, Sahoo PK, Wong AKC: **A new method for gray-level picture thresholding using the entropy of the histogram.** *Computer vision, graphics, and image processing* 1985, **29:**273-285.
33. Lehmussola A, Ruusuvuori P, Selinummi J, Huttunen H, Yli-Harja O: **Computational Framework for Simulating Fluorescence Microscope Images With Cell Populations.** *IEEE Trans Med Imag* 2007, **26(7):**1010-1016.
34. Lehmussola A, Ruusuvuori P, Selinummi J, Rajala T, Yli-Harja O: **Synthetic Images of High-Throughput Microscopy for Validation of Image Analysis Methods.** *P IEEE* 2008, **96(8):**1348-1360.
35. Huh WK, Falvo JV, Gerke LC, Carroll AS, Howson RW, Weissman JS, O'Shea EK: **Global analysis of protein localization in budding yeast.** *Nature* 2003, **425(6959):**686-691.
36. Fawcett T: **An introduction to ROC analysis.** *Pattern Recogn Lett* 2006, **27:**861-874.
37. Popovic A, de la Fuente M, Engelhardt M, Radermacher K: **Statistical validation metric for accuracy assessment in medical image segmentation.** *Int J CARS* 2007, **2:**169-181.
38. Carpenter A, Jones T, Lamprecht M, Clarke C, Kang I, Friman O, Guertin D, Chang J, Lindquist R, Moffat J, Golland P, Sabatini D: **CellProfiler: image analysis software for identifying and quantifying cell phenotypes.** *Genome Biol* 2006, **7(10):**R100.

doi: 10.1186/1471-2105-11-248
Cite this article as: Ruusuvuori *et al.*, Evaluation of methods for detection of fluorescence labeled subcellular objects in microscope images *BMC Bioinformatics* 2010, **11**:248

Publication IV

A.-B. Muthukrishnan, M. Kandhavelu, J. Lloyd-Price, F. Kudasov, S. Chowdhury, O. Yli-Harja, and A.S. Ribeiro, "Dynamics of transcription driven by the tetA promoter, one event at a time, in live Escherichia coli cells," *Nucleic Acids Research*, 40(17):8472-8483, September 2012.

8472–8483 *Nucleic Acids Research, 2012, Vol. 40, No. 17* *Published online 22 June 2012*
doi:10.1093/nar/gks583

Dynamics of transcription driven by the *tetA* promoter, one event at a time, in live *Escherichia coli* cells

Anantha-Barathi Muthukrishnan[1], Meenakshisundaram Kandhavelu[1], Jason Lloyd-Price[1], Fedor Kudasov[1], Sharif Chowdhury[1], Olli Yli-Harja[1,2] and Andre S. Ribeiro[1,*]

[1]Laboratory of Biosystem Dynamics, Computational Systems Biology Research Group, Department of Signal Processing, Tampere University of Technology, FI-33101 Tampere, Finland and [2]Institute for Systems Biology, 1441N 34th St, Seattle, WA, 98103-8904, USA

Received February 3, 2012; Revised May 22, 2012; Accepted May 23, 2012

ABSTRACT

In *Escherichia coli*, tetracycline prevents translation. When subject to tetracycline, *E. coli* express TetA to pump it out by a mechanism that is sensitive, while fairly independent of cellular metabolism. We constructed a target gene, P_{tetA}-mRFP1-96BS, with a 96 MS2-GFP binding site array in a single-copy BAC vector, whose expression is controlled by the tetA promoter. We measured the *in vivo* kinetics of production of individual RNA molecules of the target gene as a function of inducer concentration and temperature. From the distributions of intervals between transcription events, we find that RNA production by P_{tetA} is a sub-Poissonian process. Next, we infer the number and duration of the prominent sequential steps in transcription initiation by maximum likelihood estimation. Under full induction and at optimal temperature, we observe three major steps. We find that the kinetics of RNA production under the control of P_{tetA}, including number and duration of the steps, varies with induction strength and temperature. The results are supported by a set of logical pairwise Kolmogorov-Smirnov tests. We conclude that the expression of TetA is controlled by a sequential mechanism that is robust, whereas sensitive to external signals.

INTRODUCTION

Tetracycline is a polycyclic naphthacene carboxamide (1), isolated from Streptomyces genus of Actinobacteria (2), which prevents bacterial cell growth by binding to the 30 S ribosomal subunit. This binding interferes with the attachment of aminoacyl-tRNA to the mRNA-ribosome translation complex, inhibiting protein synthesis (3,4). In *Escherichia coli*, resistance to tetracycline is conferred by the extra-chromosomal Tn*10* transposon encoded class B molecular determinants, forming the *tet* operon (5–8) (also named divergon (9) or regulon (10)). This operon consists of two structural genes, *tetA* and *tetR*. *tetA* is essential for tetracycline resistance (11), as it encodes for a membrane-targeted antiporter protein, TetA, responsible for active efflux of tetracycline, whereas *tetR* codes for TetR that regulates the *tet* operon.

In the absence of tetracycline, TetR binds to the operator sites of *tetA* and *tetR*, preventing their transcription (12). In the presence of tetracycline, TetR binds as a dimer to the biologically active tetracycline–Mg^{2+} complex, causing an allosteric conformational change in the repressor protein (13). This releases the repressor from the DNA, allowing RNA polymerase to bind and initiate transcription of *tetA* and *tetR*. The *tet* operon is thus a self-repressing system (12,14), capable of fast and efficient response to tetracycline. Its expression activity is largely independent of the metabolic state of the host cell, making it a preferential system to control recombinant gene expression (15) and to study mechanisms of gene expression (13). Studies of the β-galactosidase activity of the Tn*10 tetR-tetA* promoter have showed that P_{tetA} is the strongest of the three promoters of this operon (16). It has thus been isolated, modified, and used in several studies (namely the *tetR/O* region) of gene expression (4), and its derivatives have been used in several synthetic circuits (17–23).

Studies suggest that gene expression kinetics in prokaryotes appears to be mainly controlled at the transcriptional level, particularly in initiation (24). *In vitro* measurements suggest that, in *E. coli,* transcription initiation is a sequential process (25). The first step, named 'closed complex formation', is the binding of the RNA polymerase enzyme to the promoter region and finding of the transcription start site (TSS). This is followed by isomerization, DNA unwinding and loading of the

*To whom correspondence should be addressed. Tel: +358331153928; Fax: +358331154989; Email: andre.ribeiro@tut.fi

nucleotide strand (the 'open complex formation') (25). Afterwards, elongation of the RNA strand takes place (26), and once the termination site is reached, the single-stranded RNA molecule and the RNA polymerase are released (27). This sequential process (28) is subject to tight regulation that takes place at one or more stages.

Evidence suggests that, for most promoters in *E. coli*, the open complex formation is the main rate-determining step in initiation (29,30). However, the durations of other steps, namely the closed complex formation, isomerization, and promoter clearance are also sequence-dependent, differing widely between promoters and in different conditions (31). Environmental factors can also affect this kinetics (32,33). For example, apart from induction (34), factors such as temperature and pH can also affect the "rate-limiting" steps in initiation (30,35).

Changes in the kinetics of these steps allows the overall expression rate of a gene to be changed (8,25). For example, *in vivo* measurements of the expression of the synthetic promoter $P_{LtetO-1}$ using the luciferase reporter system have shown that the rate of RNA production can change by 5000-fold with induction by anhydrotetracycline (aTc) (8). However, it is noted that this promoter was engineered with the aim of allowing tight regulation (wide range of induction) (8). Among the several tetracycline analogs, aTc was found to be an effective inducer even at very low concentrations (<50 ng/ml), as it binds to the TetR protein with very high affinity (~35-fold higher than tetracycline) (36–38) and is less toxic to cells with a minimal inhibitory concentration of 4 μg/ml (39).

If transcription initiation is the rate-determining step in RNA production, and if it is composed of several sequential steps (30–32,40,41), provided that these are approximately exponentially distributed in duration, one would expect that transcript production is a sub-Poissonian process (40). However, recent measurements of *in vivo* cell-to-cell diversity in RNA numbers have exhibited higher diversity in RNA numbers than would be expected from a sub-Poissonian process of transcript production (42–44). In (44), it was hypothesized that this was because of either super-Poissonian RNA production or non-Poissonian RNA degradation. In (42,43), it was hypothesized that the cause is the existence of periods of activity and inactivity of the promoter. It is noted that measurements of cell-to-cell diversity in either RNA or protein numbers are affected by several processes other than transcription and translation. Specifically, the kinetics of degradation of RNA and proteins can be complex (45), that is, non-Poissonian, and there may be non-negligible differences in measurements using *in vivo* and *in vitro* techniques (24). Finally, another event that affects cell-to-cell diversity in RNA numbers is cell division, particularly because the intracellular environment of *E. coli* is not well-stirred (46). Even if the RNA molecules are partitioned in an unbiased fashion, the stochastic nature of this process will enhance the cell-to-cell diversity in the numbers of these molecules following division events (47,48). In addition, bacteria are known to partition unwanted protein aggregates in a biased fashion (49,50), including, for example, RNA tagged with MS2 coat protein fused with Green Fluorescent Protein (MS2-GFP) (51,52), and fluorescent proteins such as Tsr-Venus (53,54,55). This bias in partitioning ought to exacerbate cell-to-cell diversity in RNA and protein numbers when assessed by these methods. The degree of stochasticity in transcription thus needs to be assessed without the interference of subsequent events, by measuring transcript production one event at a time (40).

Here, using *in vivo,* single-molecule based techniques, we characterize the kinetics of initiation of P_{tetA} (15,56), including its stochasticity and how it changes with induction strength and temperature. Namely, we assess the transcript production dynamics at the single event level. This is possible by a method recently developed to tag RNA *in vivo* in *E. coli* with MS2-GFP proteins, which allows individual transcription events to be detectable shortly after production (55,57), and the behaviour is similar to that of the unlabelled system (57).

We report measurements of time intervals between consecutive productions of RNA molecules under the control of P_{tetA} when subject to several induction strengths and temperatures. From the distribution of these intervals, we analyse the dynamics of this promoter. We address the following questions. What is the *in vivo* kinetics of RNA production, one event at a time, under the control of P_{tetA}, when fully induced? How does the *in vivo* kinetics of transcription change with induction? How noisy is this process? Finally, from the inference of number and durations of the rate-limiting steps, we address how the kinetics of the rate-limiting steps changes with temperature. In the end, we compare the kinetics of initiation of P_{tetA} with that of the $P_{lac/ara-1}$ promoter, also named P_{lar}, which has been recently characterized (40) using the same methods.

MATERIALS AND METHODS

Chemicals

For routine cultures, the components of Luria-Bertani (LB) broth (Tryptone, Yeast extract and NaCl) were purchased from LabM (UK) and antibiotics from Sigma-Aldrich (USA). Phusion high-fidelity polymerase and other PCR reagents are from Finnzymes (Finland). Fermentas kits (Finland) for Plasmid isolation and PCR product extraction and purification were made as per the instructions provided. To perform qPCR, cells were fixed with RNAprotect bacteria reagent (Qiagen, USA). The Tris and EDTA for lysis buffer were purchased from Sigma-aldrich (USA) and lysozyme from Fermentas (USA). The total RNA extraction was done with RNeasy RNA purification kit (Qiagen, USA). DNase I, RNasefree for RNA purification, was purchased from Promega (USA). iScript Reverse Transcription Supermix for cDNA synthesis and iQ SYBR Green supermix for qPCr were purchased from Biorad (USA). Agarose for microscopic slide gel preparation and electrophoresis and isopropyl b-D-1-thiogalactopyranoside (IPTG) and aTc for induction of cells are from Sigma-Aldrich (USA). For staining DNA and RNA on gels, SYBR-Safe from Invitrogen (USA) was used.

Bacterial strain and growth conditions

The strain *E. coli* DH5α-PRO (identical to DH5α-Z1) (57) was used to clone and express the target and reporter genes. For overnight cultures, the strain from glycerol stock was inoculated in LB broth 10 g of tryptone, 5 g of yeast extract and 5 g of NaCl per litre, pH 7.0) (56) with appropriate antibiotics (100 μg/ml ampicillin and 35 μg/ml chloramphenicol) and incubated at 37°C with shaking (250 rpm).

Genetic constructs

We constructed the target gene P_{tetA}-*mRFP1-96BS* with a 96 MS2-GFP binding site array in a single-copy BAC vector by restricting out the P_{lar} promoter with BamH1 restriction endonuclease from a BAC clone carrying a target gene P_{lar}-*mRFP1-96BS* (42) (a kind gift from Ido Golding, University of Illinois, IL), and replacing it with P_{tetA} amplified from the pTetLux1 plasmid (56). The primers (Forward: 5′GGGATCCCTCACATGACCCGA CAC 3′ and Reverse: 5′GGGATCCACTGCAATCGCG ATAGC 3′) were designed to amplify the P_{tetA} promoter with BamHI restriction site flanking regions. The amplicon and the BAC vector were subjected to BamH1 restriction digestion, followed with ligation of the amplified product into the BAC vector. Thus, we obtained a single copy F-based plasmid carrying the target region P_{tetA}-*mRFP1-96BS*. This product was transferred into the competent *E. coli* strain DH5α–PRO host cells. The recombinants were selected with antibiotic screening and further confirmed with sequence analysis. The reporter molecules to visualize the target RNA were expressed from the pZS12MS2-GFP plasmid (55) (SC101 origin, 6–8 copies per cell, Amp^R, $P_{LlacO-1}$ promoter) cloned into the host strain, a kind gift from Philippe Cluzel, University of Chicago, IL. The *tetR* gene that encodes for a regulatory protein TetR, is integrated into the chromosome of *E. coli* strain DH5α–PRO, under the control of a strong promoter P_{N25}, that ensures appropriate levels of repressor proteins for tight regulation and full induction, in spite of the residual binding affinity of tetR-aTc complex to DNA (8,55).

A detailed map of the *tetA* promoter sequence with the crucial elements, such as the TetR binding site, the −10/–35 regions, the TSS and the ribosome binding site region, as well as the beginning of the MS2-GFP binding region is shown in Figure 1. Note that there is no *tetA* gene in the genome of *E. coli* DH5α–PRO or in the genetic constructs that were transformed into the strain.

Induction of expression of the target gene and of the reporter gene

From the overnight culture, cells were inoculated into a fresh LB medium supplemented with antibiotics, with initial OD of 0.1 at 600 nm and incubated at a specific temperature (24°C or 37°C) to mid-logarithmic phase with 0.5 OD. To induce the production of MS2-GFP proteins, IPTG (1 mM) was added in the medium at 0.35 OD. The target mRNA from P_{tetA}-*mRFP1-96BS* was then induced by adding aTc to the liquid culture. The target mRNA is rapidly tagged by the MS2-GFP proteins in the cytoplasm and can be detected as fluorescent spots soon after transcription occurs (57).

Quantitative PCR for mean mRNA quantification

The quantification of changes in the mean transcripts production rate of the target gene with induction strength and temperature, relative to a reference gene, were validated with qPCR. For the experimental samples, 10 ml of cells with 0.5 OD at 600 nm were induced with aTc (5–25 ng/ml) alone for 1 hour in liquid culture at a specific temperature (24°C or 37°C). Cells were then immediately fixed with RNAprotect bacteria reagent followed by enzymatic lysis with Tris-EDTA lysozyme buffer (pH 8.3). From the lysed cells, total RNA was isolated with RNeasy RNA purification kit. The total RNA was separated by electrophoresis through a 1% agarose gel and stained with *SYBR® Safe* DNA Gel Stain. The RNA was found intact with discreet bands for 16 S and 23 S ribosomal RNAs. To remove DNA contamination, RNA samples were treated with DNase I, RNase-free enzyme as per manufacturer's instructions. The A 260 nm/280 nm ratio for the RNA samples assessed using GeneQuant pro UV/Vis Spectrophotometer (80-2114-98) were 2.0–2.1, indicating highly purified RNA, and the yield was estimated to be 0.4–0.5 μg/μl. cDNA was synthesized from 1 μg of RNA with iScript Reverse Transcription Supermix according to manufacturer's instructions and stored at −20°C. The qPCR master mix contained iQ SYBR Green supermix with primers for the target and reference genes at a final concentration of 200 nM. We used three reference genes (16 S rRNA (42,58), 23 S rRNA (59) and *dxs* (60)) for internal reference, and similar patterns were observed in all cases. In the results section, we show the data relative to the 16 S rRNA reference gene, whereas in the supplement, we show the data relative to *dxs* (Supplementary Figure S2).

The primers for the target mRNA were (Forward: 5′ TA CGAC GCCGAGGTCAAG 3′ and Reverse: 5′ TTGTG GGAGGTGATGTCCA 3′) to the region of *mRFP1* (GenBank Accession Number: AF506027) (61) with amplicon length 90 bp and for the reference gene 16 S rRNA (EcoCyc Accession Number: EG30090) (Forward: 5′ CGTCAGCTCGTGTTGTGAA 3′ and Reverse: 5′ GGACCGCTGGCAACAAAG 3′), with amplicon length 74 bp (40), and primers were obtained from Thermo Scientific. The template for the reaction was 20 ng of cDNA with similar PCR efficiencies for both the target and reference genes, both greater than 95%. The thermal cycling protocol used was: 94°C for 15 s, 54°C for 30 s, and 72°C for 30 s up to 36 cycles, and in the end, one cycle of 94°C for 15 s. The fluorescence was read at the end of each cycle. These reactions were performed in three experiments, each with three replicates per condition with a final reaction volume of 50 μl. No-RT controls and no-template controls were used to crosscheck non-specific signals and contamination. The reaction was carried out in low-profile tube strips in a MiniOpticon Real time PCR system (Biorad). The Cq values generated

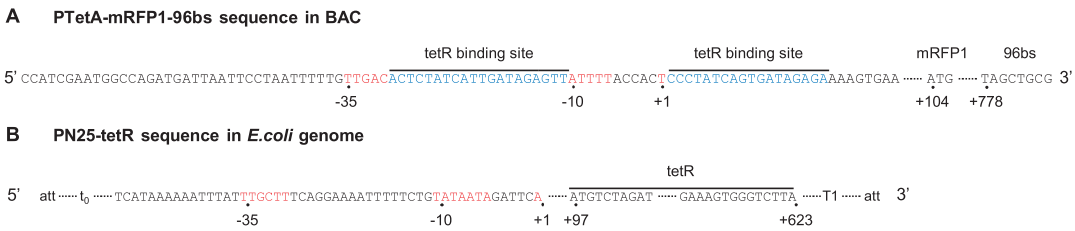

Figure 1. (**A**) P_{tetA}-*mRFP1-96bs*-BAC plasmid map: nucleotide sequence of the *tet* regulatory region on the BAC plasmid, beginning with P_{tetA} (-35 and −10 consensus sequences), TSS (+1), palindromic patterns corresponding to two TetR binding sites (blue), mRFP1 start site at +104, and 96bs start site at +778. (**B**) P_{N25}-*tetR* sequence integrated in the *E. coli* genome: P_{N25} controlled TetR protein coding gene and the lambda *attP* site. Terminators t_0 and T1 prevent transcription from the integrated promoters into the neighbouring regions of the *E. coli* genome.

by CFX Manager™ Software were imported into Microsoft Excel, and the data were analysed following the Livak method (62) to obtain the fold changes in the target gene, normalized to the reference gene, and to calculate the standard error between experiments.

Fluorescent microplate reader measurement for mean protein levels

The mean fluorescence of the mRFP1 protein under the control of P_{tetA} was measured with a Thermo Scientific* Fluoroskan Ascent Microplate Fluorometer. Cells at 0.5 OD_{600nm} were induced with 15 ng/ml of aTc and incubated at a specific temperature (24°C or 37°C) for 1 hour with shaking. The optical density of induced and non-induced cells was measured after 1 hour. From that, 0.5 OD_{600nm} of cells were taken, centrifuged and then re-suspended with fresh medium of 1:200 folds dilution. From this, 150 µl of cells were taken and placed on 96 well microplate and measured for relative fluorescence levels of mRFP1 protein with excitation (584 nm) and emission (607 nm) wavelengths (61). The cell density was kept identical in all wells of the plate for all measured conditions. We performed three independent experiments with three replicates for each condition.

Time-lapse microscopy

Cells were induced with IPTG and aTc as described earlier in the text. Five minutes after induction in liquid culture by aTc, cells were placed on a microscope slide between a coverslip and 1% LB-agarose gel with IPTG (1 mM) and aTc (15 ng/ml), to maintain full induction under the microscope. Cells were visualized in a Nikon Eclipse (TE2000-U, Nikon, Japan) inverted C1 confocal laser-scanning system with a 100× Apo TIRF (1.49 NA, oil) objective. The slide was kept in a temperature-controlled chamber, and the cells were focused within a few seconds under light microscope. Images were collected once per minute up to 1 hour under the fluorescence confocal microscope. Image acquisition began approximately 20 minutes after induction (including the 5 minutes induction in liquid culture). This interval is sufficient to reach a steady state level of induction (55,63). For image acquisition, we used Nikon software EZ-C1, under dark condition to minimize photolysis of aTc (photobleaching and nutrient depletion only become significant after 2 or more hours). GFP fluorescence was measured using a 488 nm argon ion laser (Melles-Griot) and a 515/30 nm detection filter. Images were acquired using medium pinhole, gain 130 and 1.68 µs pixel dwell. On the slide, the division time of the cells was approximately 40 minutes, likely because of the imaging.

We used a recent interacting multiple model filter based autofocus strategy (64). The method relies on the nature of the focal drift and exploits the interacting multiple model filter algorithm to predict the focal drift at time *t* based on the measurement at time *t-1*. It allows a drastic reduction of the number of required z-slices for focal drift correction, thus minimizing photo bleaching.

Cells and spots segmentation and the intensity jump-detection method

Detection of cells from the images is performed by a semi-automatic method (40). It consists of manually masking the regions that cells occupy during the imaging. For each image, the locations, dimensions and orientations of the cells within their masks were estimated by principal component analysis, assuming that the fluorescence inside the cell is uniformly distributed. This assumption is supported by measurements of the pixels intensities inside each cell, which were found to be fairly uniform (40). The segmentation of fluorescent spots (tagged RNAs) was performed by a kernel density estimation method (65) with a Gaussian kernel. An example of the results of the segmentation is shown in Supplementary Figure S1.

From these data, we compute the cell-background-subtracted total spot intensity time traces for each cell. Because the tagged RNAs do not degrade during the experiment (shown in the 'Results' section), this intensity should follow a monotonically increasing piecewise-constant function, where the jumps correspond to the appearance of novel mRNAs. This was verified by inspection (40). We fit such a function to the time trace by least squares, where the number of pieces in the function is determined by an *F*-test with a *P* value of 0.01, thus requiring higher order curves to fit significantly better to justify their use. Some intermediate results of this procedure, along with raw data, are shown in Figure 2. In Supplementary Data, we provide movies of two cells showing the time (in seconds) when each frame was obtained following induction of the target gene.

Inference of the number and duration of the sequential steps in transcription

From the distribution of intervals between productions of consecutive RNA molecules, we infer by maximum-likelihood the number and duration of the sequential steps in transcription initiation (40). We assume that the duration of each of the sequential steps follows an exponential distribution (40). Although the steps in initiation, such as the open complex formation, are likely not elementary (25), it was possible by this method to fit well the measured distributions in the case of P_{lar} using a small number of steps that is consistent with the number of steps believed to be rate-limiting from *in vitro* studies (31,32). To support the results of the inference, we perform Kolmogorov-Smirnov tests to compare the measured distribution with the inferred one that best fits the data. This test is used to determine whether the inferred distribution does not fit the measured distribution.

The inference procedure assumes that the measured intervals between the productions of consecutive RNA molecules are not significantly affected by elongation. This relies on the fact that the mean duration of the intervals between consecutive transcription events is of the order of 600 s or higher, depending on induction strength and temperature (see Results section and *in vitro* studies (8)). On the other hand, elongation of the target gene was measured to take only tens of seconds (57). Possible sequence-dependent events, such as long transcriptional pauses, can also be ruled out as affecting significantly the measured distributions because, if existing, they would last only 10–100 s (e.g. 32 s half-life for the *ops* pause and 52 s for the *his* pause) (66). In addition, target RNA molecules become visible even while elongating (57), further diminishing possible effects of events in elongation in the measured distributions. In any case, although the elongation process may increase the variance of the distributions, it would not affect their means. Finally, the eventuality of possible premature terminations of transcription events can be ruled out in this case because they would generate distributions of intervals between transcription events with multiple peaks, centered on multiples of the mean interval between productions, which were not observed (see 'Results' section).

Here, we assume a d-steps model such that the durations of the d steps are exponentially distributed and are independent, with possibly different rates. The fit for each d-steps model is obtained by maximum likelihood estimation. The likelihoods are compared using likelihood ratio test, and the model with smallest d is selected that cannot be rejected at the significance level 0.01 in favour of a higher order model. This method was found to reliably distinguish the number of steps and the duration between any two steps when they differ by ~25% or more in duration, from 200 intervals sampled from a stochastic model of gene expression with d exponentially distributed steps (40). Note that this method does not allow us to determine the temporal order of the sequential steps inferred. Only their number and durations can be assessed.

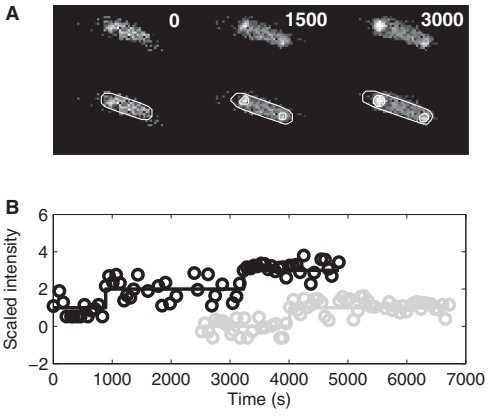

Figure 2. Tagged RNAs in *E. coli* cells. (**A**) Unprocessed frames and segmented cells and RNA spots. The moments when images were taken are shown for each frame. (**B**) Examples of time series of scaled spot intensity levels from individual cells (circles) and the corresponding estimated RNA numbers (solid lines). The cell shown in (A) does not correspond to any of the traces in (B).

RESULTS

We study the *in vivo* kinetics of production of individual RNA molecules, as a function of inducer concentration and temperature, under the control of P_{tetA}. First, we measured the relative mean RNA levels by qPCR as a function of induction and temperature. In Figure 3, we show the results using the 16 S rRNA gene as reference, whereas in supplement, we show the results using *dxs* as reference (Supplementary Figure S2), which are similar to 16 S rRNA. Previous studies suggest that the maximum induction is achieved with a concentration of aTc of 20 ng/ml or higher (8,56). The results (Figure 3 and Supplementary Figure S2) are in agreement, indicating that there is no significant increase in the rate of RNA production beyond 15 ng/ml of aTc. From these figures, we find that both the temperature and the inducer concentration

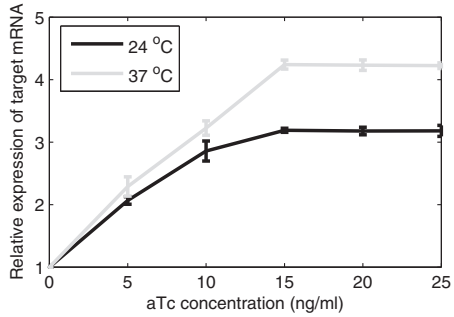

Figure 3. Relative expression level of target mRNA induced with different concentrations of aTc (ng/ml) at 24°C and 37°C, quantified by qPCR using the 16 S rRNA gene as reference. The standard deviation bars are from three independent experiments. In some cases, these bars' lengths are too small to be visible.

significantly affect the rate of transcription under the control of P_{tetA}.

From here onwards, we focus on three conditions. Specifically, we measure gene expression in the absence of aTc at 37°C, and with 15 ng/ml aTc at both 37°C and 24°C so as to study how the kinetics changes with induction and temperature. First, we verify whether, for these conditions, the relative protein expression levels follow those of the RNA. Results of the measurements of relative fluorescence levels by microplate fluorometer are shown in Figure 4, and confirm that the protein levels follow the RNA levels. They also show similarity (same order of magnitude) to the measurements reported in (56) for this promoter using a luminescent reporter system, even though the cells in (56) were in late log-phase and had a 90 min induction period.

We next study the kinetics of RNA production in live, individual cells using the MS2-GFP tagging method (40,42). As described in the Methods section, the expression of the target gene is controlled by P_{tetA} and is induced by aTc. The sequence of the target gene contains 96 binding sites for the MS2 coat protein. Because of these, the reporter proteins (MS2-GFP) can bind to the target RNA, producing a fluorescent spot that is detectable from fluorescence microscopy images.

Using this system, we first measured the cell-to-cell diversity in the number of tagged RNA molecules produced by individual cells over a certain period of time in all three conditions. In both the induced and non-induced cases, cells are placed under the confocal microscope 2 h following induction by IPTG. In the induced cases, the induction by aTc is done 1 h following the induction by IPTG.

From the images, we extracted the number of target RNA molecules in each cell, and calculated the mean and standard deviation of the number of RNA molecules in individual cells (Figure 5). We observe that the measured mean is in agreement with the measurements by qPCR (Figure 3), though the *in vivo* measurements have a slightly smaller relative increase with induction.

We also extracted the fraction of cells with a given number of RNA molecules (Figure 6). In the non-induced case (0 ng/ml aTc, 37°C), the variance of the distribution is 0.62, and the mean is 1.0. In the induced case, the variance is 2.5, and the mean is 3.6. Finally, for cells induced with 15 ng/ml aTc and incubated at 24°C, the variance of the distribution is 1.2, and the mean is 2.2. These values are of significance in that, in all cases, the variance is smaller than the mean (i.e. the Fano factor of the distribution is smaller than 1). If the process of RNA production was Poissonian, that is, if the intervals between consecutive productions were independent and followed an exponential distribution, the variance ought to be equal to the mean (i.e. Fano factor equal to 1). Because the tagged RNA molecules do not degrade, this can only be explained either by the dynamics of RNA production or of RNA partitioning in division (or the combination of these processes).

To investigate this, we obtained distributions of intervals between productions of consecutive RNA molecules in individual cells in the three conditions (Figure 7). These distributions are not affected by the dynamics of RNA partitioning in division because we only count intervals between consecutive RNAs in single cells. In each case, several independent measurements were made, and the results were combined.

The number of cells observed in each condition is shown in Table 1 along with the number of intervals detected, as well as the square of the coefficient of variation (CV^2, defined as the variance over the mean squared) of the intervals. It is noted that the mean duration of the intervals for the aTc 15 ng/ml (37°C) condition is in close agreement with *in vitro* measurements of the time it takes for a transcription initiation event to be completed once initiated (35).

From Figure 7, in all cases, the shapes of the distributions of intervals are not exponential-like. This implies that the process of RNA production under the control of P_{tetA} is not Poissonian. Instead, because the standard

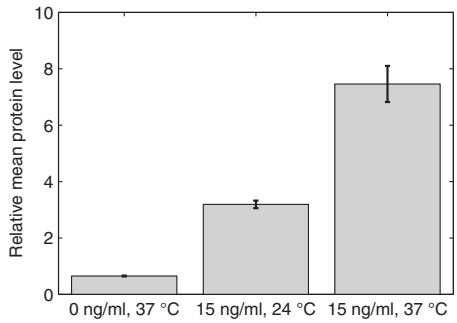

Figure 4. Relative mean expression level of target proteins (mRFP1) estimated by microplate fluorometer in three conditions. The error bars are the standard deviation from the measurements in the different wells. For precise quantities, see Supplementary Table S1.

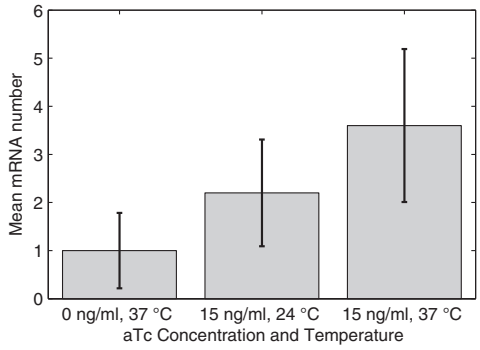

Figure 5. Mean levels of the target mRNA relative to the non-induced condition at 37°C obtained from live cell imaging of the RNA tagged with MS2-GFP under the confocal microscope. Images taken 1 h after induction by aTc in three conditions. The error bars are the standard deviation of the number of RNA molecules in each cell. For precise quantities, see Supplementary Table S2.

deviations of the distributions are smaller than the means, resulting in a CV^2 below 1 (Table 1), we can conclude that this process is sub-Poissonian. This explains the low values of cell-to-cell diversity in RNA numbers observed in cell populations (Figure 6).

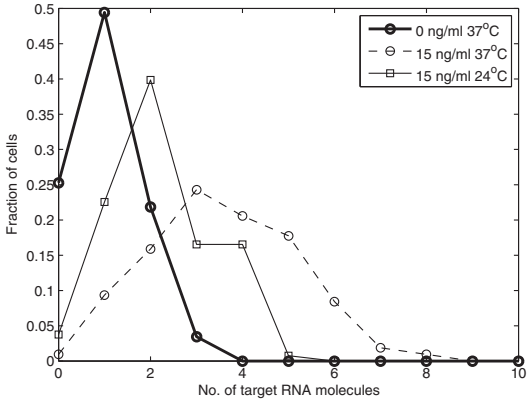

Figure 6. Distribution of the fraction of cells with a given number of mRNA molecules, 1 h following induction by aTc (when induced) obtained from live cell imaging in three conditions.

From the comparison of the distributions A and C in Figure 7, we can assess the effects of induction in the dynamics of transcription under the control of P_{tetA}. Note how distribution C, aside from having a smaller mean, is also slightly more exponential-like, explaining why the CV^2 in RNA numbers is closer to 1 in case C than in case A (Table 1). From the comparison of the distributions B and C, we can assess the effects of lowering the temperature in the dynamics of transcription under the control of P_{tetA}. When the temperature is reduced from 37°C (distribution C) to 24°C (distribution B), the mean interval between transcription events increases, and the shape of the distribution changes significantly. Namely, distribution B, corresponding to full induction at 24°C, is more exponential-like than distribution C.

These results rely on the intensity jump-detection method. This method assumes that the target RNA molecules are quickly bound by the MS2-GFP tagging proteins once transcribed (which was verified in (55)) and that, once that occurs, they do not degrade during the measurement. To validate this assumption of "immortality", we studied the kinetics of degradation of these complexes. The MS2-GFP proteins used here are an assembly-defective mutant with the FG loop deleted (55,67). A recent study suggested that when using a target RNA with 48 binding sites for these MS2-GFP

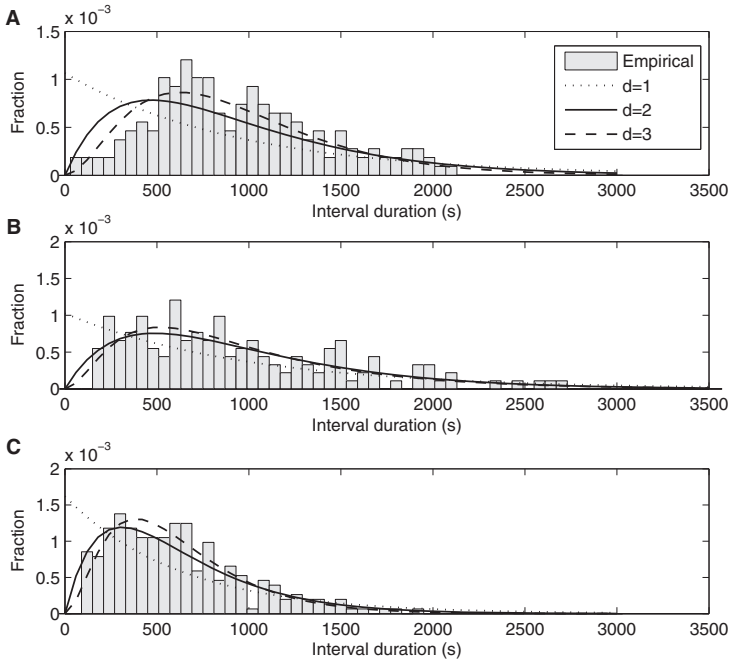

Figure 7. Distributions of time intervals between productions of consecutive mRNA molecules in individual cells under the control of P_{tetA} in conditions: (**A**) 0 ng/ml aTc at 37°C, obtained from 157 cells and 43 intervals (**B**) 15 ng/ml aTc at 24°C, obtained from 119 cells and 100 intervals, and (**C**) 15 ng/ml aTc at 37°C, obtained from 113 cells and 254 intervals. The probability density functions of inferred models of transcription initiation with differing number of rate-limiting steps are also shown in each plot. Note the different scales in the *y*-axis.

proteins, the resulting RNA-MS2-GFP complex may degrade during measurement sessions of a couple of hours (46). This would interfere, to some extent, with the intensity jump-detection method (see 'Materials and Methods' section). However, our target mRNA has 96 binding sites, and therefore the kinetics of degradation likely differs. We studied the degradation kinetics of the target RNA when bound the MS2-GFP and observed ~120 RNA-MS2-GFP complexes produced in 50 cells for up to 2 h. We did not observe any degradation event of these complexes nor did we observe any significant loss of brightness in individual spots. We conclude that the additional MS2-GFP molecules provide sufficient stability to the complex, for us to consider them to be immortal for all practical purposes, implying that the total brightness of the spots within a single cell monotonically increases with time.

We next study the kinetics of the underlying processes responsible for shaping the interval distributions (Figure 7) and thus the observed cell-to-cell diversity in RNA numbers (Figure 6). For this, certain assumptions are necessary. First, we assume that the distributions are mainly shaped by the kinetics of transcription initiation. This relies on the following: in all distributions in Figure 7, the mean interval duration is higher than ~500 s. Therefore, elongation is not expected to play a significant role in shaping the distributions because it lasts only tens of seconds (57). Also, as noted, the target RNA, when bound by MS2-GFP proteins, does not degrade during the measurements. Because of this, we assume that the distributions are shaped by transcription initiation, which includes steps such as the closed complex formation, isomerization and open complex formation (8,25–32,35,40,41,68).

We estimate by maximum likelihood the number and duration of the most prominent "rate-limiting" steps, that is, the ones that shape the distributions of intervals between transcription events (40). The results are shown in Figure 7 for each condition when assuming one, two and three steps. In Table 2, we show the log-likelihood values and the durations of the inferred steps for 1-step, 2-step and 3-step models, for each condition. The number of steps can be determined by using a likelihood-ratio test between pairs of models to reject a lower-degree model in favour of a higher-degree one (55). In Table 3, we show the results of the likelihood-ratio tests. For all distributions, the test rejects the 1-step (exponential) model in favour of the 2-step model (P values $< 8.32 \times 10^{-7}$). For distributions A and C, the 2-step model is also rejected in favour of the 3-step model (P values < 0.0019).

The time scales of the steps (for d = 2) are identical for all cases. As discussed in a previous work (40) this may be because of some unknown artefact of the inference method or be representative of the real kinetics of transcription initiation of this promoter. The method of inference was found to reliably distinguish the duration of each step when they differ by approximately 25% or more in duration, from 200 intervals sampled from a model of gene expression (40). For smaller differences, the solution can be biased toward inferring steps with identical durations, for unknown reasons. Nevertheless, given the number of intervals measured, it is possible to conclude that the steps do not differ by more than approximately 25%.

From Tables 2 and 3, provided that the assumed sequential model of transcription initiation (8,25–32,35,40,41,68) is correct, we conclude that, when not induced with aTc, transcription initiation controlled by P_{tetA} has 3 rate-limiting steps, which are similar in duration (differing by less than 100–150 s between them). When fully induced, at 24°C, there are two dominant rate-limiting steps, similar in duration. Finally, at 37°C under full induction, there are three rate-limiting steps, two longer and similar in duration, and a (clearly) shorter third step. No significant improvement was obtained in the fit with more steps in any of the conditions.

We conclude that there are three rate-limiting steps in transcription initiation of P_{tetA}. By lowering the temperature, two of the steps become longer in duration, whereas the third step remains unaltered and, because of its now relatively much shorter duration, it becomes barely detectable (P value of 0.0268, Table 3). Interestingly, the other two steps are not significantly affected by temperature (compare cases B and C in Table 2). Induction on the

Table 1. Number of cells analysed, number of intervals between productions of consecutive RNA molecules detected in individual cells, mean interval duration, standard deviation of interval durations and CV^2 of the interval durations for each condition

Condition	aTc 0 ng/ml (37°C)	aTc 15 ng/ml (24°C)	aTc 15 ng/ml (37°C)
No. cells	504	178	113
No. intervals	180	152	254
Interval mean (s)	939	974	617
Interval std (s)	459	676	367
Interval CV^2	0.21	0.48	0.35

Table 2. Log-likelihood and durations of the steps of the inferred models with d steps, for each condition

	aTc 0 ng/ml (37°C)		aTc 15 ng/ml (24°C)		aTc 15 ng/ml (37°C)	
d	Log-likelihood	Durations (s)	Log-likelihood	Durations (s)	Log-likelihood	Durations (s)
1	–1412	939	–1198	975	–1886	617
2	–1369	(470, 470)	–1174	(487, 487)	–1836	(309, 309)
3	–1356	(313, 313, 313)	–1171	(620, 240, 115)	–1828	(254, 254, 109)

There is no implied temporal order for the steps.

Table 3. Likelihood-ratio test P values between pairs of models for each condition

(d_0, d_1)	aTc 0 ng/ml (37°C)	aTc 15 ng/ml (24°C)	aTc 15 ng/ml (37°C)
(1, 2)	0	3.02×10^{-12}	0
(2, 3)	7.27×10^{-7}	0.027	1.20×10^{-4}
(3, 4)	0.342	0.268	0.370

The null model is the d_0 step model (where d_0 is 1, 2, or 3) while the alternative model is the d_1 step model (where $d_1 = d_0 + 1$)

Table 4. P values from the Kolmogorov-Smirnov test between the empirical distribution and the various inferred models with d steps

d	aTc 0 ng/ml (37°C)	aTc 15 ng/ml (24°C)	aTc 15 ng/ml (37°C)
1	4.84×10^{-13}	4.81×10^{-5}	1.27×10^{-11}
2	1.10×10^{-4}	0.725	0.0485
3	0.0782	0.844	0.378
4	0.662	0.842	0.272

other hand affects the duration of the three steps (compare cases A and C in Table 2).

It is possible to provide additional support to these results, as well as to the assumption that each step follows an exponential distribution in duration, using a set of logical pairwise Kolmogorov-Smirnov (K–S) tests. One can compare the distributions of intervals between transcription events, for each condition, between the empirical cumulative distribution function of each case and the corresponding cumulative distribution function of the inferred models with d-steps, for all values of d. If the model accurately describes the measurements, the empirical and the inferred distributions should be indistinguishable by the K–S test. The comparisons (i.e. the P values) are shown in Table 4. Usually, for P values smaller than 0.01, it is concluded that the two distributions differ significantly.

From Table 4, in case A (aTc 0 ng/ml, 37°C), the models with less than 3 steps do not accurately match the measured data. In case B (aTc 15 ng/ml, 24°C), only the 1-step model does not accurately match the data. This, as noted, is because of the increase in duration in two of the steps because of the lower temperature, rendering the effects of the third step much less significant in the overall distribution of intervals. Finally, in case C, we have the same result as in case A, that is, models with less than 3 steps do not accurately match the measured data. These results support the previous conclusions, using the likelihood ratio test, regarding the number of sequential steps that determine the shape of the distribution of intervals in each condition.

Finally, we tested whether during our *in vivo* measurements, the kinetics of production of RNA changed over time because of possible changes in the intracellular concentration of aTc. This could occur if degradation because of light sensitivity of intracellular aTc or its slow diffusion across the membrane were significant. That is, if either effect is significant, it should be possible to distinguish between the distributions of intervals obtained in the first 30 min and those obtained in the last 30 min of the hour-long measurements. We extracted these two sub-distributions from each induction condition and compared them with the Kolmogorov-Smirnov test. The Kolmogorov-Smirnov test was unable to differentiate the two distributions in any condition (all P values > 0.1), demonstrating that the measurements were done at an approximate steady state. In particular, for case A (aTc 0 ng/ml, 37°C), the P value was 0.32; for case B (aTc 15 ng/ml, 24°C); it was 0.16 and for case C (aTc 15 ng/ml, 37°C), it was 0.78.

DISCUSSION

Previous studies have shown that the kinetics of transcription initiation of P_{tetA} is heavily dependent on induction and on environmental factors such as temperature (8,16,35,56). Other studies have shown that RNA production in bacteria is a stochastic (24,69) and a multi-step process (30), generally subject to complex regulatory mechanisms (8). Finally, recent studies have shown that the cell-to-cell diversity in RNA numbers, and likely protein numbers, can be significantly affected by processes other than gene expression (47,48,51). Therefore, the assessment of the kinetics of gene expression and regulation requires *in vivo* measurements of RNA production dynamics in individual cells, one event at a time, under various induction and environmental conditions (40).

The measured *in vivo* distributions of intervals between consecutive productions of RNA molecules in single cells are found to be sub-Poissonian, for the induction levels and temperatures tested. This was also observed in the case of P_{lar} (40). The sub-Poissonian nature of the kinetics explains the low cell-to-cell diversity in RNA numbers observed at the cell population level. Relevantly, the distributions of intervals, including their mean and variance, are found to respond readily and discernibly to induction as well as temperature, revealing the plasticity of the expression mechanism of TetA. The plasticity appears to arise from the diversity of the changes in the durations of the various steps in response to differing induction levels and temperature.

Our results assume that the measurements are only affected by intrinsic noise sources in transcription. Downstream events, such as translation or RNA degradation, do not affect the results, as we detect RNA molecules as soon as these are produced and study only the time intervals between these events. It is necessary to discuss if other noise sources, aside intrinsic noise in transcription, could affect diversity in number of produced RNA molecules per cell. It may be that differences in the amounts of TetR and/or aTc in each cell could contribute to this diversity (i.e. be a significant source of extrinsic noise (70)). First, the strain used here overexpresses TetR (DH5αPRO produces constitutively around 7000 dimeric Tet repressors per cell during logarithmic growth (8)); thus, we expect the contribution of

diversity in TetR numbers to the diversity in RNA numbers to be negligible. As for aTc, we found no evidence, at least at the population level, of varying rates of transcription initiation because of varying concentrations of aTc over time (e.g. because of depletion), as we found no difference in the kinetics of RNA production during the first and second half of the measurement period. Additionally, the *tetA* gene, responsible for expressing TetA, which confers tetracycline resistance (11) (by pumping it out of the cell) is not present in our strain. Finally, diversity in the numbers of either aTc or TetR in the cells is expected to only increase diversity, not decrease it (and thus cannot be the explanation for the observed sub-poissonian kinetics). Nevertheless, it is stressed that our measurements are not sufficient to predict the cell to-cell-diversity in number of RNA molecules under the control of P_{tetA} as other factors, such as RNA degradation (45) and RNA partitioning in cell division (47) need to be considered.

In this regard, measurements by fluorescent *in situ* hybridization of RNA numbers under the control of 20 *E. coli* promoters (42,43) exhibited high values of cell-to-cell diversity. Another work reported Fano factors of mRNA numbers for 137 highly expressed genes in *E. coli*, ranging from 1 to 3, using a yellow fluorescent protein fusion library for *E. coli* (44). Although these results could be because of super-Poissonian transcript production from the strongly expressing promoters studied, other explanations cannot be ruled out. For example, it may be that although the production is sub-Poissonian, the observed diversity is a result of the subsequent contribution from complex RNA degradation mechanisms (45) and imperfect partitioning of RNA molecules in cell division ([47,48,51), among other things such as the biased segregation of unwanted substances (e.g. the fluorescent molecules used to tagged the RNA) (49,52). In any case, we note that our measured distributions of intervals between transcription events cannot be explained by models, such as the ''on-off'' model of transcription initiation (43,71), as this model entails super-Poissonian kinetics.

The kinetics of RNA production under the control of P_{tetA} can be explained by a model of transcription initiation with successive ''rate-limiting'' steps, each of which is exponentially distributed in duration. From the inference of the number and duration of these steps in several conditions, we found that induction with aTc significantly changes the RNA production kinetics by reducing the duration of all rate-limiting steps, to various degrees. In particular, one of the steps becomes almost indiscernible. Meanwhile, lowering temperature under full induction by aTc increases the duration of two of the steps, but not of the third step, causing the kinetics to be well-fit by a two-step model under these conditions. Note that it is not possible to determine which steps [e.g. closed complex, open complex or isomerization (28)] are affected by aTc and temperature. Novel experimental techniques are necessary to perform this study *in vivo*. However, we can rule out TetR dissociation from the promoter as one of the rate-limiting steps. The complex TetR-promoter has a half-life of 12 s (37), which is a much faster process than the measured rate-limiting steps. Additionally, although TetR, when bound by aTc, may retain some ability to bind to the DNA [although this ability is reduced by approximately 9 orders of magnitude (72)], there is no evidence that this complex would have a longer half-life than when the DNA is bound by TetR alone.

A recent work used the methods used here to analyse the kinetics of P_{lar} (40). The measurements were made at 24°C. It is of interest to compare them with our measurements regarding the response to induction. First, the kinetics of RNA production of P_{lar} is also sub-Poissonian. Also, induction of P_{lar} with IPTG and arabinose reduces the duration of the rate-limiting steps. The main differences between these two promoters are in the mean duration of the intervals at 24°C ([for P_{lar}, this mean duration is ~1500 s (40), whereas for P_{tetA}, it is ~1000 s]) and in the variability of the intervals. For P_{lar}, the CV^2 of the durations of these intervals is 0.70, whereas for P_{tetA}, it is 0.52. From this, we conclude that the kinetics of transcription initiation of P_{tetA} is less noisy than that of P_{lar}. It is worthwhile to mention that the observations of the behaviour of P_{tetA} (a native promoter) suggest that the sub-Poissonian kinetics of RNA production is not, for example, an artefact of the synthetic nature of P_{lar}, and that it may be a common feature of the dynamics of transcript production in *E. coli*. Also, the results support several previous observations on the effect of temperature on the kinetics of transcription, but further show that the changes in kinetics are due, in part, to the alteration of the mean duration of the intermediate steps in transcription initiation.

P_{tetA} controls the expression of TetA, which is responsible for the active efflux of tetracycline-Mg^{2+} complexes. This protein's function justifies the need for such a stringent regulatory mechanism so as to ensure that TetA is present in the appropriate amount because both tetracycline and TetA (in high amounts) are harmful to the cell (12). We find that this control is achieved not only by the negative feedback mechanism of the *tet* operon (12) but also by a sub-Poissonian kinetics of transcription initiation. Relevantly, although robust (less noisy than a Poisson process), this system is nevertheless sensitive to external stimuli, such as tetracycline, and temperature because its behaviour discernibly changes with temperature and inducer concentration.

In the future, it will be of interest to further analyse how the dynamics of P_{tetA} differs in other environmental conditions, such as in differing concentrations of hydrogen ions and metabolites. Such studies may provide insights on the plasticity of the kinetics of gene expression in bacteria and thus guide the engineering of synthetic genetic circuits with specific behavioural patterns.

SUPPLEMENTARY DATA

Supplementary Data are available at NAR Online: Supplementary Tables 1 and 2, Supplementary Figures 1 and 2 and Supplementary Movies 1 and 2.

ACKNOWLEDGEMENTS

The authors thank F.G. Biddle for useful advice. A.-B. M. executed the qPCR measurements.

FUNDING

Academy of Finland [126803 to A.S.R.]; Finnish Funding Agency for Technology and Innovation (TEKES) [40284/08 to O.Y.-H.]; TUT President's Doctoral Programme. Funding for open access charge: TEKES [40284/08 to O.Y.-H.].

Conflict of interest statement. None declared.

REFERENCES

1. McNaught,A.D. and Wilkinson,A. (1997) IUPAC. Compendium of Chemical Terminology. (the "Gold Book"). 2nd edn. Blackwell Scientific Publications, Oxford.
2. Duggar,B.M. (1948) Aureomycin: a product of the continuing search for new antibiotics. *Ann. N. Y. Acad. Sci.*, **51**, 177–181.
3. Connel,S.R., Tracz,D.M., Nierhaus,K.H. and Taylor,D.E. (2003) Ribosomal protection proteins and their mechanism of tetracycline resistance. *Antimicrob. Agents Chemother.*, **47**, 3675–3681.
4. Schnappinger,D. and Hillen,W. (1996) Tetracyclines: antibiotic action, uptake, and resistance mechanisms. *Arch. Microbiol.*, **165**, 359–369.
5. Hillen,W., Scholimeier,K. and Gatz,C. (1984) Control of expression of the Tn10-encoded tetracycline resistance operon II. Interaction of RNA polymerase and TET repressor with the tet operon regulatory region. *J. Mol. Biol.*, **172**, 185–201.
6. Gossen,M. and Bujard,H. (1992) Tight control of gene expression in mammalian cells by tetracycline-responsive promoters. *Proc. Natl. Acad. Sci. USA.*, **89**, 5547–5551.
7. Nguyen,T.M.N., Phan,Q.G., Duong,L.P., Bertrand,K.P. and Lenski,R.E. (1989) Effects of carriage and expression of the Tn10 tetracycline-operon on fitness of *E. coli cells. Mol. Biol. Evol.*, **6**, 213–225.
8. Lutz,R. and Bujard,H. (1997) Independent and tight regulation of transcriptional units in *Escherichia coli* via the LacR/O, the TetR/O and AraC/I1-I2 regulatory elements. *Nucleic Acids Res.*, **25**, 1203–1210.
9. Lazarevic,V., Margot,P., Soldo,B. and Karamata,D. (1992) Sequencing and analysis of the Bacillus subtilis lytRABC divergon: a regulatory unit encompassing the structural genes of the N-acetylmuramoyl-L-alanine amidase and its modifier. *J. Gen. Microbiol.*, **138**, 1949–1961.
10. Collier,G.B., Mattson,T.L., Connaughton,J.F. and Chirikjian,J.G. (1994) A novel Tn10 tetracycline regulon system controlling expression of the bacteriophage T3 gene encoding S-adenosyl-L-methionine hydrolase. *Gene*, **148**, 75–80.
11. Beck,C.F., Mutzel,R., Barbe,J. and Müller,W. (1982) A multifunctional gene (*tetR*) controls Tn*10*-encoded tetracycline resistance. *J. Bacteriol.*, **150**, 63–642.
12. Hillen,W. and Berens,C. (1994) Mechanisms underlying expression of Tn*l0* encoded tetracycline resistance. *Annu. Rev. Microbial.*, **48**, 345–369.
13. Orth,P., Schnappinger,D., Hillen,W., Saenger,W. and Hinrichs,W. (2000) Structural basis of gene regulation by the tetracycline inducible Tet repressor-operator system. *Nat. Struct. Biol.*, **7**, 215–219.
14. Biliouris,K., Daoutidis,P. and Kaznessis,Y.N. (2011) Stochastic simulations of the tetracycline operon. *BMC Syst. Biol*, **5**, 9.
15. Skerra,A. (1994) Use of the tetracycline promoter for the tightly regulated production of a murine antibody fragment in *Escherichia coli. Gene*, **151**, 131–135.
16. Bertrand,K.P., Postle,K., Wray,L.V. Jr and Reznikoff,W.S. (1984) Construction of a single-copy promoter vector and its use in analysis of regulation of the transposon Tn*10* tetracycline resistance determinant. *J. Bacteriol.*, **158**, 910–919.
17. Gardner,T.S., Cantor,C.R. and Collins,J.J. (2000) Construction of a genetic toggle switch in Escherichia coli. *Nature*, **403**, 339–342.
18. Elowitz,M.B. and Leibler,S. (2000) A synthetic oscillatory network of transcriptional regulators. *Nature*, **403**, 335–338.
19. Becskei,A. and Serrano,L. (2000) Engineering stability in gene networks by autoregulation. *Nature*, **405**, 590–593.
20. Becskei,A., Séraphin,B. and Serrano,L. (2001) Positive feedback in eukaryotic gene networks: cell differentiation by graded to binary response conversion. *EMBO J.*, **20**, 2528–2535.
21. Deans,T.L., Cantor,C.R. and Collins,J.J. (2007) A tunable genetic switch based on RNAi and repressor proteins for regulating gene expression in mammalian cells. *Cell*, **130**, 363–372.
22. Nevozhay,D., Adams,R.M., Murphy,K.F., Josic,K. and Balázsi,G. (2009) Negative autoregulation linearizes the dose-response and suppresses the heterogeneity of gene expression. *Proc. Natl. Acad. Sci. U.S.A.*, **106**, 5123–5128.
23. Nandagopal,N. and Elowitz,M.B. (2011) Synthetic biology: integrated gene circuits. *Science*, **333**, 1244–1248.
24. Kaern,M., Elston,T.C., Blake,W.J. and Collins,J.J. (2005) Stochasticity in gene expression: from theories to phenotypes. *Nat. Rev. Genet.*, **6**, 451–464.
25. McClure,W.R. (1985) Mechanism and control of transcription initiation in prokaryotes. *Annu. Rev. Biochem.*, **54**, 171–204.
26. Uptain,S., Kane,M. and Chamberlin,M. (1997) Basic mechanisms of transcript elongation and its regulation. *Annu Rev Biochem.*, **66**, 117–172.
27. Browning,D.F. and Busby,S.J. (2004) The regulation of bacterial transcription initiation. *Nat. Rev. Microbiol.*, **2**, 57–65.
28. deHaseth,P.L., Zupancic,M.L. and Record,M.T. (1998) RNA polymerase-promoter interactions: the comings and goings of RNA polymerase. *J. Bacteriol.*, **180**, 3019–3025.
29. Nierman,W.C. and Chamberlin,M.J. (1979) Studies of RNA chain initiation by *Escherichia coli* RNA polymerase bound to T7 DNA. Direct analysis of the kinetics and extent of RNA chain initiation at T7 promoter A1. *J. Biol. Chem.*, **254**, 7921–7926.
30. McClure,W.R. (1980) Rate-limiting steps in RNA chain initiation. *Proc. Natl. Acad. Sci. U.S.A.*, **77**, 5634–5638.
31. Lutz,R., Lozinski,T., Ellinger,T. and Bujard,H. (2001) Dissecting the functional program of *Escherichia coli* promoters: the combined mode of action of Lac repressor and AraC activator. *Nucleic Acids Res.*, **29**, 3873–3881.
32. Buc,H. and McClure,W.R. (1985) Kinetics of open complex formation between *Escherichia coli* RNA polymerase and the lac UV5 promoter. Evidence for a sequential mechanism involving three steps. *Biochemistry*, **24**, 2712–2723.
33. Kandhavelu,M., Lihavainen,E., Muthukrishnan,A.B., Yli-Harja,O. and Ribeiro,A.S. (2012) Effects of Mg2+ on in vivo transcriptional dynamics of the lar Promoter. *Biosystems*, **107**, 129–134.
34. Smolander,O.P., Kandhavelu,M., Mannerström,H., Lihavainen,E., Kalaichelvan,S., Healy,S., Yli-Harja,O., Karp,M. and Ribeiro,A.S. (2011) Cell-to-cell diversity in protein levels of a gene driven by a tetracycline inducible promoter. *BMC Mol. Biol.*, **12**, 21.
35. Bertrand-Burggraf,E., Lefèvre,J.F. and Daune,M. (1984) A new experimental approach for studying the association between RNA polymerase and the tet promoter of pBR322. *Nucleic Acids Res.*, **12**, 1697–1706.
36. Degenkolb,J., Takahashi,M., Ellested,G.A. and Hillen,W. (1991) Structural requirements of tetracycline-Tet repressor interaction: determination of equilibrium binding constants for tetracycline analogs with the Tet repressor. *Antimicrob. Agents Chemother.*, **35**, 1591–1595.
37. Murphy,K.F., Adams,R.M., Wang,X., Balázsi,G. and Collins,J.J. (2010) Tuning and controlling gene expression noise in synthetic gene networks. *Nucleic Acids Res.*, **38**, 2712–2726.
38. Schubert,P., Pfleiderer,K. and Hillen,W. (2004) Tet repressor residues indirectly recognizing anhydrotetracycline. *Eur. J. Biochem.*, **271**, 2144–2152.
39. Oliva,B., Gordon,G., McNicholas,P., Ellestad,G. and Chopra,I. (1992) Evidence that tetracycline analogs whose primary target is not the bacterial ribosome cause lysis of *Escherichia coli. Antimicrob. Agents Chemother.*, **36**, 913–919.

40. Kandhavelu,M., Mannerström,H., Gupta,A., Häkkinen,A., Lloyd-Price,J., Yli-Harja,O. and Ribeiro,A.S. (2011) In vivo kinetics of transcription initiation of the lar promoter in *Escherichia coli*. Evidence for a sequential mechanism with two rate limiting steps. *BMC Sys. Biol.*, **5**, 149.
41. Saecker,R.M., Record,M.T. and deHaseth,P.L. (2011) Mechanism of bacterial transcription initiation: RNA polymerase - promoter binding, isomerization to initiation-competent open complexes, and initiation of RNA synthesis. *J. Mol. Biol.*, **412**, 754–771.
42. Golding,I., Paulsson,J., Zawilski,S.M. and Cox,E.C. (2005) Real-time kinetics of gene activity in individual bacteria. *Cell*, **123**, 1025–1036.
43. So,L.H., Ghosh,A., Zong,C., Sepúlveda,L.A., Segev,R. and Golding,I. (2011) General properties of transcriptional time series in *Escherichia coli*. *Nat. Genet.*, **43**, 554–560.
44. Taniguchi,Y., Choi,P.J., Li,G.W., Chen,H., Babu,M., Hearn,J., Emili,A. and Xie,X.S. (2010) Quantifying E. coli proteome and transcriptome with single-molecule sensitivity in single cells. *Science*, **329**, 533–538.
45. Yarchuk,O., Jacques,N., Guillerez,J. and Dreyfus,M. (1992) Interdependence of translation, transcription and mrna. *J. Mol. Biol.*, **5**, 581–596.
46. Llopis,P.M., Jackson,A.F., Sliusarenko,O., Surovtsev,I., Heinritz,J., Emonetand,T. and Jacobs-Wagner,C. (2010) Spatial organization of the flow of genetic information in bacteria. *Nature*, **466**, 77–81.
47. Huh,D. and Paulsson,J. (2010) Non-genetic heterogeneity from stochastic partitioning at cell division. *Nat. Genet.*, **43**, 95–100.
48. Huh,D. and Paulsson,J. (2011) Random partitioning of molecules at cell division. *Proc. Natl Acad. Sci. USA.*, **108**, 15004–15009.
49. Lindner,A.B., Madden,R., Demarez,A., Stewart,E.J. and Taddei,F. (2008) Asymmetric segregation of protein aggregates is associated with cellular aging and rejuvenation. *Proc. Natl Acad. Sci. USA.*, **105**, 3076–3081.
50. Stewart,E., Madden,R., Paul,G. and Taddei,F. (2005) Aging and death in an organism that reproduces by morphologically symmetric division. *PLoS Biol.*, **3**, 295–300.
51. Lloyd-Price,J., Lehtivaara,M., Kandhavelu,M., Chowdhury,S., Muthukrishnan,A.B., Yli-Harja,O. and Ribeiro,A.S. (2011) Probabilistic RNA partitioning generates transient increases in the normalized variance of RNA numbers in synchronized populations of *Escherichia coli*. *Mol. Biosyst.*, **8**, 565–571.
52. Lloyd-Price,J., Häkkinen,A., Kandhavelu,M., Marques,I.J., Chowdhury,S., Lihavainen,E., Yli-Harja,O. and Ribeiro,A.S. (2012) Asymmetric disposal of individual protein aggregates in *Escherichia coli*, one aggregate at a time. *J. Bact.*, **194**, 1747–1752.
53. Yu,J., Xiao,J., Ren,X., Lao,K. and Xie,X.S. (2006) Probing gene expression in live cells. *Science*, **311**, 1600–1603.
54. Xie,X.S., Choi,P.J., Li,G.W., Lee,N.K. and Lia,G. (2008) Single-molecule approach to molecular biology in living bacterial cells. *Annu. Rev. Biophys.*, **37**, 417–444.
55. Le,T.T., Harlepp,S., Guet,C.C., Dittmar,K., Emonet,T., Pan,T. and Cluzel,P. (2005) Real-time RNA profiling within a single bacterium. *Proc. Natl Acad. Sci. USA.*, **102**, 9160–9164.
56. Korpela,M., Kurittu,J.S., Karvinen,J.T. and Karp,M.T. (1998) A recombinant *Escherichia coli* sensor strain for the detection of tetracyclines. *Anal. Chem.*, **70**, 4457–4462.
57. Golding,I. and Cox,E. (2004) RNA dynamics in live Escherichia coli cells. *Proc. Natl Acad. Sci. USA.*, **101**, 11310–11315.
58. Nevo-Dinur,K., Nussbaum-Shochat,A., Ben-Yehuda,S. and Amster-Choder,O. (2011) Translation-independent localization of mRNA in *Escherichia coli*. *Science*, **25**, 1081–1084.
59. Chini,V., Foka,A., Dimitracopoulos,G. and Spiliopoulou,I. (2007) Absolute and relative real-time PCR in the quantification of tst gene expression among methicillin-resistant Staphylococcus aureus: evaluation by two mathematical models. *Lett. Appl. Microbiol.*, **45**, 479–484.
60. Lee,C., Kim,J., Shin,S.G. and Hwang,S. (2006) Absolute and relative QPCR quantification of plasmid copy number in *Escherichia coli*. *J. Biotec.*, **123**, 273–280.
61. Campbell,R.E., Tour,O., Palmer,A.E., Steinbach,P.A., Baird,G.S., Zacharias,D.A. and Tsien,R.Y. (2002) A monomeric red fluorescent protein. *Proc. Natl Acad. Sci. USA.*, **99**, 7877–7882.
62. Livak,K.J. and Schmittgen,T.D. (2001) Analysis of relative gene expression data using real-time quantitative PCR and the 2(−Delta Delta C(T)) Method. *Methods*, **25**, 402–408.
63. Shales,S.W., Chopra,I. and Ball,P.R. (1980) Evidence for more than one mechanism of plasmid-determined tetracycline resistance in *Escherichia coli*. *J. Gen. Microbiol.*, **121**, 221–229.
64. Chowdhury,S., Kandhavelu,M., Yli-Harja,O. and Ribeiro,A.S. (2011) An interacting multiple model filter based autofocus strategy for confocal time-lapse microscopy. *J. Microscopy*, **245**, 265–275.
65. Chen,T.B., Lu,H., Lee,Y.S. and Lan,H.J. (2008) Segmentation of cDNA microarray images by kernel density estimation. *J. Biomed. Info.*, **41**, 1021–1027.
66. Toulokhonov,I. and Landick,R. (2006) The flap domain is required for pause RNA hairpin inhibition of catalysis by RNA polymerase and can modulate intrinsic termination. *Mol. Cell*, **12**, 1125–1136.
67. Peabody,D.S. (1993) The RNA binding site of bacteriophage MS2 coat protein. *EMBO J.*, **12**, 595–600.
68. China,A., Tare,P. and Nagaraja,V. (2010) Comparison of promoter-specific events during transcription initiation in mycobacteria. *Microbiology*, **156**, 1942–1952.
69. Arkin,A., Ross,J. and McAdams,H.M. (1998) Stochastic kinetic analysis of developmental pathway bifurcation in phage λ-infected *Escherichia coli* cells. *Genetics*, **149**, 1633–1648.
70. Elowitz,M.B., Levine,A.J., Siggia,E.D. and Swain,P.S. (2002) Stochastic gene expression in a single cell. *Science*, **297**, 1183–1186.
71. Peccoud,J. and Ycart,B. (1995) Markovian modelling of gene product synthesis. *Theor. Popul. Biol.*, **48**, 222–234.
72. Lederer,T., Takahashi,M. and Hillen,W. (1995) Thermodynamic analysis of tetracycline-mediated induction of Tet repressor by a quantitative methylation protection assay. *Anal. Biochem.*, **232**, 190–196.

Publication V

S. Chowdhury, P. Ruusuvuori, P. Liberali, P. Rämö, L. Pelkmans, and O. Yli-Harja, "Automated cell tracking and cell lineage construction with improved performance," In *Proceedings of the 6th International Workshop on Computational Systems Biology*,(Århus), Denmark, June 10-12, 2009, pp. 27-30.

AUTOMATED CELL TRACKING AND CELL LINEAGE CONSTRUCTION WITH IMPROVED PERFORMANCE

Sharif Chowdhury[*a], *Pekka Ruusuvuori*[a], *Prisca Liberali*[b], *Pauli Rämö*[b], *Lucas Pelkmans*[b], *Olli Yli-Harja*[a]

* Corresponding Author. E-mail: sharif.chowdhury@tut.fi
[a]Department of Signal Processing, Tampere University of Technology, Tampere, Finland.
[b]Swiss Federal Institute of Technology, Zürich, Switzerland.

ABSTRACT

Automated nuclei tracking is a challenging problem in computational biology. In this paper we considered a state of the art algorithm which solved this problem by exploiting level set method and interacting multiple model (IMM) filter. However, we experienced that the level set method often suffered from imbalanced area distribution among cells that are in close contact; whose continuation in several frames led to false positive cell divisions. Cell lineage construction was affected a lot by this kind of error scenario. In order to equalize area distribution among the nuclei that were interacting with each other we applied k-means clustering algorithm as a post processing step of level set and this post processing improved accuracy of cell lineage construction in the range of 9-16%.

1. INTRODUCTION

With the increased power of modern computing and imaging technology, biology became much more computational discipline than it was before. With the aid of high throughput technologies it is common in cell or molecular biology research to obtain time series digital images from microscope. Yet, to accelerate research, high throughput imaging needs to be paired with automated analysis. The most studied analysis for microscopic images is object detection. The results of automated detection have led to subsequent analyses e. g. object tracking in time series images. Several attempts have been made by many research group for microscopic object tracking in time-laps images [1-5]. In this paper we considered a recent solution for cell tracking, which was originally proposed in [4], and extended this method to achieve higher level of accuracy in the sense of lineage construction.

In section two of this article we briefly discuss different algorithms for microscopic object tracking. Section three describes the base algorithm, our proposed modification as well as an example scenario to illustrate the effect of modification. In section four we compare achieved results from modified algorithm against original algorithm and finally in section five we conclude the paper.

2. RELATED WORK

Cell or nuclei tracking solutions can be classified into two major classes – 1) tracking by detection and 2) tracking by model evolution [4]. In tracking by detection approach cells are detected independently in every frame and the detection results are fed to the tracking module. Usually, the tracking module links objects between consecutive frames by optimizing one or more matching parameters. The object tracking solutions proposed in [3, 5] are some examples of this kind of solution. Tracking by detection and parameter optimization is efficient in the sense that it requires less computation. Indeed, such method may be accurate enough when objects are sparsely populated and imaging has been done with reasonably high value of SNR [4, 6-7].

The second class of tracking algorithm uses model evolution to track objects from one frame to another. In this class of algorithms, the 'tracking by geometric active contour model evolution' is reported as one efficient approach because of its higher tracking accuracy [4]. On the other hand, active contour evolution potentially requires more computation. Indeed, recent works [8, 9] had minimized this computational cost, enabling its use in cell tracking [4]. The discussed method in this paper also belongs to this second class of algorithm.

Most of the tracking algorithms, whether exploiting detection or model evolution, apply probabilistic filter for future state prediction. Kalman filtering is the most general tool for future state prediction in tracking systems, which relying on two different models namely motion model and measurement model expressed in (1) and (2) respectively.

$$S_k = FS_{k-1} + V_{k-1} \quad (1)$$

$$Z_k = HS_k + W_k \quad (2)$$

Here, S_k is the state of the system (i. e. location, speed, acceleration), F is the state transition model, H is the measurement model, V_k, W_k are motion model noise and measurement model noise, having zero mean and Gaussian distribution, Z_k (location) is the measured state and the subscript k represents the time point. In practice, however often some variation of Kalman filter or some other probabilistic filter e. g. interacting multiple model filter (IMM), joint probabilistic data association filter (JPDAF) or particle filter are often used for future state prediction [2, 4, 10].

3. PROPOSED SOLUTION

The proposed tracking algorithm is an extension of the work presented in [4]. In brief, the algorithm can be divided in to two independent steps- 1) nuclei region segmentation and 2) trajectory linking. For nuclei region segmentation, we applied a variation of Otsu's threshold [11] known as Otsu adaptive threshold. It is worth to mention that further separation among cells that are in contact with each other is no longer necessary. Since, level set evolution can automatically separate cells if they were separated in any earlier frame [4]. The trajectory linking process consists of two different tracking algorithms in series. The first one applies geometric active contour evolution based level set algorithm. The result from level set evolution is used by a Kalman filtering steps having multiple interacting motion patterns known as interacting multiple model filter. The whole linking process can be illustrated in the following eight steps.

`Step-1:` Apply level set evolution to evolve nuclei from predicted state to detected state.
`Step-2:` Update IMM filter coefficients based on level set evolution for further prediction.
`Step-3:` Identify the nuclei which are divided in between time point or frame K-1 and K and introduce new trajectory for each of these new born nuclei.
`Step-4:` Identify the nuclei which entered into the field of view from outside and add new trajectory for each of them.
`Step-5:` Try to link the newly entered nuclei with the trajectories lost in earlier frames using linear programming.
`Step-6:` Predict the next frame K+1 from current frame K using the IMM filter.
`Step-7:` Redistribute the pixels among the nuclei are in close contact or interacting with each other by K-means clustering algorithm.
`Step-8:` Apply the steps 1-7 for K = 1 to N. Where, N is the total number of time points.

The description of steps one to six as well as their application for cells or nuclei tracking has been discussed in [4, 8, 9, 12, 13]. Due to space limitations, we omit these details and refer the reader to the respective articles.

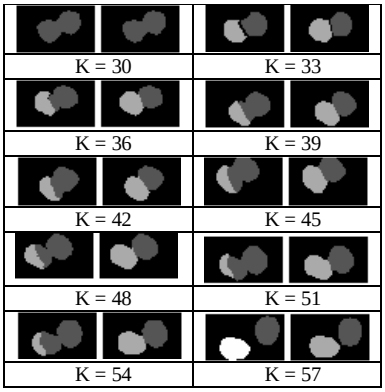

Figure-1(a): Effect of modification. (The left part represents the result from original algorithm and right part result from modified algorithm). The original parent cell started with dark color. After first time division at K= 33 one of the new born cell got level gray. In the original algorithm the gray cell detected as dead at K = 57 and the dark cell was divided once more.

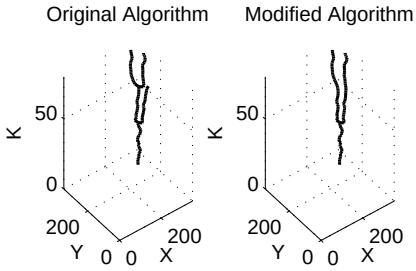

Figure-1(b): Effect of modification (time line presentation). The scenario presented in Figure-1(a) is presented in timeline.

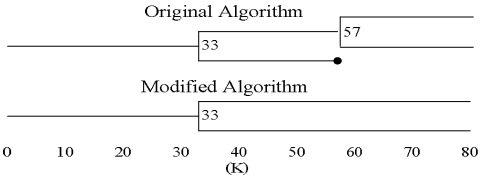

Figure 1(C): Lineage Representation of figure 1(b). Lineage with text presents cell division. Black circle indicates cell death. K is the frame number.

However, the modification we proposed is listed in step seven. The modification is based on the fact that if two or more cells were interacting with each other for long time then often some of the interacting nuclei acquire pixels which originally belonged to some other nuclei. This kind of artifact usually occurs due to noisy IMM filter prediction or complex dynamics of one or more interacting cells. Continuation of such of false pixel assignment for several frames may lead to false positive cell division as well as erroneous cell death detection.

To prevent such error, we applied K-means clustering algorithm for pixel assignment among the cells that were in close contact or interacting with each other. Generally, one drawback in K-means clustering algorithm is to find out the value of K, that is the number of clusters. Nevertheless, in this case the number of nuclei in contact with each other can be used as the number of existing clusters K. Here, we used the Euclidean distance from spatial centre of the cluster as distance metric for clustering. This modification did not introduce any artifacts, due to the fact that nuclei usually have round or elliptic shape with high compactness value. The effect of the improvement is illustrated in Figure-1(a) and Figure-1(b). In Figure-1(a), the left part of each image is the result from tracking algorithm without K-means clustering and the right part from algorithm with K-means clustering. A closer look at Figure-1(a) makes it clear that K-means clustering prevented false detection of cell death and as well as false positive cell division (K = 57). The Figure 1(b) and Figure (1c) represent the same scenario in timeline and lineage presentation, respectively.

4. RESULTS

We evaluated our proposed method with three different test cases. All the test cases contain nuclei from Hela cells. The first test case contained 10 nuclei in the starting frame and 41 nuclei in the final frame. Each frame had 512x512 pixels. The imaging was done at 20x magnification and the whole sequence contained 240 frames. The second and third sets were taken with identical imaging parameters both sets contained 1392x1040 pixels in each frame. Imaging was done over three days with 10x magnification at an interval of twenty minutes.

We evaluated the achieved results in three different ways. First, we considered the accuracy in nuclei detection for evaluation. We listed both results in Table-1.

Second, we considered the number of correct trajectory linking decisions made by both algorithms and total number of manual trajectory linking decisions. The obtained results and the comparisons are in Table-2. In Set-2, two cell regions were not identified throughout the whole sequence, which lead to less accurate overall results both in nuclei linking and lineage construction.

Table-1: Nuclei detection result.

Test Case	Number of Counted Nuclei	Number of Detected Nuclei.	Correctness (%)
Set-1	6093	6042	99
Set-2	6752	6330	94
Set-3	5870	5855	99
Overall	18715	18227	97

Table-2: Nuclei linking result.

Test Case	Manual Linking Count	Correct Linking (Modified Algorithm)		Correct Linking (Base Algorithm)	
		Total	%	Total	%
Set -1	6083	6030	99	6013	98
Set -2	6728	6311	93	6295	93
Set -3	5842	5824	99	5819	99
Overall	18653	18165	97	18127	97

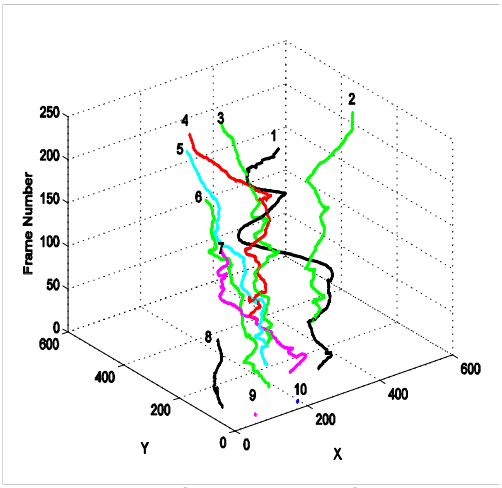

Figure-2: Nuclei trajectory in Timeline.

The main focus of this work is to improve lineage construction, which is presented in the third kind of result. In this result, we considered number of cells that were assigned in to correct lineage as evaluation metric. In Table-3 we compared the obtained result with modified algorithm against the original algorithm. At this point, it is worth noting that even small amount of errors in tracking decisions can affect the lineage accuracy a lot [4].

Finally, Figure-2 represents part of the results obtained by the modified algorithm in timeline presentation of nuclei trajectory. For illustration purpose, we plotted trajectories of only ten nuclei. Out of ten trajectories the nuclei related to trajectory numbers 8, 9 and 10 had gone out of the field of view in first few.

Table-3: Lineage Construction Result

Test Case	Cells in Manually constructed lineage	Correct Lineage (Modified Algorithm)		Correct Lineage (Base Algorithm)	
		Total	%	Total	%
Set -1	6093	6026	98	5041	82
Set -2	6752	6168	91	5597	82
Set -3	5870	5705	97	5189	88
Overall	18715	17899	95	15827	85

5. CONCLUSION

In this article we presented an algorithm for nuclei tracking, which is extended from [4]. The presented algorithm performed better in terms of nuclei lineage construction accuracy. Considering tracking decision, both algorithms performed almost equally well. On the other hand, considering lineage construction accuracy, the modified version outperformed the original algorithm by at least 9%. In our test cases, the results achieved for the original algorithm were much better than that reported in the article [4]. A possible reason behind this is the fact that the original algorithm was developed and tested with phase contrast images, whereas we applied for fluorescent microscope images. Generally it is accepted that detection and tracking is more challenging in phase contrast microscopy than in fluorescence microscopy. Finally, though, the proposed algorithm performed well in terms of lineage construction, it was slower still in comparison to parametric methods. Improving the computational efficiency will be a motivation for future development.

6. ACKNOLEDGEMENT

This work was supported by the National Technology Agency of Finland and the Academy of Finland, project No. 213462 (Finnish Centre of Excellence program (2006 - 2011)).

7. REFERENCES

[1] I. F. Sbalzarini and P. Koumoutsakos, "Feature Point Tracking and Trajectory Analysis for Video Imaging in Cell Biology," *Journal of Structural Biology*, vol. 151, no. 2, pp. 182-195, 2005.

[2] I. Smal, W. Niessen, E. Meijering, "New Detection Scheme for Multiple Object Tracking in Fluorescence Microscopy by Joint Probabilistic Data Association Filtering," *Biomedical Imaging: From Nano to Macro, 2008. ISBI 2008. 5th IEEE International Symposium*, pp. 264 – 267, May 2008.

[3] Xiaowei Chen, Xiaobo Zhou, and Stephen T. C. Wong, "Automated Segmentation, Classification, and Tracking of Cancer Cell Nuclei in Time-Lapse Microscopy," IEEE Transaction on Biomedical Engineering, pp. 762-766, April 2006.

[4] Kang Li, Eric D. Miller, Mei Chen, Takeo Kanade, Lee E. Weiss and Phil G. Campbell, "Cell population tracking and lineage construction with spatiotemporal context," *Medical Image Analysis*, Volume 12, Issue 5, pp. 546-566, Oct. 2008.

[5] Al-Kofahi, O., Radke, R.J., Goderie, S.K., Shen, Q., Temple, S., Roysam, B., "Automated cell lineage construction: a rapid method to analyze clonal development established with murine neural progenitor cells," *Cell Cycle*, Volume 5, Issue. 3, pp. 327–335, 2006.

[6] D. Thomann, D. R. Rines, P. K. Sorger, and G. Danuser, "Automaticfluorescent tag detection in 3D with superresolution: application to the analysis of chromosome movement," J. Microsc., Volume 208, Issue 1, pp.49–64, Oct. 2002.

[7] M. K. Cheezum, W. F.Walker, andW. H. Guilford, "Quantitative comparison of algorithms for tracking single fluorescent particles," *Biophys. J.*, Volume 81, Issue. 4, pp. 2378–2388, Oct. 2001.

[8] Shi, Y., Karl, W.C., "A fast level set method without solving PDEs," *Proceedings of the IEEE International Conference Acoustics Speech and Signal Processing*, Volume 2, pp. 97–100, 2005.

[9] Shi, Y., Karl, W.C., "Real-time tracking using level sets," *Proceedings of the IEEE Conference on Computer Vision and Pattern Recognition*, Volume 2, pp. 34–41, 2005.

[10] I. Smal, K. Draegestein, N. Galjart, W. Niessen, E. Meijering, "Particle Filtering for Multiple Object Tracking in Dynamic Fluorescence Microscopy Images: Application to Microtubule Growth Analysis," *IEEE Transactions on Medical Imaging*, Volume 27, Issue 6, pp. 789-804, June 2008.

[11] N. Otsu (1979), "A threshold selection method from graylevel histograms," *IEEE Trans. Sys., Man., Cyber*. Volume 9, Issue 1, pp. 62–66 Jan. 1979.

[12] Kang Li, Takeo Kanade, "Cell Population Tracking and Lineage Construction Using Multiple-Model Dynamics Filters and Spatiotemporal Optimization," *Proceedings of the 2nd International Workshop on Microscopic Image Analysis with Applications in Biology (MIAAB)*, September, 2007.

[13] H. A. P. Blom, "An efficient filter for abruptly changing systems," *Proc. 23rd IEEE Conference on Decision and Control*, pp. 656–65, Dec. 1985

Tampereen teknillinen yliopisto
PL 527
33101 Tampere

Tampere University of Technology
P.O.B. 527
FI-33101 Tampere, Finland

ISBN 978-952-15-3732-5
ISSN 1459-2045